Gold Nanoparticles as Drug Delivery Systems for Brain Cancer Therapy

Inaugural dissertation

for the attainment of the title of doctor
in the Faculty of Mathematics and Natural Sciences

at the Heinrich Heine University Düsseldorf

presented by

Beatriz Eugenia Maria (Melara Benitez) Giesen

from San Salvador, El Salvador

Düsseldorf, May 2021

from the institute for Inorganic Chemistry and Structural Chemistry I
at the Heinrich Heine University Düsseldorf

Published by permission of the
Faculty of Mathematics and Natural Sciences at
Heinrich Heine University Düsseldorf

Supervisor: Prof. Dr. Christoph Janiak
Co-supervisor: PD Dr. Ulf Dietrich Kahlert

Date of the oral examination: 02.07.2021

Eidesstattliche Erklärung

Ich, Frau Beatriz Eugenia Maria Giesen, versichere an Eides statt, dass die vorliegende Dissertation von mir selbstständig und ohne unzulässige fremde Hilfe unter Beachtung der „Grundsätze zur Sicherung guter wissenschaftlicher Praxis“ an der Heinrich-Heine-Universität Düsseldorf erstellt worden ist. Die aus fremden Quellen direkt oder indirekt übernommenen Gedanken sind als solche kenntlich gemacht. Die Arbeit wurde bisher weder im Inland noch im Ausland in gleicher oder ähnlicher Form einer anderen Prüfungsbehörde vorgelegt. Es wurden keine früheren erfolglosen Promotionsversuche unternommen.

Düsseldorf, 11.05.2021
……

Ort, Datum

Beatriz Giesen
……

Unterschrift

Acknowledgments

First and foremost, I would like to thank Prof. Dr. Christoph Janiak for the opportunity to be a part of his research group and providing me with such an interesting and meaningful topic for my PhD project. Your excellent supervision and model of leadership throughout my doctoral studies, both inside and outside of academia, deserve my endless gratitude. Thank you for your valuable assistance and dedication in the preparation and publication of my results for this dissertation. Furthermore, I am grateful for your support personally regarding the long process of my “Einbürgerung”, which would not have been possible without you.

I would also like to acknowledge PD Dr. Ulf Kahlert for welcoming me into the neurooncology group at Universitätsklinikum Düsseldorf and for taking over the co-supervision of this work. Thank you for introducing me to the exciting and new aspects of biomedicine involving my research and for your confidence in me. I greatly appreciate your helpful ideas and discussions during this time, as well as the supportive working environment you provide.

My gratitude also goes to Prof. Dr. Christian Ganter for his valuable suggestions, particularly concerning challenges in organic synthesis. I would like to thank all cooperation partners involved in my publications, especially Dr. Ann-Christin Nickel, whose expertise was crucial to the success of this project. Thank you for your hard work and your friendship. In addition, I would like to acknowledge Dr. Juri Barthel from Forschungszentrum Jülich for being an exceptional TEM mentor during these past four years. I appreciate the long hours of training and dedication you spent with me.

A special thanks goes to my dear nano-colleagues Seçil Öztürk, Dr. Alexa Schmitz, Dr. Marvin Siebels, Dr. Laura Schmolke and Dr. Karsten Klauke for their much-appreciated assistance professionally, as well as for the nice moments we spent together outside of the lab. I express my dearest gratitude to all members of the AC1 and neuropathology group for the friendly atmosphere and willingness to help. Furthermore, I am thankful for my friends Angela Rincón and Agustín Penagos for their contributions and most of all, for making me laugh and have fun even at the most stressful times.

My greatest thanks go to my family for their support and encouragement throughout my PhD and all my studies in Germany. To my parents *Any* and *Walter Melara*: All my success and knowledge, I owe to you and your many efforts. Special mention to my sisters *Ana* and *Ximena Melara* and my tía *Regina Benitez* for always believing in me and constantly cheering me on. To my *abuelita Susy* for being a source of inspiration throughout my education and especially for this work. Most importantly I would like to thank my husband *Dr. Kai Giesen* for always being there for me. Your unconditional love and support have made me achieve things I never thought possible. Tqm.

Dedicado a mis padres…

Table of Contents

Abstract

Glioblastoma (GB) is the most common and most aggressive type of primary brain tumor with an average two-year survival rate of patients after consensus therapy consisting of surgical gross resection, followed by adjuvant chemo- and radiotherapy. The reason for its occurrence, invasive behavior to other healthy tissues and constant recurrence upon surgical resection can be attributed to the existence of an aggressive subpopulation of tumor cells called GB stem cells (GSCs). GSCs, characterized by the expression of neural stem cell markers and their capacity of self-renewal, possess very efficient and augmented DNA repair and protection programs, translating to a clinically unwanted therapy resistance of the tumor. Even though promising pharmacotherapies with great potential to target GSCs have been identified, their desired bioavailability inside the target site is still limited due to cellular defense mechanisms of GSCs. In this work, gold nanoparticles (Au NPs) were designed to serve as drugs carriers able to penetrate GSCs and enhance the stability and solubility of therapeutics. Due to their biocompatibility, straight-forward functionalization and unique optical properties, Au NPs are suitable candidates to improve GB therapy.

In the initial part of this project, the optimal synthesis parameters and ligand composition of Au NPs needed to achieve a high internalization degree into GSCs was investigated. Au NPs were synthesized in a fast microwave-assisted reaction using the polymer polyethylenimine (PEI) as a reducing agent for the Au(III) precursor, a stabilizer against NP agglomeration and a platform for subsequent gene or drug conjugation. In order to track the Au NPs inside the cells, the fluorescent marker fluorescein isothiocyanate (FITC) was bound to the NP surface. The fluorescence emitted by the AuPEI-FITC NPs allowed their quantification after incubation into the cells, as well as a differentiation between cell-surface-bound and internalized NPs. *In vitro* experiments with GSCs indicated no apparent cytotoxicity for AuPEI-FITC NPs. The maximal NP internalization was 61%, depending on the NP synthesis method and the cell type tested.

Following these findings, the ability of Au NPs to load and deliver the promising clinical drug candidate CB839 into GSCs was studied. First, five different Au NPs with polymeric and non-polymeric capping ligands were synthesized and reacted with CB839 to form an Au-ligand-CB839 conjugate. The drug loading efficiency (DLE) for each NP type was evaluated using high-performance liquid chromatography, accompanied by qualitative microscopic and spectroscopic investigations. Despite the chemical inertness and poor-water solubility of CB839, Au-polymer NPs reached a DLE of up to 12%. Assessments in GSC *in vitro* models showed an increased therapeutic potential of the nano-delivered CB839, compared to CB839 alone. Optical assessment proved the successful high rate of intracellular penetration of Au-CB839 NPs into GSCs.

Kurzzusammenfassung

Das Glioblastom (GB) ist einer der am häufigsten auftretenden und aggressivsten primären Hirntumore. Die aktuell eingesetzte Standardtherapie, bestehend aus chirurgischer Entfernung gefolgt von adjuvanter Chemo-Strahlentherapie, führt nur zu unzureichenden klinischen Erfolgen mit einer mittleren Überlebenszeit der Patienten von weniger als 2 Jahren. Charakteristisch für diesen Tumor ist seine starke Invasivität in umliegendes Gewebe, seine Chemoresistenz und eine hohe Rezidivrate. Neuere Befundungen deuten darauf hin, dass Tumorzellen mit Stammzelleigenschaft, sogenannte Glioblastom-Stammzellen (glioblastoma stem cells, GSCs) maßgeblich an der Entstehung der Erkrankung und der Vermittlung der beschriebenen Eigenschaften beteiligt sind. Insbesondere die effektiven DNA-Reparatur und Schutzmechanismen von GSCs – die sich in der Therapieresistenz des Tumors widerspiegeln – stellen ein entscheidendes, ungelöstes klinisches Problem dar. Obwohl verheißungsvolle Pharmakotherapien zur Zerstörung von GSCs identifiziert wurden, stellt die limitierte Bioverfügbarkeit solcher neuen Substanzen in den GSCs, d.h. dem gewünschten Zielort, eine große Herausforderung in der nachhaltigen, translational-relevanten Entwicklung solcher Therapien dar. In dieser Arbeit wurden Gold-Nanopartikel (Au-NPs) entwickelt, die als Wirkstoffträger dienen und in der Lage sind, GSCs zu durchdringen und die Stabilität und Löslichkeit von Therapeutika zu verbessern. Aufgrund ihrer Biokompatibilität, einfachen Funktionalisierung und einzigartigen optischen Eigenschaften sind Au-NPs geeignete Kandidaten zur Verbesserung der GB-Therapie.

Im ersten Teil dieser Arbeit wurden die Syntheseparameter und die Ligandenzusammensetzung von Au-NPs hin zu einem maximalen Internalisierungsgrad in GSCs optimiert. Au-NPs wurden in einer mikrowellen-unterstützten Reaktion synthetisiert, wobei das Polymer Polyethylenimin (PEI) als Reduktionsmittel für den Au(III)-Präkursor, als Stabilisator gegen NP-Agglomeration und als Plattform für die anschließende Gen- oder Wirkstoffkonjugation verwendet wurde. Um die Au-NPs innerhalb von Zellen zu verfolgen, wurde der Fluoreszenzmarker Fluoresceinisothiocyanat (FITC) an die NP-Oberfläche gebunden. Die von den AuPEI-FITC NPs emittierte Fluoreszenz ermöglichte deren Quantifizierung nach der Inkubation in Zellen sowie eine Differenzierung zwischen oberflächengebundenen und internalisierten NPs. *In vitro* Experimente zeigten keine relevante Zytotoxizität von AuPEI-FITC NPs gegenüber GSCs. Die maximale NP-Internalisierung betrug 61%, abhängig von der NP-Synthesemethode und dem getesteten Zelltyp.

Anschließend wurde im zweiten Teil dieser Arbeit die Fähigkeit von Au-NPs als Transporter für den vielversprechenden Medikamentenkandidaten CB839 untersucht. Zunächst wurden fünf verschiedene Au-NPs mit polymeren und nicht-polymeren Oberflächenliganden synthetisiert und mit

CB839 zu einem Au-Ligand-CB839-Konjugat umgesetzt. Die Wirkstoffbeladungseffizienz (drug loading efficiency, DLE) für jeden NP-Typ wurde mittels Hochleistungsflüssigkeitschromatographie und qualitativen mikroskopischen und spektroskopischen Untersuchungen bewertet. Trotz der chemischen Inertheit und schlechten Wasserlöslichkeit von CB839 erreichten die Au-Polymer-NP eine DLE von bis zu 12%. Untersuchungen in pathophysiologisch-relevanten Modellen von GSCs zeigten ein erhöhtes therapeutische Potential des nano-verabreichten CB839 im Vergleich zu CB839 alleine. Darüber hinaus konnte die erfolgreiche hohe Rate der intrazellulären Internalisierung von Au-CB839 NPs in GSCs durch optische Methoden bestätigt werden.

List of Abbreviations

5-ALA	5-aminolevulinic acid hydrochloride
ADO	adenosine
AFM	atomic force microscopy
AMP	adenosine monophosphate
APCP	adenosine 5'-(α,β-methylene)diphosphate
ATP	adenosine triphosphate
BBB	blood-brain-barrier
BCE	before the common era
[BMIm][NTf_2]	1-butyl-3-methylimidazolium bis(trifluoromethylsulfonyl)imide
BPTES	bis-2-(5-phenylacetamido-1,3,4-thia-diazol-2-yl)ethyl sulfide
(BTSC)407	a glioblastoma cell line
CAU	Christian-Albrechts-Universität
CB839	*N*-[5-[4-[6-[[2-[3-(trifluoromethoxy) phenyl]-acetyl]amino]-3-pyridazinyl]butyl]-1,3,4-thiadiazol-2-yl]-2-pyridine-acetamide (brand marked as Telaglenastat)
CFE	colony forming efficiency
Cit	citrate
CNS	central nervous system
COD	cyclooctadiene
Cp*	1,2,3,4,5-pentamethylcyclopentadiene
CT	computed tomography
CTAB	cetyltrimethylammonium bromide
CTF(s)	covalent triazine framework(s)
DCC	N,N′-dicyclohexylcarbodiimide
DLE	drug loading efficiency
DLS	dynamic light scattering
DLVO	Dejaguin-Landau-Verwey-Overbeek
DMDACH	dimethyl-1,2-diaminocyclohexane
DMEM	Dulbecco's Modified Eagle Medium
DMF	dimethylformamide
DMSO	dimethylsulfoxide
DNA	deoxyribonucleic acid

DON	6-diazo-5-oxo-L-norleucine
DOX	doxorubicin, a chemotherapeutic
e.g.	exempli gratia, for example
EDC	1-ethyl-3-(3-dimethylaminopropyl)carbodiimide hydrochloride
EDX	energy dispersive X-ray spectroscopy
EMT	epithelial-mesenchymal transition
EPR	enhanced permeation and retention
et al.	et alia, and others
etc.	et cetera
FACS	fluorescence-activated cell sorting
FBS	fetal calf serum
fcc	face-centered cubic
FDC	2,5-furandicarboxylate
FITC	fluorescein isothiocyanate
FRET	fluorescence resonance energy transfer
(FT)-IR	(Fourier transform) infrared
FUS	focused ultrasound
GB	glioblastoma
GFP	green fluorescent protein
GLS1	glutaminase1 enzyme
GSC(s)	glioblastoma stem cell(s)
HAADF	high-angle annular dark-field
HEK	human embryonic kidney cells
HEPES	4-(2-hydroxyethyl)-1-piperazineethanesulfonic acid
HIV	human immunodeficiency virus
HPLC	high-performance liquid chromatography
i.e.	id est, that is
IL	ionic liquid
JHH520	a glioblastoma cell line
LDH	lactate dehydrogenase
LGK974	2-(2',3-dimethyl-2,4'-bipyridin-5-yl)-N-(5-(pyrazin-2-yl)pyridin-2-yl)acetamide, a Wnt pathway inhibitor
LSPR	localized surface plasmon resonance
MeAMD	amidinate

MIL	Matériaux de l'Institut Lavoisier
MOF(s)	metal organic framework(s)
MRI	magnetic resonance imaging
MSAB	methyl 3-{[(4-methylphenyl)sulfonyl]amino}benzoate, a Wnt pathway inhibitor
MTT	3-(4,5-dimethylthiazol-2-yl)-2,5-diphenyltetrazolium bromide
NC(s)	nanocluster(s)
NHS	N-hydroxy succinimide
NIR	near-infrared
NMR	nuclear magnetic resonance
NP(s)	nanoparticle(s)
NR(s)	nanorod(s)
ODC	octadecene
OER	oxygen evolution reaction
[OPy][NTf_2]	1-octylpyridinium bis(trifuoromethylsulfonyl)imide
ORR	oxygen reduction reaction
PA	photoacoustic imaging
PBS	phosphate-buffered saline
PC	propylene carbonate
PDT	photodynamic therapy
PEG	polyethylene glycol
PEI	polyethylenimine
PET	positron emission tomography
PSMA	prostate specific membrane antigen
PTX	Pentoxifylline, a phosphodiesterase inhibitor
PVA	polyvinyl alcohol
PVP	polyvinyl pyrrolidone
PXRD	powder X-ray diffraction
RAV19	a glioblastoma cell line
ref.	reference
RNA	ribonucleic acid
ROS	reactive oxygen species
RT	radiotherapy
SAED	selected area electron diffraction
SEM	scanning electron microscopy

SERS	surface-enhanced Raman scattering
Sf188	a glioblastoma cell line
SH-cyclodextrin	heptakis(6-deoxy-6-thio)-β-cyclodextrin
SPECT	single-photon emission computed tomography
SPR	surface plasmon resonance
SSNMR	solid-state nuclear magnetic resonance spectroscopy
STEM	scanning transmission electron microscopy
TAT	transactivating transcriptional activator, a cell-penetrating peptide
TDC	2,5- thiophenedicarboxylate
TEM	transmission electron microscopy
TGA	thermogravimetric analysis
THF	tetrahydrofuran
ThioPEG	polyethylene glycol methyl ether thiol
ThioPEI	thiol-terminated polyethylenimine
TOP	trioctylphosphine
UV	ultraviolet
VIS	visible
WHO	World Health Organization
Wnt	wingless-related integration site
XPS	X-ray photoelectron spectroscopy
β-CD	β-cyclodextrin (7 glucose subunits)
233	a glioblastoma cell line

Physical quantities

°C	degree Celsius
cm	centimeter (10^{-2} m)
eV	electronvolt
g	gram
h	hour
Hz	herz (1 s^{-1})
K	Kelvin

kDa	kilodalton (1000 Da = $1.6601 \cdot 10^{-24}$ kg)
kg	kilogram
kV	kilovolt
L	liter
m	meter
MHz	megahertz (10^6 Hz)
min	minute (60 s)
µL	microliter (10^{-6} L)
mL	milliliter (10^{-3} L)
µm	micrometer (10^{-6} m)
µmol	micromol (10^{-6} mol)
mm	millimeter (10^{-3} m)
mmol	millimol (10^{-3} mol)
mol	mole (amount of substance, $6.02 \cdot 10^{23}$ particles)
nm	nanometer (10^{-9} m)
ppm	parts per million
rpm	revolutions per minute
s	second
W	Watt

1. Introduction

1.1. Nanomaterials

The term “nano” comes from the greek word *nanos* for “dwarf” and is used as a prefix to describe a size of 10^{-9} m = 1 nm.[1] Nanomaterials are defined as structures with sizes between 1 and 100 nm in at least one spatial dimension and with unique chemical and physical properties.[2] A length scale comparing the size of nanomaterials with common biological structures is shown in Figure 1. The novelty of nanomaterials relies not only on their small size but on their large surface-to-volume ratio, which provides a higher number of more reactive surface atoms with unsaturated bonds and free coordination sites, compared to bulk materials.[3-5] These allow for nanostructures to exhibit different electronic, conductive, optical and magnetic behaviors than their bulk counterparts, which have awaked significant interest across many scientific fields, such as chemistry, biology, medicine, physics, material science and engineering.[6-10] Their size-, shape- and composition-dependent properties are exploited for the fabrication of a variety of consumer products like paints,[11] textiles,[12] food,[13] cosmetics,[14] pharmaceutics,[15] etc. Due to their distinct chemical reactivity, nanomaterials are also used in fuel cells,[16] hydrogen storage devices,[17] sensors[18] and in catalysis.[19]

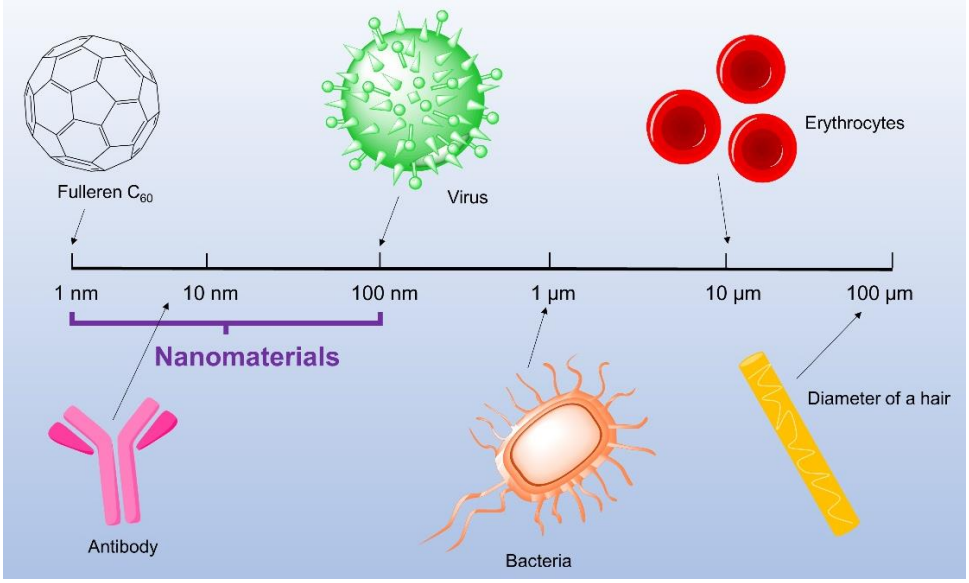

Figure 1. Scale comparing the size of nanomaterials with biological agents, modified from ref. 1.

Nanomaterials are synthesized by either “top-down” or “bottom up” strategies (Figure 2).[20,21] In “top-down” methods, bulk materials are broken down into nanoparticles (NPs) through processes such as grinding, mechanical attrition, laser ablation, etching or lithography.[22] While there have been significant improvements in the last decades, control over the size distribution and morphology of nanomaterials synthesized by “top-down” methods is difficult to achieve.[23]

In “bottom up” approaches, atoms and molecules are used as building blocks to synthesize materials at the nanoscale.[24] Common examples are precipitation,[25] sol-gel[26] and thermal-[27] or microwave-assisted decompositions reactions.[28] Besides liquid phase methods and hydrothermal treatments, high purity nanomaterials can also be produced in the gas phase using techniques such as chemical vapor deposition and magnetron-sputtering.[29,30] In “bottom up” methods, the size and morphology of nanomaterials can be controlled by variation of temperature, time, pH and other reaction parameters.[31] The choice of starting materials (“precursors”), reducing agents, stabilizers and solvents also play a key role in the synthesis outcome.[32-34]

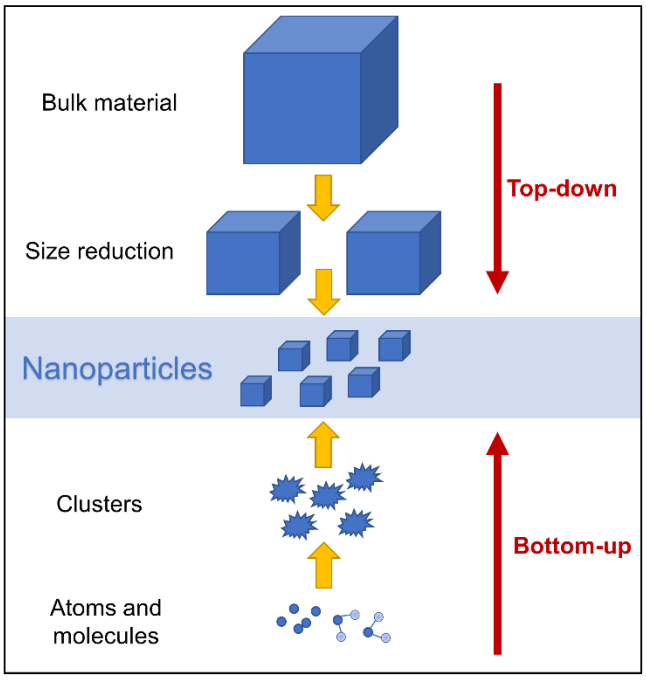

Figure 2. "Top-down" and "bottom-up" approach for the synthesis of nanomaterials.

While NPs of homogenous size and dispersity can be successfully synthesized by liquid-phase methods, such “nanosuspensions” are only moderately stable. American chemist *Victor LaMer*

explained the formation and growth of monodisperse colloids through a kinetic model, where a saturated concentration of precursor is reached before nuclei are formed.[35] Once this critical concentration is reached, spontaneous nucleation to nanoparticles occurs at such a high rate that nuclei of the same size are formed throughout the entire solution. The supersaturation then drops to stop nucleation and the remaining precursor diffuses into the formed particles, resulting in size increase.[36] While breaking bonds from the precursors and eliminating solvate shells is an endothermic process, the growth process and agglomeration of nanoparticles to form macroscopic systems with lower surface energy – known as Ostwald Ripening – is an exothermic process and much more energetically favorable.[37] Thus, agglomeration naturally occurs to relieve the energetically unfeasible state of NPs by minimizing the surface area and by saturation of the binding and coordination sites of its surface atoms.[5,6] In order to avoid losing the special physicochemical features of nanomaterials, NPs must be protected against agglomeration through steric, electrostatic or electrosteric stabilization (Figure 3).[38]

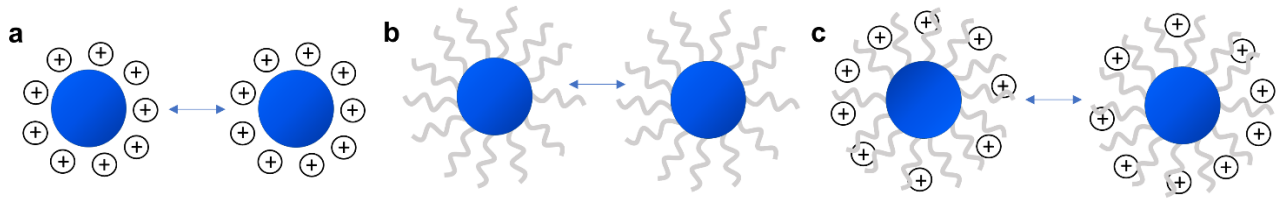

Figure 3. Schematic representation of electrostatic (a), steric (b) and electrosteric (c) stabilization of NPs.

Electrostatic stabilization is based on a theory by *Derjaguin, Landau, Verwey* and *Overbeek* (DLVO), where the naturally occurring attractive van der Waals forces between NPs are counterbalanced by stronger repulsive Coulomb forces.[39,40] If NPs are combined with electrostatically charged surfactants (*e.g.* carboxylates, sulphates) during or after synthesis, these compounds are able to form a layer around the nanoparticle surface, which repels when particles approach each other.[41] On the other hand, a steric stabilization consists of binding or adsorbing sterically demanding additives onto the NP surface to avoid a decrease in interparticle distance.[42] Some examples are long-chain alkyl compounds, polysaccharides and polymers.[1,43] Lastly, an electrosteric stabilization can be considered as a combination of both strategies.

1.2. Gold and Gold Nanoparticles

Gold (Au) has been the object of fascination of several civilizations in the past, even before the existence of nanomaterials was known. The earliest findings of the shiny metal date back to the 9000s BCE (before the common era). Between 2000 and 325 BCE, the Egyptians and the Greeks had mined gold across Egypt and Anatoly, while the Romans also pioneered a technique for its separation, refining and alloying.[44] On the other side of the world, among the indigenous people of Central and South America, gold was also used to make ornaments, tools, relics and ceremonial objects (Figure 4).[45] In the Aztec, Mayan and Inca cultures, gold was related to the gods and referred to as the "sweat of the sun".[46]

Figure 4. Gold objects from the Sican and Aztec civilization. Images from the open access collection of the Metropolitan Museum of Art, New York City.

The first uses of gold in the form of nanoparticles are linked to the history of ruby-colored glass starting in Roman times in the fourth century.[47] The dichroic effect of the Lycurgus cup (Figure 5) – which shows a green color when illuminated from the outside and a red color when light is transmitted through it – is still a symbol of the peculiarity of Au NPs, as this effect can be attributed to the presence of gold-silver NP alloys of 50-100 nm.[48] Glass and porcelain staining with Au NPs yields red, wine-red and purple tones as the color correlates with the NP size and shape[44] (see chapter 1.3.2, optical properties of Au NPs).

Figure 5. Lycurgus cup illuminated from the outside (left) and illuminated from the inside (right), from the British Museum free image service, © The Trustees of the British Museum.

In the modern field of nanotechnology, Au NPs are exploited in chemistry, biology, physics, material science and medicine due to their unique properties.[49,50] Gold is the most electronegative metal on the Pauling scale and the most noble of all metals; it is chemically stable and possesses high density and resistance to corrosion.[51] Its softness and ductility can be attributed to its face-centered cubic (fcc) crystal structure, which makes it an ideal starting material in the top-down synthesis of NPs, compared to other metals.[52]

Au NPs are typically produced in liquid media through reduction of chloroauric acid or alkali metal tetrachloroaurates(III).[53] One of the most notorious methods was described by *Turkevich et al.* in 1951, who synthesized monodisperse spherical Au NPs between 10 and 20 nm by reduction of chloroauric acid with sodium citrate in water.[54] Similarly, Au NPs can be formed in organic solvents by using sodium borohydride as a reducing agent, as *Brust* and *Schiffrin* published in 1994.[55] Other reducing agents used for $HAuCl_4$ are hydroquinones, acetylacetonates and even biological agents such as the bacteria *Bacillus licheniformis*.[56-58] Since the 1980s, Au NPs have also been synthesized by means of sonolysis, combining ultrasound and electrochemistry.[59-61] Other techniques such as photochemistry (using UV light) and microwave-assisted decomposition have also been widely popular.[62,63] In so called “one-pot” synthesis routes, polymers such as polyethylenimine (PEI) and polyvinyl pyrrolidone (PVP) are employed as both reductants and surface capping ligands, directly forming Au NPs and protecting them against agglomeration.[64,65]

While Au nanoparticles in the form of spheres are the most common in numerous applications, gold can form nanostructures of many different shapes (Figure 6). Morphologies such as nanorods, nanoshells, nanocages, nanocubes and nanostars are some examples of the versatility and tuneability of gold at the nanoscale.[66]

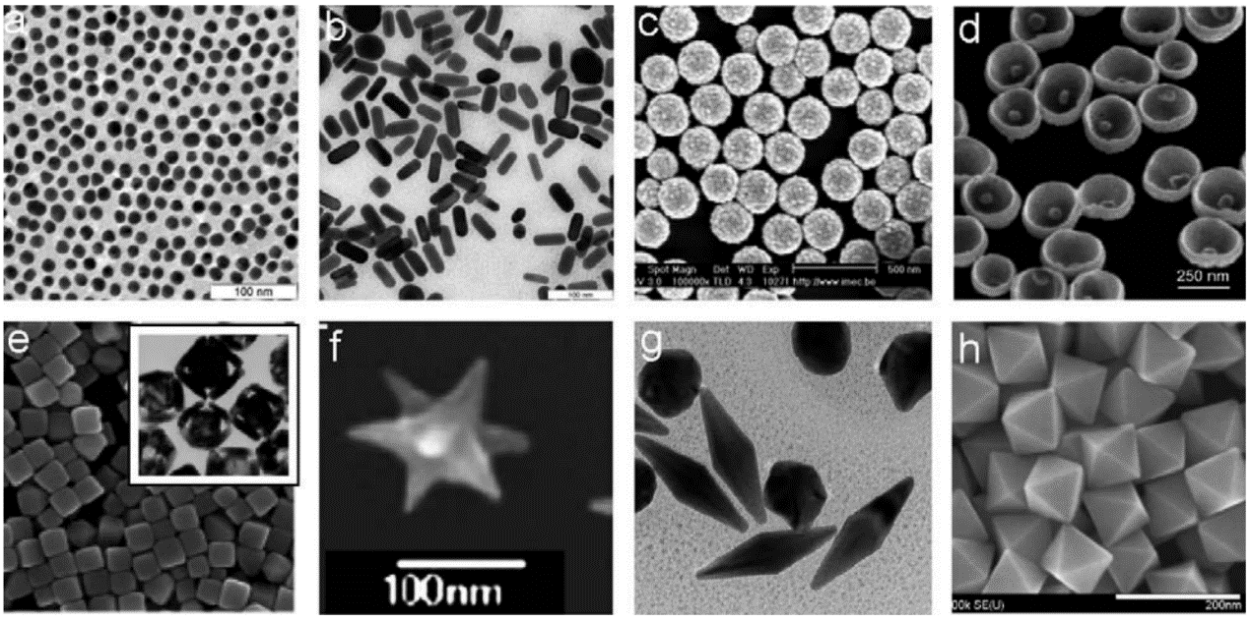

Figure 6. TEM and SEM images of Au NPs (a), Au nanorods (b), Si(core)-Au(shell) NPs (c), Au nanobowls (d), Au nanocages (e), nanostar (f), bipyramids (g) and octahedral particles. Reprinted with permission from ref. 66, copyright (2010) Elsevier.

Besides studying the size and morphology of Au NPs through scanning and transmission electron microscopy (as shown in Figure 6), several other techniques have been developed for NP characterization. Other properties such as size distribution, hydrodynamic diameter, surface charge, absorption, crystallinity and chemical composition can be further investigated using atomic force microscopy (AFM),[67] dynamic light scattering (DLS),[68] zeta potential measurements,[69] UV-VIS spectroscopy,[70] energy dispersive X-ray spectroscopy (EDX) analysis,[71] powder X-ray diffraction (PXRD),[72] selected area electron diffraction (SAED),[73] etc. Additionally, methods such as X-ray photoelectron spectroscopy (XPS),[74] Fourier transform infrared (FTIR) spectroscopy[75] and solid-state nuclear magnetic resonance spectroscopy (SSNMR)[76] can be used to gain information about the surface chemistry of Au NPs.

1.3. Physicochemical Properties of Au NPs

While Au NPs have characteristics such as lower melting points, catalytic activity and higher chemical reactivity, which can be attributed to the large surface-to-volume ratio true for most NPs,[1] this chapter will focus on some of the physicochemical properties specific to gold.

1.3.1. Binding Affinity with Other Molecules

Au NPs present an ideal platform to conjugate a variety of ligands on their surface. Au can be easily functionalized with other molecules through covalent linkage or other non-covalent interactions (*e.g.* physisorption, electrostatic effects).[44] Known examples of the covalent approach is the reaction between Au and sulfur-containing compounds such as thiols, disulfides, isothiocyanates and cysteine groups.[77] This strong Au-S bond is the root of the success of Au NPs in sensing, catalysis and targeted drug delivery applications, since it allows the integration of additional functionalities to the surface of the NPs, such as reactive ligands, antibodies and drugs.[78]

According to the "hard and soft acids and bases" (HSAB) principle, the soft character of gold and sulfur[79] allows the formation of a strong gold–thiolate bond, which, under mild conditions, does not break when other competing substances approach the gold surface.[55] Typically, end-terminated organo- or alkanethiols are used to functionalize Au NPs during synthesis or as post-synthetic ligand exchange treatment.[80] Besides thiols, amines and phosphines can also be used to stabilize Au NPs.[81,82] Even though their affinity for gold is not as strong, compounds such as hexyl-, dodecyl- and octadecylamine have been known to protect Au NPs against agglomeration, even in organic solvent media such as toluene and tetrahydrofurane.[81,83]

1.3.2. Optical Properties of Au NPs

Au NPs have a unique way to interact with light, which gives rise to their remarkable optical properties. The most particular phenomenon occurring in gold nanostructures is known as localized surface plasmon resonance (LSPR). Irradiation of Au NPs (and sometimes NPs of Ag, Cu and Al) causes the conduction electrons of the metal to be polarized to one side of the surface and to oscillate in resonance with the electromagnetic field of light.[84,85] At a defined frequency,

this oscillation reaches a maximum, which greatly depends on the size, shape, solvent, surface ligand, core charge and temperature of the materials, as well as the proximity of other NPs.[80] Light of a specific wavelength is absorbed, resulting in a variety of colors in transmission (Figure 7).[86] Au NPs of 10–50 nm absorb blue and green light (wavelengths between 520 and 540 nm), causing a wine-red colored suspension, the prevalent color of the remaining light.[52]

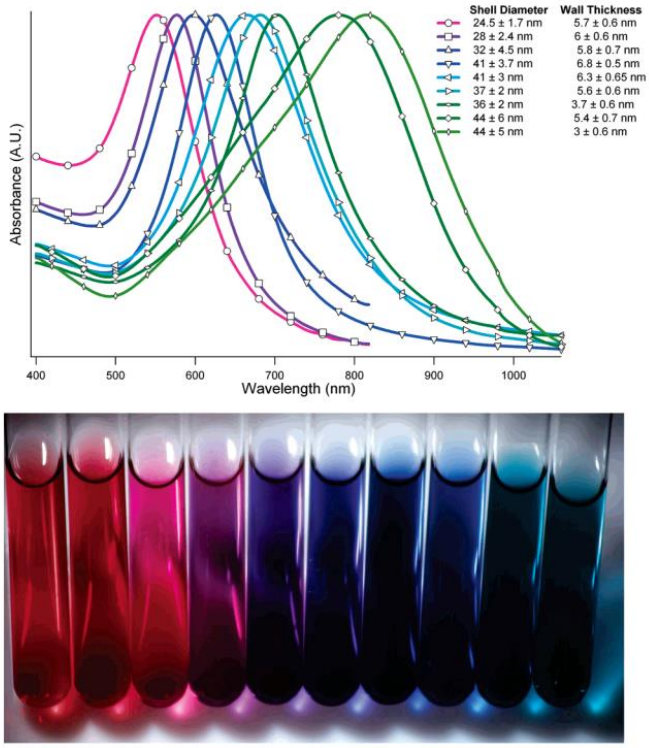

Figure 7. Size-dependent color change of hollow Au NPs. Above: UV-VIS absorption spectra of NPs with varying diameters and wall thicknesses, below: color range of solutions. Reprinted with permission from ref. 86, copyright (2006) American Chemical Society.

Apart from being responsible for a size- and shape-dependent color change in Au NPs, the LSPR can significantly enhance the electric field of NPs within close distance, which shows great potential for optimization of Raman and other spectroscopy techniques.[87,88] Moreover, when Au plasmons are excited by light, a great deal of energy is absorbed rather than scattered. The surface plasmon oscillation decays by converting energy to heat and thus raising the NP temperature.[52] Additionally, compared to photosensitizer dyes – capable of transferring light energy to other compounds – Au NPs can generate heat more effectively without photobleaching.[89] Along these lines, photothermal and photodynamic therapy (PDT) using Au

NPs is already being tested to eradicate malignant cells in a variety of tumors via oxidative damage.[90,91]

Additionally, the light emitting properties of Au NPs have also been the subject of many scientific studies.[92-94] For Au NPs with a size smaller than 2 nm, fluorescent effects analogue to those of semi-conductor quantum dots were discovered.[95] On the other hand, larger sized Au NPs also have shown to quench fluorescence because of the overlap between the emission spectrum of excited fluorophores and the LSPR, causing a fluorescence resonance energy transfer (FRET).[96,97] A more unusual feature of Au NPs is photoluminescence, which initially did not gain much attention among scientists due to the relatively low quantum yield, compared to conventional fluorophores.[98] Nowadays, new generation Au NPs with luminescence at 560 nm are capable of reaching quantum yields a million times higher than that of bulk gold metal,[99] as a result of enhanced electron and hole interband recombination caused by LSPR.[100]

1.4. Applications of Au NPs

Due to the properties explained in chapter 1.3 and many others, Au NPs are widely applied in the fields of physics, chemistry, biology and medicine. In chapter 1.4, some applications relevant to this work are described, mainly for biomedical purposes.

1.4.1. Sensing

Au NPs are widely used as chemical and biological sensors to efficiently detect metal ions,[101] toxic compounds,[102] proteins,[103] DNA,[104] etc. The detection mode of these nanosensors can either be colorimetric, fluorescence-based, electrical and electrochemical, LSPR-based or use a “bio-barcode”. In colorimetric assays, the color change after aggregation of Au NPs is exploited, while in fluorescence-based sensors, the fluorescence-quenching properties of Au NPs are utilized. Thus, these types of assays can provide a rapid and simple detection by observation with the naked eye or use of UV-VIS spectrometers and fluorometers.[105]

Due to their high surface energy and good conductivity, Au NPs can also be used as electrochemical biosensors, acting as an "electron wire" to amplify electrical signals that can be

later detected.[106] An example of this is the measurement of the enzyme activity of glucose oxidase using a Au NP electrode.[107]

The dependence of the LSPR on a change in refractive index is the foundation of the use of Au NPs for optical sensing, where a typical experiment involves monitoring a shift in LSPR frequency.[44] This way, signals in surface-enhanced Raman scattering (SERS) can successfully be enhanced by Au NPs to create efficient biosensors for the detection of oligonucleotides,[108] proteins,[103] antibodies,[109] viruses,[110] etc.[111] Au nanosensors have been incorporated in microfluidics or paper-based flow assays for quick diagnosis, *e. g.* antibody-conjugated Au NPs for pregnancy testing or the antigen-based assay using colloidal gold for the detection of the SARS-CoV-2 corona virus.[112,113] In "bio-barcode" assays, the easy modification of the surface chemistry of gold colloids can be tailored to react with specific biological markers of a disease to enhance their detection limits,[114] as is the case for the p24 antigen of the human immunodeficiency virus (HIV).[109]

1.4.2. Imaging

In imaging applications, the straight-forward surface functionalization and exceptional optical properties of Au NPs have been exploited to design efficient contrast agents and signal enhancers in techniques such as computed tomography (CT) and photoacoustic imaging (PA).[115] Due to its high atomic number and electron density, Au can be used as a potent contrast agent for CT scans. Since CTs are reconstructed from a variety of X-ray images from tissues taken at different angles, the X-ray attenuation ability of Au NPs can facilitate acquiring high-quality images.[116] Moreover, contrary to conventional near-infrared (NIR) organic dyes, Au contrast agents present high permeability, better detection sensitivity, more hydrophilicity and improved stability in biological systems.[105] For example, compared to the common CT contrast agent Idohexol, 13 nm Au NPs have achieved a higher attenuation intensity of about 20%.[117] In PA, laser energy produces acoustic waves by thermal expansion, which can later be detected on tissues by ultrasound and reconstructed as an image.[118] Using Au NPs, this PA signal can be increased through plasmonic effects, resulting in an image with higher resolution able to guide intratumoral treatment and monitor its efficacy *in vivo*.[119]

Additionally, the light absorbing and scattering properties of Au NPs can enhance the contrast of dark-field or dual-photon luminescence microscopy,[120,121] as well as enhance the image resolution in magnetic resonance imaging (MRI) or focused ultrasound (FUS).[122,123] When targeting

antibodies are attached to Au NPs, an easier detection of tumors or specific cell types is possible *in vitro* and *in vivo* by methods such as noninvasive fluorescent imaging (Figure 8) or SERS imaging.[124,125]

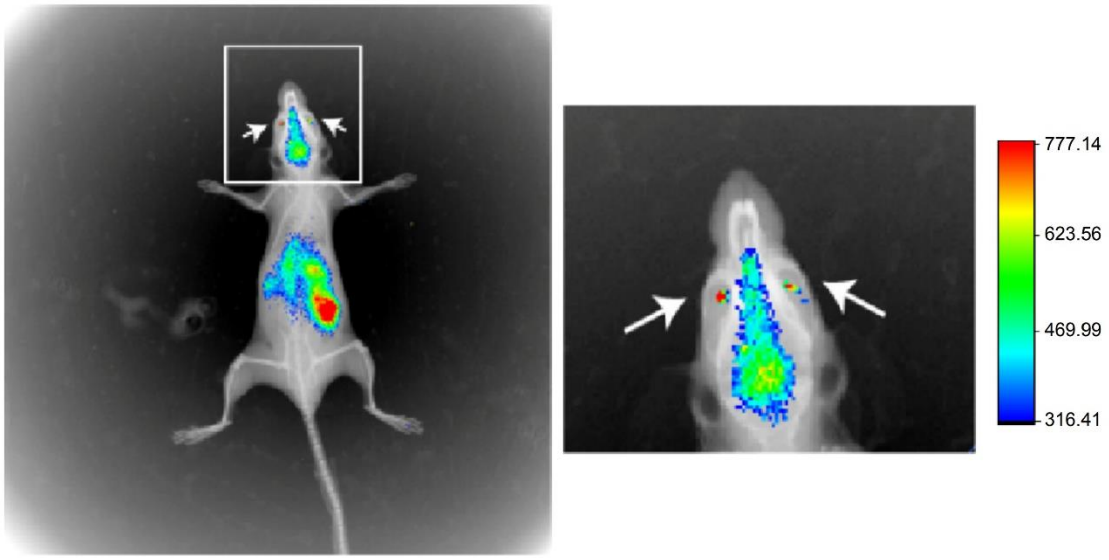

Figure 8. Noninvasive fluorescence imaging of mice after intravenous injection of Au nanoclusters (Au NCs) conjugated with a brain-targeting peptide. The Au NCs can specifically penetrate and detect neural cells *in vivo*. Reprinted with permission from ref. 124, copyright (2015) Dove Medical Press.

1.4.3. Drug and Gene Delivery

Based on the binding affinities with other compounds described in section 1.3.1, the surface of Au NPs can be specifically tailored to bind and deliver various therapeutic agents like drugs, proteins, nucleic acids and genes more effectively. This delivery can be either targeted or non-targeted.[115] In a targeted approach, usually an antibody or a peptide ligand able to reach a specific receptor is attached to the NP surface to release the attached drug only in target tissues.[126] On the other hand, a non-targeted delivery will release the payload into any medium, *i. e.* to both healthy and unhealthy cells. By choosing a targeted delivery, higher drug concentration can be given without the risk of collateral damage or unwanted side-effects.[127] For these reasons, Au NPs are currently being applied in genetic regulation and drug therapy of several diseases.[105] Furthermore, Au NPs have also been employed to deliver antibiotic and antiviral agents, showing great potential against several strains.[128,129]

Drug and gene release from the Au NP surface to the area of interest can be achieved by either internal stimuli (*e.g.* pH) or via external stimuli, such as heating or irradiation.[130] In 2011, *Hribar*

et al. synthesized a doxorubicin-loaded nanorod able to release the drug after exposure to NIR light.[131] Similarly, pH-responsive Au NPs have been designed to allow drug release when exposed to acidic conditions, like those found in tumors or damaged tissues.[132]

1.4.3.1. Loading strategies

The strategies to effectively load drugs or genes to Au NPs greatly depend on the size, stability and chemical nature of the compound. In general, these methods can be either be based on physical adsorption, hydrophobicity, electrostatic interactions or hydrogen bonding (from here on referred to as "non-covalent" loading) or rely on covalent bonding between drug and Au carrier.[133] Antitumor substances such as doxorubicin, prospidin and β-lapachon have been successfully attached to Au NPs through physical adsorption, while other such as paclitaxel, cisplatin and tamoxifen relied on sulfur-containing linkers to covalently bind to Au NPs.[134]

1.4.3.1.1. Covalent Loading

If thiols or free amines are present in their structure, drugs and genes can form Au–S or Au–N bonds of different strengths on the NP surface. This difference can even be exploited to control the delivery rate of the loaded compound, since a strong Au–S bond will result in a more stable probe with retarded release, *e.g.* for imaging purposes.[130] It has been reported that RNA can be easily modified with thiol groups for grafting onto Au NPs through covalent bonds.[135] Moreover, strong linking can also be formed between a ligand with sulfur at one side and a functional group on the other side, where additional molecules can attach, as seen for thiol-polyethylene glycol (PEG-SH) modified Au NPs with conjugated plasmids.[136]

Besides directly attaching thiolates the NPs surface, covalent bonding can also be formed through a linker ligand and the drug/gene of interest. Popular examples of the linker strategy are 1-ethyl-3-(3-dimethylaminopropyl) carbodiimide hydrochloride/N-hydroxy succinimide (EDC/NHS) chemistry and *click* reactions.[137-139] Consequently, by using a pre-grafted ligand on the NP surface, the free drug can react with the functional groups on the outside of the linker to form a covalent conjugation.[97]

While covalent loading might achieve higher drug loading efficiencies, using the capping ligand as a linker might reduce the stability of the Au-drug complex and cause NP agglomeration.[140]

Moreover, the chemical modification of the drug could compromise the known effect of the compound, needing additional testing of the altered drug. For this reason, mainly non-covalent approaches for drug delivery were chosen in this work.

1.4.3.1.2. Non-covalent Loading

Non-covalent loading methods are broadly employed in delivery and sensing applications because of their fast and sometimes reversible release behavior.[97] This strategy is once again based on the interactions between Au capping agents and drugs. These ligands can facilitate bonding through physical adsorption on the surface using amphiphilic groups, electrostatic charges, proton-donor or -acceptor moieties, etc. Non-covalent ligands can be formed with surfactants like cetyltrimethylammonium bromide (CTAB), which can take up water-insoluble molecules in its hydrophobic core;[141] or host-guest systems such as cyclodextrins, which can capture them on their inside.[142] These cyclic oligosaccharides are able to form inclusion complexes with lipophilic molecules due to their amphiphilic structure with a hydrophobic core and a hydrophilic outer shell. Cyclodextrins are often used in drug delivery, as they can increase water solubility and reduce cell toxicity of the conjugate, while protecting drug degradation in their cavity.[143]

A non-covalent bonding can also be formed using the so-called “layer-by-layer” approach, where a positively charged molecule is attracted to a negatively charged surface ligand or vice versa. Here, the opposite electrostatic interactions can be exploited numerous times, forming several “layers” around the NP surface (Figure 9), each with a specific targeting, encapsulating or stabilizing function.

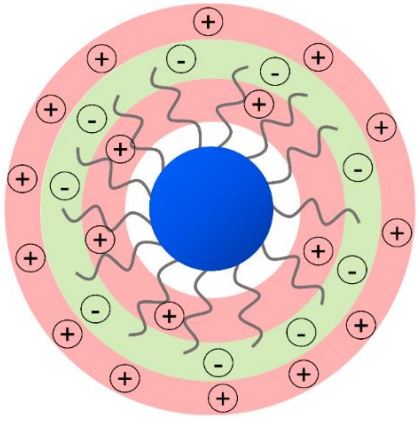

Figure 9. Schematic representation of a layer-by-layer NP assembly, stabilized by opposite electrostatic charges.

Polymers, which consist of several repeating units of the same molecule, are crucial ligands to bind drugs through non-covalent interactions, as well. Through adsorption, polymers can easily embed drugs and genes without the need for any chemical modification.[144] They can be modulated according to each delivery need to create multi-functional Au nanocarriers for therapeutics. By combining multiple functional groups among its structure, a two-component polymer (or copolymer) can hold both hydrophobic and hydrophilic sites, *e.g.* to load water-insoluble drugs on a water-soluble Au NP.[145]

Furthermore, these compounds can be modified to be pH-, thermo- or light sensitive to allow a controlled drug release after exposure to external stimuli, like in the case of "smart polymers" poly(propylacrylic acid), poly(N-isopropylacrylamide) and azobenzene-containing N-(2-hydroxypropyl) methacrylamide.[146] Polymers also allow the encapsulation of drugs on the Au NP surface by building a layer around the loaded compound to increase its solubility, stability, biocompatibility, retention time and blood circulation.[147] In contrast to "free" drugs, entrapped drugs on Au NPs have shown higher cellular uptake and pH-dependent drug-releasing properties.[148]

Polymeric ligands with a surface charge are likely to make a NP suspension more stable and are common building blocks for loading methods via charge interactions (Figure 9).[130] In gene therapy, the polymer polyethylenimine (PEI) has been repeatedly used to condensate nucleic acids on the surface of Au NPs due to its superior cationic charge density. Au-PEI NPs have demonstrated higher transfection efficiency and lower cytotoxicity than other standard transfections agents like lipofectamine and unmodified PEI.[149,150]

Lastly, besides loading on the surface of a solid Au NPs, hollow nanostructures with internal cavities can also be relevant in drug delivery applications. Examples are Au nanocages and Au nanoshells.[151,152]

1.5. Au NPs in Cancer Theranostics

As mentioned in previous chapters, Au NPs can help in early diagnosis of diseases (chapter 1.4.2), surveillance of therapy success and transport therapeutic agents into target cells bearing high drug loads (chapter 1.4.3). Currently, several Au NP candidates are in clinical trials for treatment of a variety of diseases, such as head, neck, prostate and lung cancers, as well as

atherosclerosis, diabetes, pulmonary hypertension, Parkinson's disease and gastric lesions,[105,153] indicating the great potential associated to this technology.

Cancer is commonly treated by a combination of surgery, chemotherapy and radiation, which can lead to grave systemic damage to healthy tissues in the whole body.[154] In cancer theranostics, *i.e.* simultaneous therapy and diagnosis, Au NPs surge as interesting therapeutic platforms for less invasive approaches not only because of their modifiable intrinsic functional properties but also due to their particular interactions with tumors.[155] It has been demonstrated that NPs present an enhanced permeation and retention (EPR) effect in tumors, which allows them to effectively transverse into the tumor stroma because of the disrupted vasculature.[156] This effect leads to an increased lymphatic drainage and lastly to NP accumulation at the intended site.[154,157] The EPR effect combined with higher sensitivity, cost-effectiveness and targeting potential make Au NPs extraordinary anticancer devices.

Another advantage of using Au NPs against cancer is the known chemical stability of gold, which hinders oxidation under physiological conditions thus avoiding a leaching of toxic species.[158] Moreover, as briefly stated in chapter 1.3.2, Au nanomaterials are powerful tools for targeted hyperthermia therapy (*e.g.* photothermal, photodynamic, plasmonic photothermal therapy) in cancer sites, including brain tumors, as they are able to heat and destroy tumorous cells after exposure to a heat source without unwanted side effects to healthy tissues.[159,160] Therapy parameters of this source such as wavelength, bandwidth and efficiency can be improved by adjusting the size, shape and surface coating of Au NPs.[112] Additionally, hyperthermia can also boost membrane permeability, which can lead to delivery of higher drug concentrations through improved drug diffusion into the tumor cells.[161]

Some of the many examples of successful application of Au NPs in cancer theranostics are the prostate specific membrane antigen (PSMA)-conjugated Au NPs for prostate CT imaging,[162] silica–Au nanoshells for solid tumor treatment by thermal ablation with a NIR source[153] or antibody-conjugated Au NPs for detection of cervical cancer cells.[163]

While Au NPs are promising tools in cancer applications, important aspects such as their cellular uptake, toxicity and toxicity assessment must be examined more closely before they can be applied in a clinical setting.

1.5.1. Cellular Uptake

Au NPs can improve the transport of therapeutic agents into cells by adjustment of their size, shape and surface ligand. Alongside their efficient direction/migration to the target site, the key barrier of the durable effects of Au NPs is determined by sufficient transfection into the target cells. The cellular uptake efficiency depends not only on the carrier, but also on the phenotypic properties of the cells, such as membrane composition, cellular recognition and the protein corona, which is built around the NP surface when it encounters proteins belonging to the biological microenvironment.[164] According to various investigations, NPs can be internalized in mammalian cells via passive transport across the membrane or by active processes such as phagocytosis, macropinocytosis, receptor-mediated endocytosis and independent endocytosis (Figure 10).[165] For Au particles smaller than 100 nm, receptor mediated endocytosis is believed to be the primary uptake mechanism, where specific targeting surface ligands on NPs can bind to receptors on the cell. The cell membrane can then wrap around the NP and internalize it.[166] The uptake of NPs smaller than 40 nm does not produce enough energy to overcome the less favorable deformation of the cell membrane, which is why these NPs most likely form clusters to overcome the energy barrier before they can be internalized.[167] In RAW264.7 mouse macrophage cells and Hep G2 human liver cells, Au NPs of sizes 20 nm and 5 nm showed lower uptake efficiency, compared to 50 nm Au NPs.[164] Small NPs (<6 nm) have however been shown to enter the nucleus of various cells,[168-170] which is crucial to induce cell apoptosis, *e.g.* in cancer treatment.

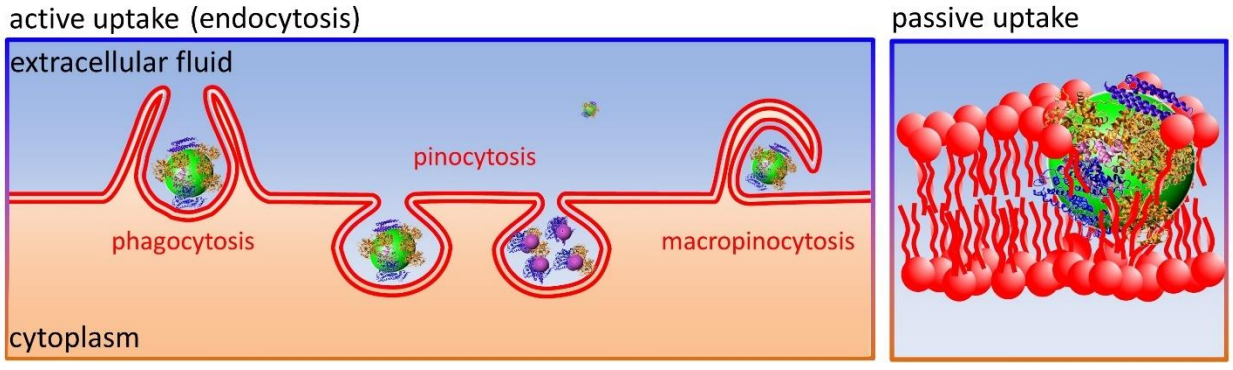

Figure 10. NP cellular internalization mechanisms, active receptor-mediated (left) or passive transport across the cell membrane (right). Reprinted with permission from ref. 165, copyright (2014) Springer Nature.

In addition, the internalization of NPs into cells is also dependent on the NP shape and its surface charge. Compared to nanorods, it has been proven that spherical Au NPs exhibit greater cellular uptake.[105] Similarly, positively charged NPs have a higher internalization degree, as they can strongly interact with the negatively charged cell membrane.[165] Nonetheless, experimental factors and the specific protein corona for each material can also alter this trend. *In vivo*, positively charged NPs can be filtered from the bloodstream more rapidly than anionic or neutral NPs, as they mostly accumulate in the spleen and liver, not in the arteries.[171]

While there are countless publications about internalization of Au NPs into cells, comparing *in vitro* results among them remains highly complex, due to the many parameters which dictate the response and biodistribution to Au NPs in each specific cell type.

1.5.2. Nanotoxicity

Alongside their ideal chemical properties to function as drug carriers from a translational point of view, special care must be taken regarding the possible toxicity of Au NPs for humans, animals and the environment, given that they are solid, non-biodegradable materials. There are several factors identified that can significantly influence this toxicity, as seen both *in vitro* and *in vivo* (some examples are portrayed in Figure 11).

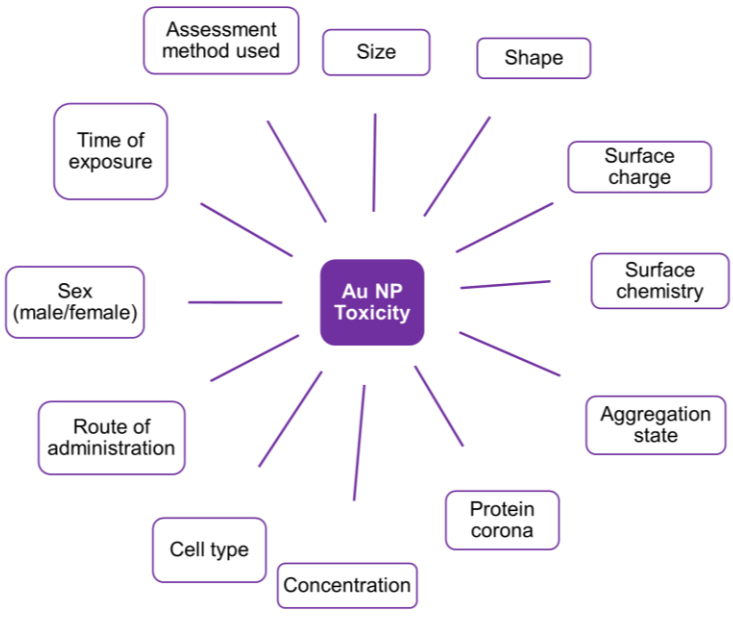

Figure 11. Factors influencing Au NP toxicity.

Regardless of the various studies stating to have found the ideal NP size for biological applications, no generalization can be made about the toxicity of Au NPs of a certain size. Results concerning citrate-covered Au NPs with sizes between 2 and 100 nm revealed that nanotoxicity does not show any clear behavior tendencies *in vivo*. While Au-citrate NPs between 10 and 40 nm caused acute toxicity after being injected to mice, NP of smaller and larger sizes did not show toxic or deathly effects on the animals.[172] Several studies contradicting or confirming the toxicity of small-sized Au NPs further prove this point.[173] A comparison between the toxicity effect of positively and negatively charged Au NPs is even more difficult, because it is impossible to have NPs with the same size, surface chemistry and dispersity using capping ligands of opposite charges.[173] Similarly, studies comparing toxicity of Au NPs based on their shape are problematic due to the different chemical approaches needed to synthesize each morphology.[174] In general, it is advisable to use non-toxic capping ligand such as PEG, PVA and PVP polymers or natural substances like dextran or chitosan to synthesize more biocompatible NPs.[105] For targeted delivery, the use of antibodies, peptides and proteins can further lower the cytotoxicity of Au NPs while increasing their cell penetrating properties.[175]

In *in vitro* models, toxicity effects can vary depending on the subtype-specific susceptibilities of each cell line tested. It is postulated that these differences originate from the individual protein corona, which is formed on the surface after the NPs enter a biological medium, combined with several other factors (see Figure 11). Frequently, the toxicity of a new nanomaterial is tested *in vitro* using standard assays based on cell viability investigations, study of reactive oxygen species, gene expression and cellular morphology.[130] While these traditional assays are widely popular due to their simplicity and low cost, they have shown a number of contradictory results when combined with Au NPs.[176] Reasons for this interference are the characteristic interactions of Au NPs with light (see chapter 1.3.2), their high adsorption capacity, thermal conductivity and catalytic activity.[177,178] Since the majority of assays are evaluated using optical detection methods (light absorption, fluorescence, luminescence), Au NPs can easily alter assay readouts and lead to false interpretations. Moreover, if Au NPs are agglomerated, the absorbance results are also biased.[179] Besides incorrect readouts, Au NPs can react with assay components or bind enzymes and assay reagents on their surface, thus changing their affinities or emission properties.[180,181]

Interference of Au NPs with tests such as the colorimetric 3-(4,5-dimethylthiazol-2-yl)-2,5-diphenyltetrazolium bromide (MTT) assay and lactate dehydrogenase (LDH) assay, the fluorescence-based Annexin-A5 assay and the luminescent Cell-Titer-Glo assay have been reported, given that these tests were originally intended for soluble compounds, not

nanomaterials.[180-182] In the MTT assay, the MTT salt is reduced to a purple-colored formazan product by mitochondrial reductase enzymes of viable cells.[183] Besides hindering the photometric quantification of formazan if gold is still present in the test medium, NPs can obstruct the intracellular trafficking of the dye and change cell activities due to redox reactions occurring in response to NPs.[184] Despite several time-consuming efforts to correct such interferences, *e.g.* by trying to quantify the absorbance attributed to NPs in cell-free media via UV-VIS measurements, an accurate measurement of cell viabilities after NP treatment using these assays continues to be challenging.[179]

As a response to these shortcomings, *Ponti et al.* suggested using the Colony Forming Efficiency (CFE) assay for early nanotoxicity screening, after reproducible results were generated when testing different NPs in 12 independent laboratories worldwide.[185] In the CFE assay, cytotoxicity is assessed by counting colonies formed by viable cells after treatment with NPs and comparing them with untreated cells (Figure 12). Because the CFE assay is label-free and does not use absorbance or fluorescence, Au NPs cannot quench or enhance detection signals. Besides, this essay can distinguish between cytotoxic and cytostatic effects by comparing colony numbers and areas.[185] Moreover, CFE is a direct functional assay and - as a cellular readout and in terms of biological meaningfulness- outperforms simple marker-based assessments scoring cellular survival, cell cycle progression or proliferation, such as performed with Annexin-5 or Ki67 staining.

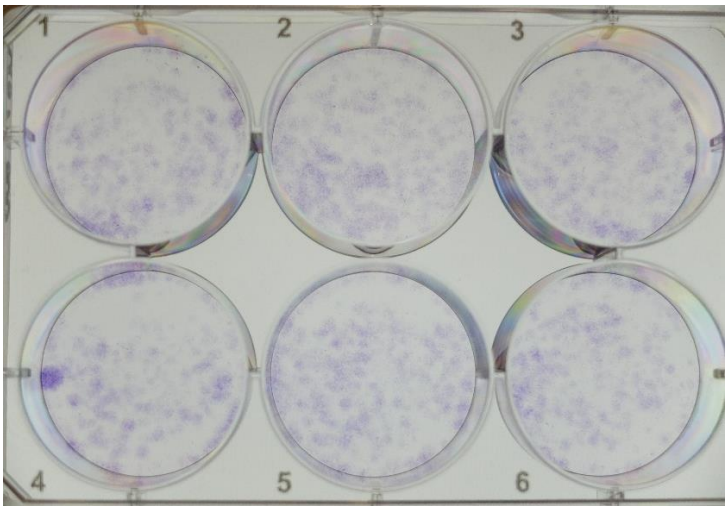

Figure 12. CFE assay showing colonies formed by U87 cells after treatment with Au NPs.

Even though *in vitro* assays provide initial information about toxicity, animal-based models should be encouraged for a more precise evaluation of Au NP toxicity. In *in vivo* models, most researchers have not found significant toxic effects of Au NPs in various animals, such as zebrafish, fruit flies, mice, rats, rabbits and pig models.[130,173] However, individual toxicities may be influenced by other factors such as the sex of the animals or the way NPs are administered. It has been noted that investigations about the uptake, biodistribution and bioaccumulation of NPs might be more valuable than toxicity results because NPs remain in the body for extended periods of time.[173] Consequently, NPs which are cleared quickly tend to reduce toxicity risks because their exposure time is reduced. *Yu et al.* suggested that the clearance pathway for NPs is most likely size-dependent, with NP smaller than 6 nm being eliminated via renal excretion (urine) and larger NPs through hepatobiliary excretion (bile to feces).[186] Besides size, NP elimination is also charge and surface ligand-dependent.[187]

In short, the toxicity of Au NPs must be assessed taking all these factors into consideration in order to obtain a general approximation of the biological effect of these materials in all organisms. Even though cell line- and patient-derived 3D spheroids are useful, cost-effective systems to study cell physiology and metabolism, their metabolic alterations compared to *in vivo* subjects are not entirely clear. Nonetheless, they are still highly practical to study therapy effects prior to investigations in preclinical tumor models and humans. In the context of oncology, non-cancer control models such as stem cells or terminally differentiated tissue cells shall be included in *in vitro* testing sequences. Results achieved on control models shall be brought in association to the results achieved with cancer *in vitro* systems, which will indicate any therapeutic index of a given intervention towards transformed cells. Moreover, modern synthetic tumor cell platform technologies, derived from a single-cell of origin and stepwise equipped with oncogenic elements,[188,189] allow biological assessments in cellular and genetic tightly controlled conditions and will surely impact the future drug development sector to complement ordinary assays based on patient-derived cell models only.

1.6. Glioblastoma

Tumors originating from glial (non-neuronal) cells of the central nervous system (CNS) are known as gliomas. Glioma is the most common type of tumor affecting the CNS and accounts for approximately 80% of all malignant tumors occurring in the brain.[190,191] In 2016, the World Health Organization (WHO) introduced a system to categorize gliomas into four groups to facilitate

choosing a course of treatment for patients.[192] According to this classification, grade I tumors have low proliferation and can be cured by surgical intervention, while grade II tumors are invasive and can often recur. Additionally, grade III tumors are usually malignant, showing anaplasia and fast cell division through mitosis; and grade IV represent the most malignant and advanced form of all gliomas.[192] Tumors in the grade IV classification – the most common subtype being glioblastoma (GB) – have the poorest prognosis with a high resistance and low survival rate. Around 48% of all malignant CNS and brain tumors can be attributed to GB.[193] With the rapid technological advancements of molecular biology in recent decades, additional stratification of brain tumors including subgrouping of GB have emerged. These latest OMICS-based classifications are centered on gene expression profiles,[194] proteomics[195] and DNA methylation,[196] to mention the most prominent. Molecular markers for GB characterization have entered the clinical routine diagnostics, such as promoter methylation status of the metabolic enzyme MGMT, DNA mutation status of the metabolic gene IDH1 or chromosome abnormality 1p/19q deletion. The field of molecular neurooncology diagnostics is developing rapidly and it is impossible to comprehensively summarize all ongoing exciting investigations in the context of this thesis. Further reading to dedicated literature is advised in case of deeper interest. In contrast, adequate advancements on molecular associated therapy options are far lagging behind, challenging the sustainability of highly specialized diagnostics, if they cannot translate to clinical benefits in the near future.

As introduced earlier, a subpopulation of GB cells showing prominent stem properties (GSCs) is thought to be responsible for the high cellular invasion potential of GB, as well as its therapy resistance.[197] These GSCs present an attractive therapeutic target to develop durable improvements in the management of this disease. However, the unequivocal identification of GSCs is challenging due to enormous inter- and intratumoral heterogeneity of GB, also affecting the dynamics of GSCs.[198,199] Single cell analysis proposed certain developmental lineages to overarchingly define the stem cell pool of the tumor, but further research have to validate this recent new concept.[200] Some studies propose that the formation of these GSCs is linked to a process called epithelial-mesenchymal transition (EMT), which is known in embryonic development, tissue regeneration and wound healing. In the case of cancer cells, EMT is not complete and cells with mixed epithelial and mesenchymal genes can transition between several EMT states.[201] These hybrid cells with disrupted cell–cell adhesion and cellular polarity can move collectively as clusters for faster migration and invasiveness.[202] With this dynamic behavior and their infinite self-renewing properties, GSCs can continuously form new tumor foci, and thus contribute to tumor recurrence.[203] Additionally, GSCs are enriched with regions of severe oxygen

deprivation (hypoxia), which significantly hinder the effects of radiation, as this therapy is based on the formation of reactive oxygen species (ROS).[204] In recent years, these cell subtypes have shown to be promising targets for GB therapy, *e.g.* through their identification and isolation using specific stem cell markers like CD133 (prominin-1), CD44, SOX2, NANOG or SSEA-1.[205-209]

1.6.1. Diagnosis and therapy

GB diagnosis normally starts with magnetic resonance imaging (MRI) to visualize the tumor structure.[210] Additionally, MRI scans can be enhanced with contrast agents and accompanied by other techniques like positron emission tomography (PET) and single-photon emission computed tomography (SPECT) to track therapy responses in active tumors (Figure 13).[211]

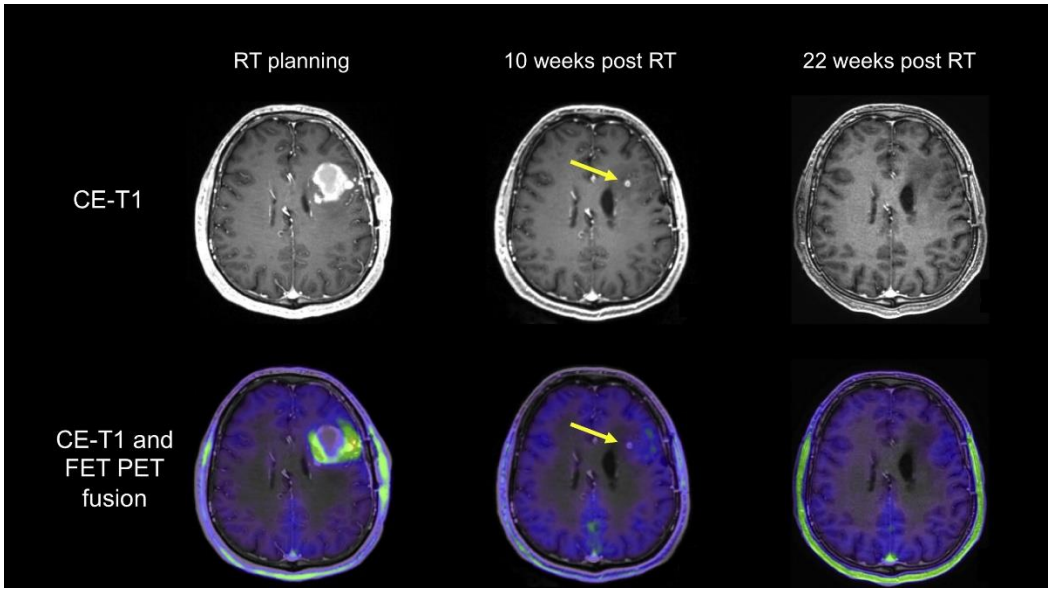

Figure 13. MR and PET images used for GB diagnosis and therapy monitoring. The tumor in the left frontal lobe remaining after resection and chemoradiation with temozolomide shows complete metabolic response after subsequent radiotherapy treatment. RT: radiotherapy, MR: magnetic resonance, CE-T1: contrast-enhanced T1-weighted MR, FET: *O*-(2-[^{18}F]fluoroethyl)-L-tyrosine tracer, PET: positron-emission-tomography. Reprinted with permission from ref. 211, copyright (2017) Elsevier.

In addition to the infiltrative nature towards adjacent tissues and the cell heterogeneity of GB, the treatment of this disease is significantly hindered by the blood-brain-barrier (BBB), a protective membrane responsible for brain homeostasis and for blocking the entrance of foreign substances

in the blood.[212] While this barrier protects the CNS against pathogens or toxins, it can be a major obstacle for the delivery of anticancer drugs. It has been demonstrated that most antibodies, proteins, polypeptides and small molecule drugs are unable to cross the BBB in pathological conditions.[213]

The current treatment of GB is based on surgical resection combined with the *Stupp* protocol, which consists of radiotherapy and chemotherapy using temozolomide, a DNA-damaging cytotoxic agent.[214] With a life expectancy of less than two years, research concerning further therapeutic approaches for GB is justified by ethical and scientific reasons. Recently, new strategies such as PDT and argon–helium cryotherapy have been used to treat brain tumors.[215,216] Other approaches with high potential to combat GB are pharmacotherapy with doxorubicin and taxanes, molecular-targeted blockers of growth factor receptors, immuno- and antimitotic therapies, microRNAs and enzymatic inhibition[210,217,218] to mention only a few attempts, further reflecting the desperate situation of clinicians to handle this unmet need. On note, a revolutionary new concept of treating GB using physical modulators has shown clinical success that led to its market approval in Germany and the US.[219] This method represents the first alternative qualified therapy after over two decades without any changes in GB treatment.

1.6.2. Glutaminase Inhibition

Recently, metabolic dependency-targeting of fast-growing tumors such as GB has manifested itself as an attractive path to develop effective new anti-cancer treatment approaches.[220] As such, interfering in the increased glucose and glutamine uptake to maintain tumor metabolism has shown promising outcomes for the treatment of GB.[221,222] The high glucose consumption of tumors is already the basis of several clinically applied imaging diagnostics such as the use of a radioactively labelled ^{18}F-fluorodeoxyglucose which gathers within the tumor and can be detected by PET.[223] Metabolic imaging is generally used in addition to classical anatomical imaging (CT) or perfusion imaging (MRI), and certainly enables an improved imaging of the bioactive tissue, which is particularly beneficial in the context of surveilling the effect of current standard diagnostics. Yet, despite the knowledge of this glucose and glutamine addiction of tumors, a clinical treatment targeting the enzymes responsible for both metabolisms in a synergistic approach is still inexistent.[223]

Unlike healthy cells, which convert glucose to pyruvate to feed mitochondria during oxidative phosphorylation for adenosine triphosphate (ATP) production, cancer cells additionally turn to glutamine for nucleotide and ATP synthesis.[224] Glutamine is an abundant amino acid from which energy can be produced after its conversion to glutamate, aspartate, pyruvate, CO_2, lactate and citrate via a process called glutaminolysis. Even though glutaminolysis takes place when healthy cells are deprived of oxygen, tumor cells have been known to follow this path even under aerobic conditions. This phenomenon is called “the Warburg effect”, after the pioneer discovery of Otto Warbung in 1956.[225] The hydrolysis of glutamine to glutamate and ammonia is catalyzed by the mitochondrial enzyme glutaminase1 (GLS1).[226] Thus, by inhibiting this enzyme, tumor cells can be deprived of important intermediates for the citrate cycle and grow more slowly or die through apoptosis.[223] Recently, GLS1 was identified in GSCs as a downstream target of the stem cell pathway Notch and a direct targeting of GLS by pharmacological means somewhat phenocopied the effect observed with Notch blockers.[227] Latter is considered a promising strategy to fight stem cells in many cancers, but its clinical translation is challenging due to off-target effects on normal stem cells.[227] Still, GLS1 offers a druggable anti-GSC target possibly presenting less off-target risk to other cells, as GLS is particularly active in tumor cells, especially at the invasive margin of gliomas.[228]

Among several tested glutaminase inhibitors, the compound *N*-[5-[4-[6-[[2-[3-(trifluoromethoxy) phenyl]-acetyl]amino]-3-pyridazinyl]butyl]-1,3,4-thiadiazol-2-yl]-2-pyridine-acetamide (CB839, brand marked under the name Telaglenastat and produced by Calithera Biosciences) shows utmost potential and is already being investigated in various clinical trials.[229-231] CB839 is derived from the previous bis-2-(5-phenylacetamido-1,3,4-thia-diazol-2-yl)ethyl sulfide (BPTES) inhibitor; it possesses good oral bioavailability and an effect about 13 times higher than its predecessor, independent from the glutamine concentration.[232] CB839 does not compete with glutamine for the binding active site in the GLS1 enzyme but instead binds to its allosteric site, causing conformational changes and a decrease in the activity of the enzyme, *i.e.* an allosteric inhibition.[233] Even though the inhibition mechanism of CB839 is not yet completely clear, it is believed that the pyridazine ring plays a role in its dose and time dependency, unlike in BPTES.[234] Contrary to GLS inhibitors 6-diazo-5-oxo-L-norleucine (DON), azaserine and acivicin, the structures of BPTES and CB839 do not resemble glutamine (Figure 14). This structural dissimilarity avoids unwanted reactions with other enzymes similar to glutaminase, as well as with other transporters or receptors.[232,234]

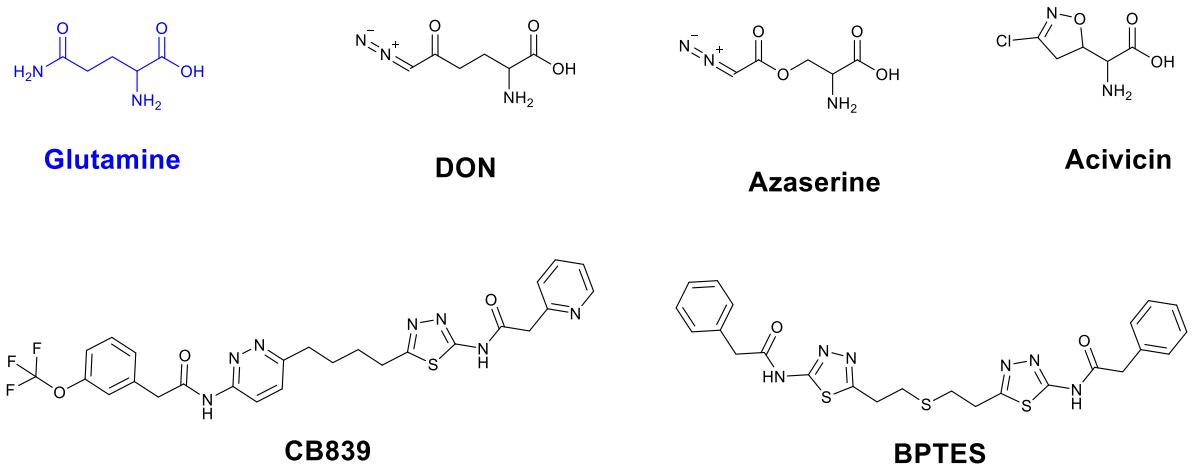

Figure 14. Molecular structures of glutamine and glutaminase inhibitors DON, azaserine, acivicin, CB839 and BPTES.

CB839 is further promoted as powerful anti-GSC candidate due to its superior target specificity and due to limited effects on non-cancer neural stem cells.[228] However, *in vivo* studies have shown that its accumulation and bioavailability in the brain is significantly lower than in other tissues, most likely due to the hurdle of passing the BBB.[232] Moreover, the antigrowth effect of CB839 seems to be subtype-specific, showing different sensitivities depending on the GB cell line tested. However, CB839 succeeded in eradicating GSCs by hampering processes necessary for cell maintenance and cycle progression.[228] Therefore, new technologies to ensure a higher efficacy and penetration of this promising drug candidate into GB tumors are imperative.

1.6.3. Glioblastoma treatment with Au NPs

In GB therapy, the singular optical qualities, straight-forward functionalization and interaction with tumor tissues and the BBB of Au NPs (chapters 1.3.1, 1.3.2 and 1.5) can be exploited to synthesize new generation theranostic probes. In an ideal combination therapy, Au NPs could serve as imaging contrast agents in diagnosis and efficiently deliver water-insoluble therapeutic drugs to specific tumor targets. Moreover, Au NPs could complement curative approaches by using additional physical methods such as hyperthermia and radiation to enhance anticancer effects, as is currently being tested in clinical treatments of cerebral tumors with PDT.[235] By actively targeting GSCs, *e.g.* using CD133 ligand-receptor docking, Au NPs could be engineered

to release drugs at the tumor site in a controlled manner, thus causing less systemic side effects to other cells.[236]

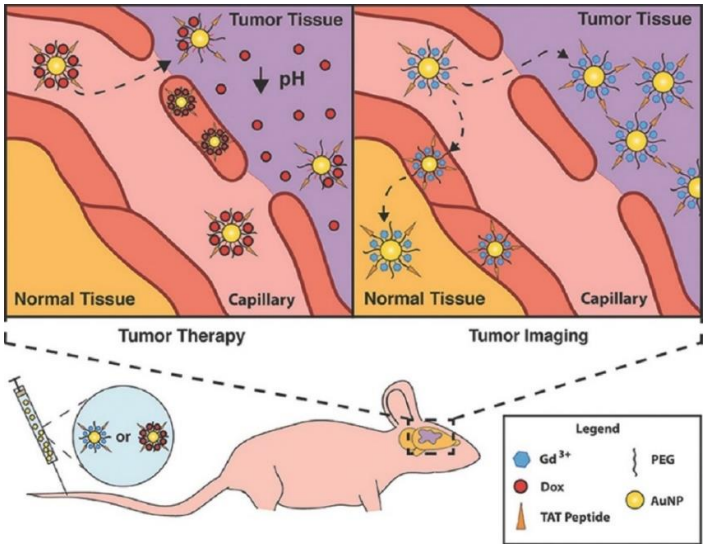

Figure 15. Targeted Au NPs carrying TAT peptide, doxorubicin (Dox) and Gd^{3+} contrast agents for glioma therapy and diagnosis. Left: Dox is conjugated via a pH-sensitive linker. Right: NPs accumulate in the tumor via the EPR effect. Reprinted with permission from ref. 239, copyright (2014) John Wiley and Sons.

Since NPs are able to pass the BBB because of their small size, they are promising delivery systems for GB therapeutics, which could be administered at lower concentrations compared to typical doses of free drugs.[237] Additionally, antibodies, growth factors and low-density lipoproteins can be attached to NPs to enhance their BBB crossing capability.[238] In a 2014 study, Au NPs combined with transmembrane peptides (TAT) delivered the anticancer drug doxorubicin into gliomas, showing a tumor killing effect up to 14 times higher than the pristine drug (Figure 15).[239] Similarly, the EPR effect of Au NPs was exploited to deliver the same chemotherapy across the BBB by a pH-sensitive process.[240] Dual functionality Au NPs targeting both the tumor and the BBB problematic have even higher infiltrative power into gliomas, due to synergistic internalization mechanisms of the ligands on a single delivery vector.[241]

In the treatment of malignant gliomas, Au NPs have been used in resection surgery to enhance MR and SERS signals and obtain a more accurate outline of the tumor.[242-244] Au NPs have also improved CT imaging resolution *in vivo* by accumulating in brain gliomas. When radiotherapy was accompanied by these Au NPs, radiosensitization triggered an improved effect in mice than radiation without NPs.[245] Besides spheric NPs, Au nanorods functionalized with cancer markers have also gained attention in GB treatment due to their prolonged circulation and specific binding to the GB cell surface.[246] In GB gene therapy, Au NPs have not caused inflammation,

immunogenicity or mutagenesis, compared to other common viral, lipid or polymeric delivery vectors. Moreover, their tunability elevated the internalization of active agents and prolonged their release.[247-249]

In conclusion, multifunctional Au nanocarriers for combined targeted GB therapy grant access to an unprecedented new field with infinite possibilities and the ability to develop a tuneable, more personalized treatment approach with subtype-specific responses.

2. Motivation and Objectives

In recent years, great progress has been made towards the development of nano-vehicles for the delivery of drugs and genes to target sites. However, some complex diseases such as GB still remain uncurable with insufficient therapy options due to its heterogeneous nature. The tunability and unique properties of Au NPs raise hope for establishing a novel more effective theranostic tool for tumor treatment, able to enhance standard chemo-, radio- and phototherapy approaches already established in clinical settings.

This work should focus on Au NPs with suitable ligands able to conjugate drugs on their surface and later release them inside GSCs. Gold is specifically chosen due to its biocompatibility, size- and shape-dependent optical characteristics, as well as its high affinity for sulfur, which allows the stable bonding of drug-carrying or cell targeting moieties. After optimization of synthesis parameters, an extensive characterization of Au NPs with various microscopic and spectroscopic methods should follow to examine their size, dispersity in solution and surface functionalization.

The issue of transversing the cell membrane barrier of GSCs should be addressed using fluorescent Au NPs and following their accumulation inside GSCs *in vitro*. In addition, the feasibility of using Au NPs as drug delivery systems to administer poorly water-soluble anticancer compounds into GSCs should be investigated.

The compound CB839, already in clinical trials for the treatment of tumors, is a promising drug candidate against GB and should be chosen for nanodelivery into GSCs. Using mostly polymeric surface ligands, CB839 should be embedded onto the Au NPs through electrostatic interactions and physical adsorption, avoiding the need for a modification of its chemical structure and thus compromising its known effect. The efficiency of this CB839 loading in different Au NPs should be assessed through qualitative and quantitative analysis. Furthermore, studies should be included about the Au NP toxicity and its therapeutic effect on GSC neurospheres to evaluate their potential application in GB therapy.

3. Cumulative Part

This section summarizes the results of the dissertation, which have been published as scientific papers in international journals. Chapters 3.1 and 3.2 show the publications as first author, followed by additional contributions as co-author (chapter 3.3). A short summary of the publication, as well as the author's own contributions is given in each chapter. Each publication has its own bibliography and enumeration of pages, chapters, figures, tables and schemes.

3.1. Influence of Synthesis Methods on the Internalization of Fluorescent Gold Nanoparticles into Glioblastoma Stem-like Cells

Beatriz Giesen, Ann-Christin Nickel, Alba Garzón Manjón, Andrés Vargas Toscano, Christina Scheu, Ulf Dietrich Kahlert, Christoph Janiak,

Journal of Inorganic Biochemistry **2020**, 203, 110952.

DOI: 10.1016/j.jinorgbio.2019.110952, reprinted from reference 250, published by Elsevier.

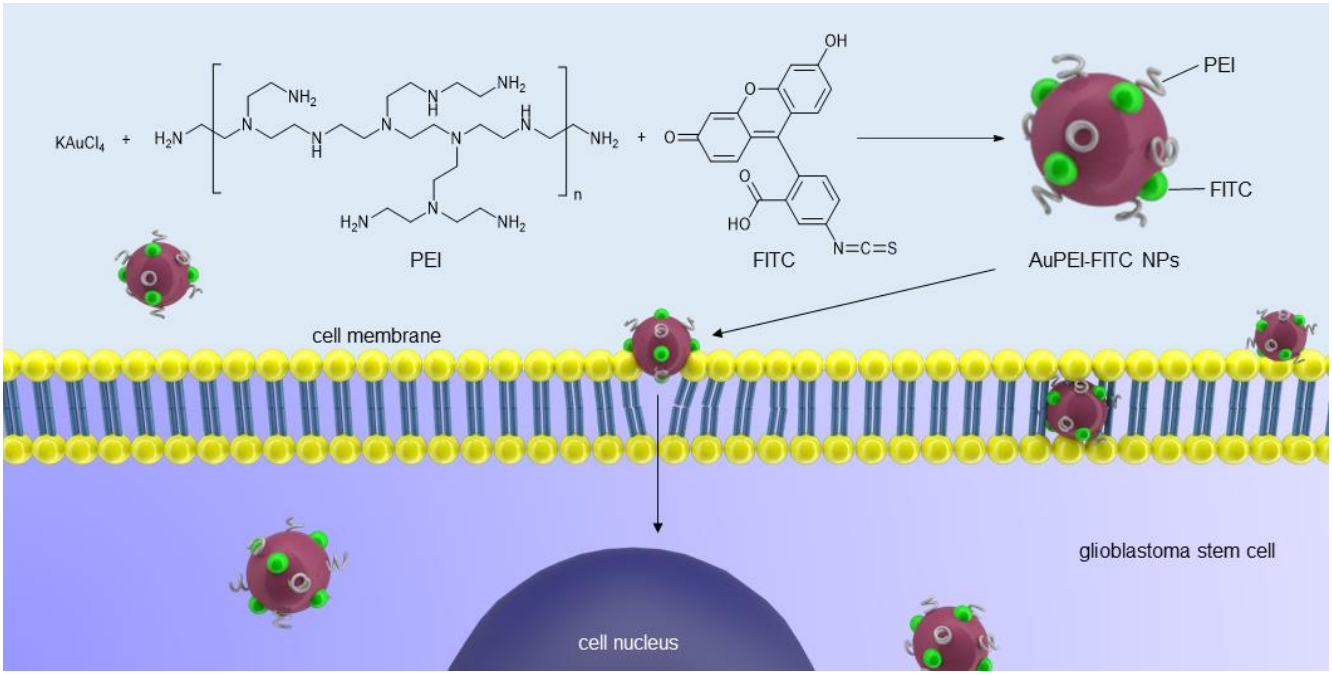

Figure 16. Graphical abstract from ref. 250. A “one-pot” synthesis produces monodisperse fluorescent gold nanoparticles in 2 minutes! A higher percentage of nanoparticles synthesized this way were internalized by glioblastoma stem-like cells compared to other samples synthesized in standard two- or three-step protocols.

Summary:

Au NPs were synthesized to serve as drug and gene delivery systems for a potential treatment of the highly aggressive GB brain tumor. In order to track the nanocarriers *in vivo* and *in vitro*, the surface of the Au NPs was functionalized with the fluorescent marker fluorescein isothiocyanate (FITC). Synthesis of the NPs was conducted in aqueous solutions using the polymer polyethylenimine (PEI) as a stabilizer against agglomeration and a reducing agent for the $KAuCl_4$ starting material. Several microwave-assisted reactions provided AuPEI-FITC NPs with core sizes between 3 and 6 nm, which were characterized using microscopic and spectrometric techniques. A thorough optimization of the parameters for synthesizing AuPEI and AuPEI-FITC NPs was conducted, given that these factors showed a significant effect on the final size, morphology and ligand composition of the product, even when using the same components. The ability of AuPEI-FITC NPs to penetrate GB patient-derived stem cells was tested *in vitro* and quantified with fluorescence-activated cell sorting (FACS) analysis, showing no apparent toxicity and an internalization in cells of up to 61%. Therefore, AuPEI-FITC NPs show great potential as vehicles to transport nucleic acids or drugs into GSCs.

Contributions to the work:

- Idea and design of synthesis methods for Au NPs using biocompatible materials.
- Synthesis and optimization of AuPEI and AuPEI-FITC NPs.
- Investigations regarding suitable purification methods for AuPEI and AuPEI-FITC NPs.
- Determination of the pH stability, stability of FITC attachment to Au and time-dependent size increase of AuPEI-FITC NPs.
- Sample preparation and characterization of NPs.
- Acquirement and analysis of TEM images, EDX spectra and SAED results.
- Further characterization with DLS, UV-VIS, IR and fluorescence spectroscopy studies.
- Evaluation and compilation of AAS and TGA results.
- Incubation of GSCs with Au NPs *in vitro* and performance of cell viability assays with the help of Dr. Ann-Christin Nickel.
- Quantification of NP uptake by GSCs through FACS measurements.
- Calculation of the percentage of fluorescent NPs with FACS and mathematical estimation of the number of NPs taken up per cell.

- Distinction between adsorbed and internalized NPs using the Trypan Blue quenching method.
- Image acquirement and assessment of cells incubated with NPs using bright field and fluorescence microscopy, with the help of Andrés Vargas Toscano.
- Analysis and compilation of all experimental results in form of a scientific publication after interpretation and extensive literature research. Continuous corrections and improvements of the manuscript throughout the peer-review process. Execution of further required experiments and preparation of the revision document.
- Coordination of experiments done by external cooperation partners, as well as communication regarding the final manuscript.
- Support with high resolution TEM and STEM measurements and access to the facilities was provided by Dr. Alba Garzón Manjón and Prof. Dr. Christina Scheu from the Max-Planck-Institut für Eisenforschung, Düsseldorf.
- Corrections and additions to the manuscript were done by Dr. Ann-Christin Nickel, Dr. Alba Garzón Manjón and Prof. Dr. Christina Scheu. Comprehensive expert review by PD Dr. Ulf Kahlert and Prof. Dr. Christoph Janiak.
- Submission to the “Journal of Inorganic Biochemistry” and final approval of the manuscript was made with Prof. Dr. Christoph Janiak.

Journal of Inorganic Biochemistry 203 (2020) 110952

Contents lists available at ScienceDirect

Journal of Inorganic Biochemistry

journal homepage: www.elsevier.com/locate/jinorgbio

Influence of synthesis methods on the internalization of fluorescent gold nanoparticles into glioblastoma stem-like cells

Beatriz Giesen[a], Ann-Christin Nickel[b], Alba Garzón Manjón[c], Andrés Vargas Toscano[b], Christina Scheu[c], Ulf Dietrich Kahlert[b,d,*], Christoph Janiak[a,*]

[a] Institut für Anorganische Chemie und Strukturchemie, Heinrich-Heine-Universität Düsseldorf, 40204 Düsseldorf, Germany
[b] Klinik für Neurochirurgie, Universitätsklinikum Düsseldorf, 40225 Düsseldorf, Germany
[c] Max-Planck-Institut für Eisenforschung GmbH, Max-Planck-Straße 1, 40237 Düsseldorf, Germany
[d] Deutsches Konsortium für Translationale Krebsforschung (DKTK), Essen/Düsseldorf, Germany

ARTICLE INFO

Keywords:
Fluorescent gold nanoparticles
Precision medicine
Rapid synthesis
Glioblastoma stem cells
Internalization

ABSTRACT

Glioblastoma (GBM) is an aggressive disease with currently no satisfying treatment option available. GBM cells with stem cell properties are thought to be responsible for the initiation and propagation of the disease, as well as main contributors to the emergence of therapy resistance. In this work, we developed a novel method to synthesize fluorescent gold nanoparticles as potential drug and gene delivery systems for GBM therapy, able to penetrate three-dimensional stem cell selected patient-derived GBM neurosphere systems *in vitro*. By using polyethylene imine (PEI) as a stabilizer and reducing agent, as well as fluorescein isothiocyanate (FITC) as a fluorescent marker, our fully *in-house* developed fluorescent gold nanoparticles (AuPEI-FITC NPs) with core sizes between 3 and 6 nm were obtained *via* a fast microwave-assisted reaction. Cytotoxicity, adsorption and internalization of AuPEI-FITC NPs into the cell lines JHH520, 407 and GBM1 were investigated using the cellular growth assay and fluorescence-activated cell sorting (FACS) analysis. AuPEI-FITC NPs showed no apparent cytotoxicity and an uptake in cells of up to ~80%. A differentiation between surface-bound and internalized AuPEI-FITC NPs was possible by quenching extracellular signals. This resulted in a maximal internalization degree of 61%, which depends highly on the synthesis method of the nanoparticles and the cell type tested. The best internalization was found for AuPEI-FITC1 which was prepared in a one pot reaction from $KAuCl_4$, PEI and FITC. Thus, appropriately synthesized AuPEI-FITC NPs show great potential as vehicles to transport DNA or drugs in GBM cells.

1. Introduction

Glioblastoma (GBM), the most common type of brain-born neoplasm, is a lethal and ultra-aggressive type of cancer with a remaining life expectancy of under two years [1]. Current therapy consists of surgical resection, administration of temozolomide and radiotherapy but fails to give a positive outcome due to the invasive and heterogeneous nature of the tumor [2]. A population of cells with stem cell properties (= brain cancer stem-like cells, BCSCs) are thought to be the reason for GBM's high cellular invasion capacity and formation of tumor foci [3]. Delivery of therapeutics to the anticipated BCSCs target site is significantly hindered by the blood-brain barrier (BBB), a major obstacle in GBM treatment [4]. Thus, novel anti-BCSC treatments with clinical applicability are of highest clinical and economical interest.

Recent studies have placed nanomaterials in the focus as the future technology for the delivery of drugs, molecules or genes to treat GBM, specifically by targeting BCSCs [5,6]. Gold nanoparticles (Au-NPs) in particular have been widely used for medicinal purposes due to their biocompatibility and unique optical properties. Due to the high permeability and enhanced permeation and retention (EPR) in solid tumors, Au-NPs can pass the BBB, accumulate in the damaged tissue and deliver inhibiting or target specific cell surface molecules like proteins or antibodies, which limit tumor cell proliferation and boost the anticancer effect of standard drugs [6–9]. In combination with radiotherapy, Au-NPs increase the DNA damage to GBM cells inflicted by ionization radiation [10]. This radiosensitization enhances the effectivity of irradiation therapy and also improves the uptake of medications in GBM cells [11,12]. Besides their therapeutic benefits, Au-NPs are also widely used for imaging and sensing applications, showing a longer blood circulation time than common contrast agents [13]. They

* Corresponding author's.
E-mail addresses: Ulf.Kahlert@med.uni-duesseldorf.de (U.D. Kahlert), janiak@uni-duesseldorf.de (C. Janiak).

https://doi.org/10.1016/j.jinorgbio.2019.110952
Received 17 September 2019; Received in revised form 14 November 2019; Accepted 22 November 2019
Available online 23 November 2019
0162-0134/

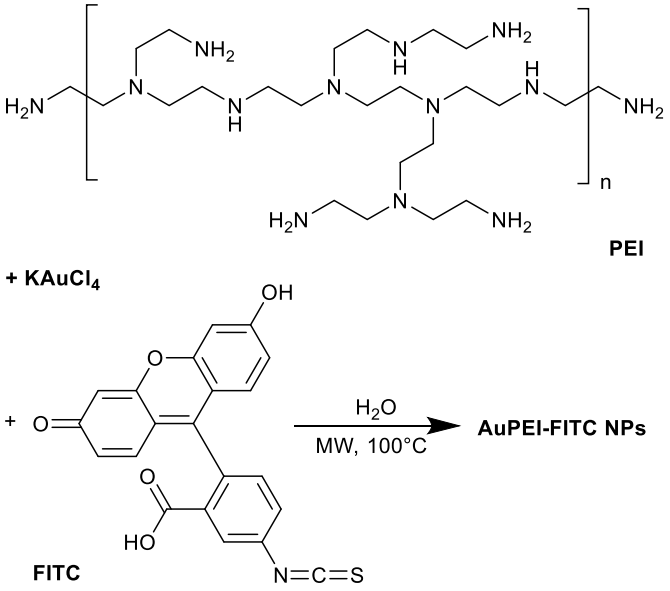

Scheme 1. Representation of the synthesis protocol for optimized AuPEI-FITC NPs for the internalization into glioblastoma GBM cells.

have allowed the accurate display of tumors for its surgical removal due to their surface enhanced resonance Raman scattering (SERRS) signals in combination with magnetic resonance imaging (MRI), as well as being introduced as precise probes for computer tomography (CT) and photoacoustic visualization of tumors [14–16]. In summary, Au-NPs are promising theranostic systems combining therapeutic anticancer effects with diagnostic features for tracking the biodistribution of GBM tumors *in vivo*.

The aqueous synthesis of Au-NPs is straight-forward, cost effective and non-toxic. Moreover, the highly stable colloids formed are modifiable in size and shape through variation of their synthesis parameters. Their surface can be functionalized with various capping ligands and shells to facilitate the loading of therapeutic agents according to specific cell or drug needs [17]. In gene therapy, polyethylene imine (PEI) (Scheme 1) constitutes a suitable capping ligand for Au-NPs because of its high cationic charge density and ability to condensate nucleic acids to the nanoparticle (NP) surface [18]. In the chemical reaction with gold, PEI acts as a three-in-one reagent: it can reduce gold(III) salts to metallic gold, it protects the formed Au-NPs from agglomeration and it can bind DNA through electrostatic interactions [19].

In nanodelivery applications, fluorescein isothiocyanate (FITC) (Scheme 1), a near-infrared organic dye, can serve as a powerful tracking device to locate NPs inside the cells after incubation due to its high extinction coefficient and great quantum yield. Due to the strong affinity of gold for sulfur, FITC can be effectively coupled to Au-NPs though electronically stable covalent bonds with its isothiocyanate group [20]. This Au-FITC combination holds a stronger fluorescent imaging effect of tumor regions compared to FITC alone, which would rapidly be metabolized and removed by cells [10]. When obtained from commercial sources, little information is given about the capping ligand of fluorescent Au-NPs, the amount of fluorophore used and, in some cases, the overall hydrodynamic size of the gold-ligand-FITC system, which is crucial for cell uptake. If the nanodelivery technology is going to become standard, there needs to be easy, reliable and fast methods to produce fluorescent nanocarriers without the need to resort to expensive outsourcing or intricate synthesis routes.

In this work, we describe a Au-NP assembly functionalized with PEI and FITC (AuPEI-FITC) able to penetrate GBM cells. AuPEI-FITC NPs were synthesized in a straight-forward manner from cheap and accessible starting materials (Scheme 1). We describe the importance of the synthesis parameters on the final size, morphology and ligand composition of the nanomaterials even when using the same components. Our GBM functional assessments are performed with three-dimensional neurospheres, selected for high percentage of stemness due to neural stem cell growth conditions [21]. The *in vitro* AuPEI-FITC NPs transfection and level of internalization in three BCSC lines are hereby tested for a potential application as a gene or drug carrier in the treatment of GBM.

2. Results and discussion

2.1. Synthesis of gold nanoparticles

Regardless of the various works stating to have found the ideal nanoparticle size and shape for a successful internalization into cells [22–24], the actual impact of these parameters still remains highly dependent on the cell type. In this study, we opted for the synthesis of small gold nanospheres up to 10 nm diameter. By starting with a small core size, multiple functionalization steps on the nanoparticle surface are possible through a layer-by-layer construct, which allows flexibility to customize and increase the size of the carrier if needed. Furthermore, round-shaped Au-NPs were selected due to their curvature, which makes them more likely to be internalized into cells compared to asymmetrical shaped NPs [25].

The synthesis of gold nanoparticles smaller than 20 nm has been documented by adding a tetrachloroaurate precursor into an aqueous PEI solution under diverse reaction conditions [19,26,27]. Size control is not always easy since a stoichiometric variation of reaction precursors also changes the size distribution and polydispersity of the solution. In order to find the necessary gold to PEI ratio for an optimal stabilization of our delivery system, the amount of $KAuCl_4$ precursor added to a solution of branched PEI was continuously increased as both components were reacted under microwave irradiation (see Supp. info. for synthesis details). Variation of the n_{KAuCl4}/n_{PEI} molar ratio between 1 and 10 (samples AuPEI1–10 accordingly) resulted in different sizes and polydispersity values, as seen from dynamic light scattering (DLS) results (Fig. 1). In our experiments, hydrodynamic diameters corresponding to the gold core and the PEI capping ligand remained between 24 and 67 nm. In some cases, various species of different sizes were detected even after post-synthesis purification. This phenomenon can be attributed to the formation of higher bridged PEI networks containing several Au cores [7].

However, there seems be an optimal ratio of PEI to Au, resulting in small AuPEI NPs with low polydispersity, as in the case of AuPEI5 and

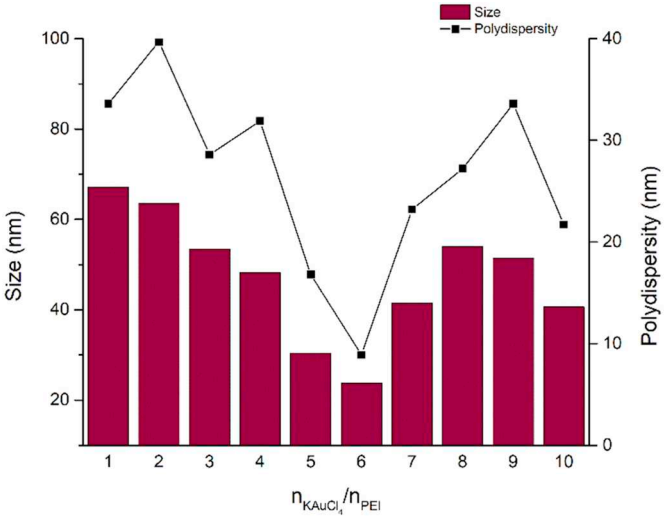

Fig. 1. Size and polydispersity of PEI-capped gold nanoparticles (Au-PEI NPs) with n_{KAuCl4}/n_{PEI} = 1–10.

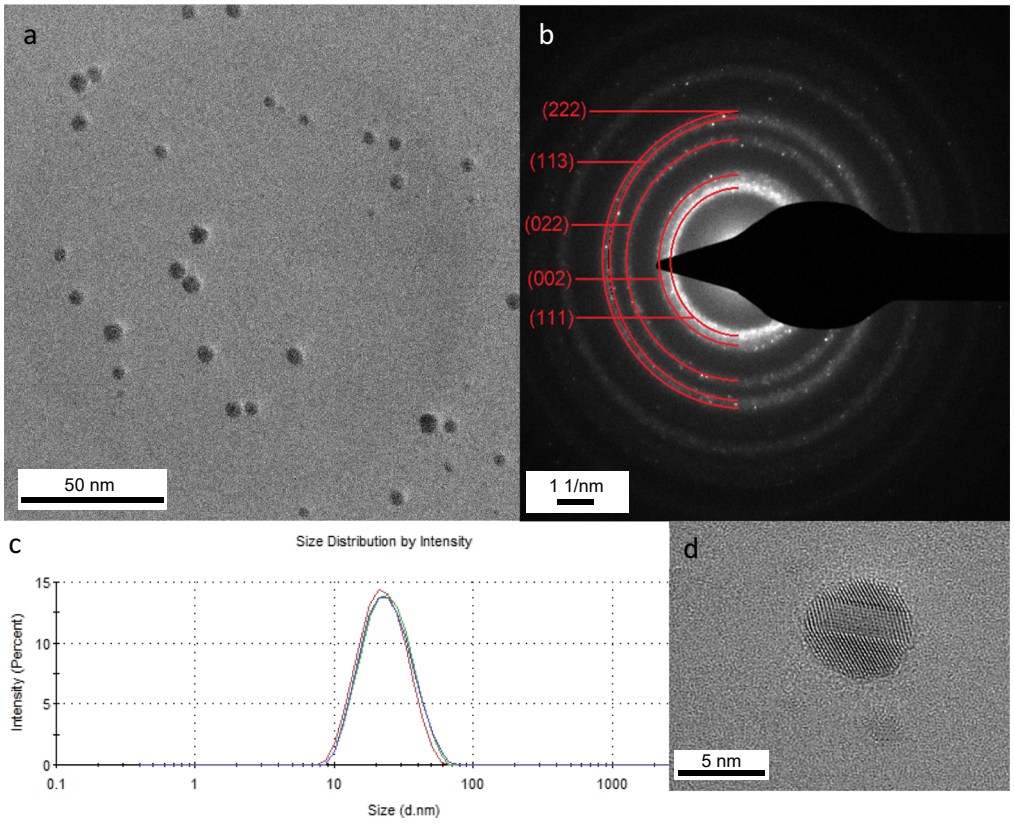

Fig. 2. Characterization of AuPEI6 NPs. a, TEM image of several NPs, b: selected area diffraction showing *hkl* values for *fcc* gold, c: DLS curve showing the size distribution by intensity of three measurements, d: HR-TEM image of an individual NP.

AuPEI6 with $n_{KAuCl4}/n_{PEI} = 5$ or 6, respectively. With a hydrodynamic diameter of 24 nm and a narrow size distribution, AuPEI6 presented the most homogeneous sample. The small size of AuPEI6 NPs was further confirmed *via* high-resolution transmission electron microscopy (HR-TEM) measurements, which revealed a gold core of about 4 ± 1 nm (Fig. 2). The sample also displayed high crystallinity and the expected face-centered cubic (*fcc*) phase.

In the reaction of $KAuCl_4$ and PEI, Au-NPs are formed due to a redox reaction between the amine groups of PEI and the tetrachloridoaurate (III) anion $AuCl_4^-$. While the Au^{III} salt is reduced to Au^0, oxidation at the alpha carbon to the amine groups of the PEI polymer chain results in the conversion of the amine into an amide [27]. This assumption was confirmed by infrared (IR) spectroscopy (Fig. S1 in SI).

Given that PEI itself has also been used as a vehicle for DNA transfection [28], it is crucial to eliminate the free unbound PEI from the gold solution in order to test the true ability of AuPEI NPs as a DNA or drug carrier. For this purpose, a thorough dialysis process was performed against water for 24 h (see Supp. info. for details, Fig. S2). When dialyzing the sample AuPEI6 for a longer time, a significant color change from dark red to purple was observed, signaling a size increase of AuPEI NPs due to a possible agglomeration. DLS results showed an increase in hydrodynamic diameter from 24 nm after 24 h to 68 nm after 48 h and ultimately 77 nm after 72 h. On the other hand, when the sample was left to dialyze for only 6 or 12 h, agglomerates of "free" PEI as large as 91 nm were still found in the sample. Thus, determination of the correct dialysis time is relevant to remove both polymer accumulations in the solution or unstable NP agglomerates which lack stabilization.

TEM images and ultraviolet–visible (UV–VIS) spectra of AuPEI6 before and after 24 h of dialysis (Fig. 3) show the importance of purification for obtaining a more homogeneous Au-NP solution. After dialysis, it was possible to remove larger agglomerates from the initial sample (Fig. 3a, b) and a narrowing of the plasmonic band at 525 nm was observed (Fig. 3c). The resulting AuPEI NPs had a size of 4 ± 1 nm. NPs of this size have successfully loaded drug molecules onto their surface and would be able to exit the body by renal excretion after drug release [29].

Subsequently, the FITC fluorophore was introduced into the AuPEI system as a NP tracking tool in the cells. Several synthesis and purification approaches were tested in order to find a suitable NP species by varying the FITC concentration, the reaction media and ligand incorporation method (Table S1). As a preliminary verification, the cell viability of human embryonic kidney cells (HEK) was monitored after 1 and 3 h of incubation with AuPEI-FITC1–10 NPs at a gold concentration between 0 and 50 mg/L (Fig. S4). Using low toxicity and a good concentration dependence as relevant criteria, samples AuPEI-FITC 1–4 were chosen for further testing in GBM cells. In these four different synthesis approaches, the reaction starting components (gold precursor, PEI and FITC) were introduced at the same ratios but in different order (Fig. 4). Reduction of the gold precursor was always achieved in a hydrothermal microwave reaction, using only PEI as the reducing agent. UV–VIS results of the four samples revealed the characteristic plasmonic peak of Au-NPs at 500 nm (Fig. S5). Solution colors ranged from light orange-red to brownish-red (Fig. S6). Size and size distribution results determined by DLS and TEM for all four synthesis routes are shown in Table S2 and Fig. S7. The morphology of the samples AuPEI-FITC1–4 is displayed in Fig. 5.

Our novel preparation of AuPEI-FITC1 through a so-called "one-pot" synthesis, resulted in the formation of small nanospheres with an average gold core of 3 ± 1 nm. Preformed AuPEI NPs were prepared with the AuPEI6 protocol (see above). When these preformed AuPEI NPs were reacted with the same amount of FITC used for AuPEI-FITC1, similar sized NPs were obtained (AuPEI-FITC2). In the last two experiments, FITC was first linked to the polymer as a PEI-FITC conjugate

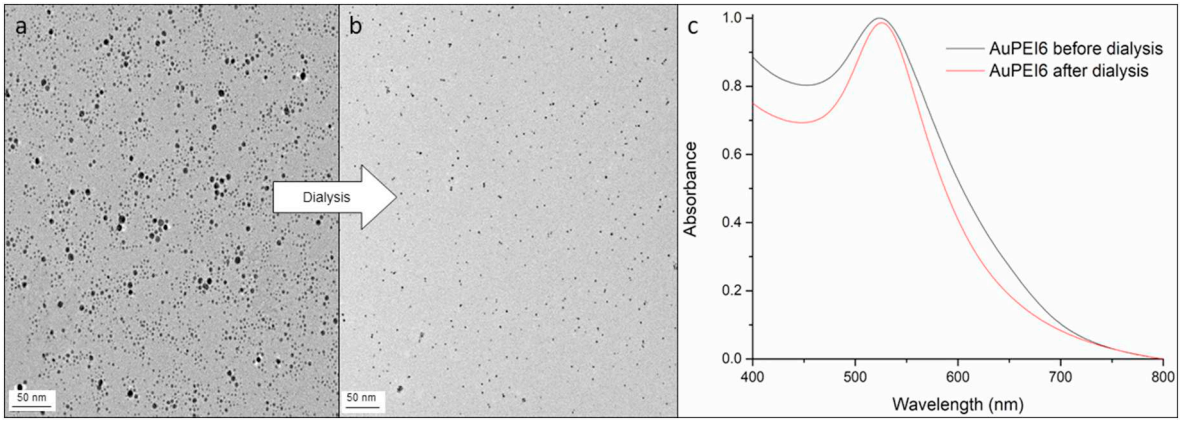

Fig. 3. Effect of purification *via* dialysis of AuPEI6. TEM micrographs of Au-NPs a: before and b: after dialysis. c: Absorbance data. The histograms and DLS measurements for the AuPEI6 NPs before and after dialysis are shown in Fig. S3, Supp. info.

and then either mixed with the preformed AuPEI NPs (for AuPEI-FITC4) or combined with an aqueous solution of $KAuCl_4$ followed by the reduction of the gold(III) precursor (for AuPEI-FITC3). For all cases, a microwave reaction at 100 °C using FITC is possible since the thiocyanate compound shows a decomposition temperature of 260 °C, according to thermogravimetric analysis results (Fig. S8).

In the case of AuPEI-FITC3, previously linking FITC to PEI resulted in the formation of a mixture of two species of NPs with slightly different sizes (Fig. 5c). Even though the PEI-FITC conjugate was purified to eliminate unbound components, there is the possibility that PEI remained either unlabeled or was separated from FITC during the thermal treatment. The parallel existence of both PEI and PEI-FITC in the solution is most likely responsible for two separate nucleation and growth processes of the Au colloids, which could result in different sized NP products. Similarly, a direct stabilization of Au-NPs by FITC instead of PEI cannot be ruled out due to the strong attraction of its thiocyanate group towards gold.

The presence of the fluorescent FITC marker on AuPEI NPs was confirmed using scanning transmission electron microscopy (STEM). Energy-dispersive X-ray spectroscopy (EDX) measurements in STEM mode were able to identify gold atoms corresponding to Au-NPs, as well as sulfur atoms from the FITC ligand in the same area. Both gold and sulfur signals are displayed in color-coded elemental maps in Figs. 6 and S9. Hence, the attachment of FITC to the surface of all AuPEI-FITC NP samples was verified. Additionally, this attachment was verified to be pH resistant between pH 6 and 8, as proven for AuPEI-FITC1 NPs in different phosphate buffers (see Fig. S10).

Due to the high extinction coefficient of Au-NPs and the overlap of their surface plasmon resonance peak with the emission maximum of FITC at 517 nm (Fig. S5), a fluorescence resonance energy transfer (FRET) from FITC to the Au-NPs can be expected [30]. As FITC interacts with the Au-NPs, its fluorescence is severely quenched, which allows further confirmation of a successful functionalization of FITC onto the gold surface. Even though the same amount of FITC was used for all AuPEI-FITC synthesis reactions, fluorescence measurements displayed various degrees of quenching, most likely due to different interactions between FITC and gold atoms in each sample (Fig. S11a).

As expected, all AuPEI-FITC solutions exhibited a lower fluorescence than the FITC control, thereby supporting the attachment of FITC onto the NP surface. AuPEI-FITC1 and AuPEI-FITC3 showed similar fluorescence intensities, contrary to the other two samples. AuPEI-FITC2 exhibited the highest fluorescence intensity (still about 50% less than the FITC control) and AuPEI-FITC4 the lowest (75% less than FITC) of all four NP types. In this case, a lower fluorescence can be the result of a stronger quenching effect and/or a lower amount of FITC being attached to the gold surface. In order to rule out the fluorescence detection from “free” FITC in the solution, AuPEI-FITC samples were centrifuged and the spectra from their supernatants were also recorded

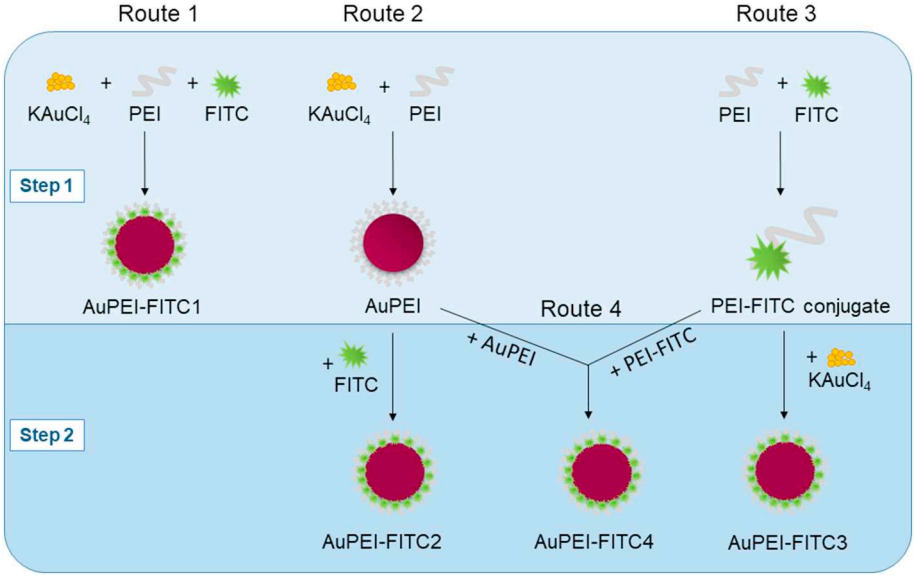

Fig. 4. Synthesis routes of AuPEI-FITC NPs.

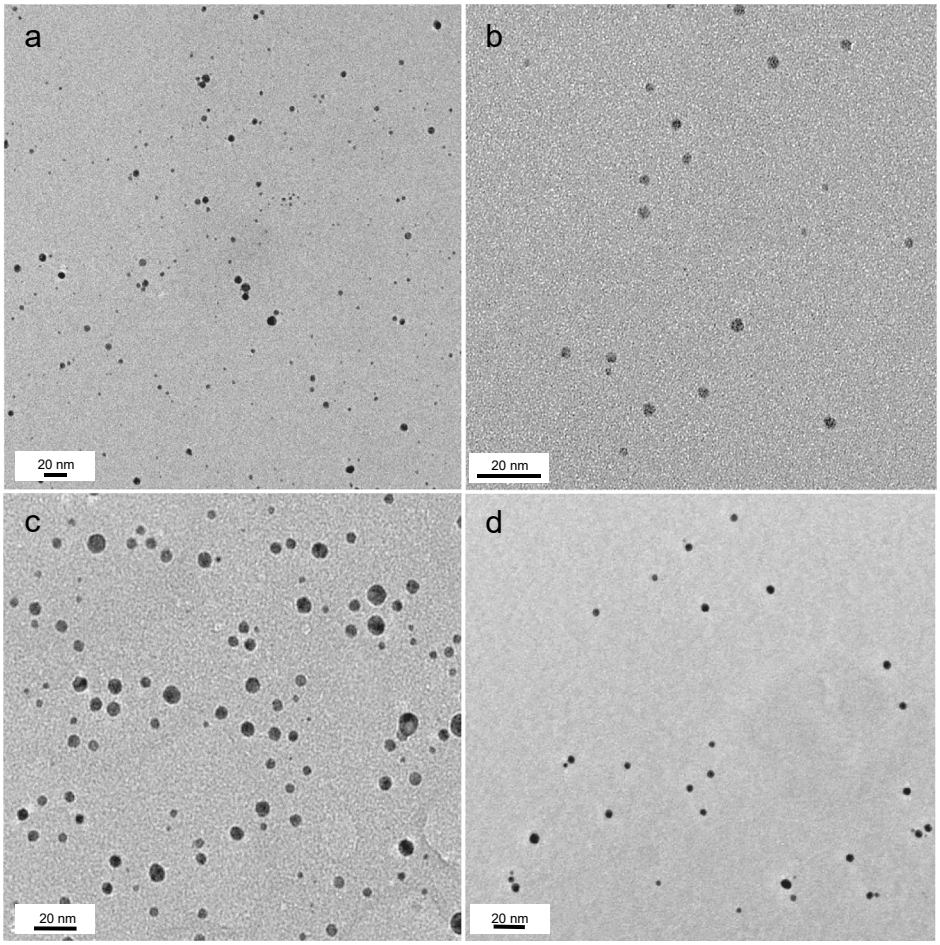

Fig. 5. TEM images of a: AuPEI-FITC1, b: AuPEI-FITC2, c: AuPEI-FITC3 and d: AuPEI-FITC4.

(Fig. S11b), showing no apparent fluorescence in the supernatants.

2.2. Cytotoxicity of AuPEI-FITC NPs

AuPEI-FITC NPs were incubated with the GBM cell lines GBM1, JHH520 and 407 at increasing concentrations for 1, 6, 12 and 24 h respectively (Fig. 7). Viability assays using the tetrazolium dye 3-(4,5-dimethylthiazol-2-yl)-2,5-diphenyltetrazolium bromide (MTT) showed that all AuPEI-FITC NPs have low impact on cell viability when added in concentrations between 0.25 and 2 mg/L, compared to untreated control cells. If NP treatment was extended for longer than 24 h, cytotoxicity of all four types of AuPEI-FITC NPs rose slightly. A possible reason for this effect can be an increased NP size or gradual loss of stabilization of the nanomaterials in culture media. Thus, we tested the stability of AuPEI-FITC NPs incubated in Dulbecco's Modified Eagle Medium (DMEM). Fig. S13 shows a rise in NP size from 118 nm to 199 nm after 3 h until a stable size of approximately 243 nm is reached between 24 and 48 h and maintained for up to two weeks of incubation in DMEM, as seen before for citrate-capped Au-NPs [31]. The greater NP size is a result of the formation of a protein corona on the surface of the NPs as they come in contact with the different proteins contained in cell culture media [32]. However, we can guarantee a stable size of the AuPEI-FITC1 system for a prolonged biomedical application. This is an important finding given that the protein corona can significantly hinder

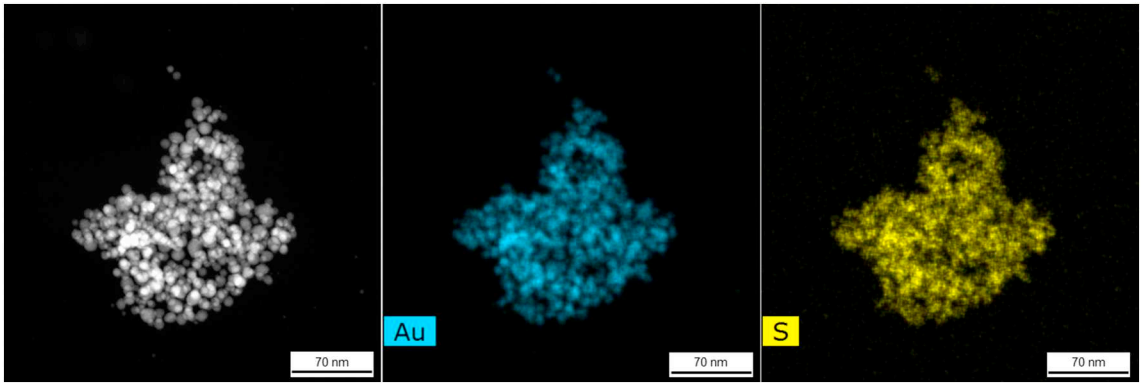

Fig. 6. STEM-EDX elemental maps of AuPEI-FITC3 showing gold (in blue) and sulfur (in yellow) atoms within the agglomerate of NPs.

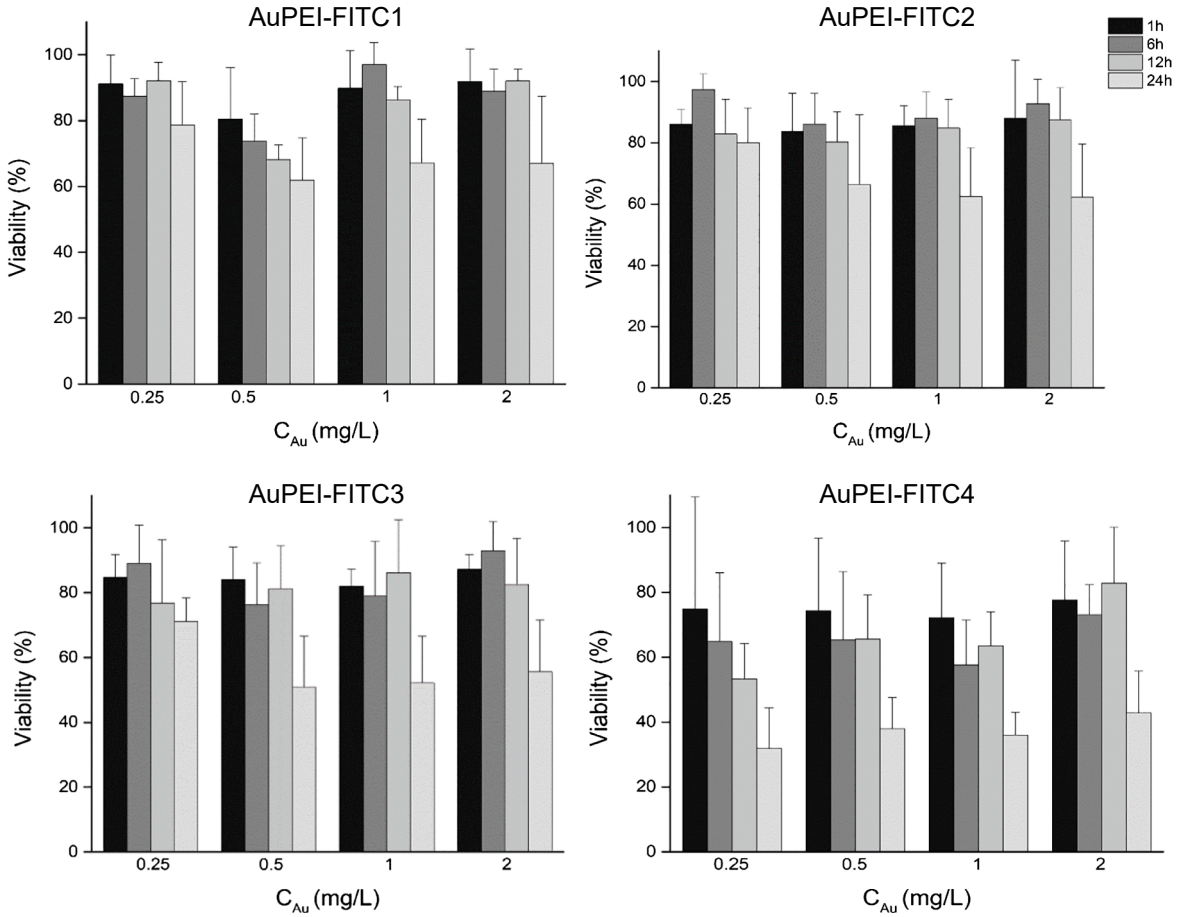

Fig. 7. Viability after 1, 6, 12 and 24 h incubation of GBM1, JHH520 and 407 cells with AuPEI-FITC NPs at increasing concentrations.

the internalization of NPs.

Other factors, such as changes in pH and ionic interactions during NP uptake processes ending in particle agglomeration and loss of their unique properties [33], could be also the reason for a lower cell viability after 24 h. Moreover, a polymer degradation and release of the PEI capping ligand from the NP surface inside the cell [34] would also account for an increased toxicity.

Additionally, our viability studies indicated some variations when incubating the same AuPEI-FITC NP sample in the different GBM cell lines. Thus, there is a dependence of the biocompatibility of AuPEI-FITC NPs on the cell type in which they were incubated. In consequence, the results displayed in Fig. 7 are sometimes widely spread around the mean value. When a mean of all concentrations and all incubation times in all cell lines was calculated (Fig. S14), AuPEI-FITC4 was identified as the least suitable for treatment with a maximum viability of only 61%. AuPEI-FITC3 showed a cell viability of 77%, whereas AuPEI-FITC1 and AuPEI-FITC2 showed values above 82%.

2.3. Uptake in glioblastoma stem-like cells

To investigate a possible uptake of AuPEI-FITC NPs into GBM stem-like cells, plated cells were investigated through a microscope after incubation, as shown in Fig. 8 for JHH520 cells treated with AuPEI-FITC4 NPs. The images in fluorescence correspond to the same area observed through a white light microscope (Fig. 8a). In these experiments, almost all neurospheres displayed fluorescent signals (Fig. 8b). This fluorescence is a result of the stable attachment of the FITC dye to the AuPEI NPs even after cell internalization. The stable dye attachment was verified through a spectroscopic investigation of the formerly internalized AuPEI-FITC1 NPs upon forced release from cells through induced osmolysis (see Fig. S15 in SI).

To rule out cell autofluorescence and to differentiate between internalized and surface-bound (adsorbed) NPs, Trypan blue quenching [35,36] was applied to inhibit extracellular fluorescence (Fig. 8c). We observed a reduction of fluorescence intensity, yet some signals remained visible after the procedure. To quantify the internalization of the NPs, we used the quantitative signal detection technology of fluorescence-activated cell sorting (FACS). In the following the term “adsorbed” refers to AuPEI-FITC NPs adhering to outside of the cell membrane (surface-bound).

2.4. Internalization of AuPEI-FITC NPs

For quantification experiments, GBM cells were treated with AuPEI-FITC NPs and measured in a buffered solution. Fig. S16 displays exemplary FACS results of untreated GBM1 cells (a), cells after incubation with AuPEI-FITC NPs (b, c) and after addition of the extracellular fluorescence quencher Trypan blue (d, e). Untreated cells showed a side scatter (SSC) under $40 \cdot 10^3$ and values lower than 10^3 when results were separated based on their fluorescence intensity (FITC scale), which can be attributed to the autofluorescence of the cells. When treated with AuPEI-FITC NPs, a new cell population (B) appeared higher on the SSC scale because of the increased complexity of cells when exposed to NPs. This population corresponded to cells which have either adsorbed only or adsorbed and internalized fluorescent NPs. As expected, such population presented higher fluorescence values due to the incorporation of the FITC fluorophore into the system. After quenching with Trypan blue, population B decreased to reveal the actual percentage of cells which have internalized fluorescent AuPEI-FITC NPs; omitting the cells with extracellular NPs (Fig. S16d, e).

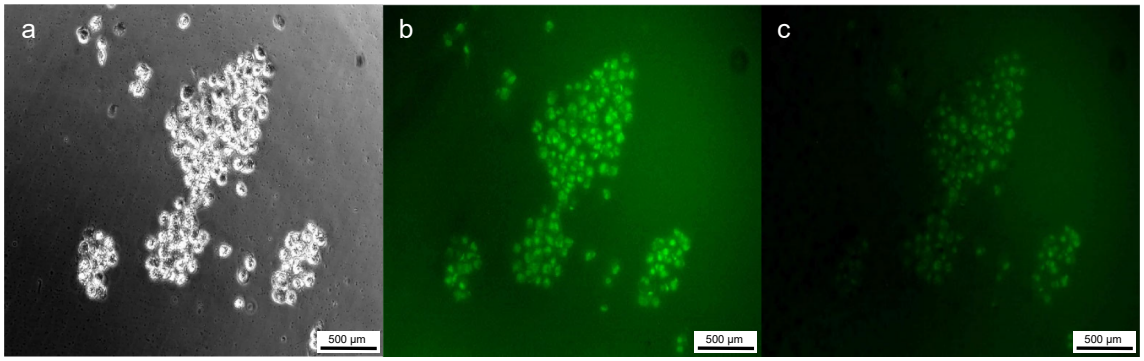

Fig. 8. Microscopic Images of JHH520 cell culture incubated with AuPEI-FITC4 NPs. Image b and c were taken using a fluorescent filter. Image b depicts the cells with adsorbed and internalized AuPEI-FITC4 NPs. Image c was taken after extracellular fluorescence quenching with Trypan blue, hence, depicts the residual internalized AuPEI-FITC4 NPs.

Moreover, analogous FSC intensities were found in both treated and untreated cells. This demonstrates again the low toxicity of our samples given that such intensity is highly dependent on cell death processes such as apoptosis.

In agreement with MTT results, FACS tests also indicated that not all cell lines react in the same way to a treatment with AuPEI-FITC NPs (Table 1). While up to 77% of JHH520 cells showed FITC fluorescence before quenching, GBM1 cells reached an adsorption plus internalization maximum of only 65% (with AuPEI-FITC4) and 407 cells yielded only 60% (with AuPEI-FITC3). From all cell lines, JHH520 cells lost the most percentage of fluorescence after quenching of the (extracellular) adsorbed AuPEI-FITC1–4 NPs. This observation highlights the importance of distinguishing between internalized and extracellular NP species. More importantly, the NP type played an even bigger role concerning their uptake in GBM cells (results after quenching). An average of the adsorbed plus internalized *versus* internalized only AuPEI-FITC NPs in all four cell lines is given at the end of Table 1. The most interesting observation was the lowest decrease in fluorescence intensity before and after quenching of AuPEI-FITC1, as well as its highest internalization average of 53% after only an hour, out of all AuPEI-FITC NPs types. Thus, this vehicle possesses the best cellular uptake potential at low NP concentrations and is hypothesized as a good candidate for treatment delivery studies against GBM.

Compliant with viability results, AuPEI-FITC4 appeared to be the most unsuitable nanocarrier, given that only ~10% of the NPs could be internalized. This realization led us to examine the nature of AuPEI-FITC4 NPs more closely. HR-TEM images revealed a polymer accumulation around the Au-NPs, sometimes even joining several gold spheres into one large agglomerate (Fig. S17). The increased amount of PEI on the NP surface would also explain the low attachment of FITC onto the AuPEI NPs and hence its lesser fluorescence intensity (Fig. S11). AuPEI-FITC4 NPs were easily adsorbed through the higher quantities of PEI polymer of AuPEI6 and the addition of the PEI-FITC conjugate (Fig. 4). This construct most likely causes strong electrostatic interactions with the cell membrane, which is negatively charged. AuPEI-FITC4 also presented the largest diameter and core size out of all AuPEI-FITC samples which probably hampers the internalization (Table S2). Overall, AuPEI-FITC4 NPs were incompatible with GBM cells, starting from their synthesis method, as they failed to well integrate the fluorescent FITC tracking system into our AuPEI NPs, contrary to the samples AuPEI-FITC1–3.

3. Conclusions

Four types of fluorescent Au-NPs with a PEI shell were reproducibly synthesized in a straight-forward manner using accessible starting materials. Gold cores sizes varied between 3 and 6 nm, according to the synthesis route. The novel one-pot method for obtaining fluorescent AuPEI-FITC NPs proved to be not only rapid and simple but also the most suitable gene vector for GBM stem-like cells. Experiments showed the importance of the synthesis method on the final morphology and internalization of gold nanocarriers. The one-pot synthesis where $KAuCl_4$, PEI and FITC were reacted together proved to be superior to two-step syntheses where two out of the three reactants were pre-reacted before being combined with the third reagents. Even though the difficulty of internalization into GBM cells remains, more than the half of the cells got nanofected for each tested cell line. Thus, we presented a quick and simple-to-adjust tool for the development of molecular-targeting Au-NPs with high clinical translational properties. Given the high chemotherapy resistance of BCSC [37], our results are promising for further experiments to develop effective drug delivery devices to eradicate that highly malignant cell population. Moreover, molecular sub-classification of brain cancers revolutionizes current neuropathology [38]. Subtype specific susceptibilities of GBM to our nanotechnology may enhance the efficacy in certain tumors. Further studies are needed to investigate any association of delivery resistance and molecular subtype. In the future, we aim to contribute to improve treatment for GBM by developing drug-conjugated vehicles equipped with epitope-specific anchor proteins such as CD133 or CD44. Efforts to attach novel discovered anti-BCSC drugs to AuPEI-NPs are underway.

Table 1
Fraction of cells with adsorbed and internalized *vs.* internalized AuPEI-FITC NPs in different GBM cell lines.[a]

Cell line	AuPEI-FITC1		AuPEI-FITC2		AuPEI-FITC3		AuPEI-FITC4	
	Adsorbed + internalized (%)	Internalized (%)	Adsorbed + internalized (%)	Internalized (%)	Adsorbed + internalized (%)	Internalized (%)	Adsorbed + internalized (%)	Internalized (%)
GBM1	63	61	56	29	52	7	65	9
JHH520	60	51	75	44	77	39	76	7
407	49	47	53	33	60	9	54	5
Average (all)	57	53	61	35	63	18	65	7

[a] 500,000 cells were incubated with 1 mg/L AuPEI-FITC NPs in PBS for 1 h. The column "Adsorbed + internalized" refers to cells before quenching. The column "Internalized" gives the fraction of cells after addition of Trypan blue solution that is quenching the extracellular NPs.

4. Experimental

4.1. Materials and methods

Branched polyethylene imine (PEI) with an average molar mass of M_W ~ 25,000 g/mol, potassium tetrachloridoaurate (III) and fluorescein isothiocyanate (FITC) were purchased from Sigma Aldrich and used without further purification. Water for the reactions was purified using the Milli-Q® purification system. Dialysis was performed using Spectra/Por® membranes from Spectrum Laboratories with a MWCO of 3.5 kDa and 50 kDa. To increase the water solubility of FITC, 50 mg (0.13 mmol) were solved in dimethyl sulfoxide (DMSO) (Honeywell, 99.7% purity) to create a FITC solution with a concentration of 4 mg/mL. This solution was then diluted to 0.05 mg/mL either in water (*FITC stock 1*) or PBS (Gibco, #10010015, Thermo Fisher Scientific, USA) buffer (*FITC stock 2*) before adding it to the nanoparticle synthesis reaction.

4.2. NP characterization

4.2.1. Transmission electron microscopy (TEM)

Sample preparation consisted on dropping 10 μL of the gold solution onto a 200 μm carbon-coated copper grid and allowing it to dry in air. TEM images were acquired on a FEI Tecnai G2 F20 electron microscope operated at 200 kV accelerating voltage and recorded with a Gatan UltraScan 1000P camera. This microscope was also used to record selected area electron diffraction (SAED) patterns. An area with sufficient material was put inside the round aperture and illuminated with widespread parallel beam to obtain focused diffraction patterns. Images were calibrated using Debye-Scherrer patterns recorded from a gold reference sample (S106, Plano GmbH, Wetzlar, Germany). High resolution TEM of gold NPs was performed using a Titan Themis 60-300 X-FEG microscope equipped with an image corrector and operated at 300 kV. Using the Gatan Digital Micrograph software, over 100 particles were counted to determine NP size and size distribution.

4.2.2. Scanning transmission electron microscopy (STEM)

STEM studies using a high-angle annular dark-field (HAADF) detector from 73 mrad to 350 mrad in combination with energy-dispersive X-ray (EDX) mapping were carried out in the Titan Themis 60–300 X-FEG microscope with a ~150 pA current, a convergence semi-angle of ~23.8 mrad and a beam size of ~0.1 nm.

4.2.3. Dynamic light scattering (DLS)

The hydrodynamic diameters of Au-NPs were determined using a Zetasizer instrument (Malvern Nano S Zetasizer) with a HeNe laser at a wavelength of 633 nm. Three measurements with four runs were assessed to calculate the mean size value.

4.2.4. Ultraviolet–visible spectroscopy (UV–VIS)

Gold nanoparticle samples were measured as synthesized on a UV-2450 spectrometer and analyzed using the UVProbe software, both from Shimadzu.

4.2.5. Fluorescence spectroscopy

300 μL of gold solution were diluted in 3 mL PBS, placed in quartz glass cuvettes and measured on a FluoroMax-4 Spectrofluorometer from HORIBA Scientific with an excitation of 490 nm.

4.2.6. Thermogravimetric analysis (TGA)

FITC decomposition studies were carried out on a Netzsch TG209 F3 Tarsus (Netzsch, Selb, Germany) instrument under a nitrogen atmosphere with a ramp between 1 and 1000 °C.

4.3. Synthesis of PEI-coated gold nanoparticles (AuPEI)

50 mg (2 μmol) of PEI were dissolved in 50 mL water and added to a round bottom flask containing a specific amount of the gold precursor $KAuCl_4$ corresponding to a n_{KAuCl4}/n_{PEI} molar ratio between 1 and 10. The yellow solution was placed in a microwave (CEM, Discover) equipped with a reflux unit and irradiated for 2 min at 100 °C and 300 W while stirring. Dialysis of the red solution was done against water for 24 h using a 50 kDa tube.

4.4. Synthesis of fluorescent gold nanoparticles (AuPEI-FITC)

4.4.1. AuPEI-FITC1

4.5 mg (12 μmol) of $KAuCl_4$ and 5 mL of *FITC stock 1* were added to a solution of 50 mg (2 μmol) of PEI dissolved in 50 mL of water and irradiated in the microwave for 2 min at 100 °C. Dialysis through a 50 kDa membrane against water for 24 h was performed as a purification step.

4.4.2. AuPEI-FITC2

4.5 mg (12 μmol) of $KAuCl_4$ were added to a solution of 50 mg (2 μmol) of PEI dissolved in 50 mL of water, irradiated in the microwave for 2 min at 100 °C and dialyzed through a 50 kDa membrane against water for 24 h. 5 mL of *FITC stock 1* were added to the AuPEI NP solution, stirred at room temperature for 8 h and dialyzed through a 3.5 kDa membrane against PBS for 24 h.

4.4.3. AuPEI-FITC3

5 mL of *FITC stock 2* were added to a solution of 50 mg (2 μmol) of PEI in 50 mL of PBS. The FITC-PEI solution was stirred at room temperature for 8 h and dialyzed through a 3.5 kDa membrane against PBS for 24 h. Afterwards, 4.5 mg (12 μmol) of $KAuCl_4$ were added, the solution was irradiated for 2 min at 100 °C and dialyzed through 3.5 kDa membrane against PBS for 24 h.

4.4.4. AuPEI-FITC4

4.5 mg (12 μmol) of $KAuCl_4$ were added to a solution of 50 mg (2 μmol) of PEI dissolved in 50 mL of water, irradiated in the microwave for 2 min at 100 °C and dialyzed through a 50 kDa membrane against water for 24 h. Volume was adjusted to 40 mL. 5 mL of *FITC stock 2* were added to a solution containing 50 mg (12 μmol) of PEI in 10 mL of PBS, stirred at room temperature for 8 h and dialyzed through a 3.5 kDa membrane against PBS for 24 h. AuPEI NP and FITC-PEI solutions were combined, stirred at room temperature for 8 h and dialyzed through a 3.5 kDa membrane against PBS for 24 h.

For synthesis details about samples AuPEI-FITC5–10, refer to Table S1 in Supp. info.

4.5. Cell cultures

Human embryonic kidney (HEK) cells are cultured in Dulbecco's Modified Eagle Medium (DMEM) without pyruvate (Gibco, #11965092, Thermo Fisher Scientific, USA) supplemented with 10% fetal calf serum (Gibco, #26140079, Thermo Fisher Scientific, USA). Glioma (BCSC) cells JHH520 cells were generously provided by G. Riggins (Baltimore, USA), GBM1 by A. Vescovi (Milan, Italy) and 407 by M.S. Carro (Freiburg, Germany). BCSC neurospheres were cultured in DMEM without pyruvate (Gibco, #11965092, Thermo Fisher Scientific, USA), 30% Ham's F12 Nutrient Mix (Gibco, #11765047), 2% B27 supplement (Gibco, #17504044), 20 ng/mL human basic fibroblast growth factor (Peprotech, #AF-100-18B, USA), 20 ng/mL human epidermal growth factor (Peprotech, #AF-100-15), 5 μg/mL Heparin (Sigma, #H0878, Merck KGaA, Germany). Both media contained 1× Antibiotic-Antimycotic (Gibco, #15240096). Cells are tested for their absence of mycoplasma contamination and validated for their genetic identity using short tandem repeat analysis similar as described before

using the core facility service of our institute [21].

4.6. Cell viability assay

96-well plates were coated with a laminin-PBS solution (1:20 v:v) (Sigma-Aldrich, # 2020, Germany) and left to dry in the sterile working bench. Each well was loaded with 20,000 GBM cells suspended in 100 µL culture medium. After successful cell adhesion on the bottom, medium was removed from each well and cells were incubated for 1, 6, 12 and 24 h with a nanoparticle:medium dilution at different concentrations. The gold concentration of the nanoparticle solutions was estimated assuming that all 12 µmol of $KAuCl_4$ were completely reduced to Au^0. A solution of 5 mg/mL MTT in PBS was diluted 1:10 in medium and added to each well (100 µL) after removal of the nanoparticle dilutions and washing each well with PBS. Allowing 90 min reaction time, MTT was taken out and 50 µL DMSO were pipetted to release the purple color. Absorbance was measured at 550 nm on an iMark™ Microplate Reader using the Microplate Manager® software from Biorad.

4.7. Nanoparticle uptake by GBM cells

500,000 glioblastoma cells were suspended in 500 µL PBS and incubated with nanoparticle dilutions at 1 mg/L for 1 h. To quench extracellular fluorescence, a 0.4% Trypan Blue solution (Sigma-Aldrich, # T8154, Germany) was added to the cell suspension in a 1:3 volume ratio. FACS measurements were performed on a BD FACSCanto™ flow cytometer equipped with blue (488 nm, air-cooled, 20 mW solid state) and red (633 nm, 17 mW HeNe) excitation sources and the FACSDiva™ software. Kaluza Analysis Software from Beckman Coulter was used for further analysis of scattering plots.

Declaration of competing interest

The authors declare that they have no known competing financial interests or personal relationships that could have appeared to influence the work reported in this paper.

Acknowledgments

The authors thank N. Stoecklein, Department of Surgery, Universitätsklinikum Düsseldorf (UKD) and his team for the technical support and providing the FACS infrastructure. We acknowledge Dr. Juri Barthel at the Ernst Ruska-Centre, Forschungszentrum Jülich GmbH (FZ Jülich), Germany for his technical support at the TEM facility under project number ER-C A-060. We thank Dr. Dirk Bier from FZ Jülich and Dr. Evmorfia Petropoulou from UKD for their helpful knowledge and help in this project. U.D. Kahlert thanks H.J. Steiger for his continuous support.

Appendix A. Supplementary data

The Supporting Information contains IR spectra, size and size distributions for NPs, details on synthesis and purification, viability plots, UV-Vis spectra, STEM-EDX for AuPEI-FITC NPs, stability characterizations, determinations of ratio of fluorescent NPs and of amounts of AuNPs in cells. Supplementary data to this article can be found online at https://doi.org/10.1016/j.jinorgbio.2019.110952.

References

[1] U.D. Kahlert, S.M. Mooney, M. Natsumeda, H.-J. Steiger, J. Maciaczyk, Int. J. Cancer 140 (2017) 10–22.
[2] Y. Yang, I.-Y. Hsieh, X. Huang, J. Li, W. Zhao, Front. Pharmacol. 7 (2016) 477.
[3] J.D. Lathia, S.C. Mack, E.E. Mulkearns-Hubert, C.L.L. Valentim, J.N. Rich, Genes Dev. 29 (2015) 1203–1217.
[4] B.G. Harder, M.R. Blomquist, J. Wang, A.J. Kim, G.F. Woodworth, J.A. Winkles, J.C. Loftus, N.L. Tran, Front. Oncol. 8 (2018) 462.
[5] S.S. Kim, A. Rait, F. Rubab, A.K. Rao, M.C. Kiritsy, K.F. Pirollo, S. Wang, L.M. Weiner, E.H. Chang, Mol. Ther. 22 (2014) 278–291.
[6] A. Orza, O. Soriţău, C. Tomuleasa, L. Olenic, A. Florea, O. Pana, I. Bratu, E. Pall, S. Florian, D. Casciano, A. Biris, Int. J. Nanomedicine 8 (2013) 689–702.
[7] I. Naletova, L.M. Cucci, F. D'Angeli, C.D. Anfuso, A.M. Magrì, D. La Mendola, G. Lupo, C. Satriano, Cancers 11 (2019) 1322, , https://doi.org/10.3390/cancers11091322.
[8] T.-M. Sun, Y.-C. Wang, F. Wang, J.-Z. Du, C.-Q. Mao, C.-Y. Sun, R.-Z. Tang, Y. Liu, J. Zhu, Y.-H. Zhu, X.-Z. Yang, J. Wang, Biomaterials 35 (2014) 836–845.
[9] Y. Zhong, C. Wang, R. Cheng, L. Cheng, F. Meng, Z. Liu, Z. Zhong, J. Control. Release 95 (2014) 63–71.
[10] G. Yang, S. Xiang, K. Zhang, D. Gao, C. Zheng, F. Zhao, Int. J. Clin. Exp. Med. 9 (2016) 753–759.
[11] D.Y. Joh, L. Sun, M. Stangl, A.A. Zaki, S. Murty, P.P. Santoiemma, J.J. Davis, B.C. Baumann, M. Alonso-Basanta, D. Bhang, G.D. Kao, A. Tsourkas, J.F. Dorsey, PLoS One 8 (2013) e62425, , https://doi.org/10.1371/journal.pone.0062.
[12] L. Bobyk, M. Edouard, P. Deman, M. Vautrin, K. Pernet-Gallay, J. Delarochea, J.-F. Adam, F. Estève, J.-L. Ravanat, H. Elleaume, Nanomed.-Nanotechnol. 9 (2013) 1089–1097.
[13] M.F. Kircher, A. de la Zerda, J.V. Jokerst, C.L. Zavaleta, P.J. Kempen, E. Mittra, K. Pitter, R. Huang, C. Campos, F. Habte, R. Sinclair, C.W. Brennan, I.K. Mellinghoff, E.C. Holland, S.S. Gambhir, Nat. Med. 18 (2012) 829–834.
[14] W. Shang, C. Zeng, Y. Du, H. Hui, X. Liang, C. Chi, K. Wang, Z. Wang, J. Tian, Adv. Mater. 29 (2017) 1604381.
[15] X. Gao, Q. Yue, Z. Liu, M. Ke, X. Zhou, S. Li, J. Zhang, R. Zhang, L. Chen, Y. Mao, C. Li, Adv. Mater. 29 (2017) 1603917.
[16] L. Zhao, S. Wen, M. Zhu, D. Li, Y. Xing, M. Shen, X. Shi, J. Zhao, Artif. Cell Nanomed. B. 46 (2018) 488–498.
[17] I. Fratoddi, I. Venditti, C. Cametti, M.V. Russo, J. Mater. Chem. B 2 (2014) 4204–4220.
[18] M. Saito, H. Saitoh, Biosci. Biotechnol. Biochem. 76 (2012) 1777–1780.
[19] X. Sun, S. Dong, E. Wang, J. Colloid Interface Sci. 288 (2005) 301–303.
[20] S.-C. Wei, P.-H. Hsu, Y.-F. Lee, Y.-W. Lin, C.-C. Huang, ACS Appl. Mater. Interfaces 4 (2012) 2652–2658.
[21] U.D. Kahlert, A.K. Suwala, E.H. Raabe, F.A. Siebzehnrubl, M.J. Suarez, B.A. Orr, E.E. Bar, J. Maciaczyk, C.G. Eberhart, Brain Pathol. 25 (2015) 724–732.
[22] B. Devika Chithrani, A. Ghazani, W. Chan, Nano Lett. 6 (2006) 662–668.
[23] T.D. Fernández, J.R. Pearson, M.P. Leal, M.J. Torres, M. Blanca, C. Mayorga, X. Le Guével, Biomaterials 43 (2015) 1–12.
[24] E.C. Cho, L. Au, Q. Zhang, Y. Xia, small 6 (2010) 517–522.
[25] E. Panzarini, S. Mariano, E. Carata, F. Mura, M. Rossi, L. Dini, Int. J. Mol. Sci. 19 (2018) 1305–1325.
[26] W.J. Song, J.Z. Du, T.M. Sun, P.Z. Zhang, J. Wang, small 6 (2010) 239–246.
[27] M. Ortega-Muñoz, M. Giron-Gonzalez, R. Salto-Gonzalez, A. Jodar-Reyes, S. De Jesus, F. Lopez-Jaramillo, F. Hernandez-Mateo, F. Santoyo-Gonzalez, Chem. Asian J. 11 (2016) 3365–3375.
[28] M. Thomas, A.M. Klibanov, PNAS 100 (2003) 9138–9143.
[29] H.S. Choi, W. Liu, P. Misra, E. Tanaka, J.P. Zimmer, B.I. Ipe, M.G. Bawendi, J.V. Frangioni, Nat. Biotechnol. 25 (2007) 1165.
[30] S. Wang, X. Wang, Z. Zhang, L. Chen, Colloids Surf. A Physicochem. Eng. Asp. 468 (2015) 333–338.
[31] G. Maiorano, S. Sabella, B. Sorce, V. Brunetti, M.A. Malvindi, R. Cingolani, P.P. Pompa, ACS Nano 4 (2010) 7481–7491.
[32] X. Cheng, X. Tian, A. Wu, J. Li, J. Tian, Y. Chong, Z. Chai, Y. Zhao, C. Chen, C. Ge, ACS Appl. Mater. Interfaces 7 (2015) 20568–20575.
[33] B. Halamoda-Kenzaoui, M. Ceridono, P. Urbán, A. Bogni, J. Ponti, S. Gioria, A. Kinsner-Ovaskainen, J. Nanobiotechnol. 15 (2017) 48.
[34] S. Honary, F. Zahir, Trop. J. Pharm. Res. 12 (2013) 255–264.
[35] J. Hed, G. Hallden, S.G. Johansson, P. Larsson, J. Immunol. Methods 101 (1987) 119–125.
[36] S. Vranic, N. Boggetto, V. Contremoulins, S. Mornet, N. Reinhardt, F. Marano, A. Baeza-Squiban, S. Boland, Part. Fibre Toxicol. 10 (2013) 2, https://doi.org/10.1186/1743-8977-10-2.
[37] A. Eramo, L. Ricci-Vitiani, A. Zeuner, R. Pallini, F. Lotti, G. Sette, E. Pilozzi, L.M. Larocca, C. Peschle, R. De Maria, Cell Death Differ. 13 (2006) 1238–1241.
[38] D. Capper, D.T.W. Jones, M. Sill, V. Hovestadt, D. Schrimpf, D. Sturm, et al., Nature 555 (2018) 469–474, https://doi.org/10.1038/nature26000.

Supporting Information

Influence of synthesis methods on the internalization of fluorescent gold nanoparticles into glioblastoma stem-like cells

Beatriz Giesen[a], Ann-Christin Nickel[b], Alba Garzón Manjón[c], Andrés Vargas Toscano[b], Christina Scheu[c], Ulf Dietrich Kahlert[b,d,*], Christoph Janiak[a,*].

[a] Institut für Anorganische Chemie und Strukturchemie, Heinrich-Heine-Universität Düsseldorf, 40204 Düsseldorf, Germany.

janiak@uni-duesseldorf.de, beatriz.giesen@uni-duesseldorf.de

[b] Clinic for Neurosurgery, Medical Faculty, Heinrich-Heine University Dusseldorf, 40225 Dusseldorf, Germany.

ann-christin.nickel@med.uni-duesseldorf.de, andres.vargastoscano@med.uni-duesseldorf.de

[c] Max-Planck-Institut für Eisenforschung GmbH, Max-Planck-Straße 1, 40237 Düsseldorf, Germany.

scheu@mpie.de, a.garzon@mpie.de

[d] Deutsches Konsortium für Translationale Krebsforschung (DKTK), Essen/Düsseldorf, Germany.

ulf.kahlert@med.uni-duesseldorf.de

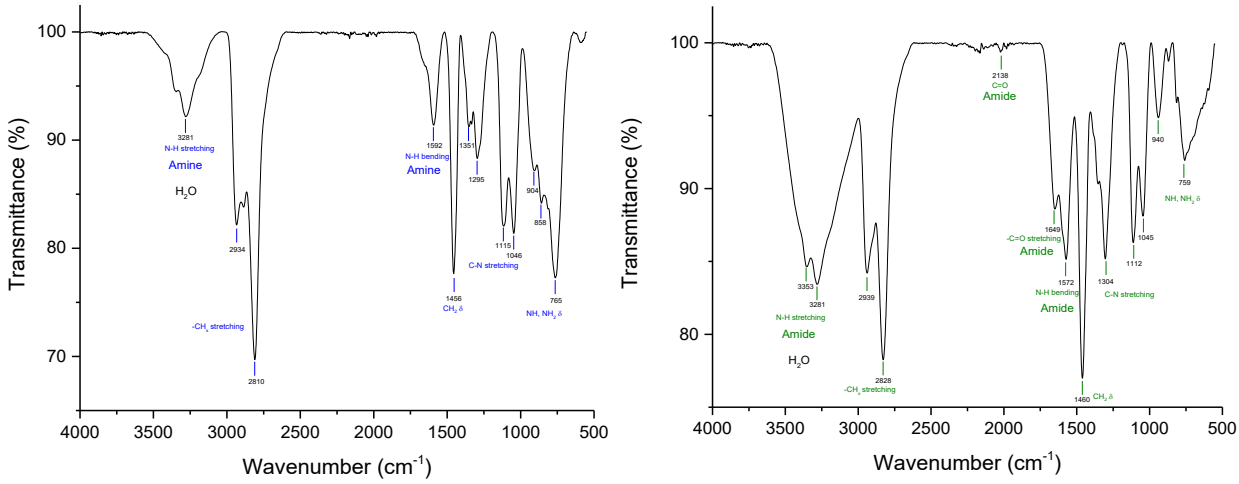

Fig. S1. IR Spectra of PEI (left) and AuPEI6 (right).

Compared to the spectrum of PEI, Au-NPs capped with PEI (AuPEI NPs) showed the appearance of a band at $\tilde{\nu}$=1649 cm^{-1}, corresponding to the C=O stretching of an amide function. Moreover, the amine N-H bend at $\tilde{\nu}$=1592 cm^{-1} of PEI shifted to $\tilde{\nu}$=1572 cm^{-1}, corresponding to an amide N-H bend, after its reaction with $KAuCl_4$.

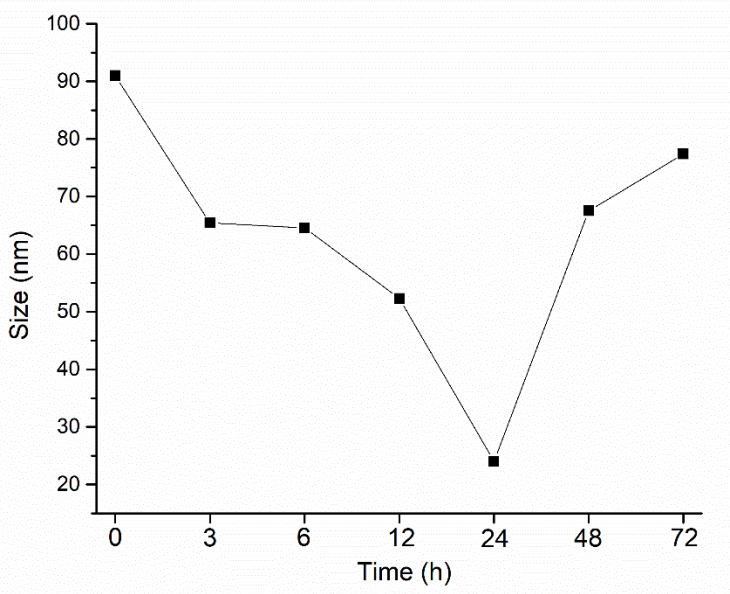

Fig. S2. Dependence of NP size by variation of dialysis time for AuPEI6.

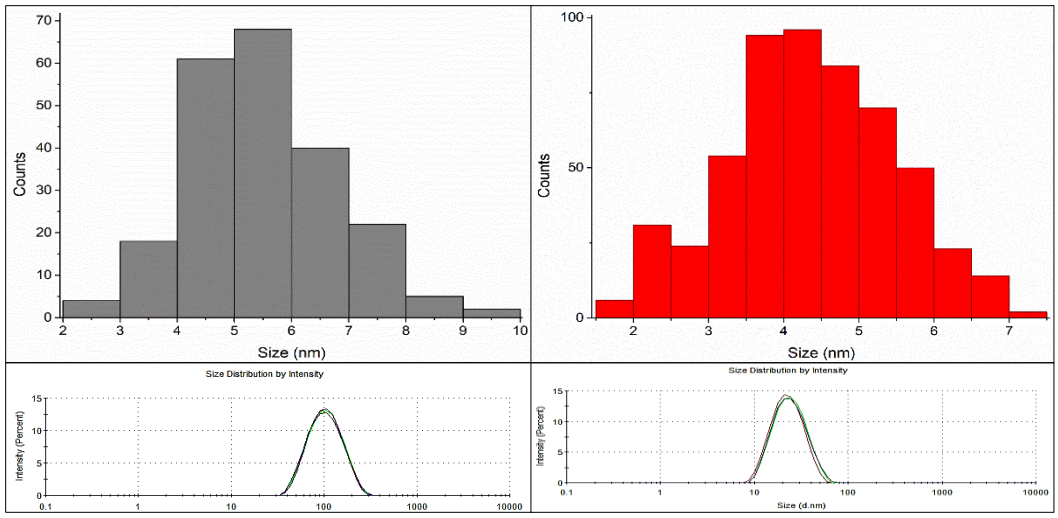

Fig. S3. Histograms and DLS measurements for AuPEI6 NPs before (left) and after dialysis (right).

Table S1. Synthesis and Purification Approaches for AuPEI-FITC NPs.

Entry	Sample name	C_{FITC} [mg/L]	Reaction medium	Dialysis
1	AuPEI-FITC1	4	water	water
2	AuPEI-FITC2	4	water	PBS
3	AuPEI-FITC3	4	PBS	PBS
4	AuPEI-FITC5	4	water	water
5	AuPEI-FITC6	40	water (Au) + PBS (PEI-FITC)	PBS
6	AuPEI-FITC7	40	water (Au) + PBS (PEI-FITC)	1. water 2. PBS
7	AuPEI-FITC4	4	water (AuPEI)+ PBS (PEI-FITC)	PBS
8	AuPEI-FITC8	4	water	water
9	AuPEI-FITC9	8	water	PBS
10	AuPEI-FITC10	40	water (AuPEI)+ PBS (PEI-FITC)	PBS

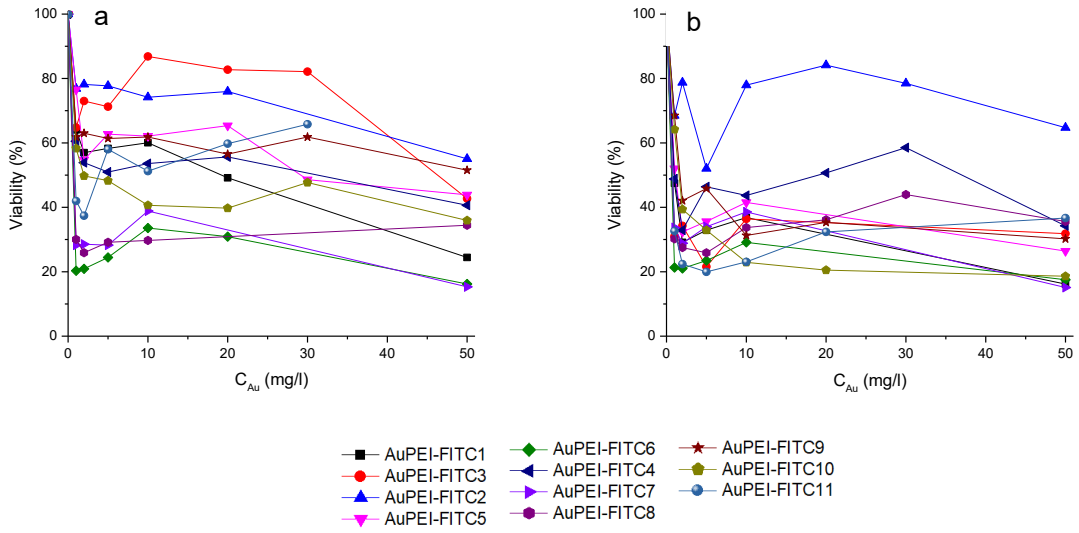

Fig. S4. Viability of AuPEI-FITC NPs in HEK cells after 1 (a) and 3 h (b).

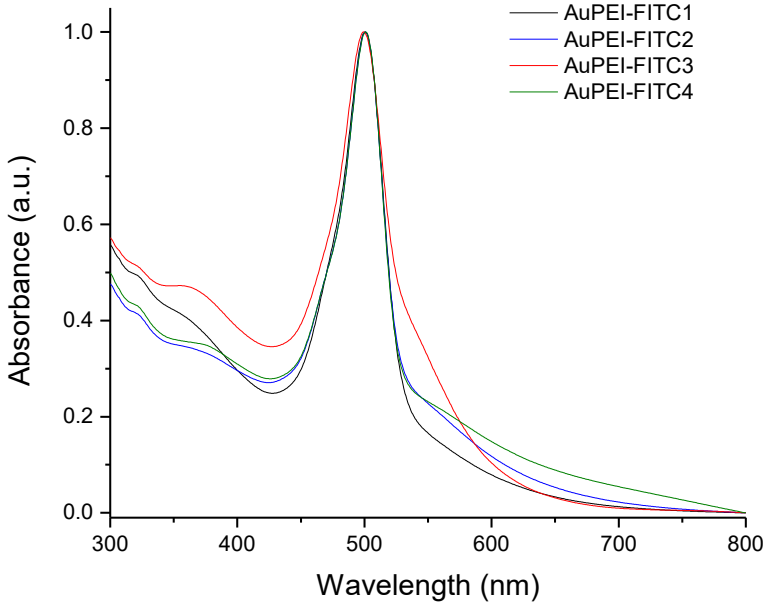

Fig. S5. UV-VIS Spectra of AuPEI-FITC NPs.

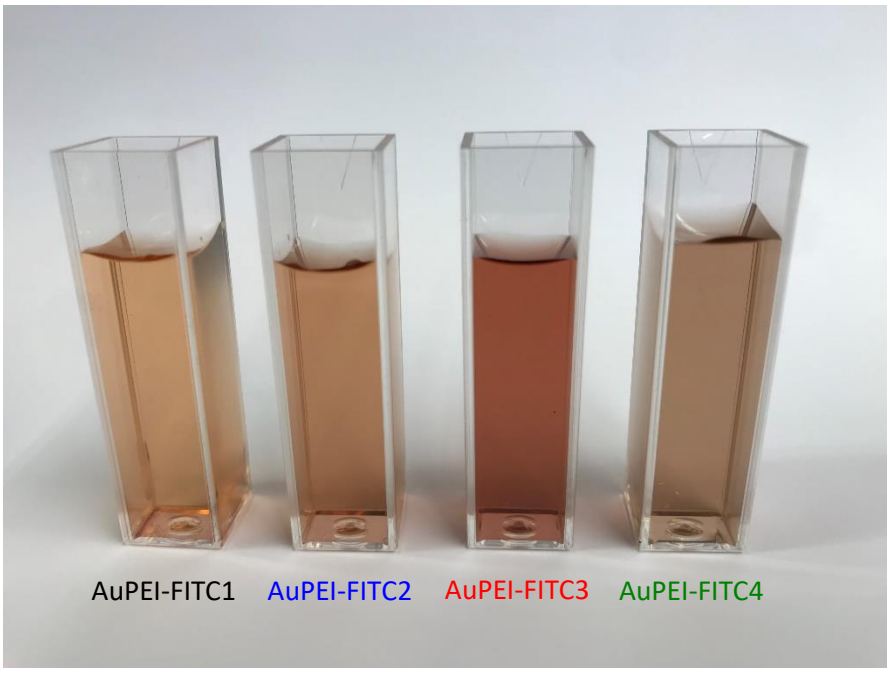

Fig. S6. AuPEI-FITC NPs solutions.

Table S2. Size of fluorescent AuPEI NPs determined by DLS and TEM.

Nanoparticle Sample	Size (nm)	
	TEM	DLS
AuPEI-FITC1	3 ± 1	118
AuPEI-FITC2	4 ± 1	47
AuPEI-FITC3	3 ± 1	115
AuPEI-FITC4	6 ± 2	129

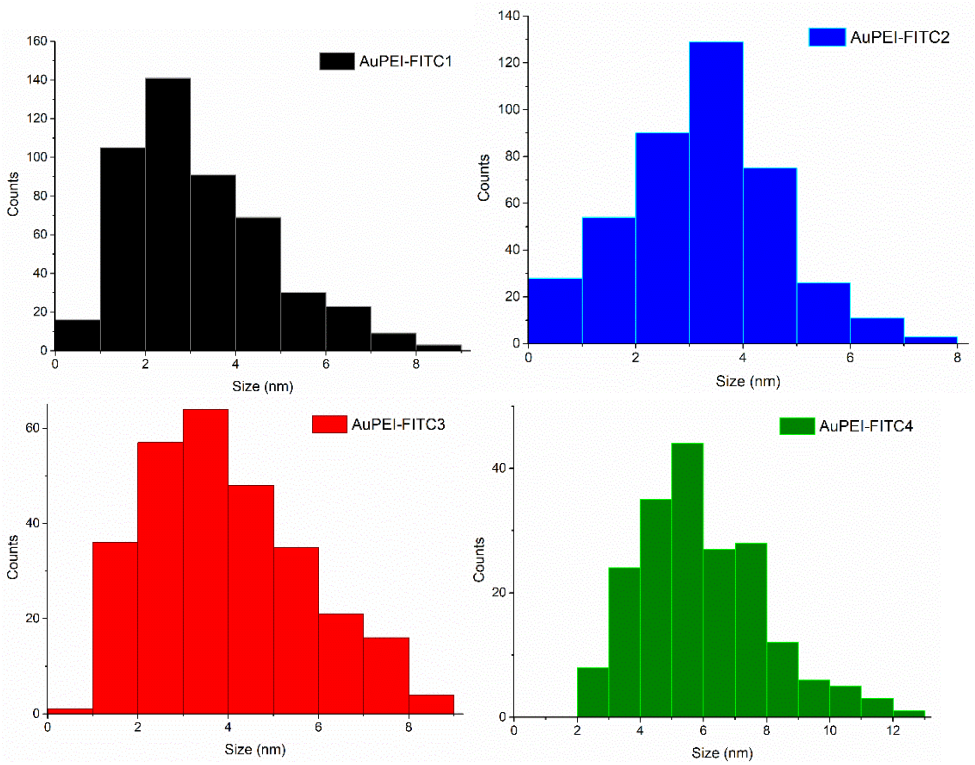

Fig. S7. Size distribution of AuPEI-FITC NPs.

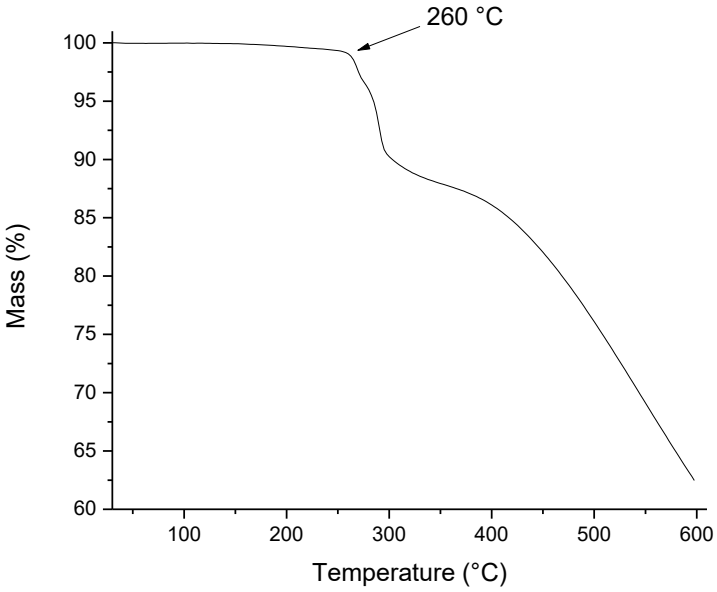

Fig. S8. Thermogravimetric analysis of FITC.

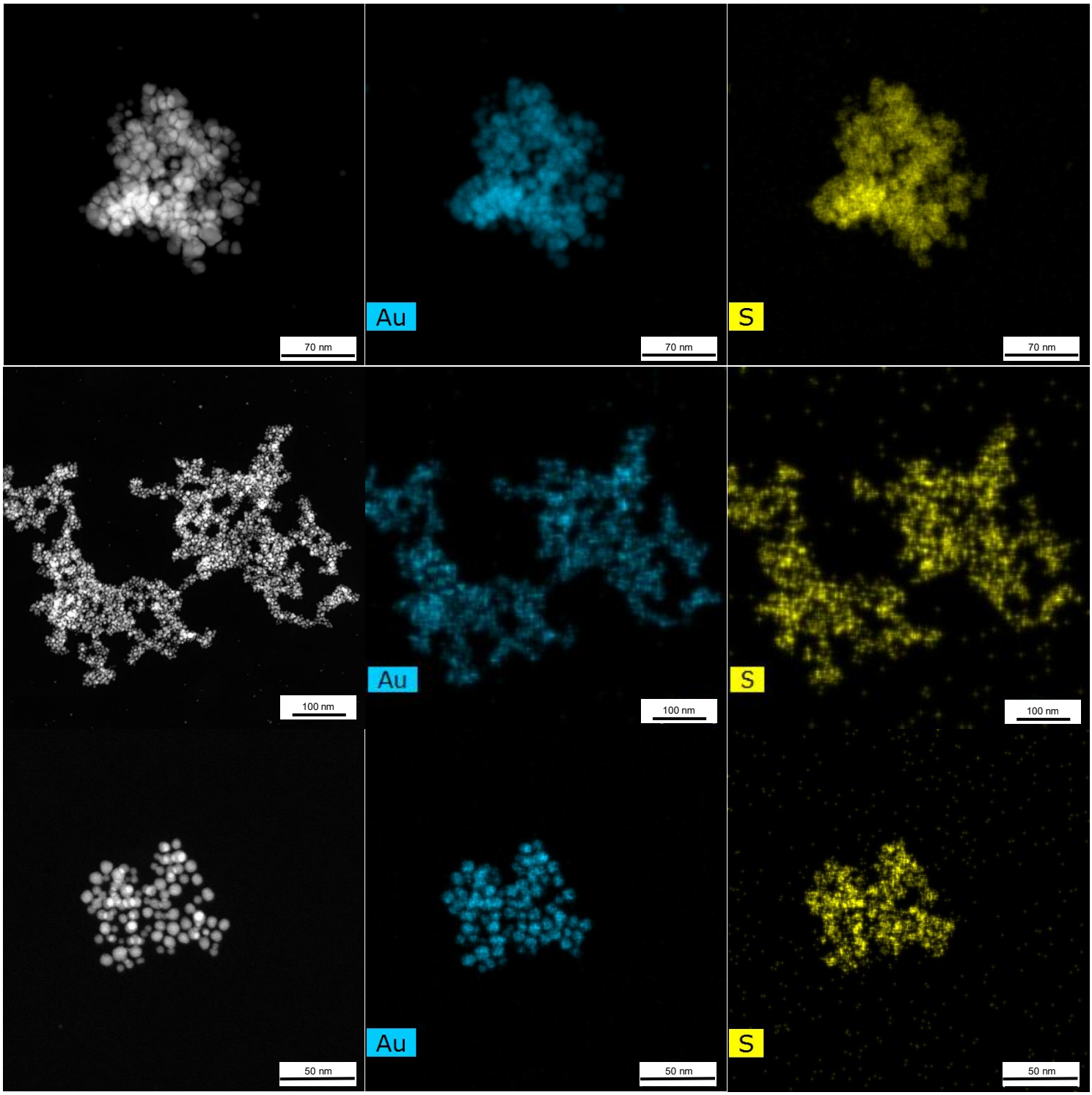

Fig. S9. STEM-EDX from AuPEI-FITC1 (top), AuPEI-FITC2 (middle) and AuPEI-FITC4 (bottom).

pH Resistance of FITC attachment to Au

AuPEI-FITC1 NPs were incubated in potassium phosphate buffers with pH values of 6, 6.5, 7, 7.5 and 8. After centrifugation (20000 rpm, 20 min), UV-VIS measurements of supernatants were performed, showing no unbound FITC at 465 nm.

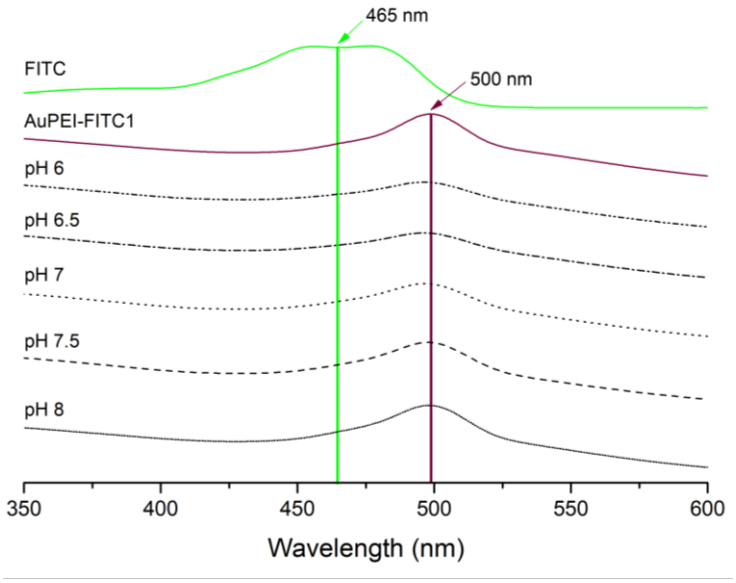

Fig. S10. UV-VIS measurements of AuPEI-FITC1 supernatants after incubation in different phosphate buffers with pH variation. The spectra of “free” FITC (green) is for comparison only, to show, that the supernatants do not give an absorption in this region. AuPEI-FITC1 (in wine red) is the reference spectrum for the as-synthesized sample as a solution in water. pH 6-8 refer to AuPEI-FITC1 NPs incubated in buffers at those pH values.

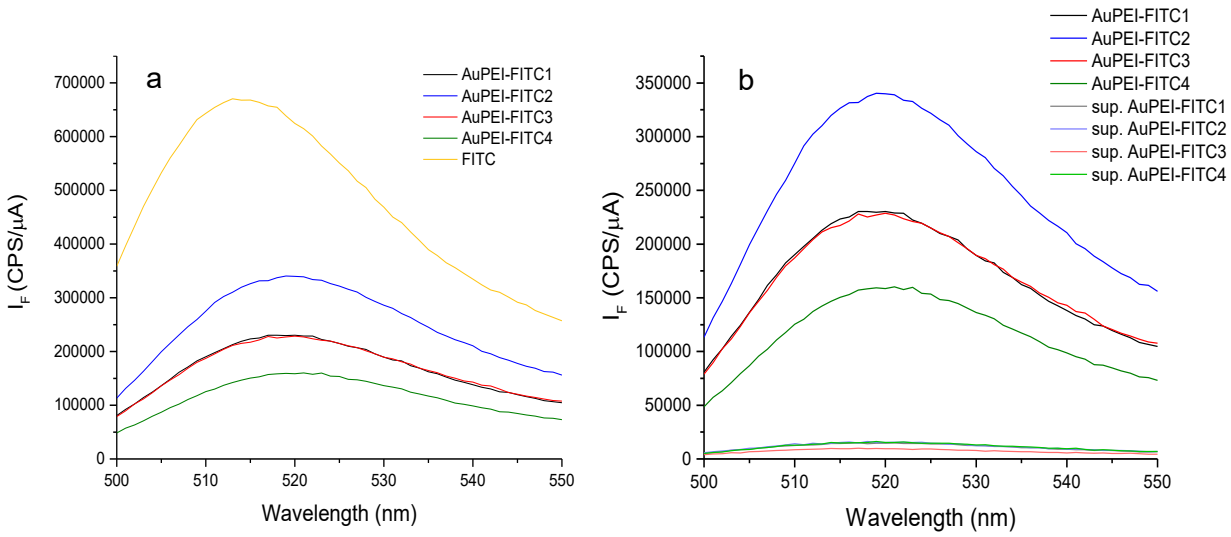

Fig. S11. Fluorescence spectra of AuPEI-FITC NPs.

Ratio of fluorescent NPs

The question of what percentage of NPs were fluorescent, was tackled by measuring FACS of one of our AuPEI-FITC NPs in solution.

In the flow cytometry scatter and gating plots of AuPEI-FITC4 NPs (Fig. S12 a), NPs appeared as a single population. However, when were separated based on their fluorescence intensity (Fig. S12 b, Count-FITC graph), we could distinguish between non-fluorescent (A) and fluorescent (B) NPs. The calculated percentage of AuPEI-FITC NPs for AuPEI-FITC4 was 52% non-fluorescent and 48% fluorescent. According to the fluorescence spectra in Fig. S11, AuPEI-FITC4 was the least fluorescent sample. The NPs AuPEI-FITC1-3 all had higher fluorescent intensities. Thus, we conclude that at least 50% of all NPs are fluorescent.

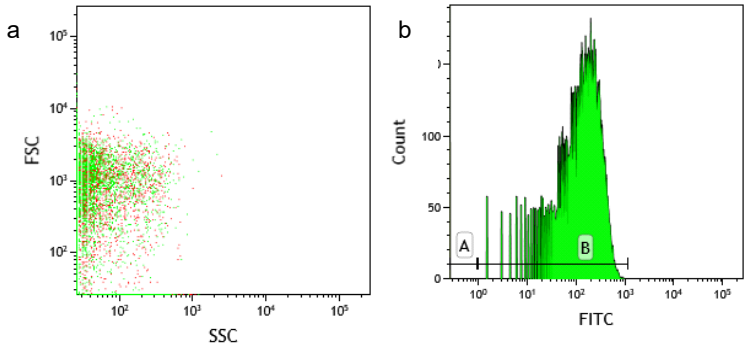

Fig. S12. Flow cytometry scatter and gating plots of AuPEI-FITC4 NPs. Population A (in red) represents NPs without fluorescence and B (in green) fluorescent NPs.

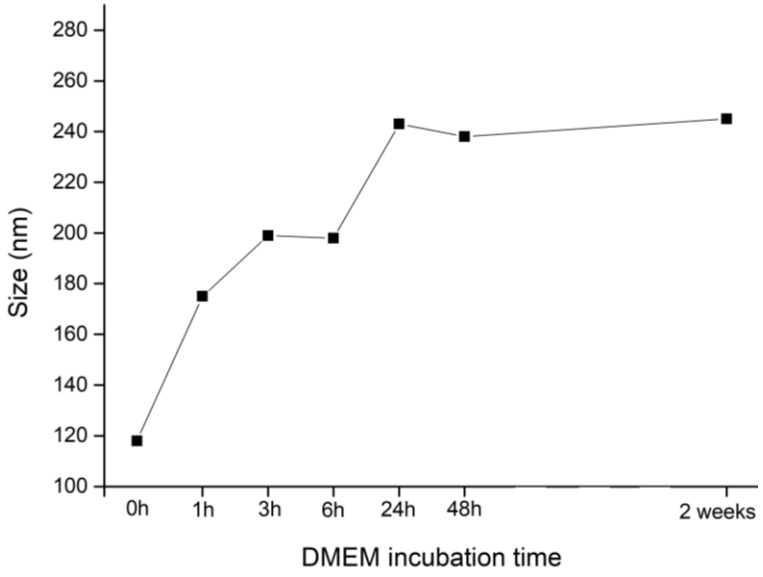

Fig. S13. Time dependent size increase of AuPEI-FITC1 NPs after incubation in DMEM culture media. Hydrodynamic diameter was determined using DLS.

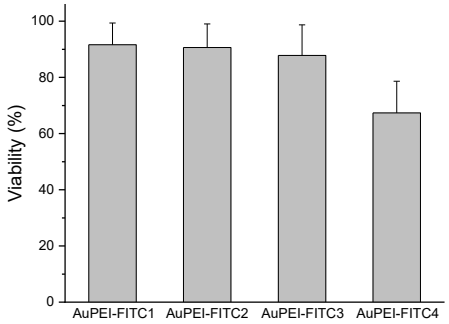

Fig. S14. Viability of all cell lines after incubation with AuPEI-FITC NPs. All concentrations and times were included in the mean calculation.

Stability of FITC attachment to Au after cell internalization

20 000 JHH520, 407 and GBM1 cells were incubated with AuPEI-FITC1 NPs and separated from the media by centrifugation (1080 rpm, 5 min). The cell pellets were washed with PBS to remove any remaining NPs on the surface and centrifuged again. Pellets were now dispersed in water to cause bursting of cell membranes and the release of internalized AuPEI-FITC NPs. High speed centrifugation (20000rpm, 20 min) isolated the remaining cells and NPs from their supernatants. UV-VIS measurements of these supernatants did not show (“free”) FITC absorption signals. Given that FITC dye which is not attached to Au-NPs (“free” FITC) does not precipitate at the chosen centrifugation speed, there is no significant loss of dye from the AuPEI-FITC NPs after internalization into GBM cells.

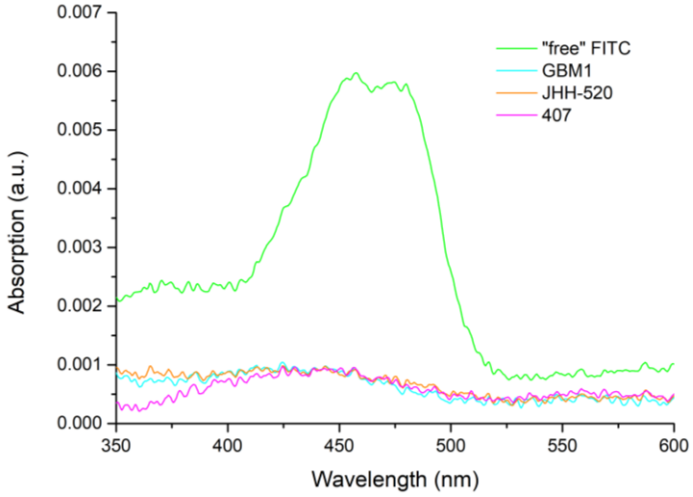

Fig. S15. UV-VIS spectra of cell supernatants after induced osmolysis of cells (JHH520, 407 and GBM1) with internalized AuPEI-FITC1 NPs. The spectrum of “free” FITC (green) is for comparison only, to show, that the cell supernatants do not give an absorption in this region.

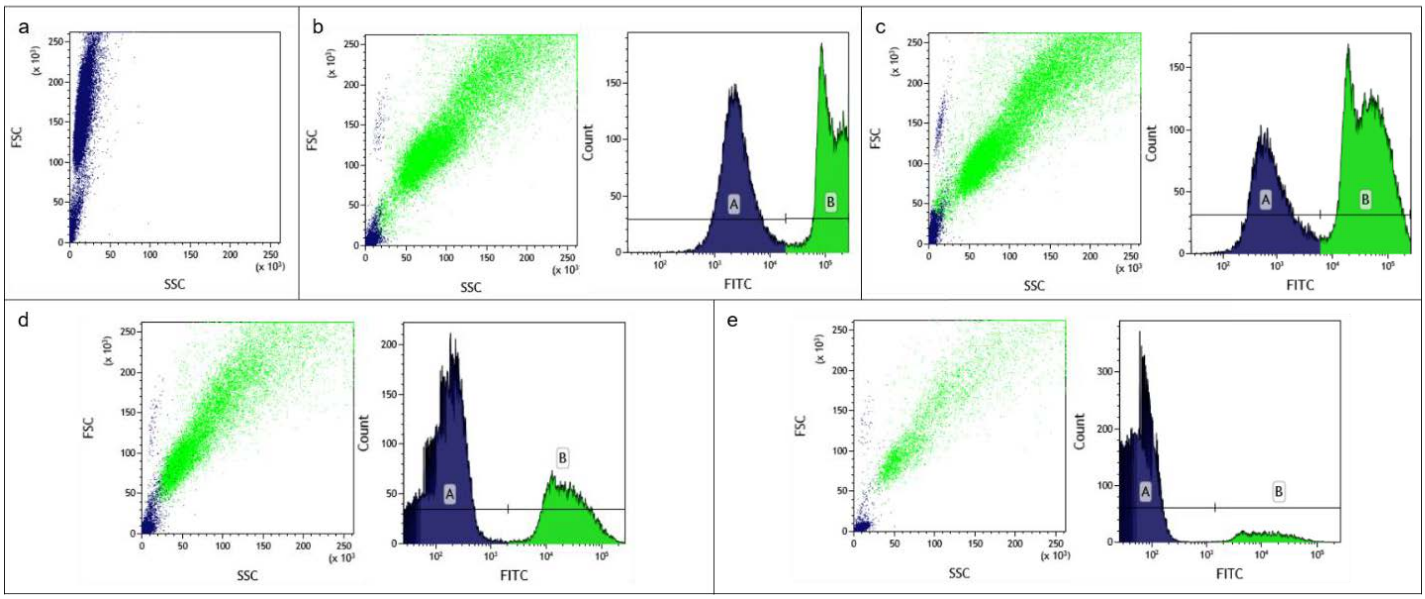

Fig. S16. Flow cytometry scatter and gating plots of GBM cells. a: untreated GBM1 cells, b: GBM1 cells treated with AuPEI-FITC2, c: GBM1 cells treated with AuPEI-FITC4, d: GBM1 cells treated with AuPEI-FITC2 after extracellular fluorescence quenching, e: GBM1 cells treated with AuPEI-FITC4 after Trypan blue quenching. Population A represents cells without fluorescent AuPEI-FITC NPs and B cells containing NPs.

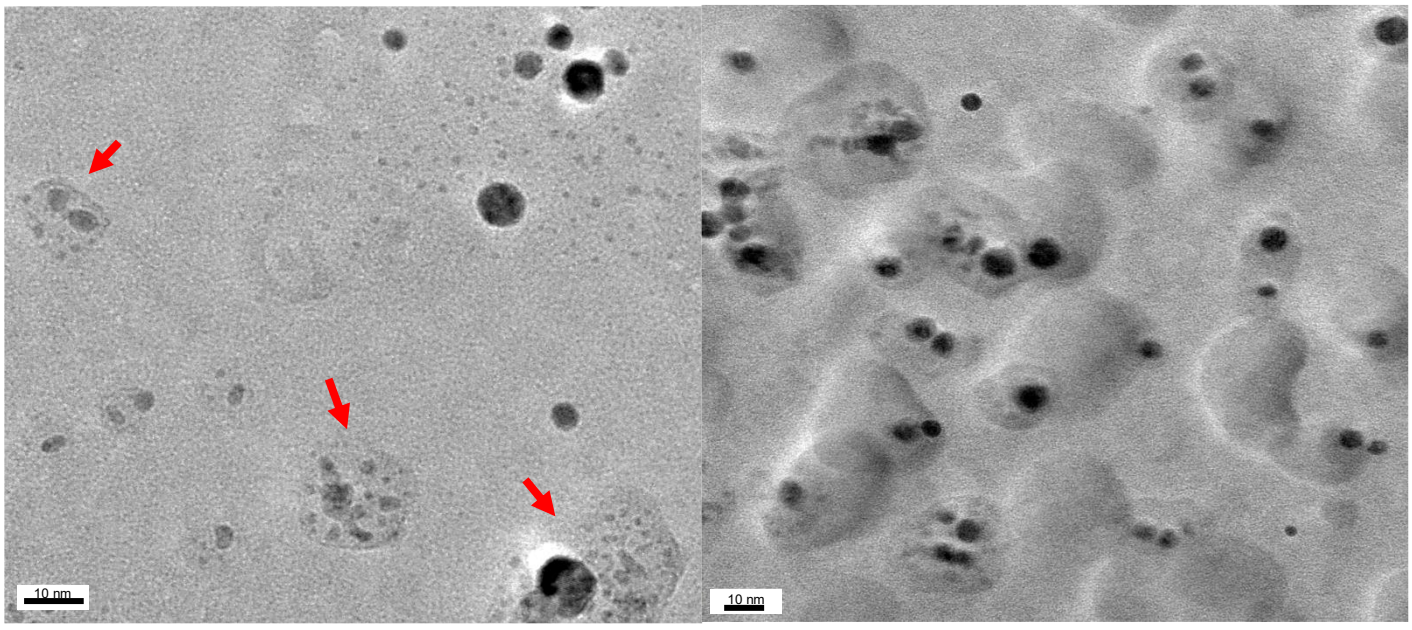

Fig. S17. HR-TEM images of AuPEI-FITC4 showing polymer accumulation (red arrows), right image taken in defocus to visualize polymer film.

Amount of NPs per cell

The most appropriate method of quantification to answer this question would be an inductively coupled plasma mass spectrometry (ICP-MS) measurement equipped with a single particle mode [1], to which we unfortunately do not access to in our institute.

Yet, for our small nanoparticles of about 3 nm Au-core diameter an ICP-MS measurement would still present a challenge, as the minimum measurable diameter for NPs has been given as 18 nm for most instruments [2].

On the other hand, a quantification through microscopy methods by counting NPs inside the cell would also be highly complex due to the small size of the AuPEI-FITC NPs (<5 nm). Nevertheless, we provide here an estimation based on a theoretical calculation and atomic absorption spectroscopy (AAS) for AuPEI-FITC1 NPs in all three GBM cell lines.

One million JHH520, 407 and GBM1 cells were incubated for 1 h with AuPEI-FITC1 NPs and then separated from the NP-containing dispersion through centrifugation. AAS measurements of these supernatants, as well as of the initial AuPEI-FITC1 NP dispersion added to the cells were performed to determine both gold concentrations. The amount of the AuPEI-FITC1 NPs which are taken up by the cells are subsequently calculated as the difference in gold amount between these two dispersions.

In order to give the gold uptake as amount of NPs per cell, the gold amount per NP was calculated as number of gold atoms per NP as follows:

From the average diameter (D) of AuPEI-FITC1 NPs determined by TEM, the total number of gold atoms (Au_T) in a single NP can be calculated according to the following equation [3]:

$$Au_T = \frac{N_A \cdot \rho \cdot V}{M_{Au}}, \text{ where } V = \frac{4}{3} \cdot \pi \cdot (\frac{D}{2})^3,$$

N_A = Avogadro constant, ρ = gold metal density, M_{Au} = gold atomic mass.

For 3 nm AuPEI-FITC1 NPs,

$$V = \frac{4}{3} \cdot \pi \cdot \left(\frac{3nm}{2}\right)^3 = 14\ nm^3 \text{ and}$$

$$Au_T = \frac{6.022 \cdot 10^{23} mol^{-1} \cdot 19.3\ {}^{g}/_{cm^3} \cdot 1.4 \cdot 10^{-20} cm^3}{196.9665\ {}^{g}/_{mol}} = 834\ Au\ atoms\ per\ NP.$$

which we rounded to 1000 Au atoms per NP for our estimation.

The AuPEI-FITC1 NP dispersion had an AAS confirmed concentration of 5.0 mg/L after 500 µL were diluted to 5 mL, corresponding to a gold mass (m_{Au}) of 25.1 µg in the sample volume of 5 mL.

An AuPEI-FITC1 NP dispersion volume of 5 mL with an Au concentration of 5.0 mg/L was used for the incubation of one million JHH520, 407 and GBM1 cells.

The supernatant from the incubation experiment then had gold concentration by AAS determined as given in entry 1 in Table S3. From the gold concentration the total mass amount of gold remaining was calculated in µg (entry 2).

The difference between the initial and remaining gold mass in the dispersion corresponds to the gold mass which is internalized and adsorbed in/on the cells (entry 3).

The gold mass is transformed into number of gold atoms (entry 4) according to (e.g. for GBM1 cells)

$$number_{Au} = \frac{m_{Au}}{M_{Au}} N_A = \frac{0.0000082g}{196.9665\,{}^{g}/_{mol}} 6.022 \cdot 10^{23} = 2.5 \cdot 10^{16}\ gold\ atoms.$$

Each Au-NP contains about 1000 NP. Hence $2.5 \cdot 10^{16}$ gold atoms correspond to about $2.5 \cdot 10^{13}$ Au-NPs which are internalized and adsorbed (entry 5).

With 10^6 cells used for the incubation, this leaves $2.5 \cdot 10^7$ Au-NPs which are internalized and adsorbed per cell (entry 6).

From the FACS experiments (see Table 1 in paper) the degree of internalization had been determined; e.g. to 61% for GBM1 cells (entry 7).

Thus, from the, e.g., $2.5 \cdot 10^7$ Au-NPs about $1.5 \cdot 10^7$ Au-NPs will be internalized.

Table S3. Estimate of the amount of NP uptake per cell.

Entry	Sample	AuPEI-FITC1 NPs added to the cells	AuPEI-FITC1 in GBM1	AuPEI-FITC1 in JHH520	AuPEI-FITC1 in 407
1	Gold conc. in dispersion (mg/L) (supernatant after cell incubation)	5.00	3.38	3.74	3.65
2	Gold mass in dispersions (µg) (supernatant after cell incubation)	25.1	16.9	18.7	18.3
3	Internalized+Adsorbed Gold mass (µg)	/	8.2	6.4	6.8
4	Number of Gold Atoms	/	$2.5 \cdot 10^{16}$	$2.0 \cdot 10^{16}$	$2.1 \cdot 10^{16}$
5	Number of Au-NPs	/	$2.5 \cdot 10^{13}$	$2.0 \cdot 10^{13}$	$2.1 \cdot 10^{13}$
6	Internalized+Adsorbed Au-NPs per cell	/	$2.5 \cdot 10^7$	$2.0 \cdot 10^7$	$2.1 \cdot 10^7$
7	Internalization degree from FACS (%)	/	61	51	47
8	**Internalized Au-NPs per cell from AAS**	/	**$1.5 \cdot 10^7$**	**$1.0 \cdot 10^7$**	**$1.0 \cdot 10^7$**
9	Fluorescence Intensity I_F at 520 nm (CPS/µA)	44780	3749	2448	2205
10	Internalized gold mass (µg)	4.50	0.38	0.25	0.22
11	Internalized number of Au-NPs (per 20 000 cells)		$1.2 \cdot 10^{12}$	$8.0 \cdot 10^{11}$	$7.2 \cdot 10^{11}$
12	**Internalized Au-NPs per cell from fluorescence spectrosc.**	/	**$6 \cdot 10^7$**	**$4 \cdot 10^7$**	**$3.6 \cdot 10^7$**

Along the same lines we double-checked the Au-NP uptake by fluorescence spectroscopy:

Here 20 000 JHH520, 407 and GBM1 cells were incubated for 1 h with AuPEI-FITC1 NPs (at a concentration of 0.9 mg/L after 100 µL were diluted to 5 mL, corresponding to a gold mass (m_{Au}) of 4.5 µg in the sample volume of 5 mL). Then the cells were removed by centrifugation, washed with PBS buffer and separated from the wash solution again through centrifugation. The

remaining cell pellets were re-dispersed in water and their fluorescence intensity was compared to that of the “free” AuPEI-FITC1 NPs in the original dispersion (Figure S18, Table S3 entry 9).

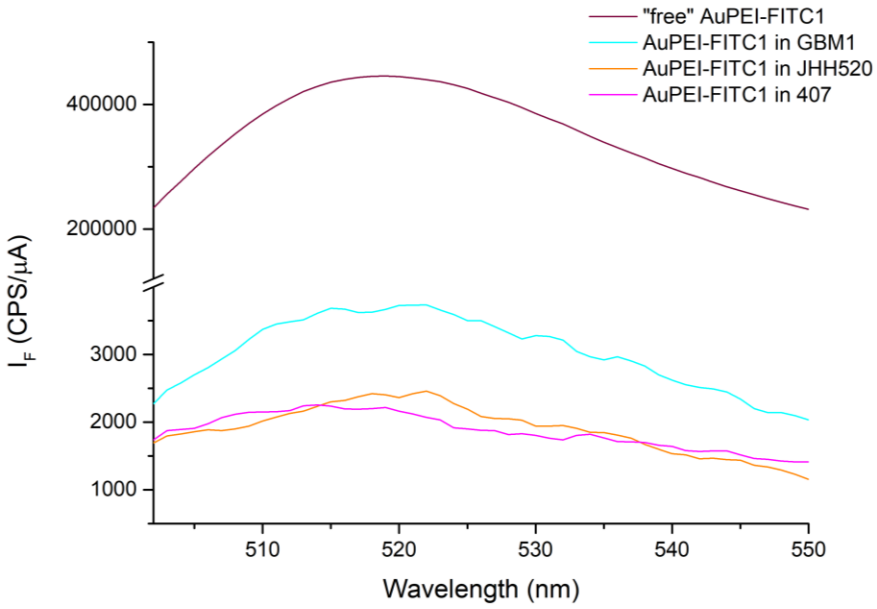

Fig. S18. Fluorescence intensity for the 0.9 mg/L AuPEI-FITC1 dispersion and the cell pellet dispersions after incubation, washing and separation by centrifugation.

The AuPEI-FITC1 dispersion concentration of 0.9 mg/L after 100 µL were diluted to 5 mL corresponds to a gold mass (m_{Au}) of 4.5 µg in our sample volume of 5 mL.

From the rule of proportion this gold mass is correlated to the gold mass in the cells through the fluorescence intensity (entry 10 in Table S3).

This gold mass is again transformed into number of gold atoms (see above) and further into number of Au-NPs (on the basis of 1000 Au-atoms/NP, see above), giving entry 11 in Table S3.

With 20 000 or $2 \cdot 10^4$ cells used for the incubation, division by 20 000 then gives the number of NPs which are internalized on average in each cell (entry 12).

The values from entry 8 (estimated internalized Au-NPs/cell from AAS) and entry 12 (estimated internalized Au-NPs/cell from fluorescence spectroscopy) match remarkably well within the same order of magnitude. Thus, we are confident that about 10^7 Au-NPs are internalized on average in each glioblastoma cell.

[1] J. Noireaux, R. Grall, M. Hullo, S. Chevillard, C. Oster, E. Brun, C. Sicard-Roselli, K. Loeschner, P. Fisicaro, Separations 6 (2019) 3. https://doi.org/10.3390/separations6010003
[2] S. Lee, X. Bi, R.B. Reed, J.F. Ranville, P. Herckes, P. Westerhoff, Environ. Sci. Technol. 48 (2014) 10291–10300. doi: 10.1021/es502422v
[3] L. Schmolke, S. Lerch, M. Bülow, M. Siebels, A. Schmitz, J. Thomas, G. Dehm, C. Held, T. Strassner, C. Janiak, Nanoscale 11 (2019) 4073-4082.

3.2. Augmented Therapeutic Potential of Glutaminase Inhibitor CB839 in Glioblastoma Stem Cells Using Gold Nanoparticle Delivery

Beatriz Giesen, Ann-Christin Nickel, Juri Barthel, Ulf Dietrich Kahlert, Christoph Janiak,

Pharmaceutics **2021**, 13, 295.

DOI: 10.3390/pharmaceutics13020295, reprinted under the Creative Commons Attribution License from reference 251, published by the Multidisciplinary Digital Publishing Institute (MDPI).

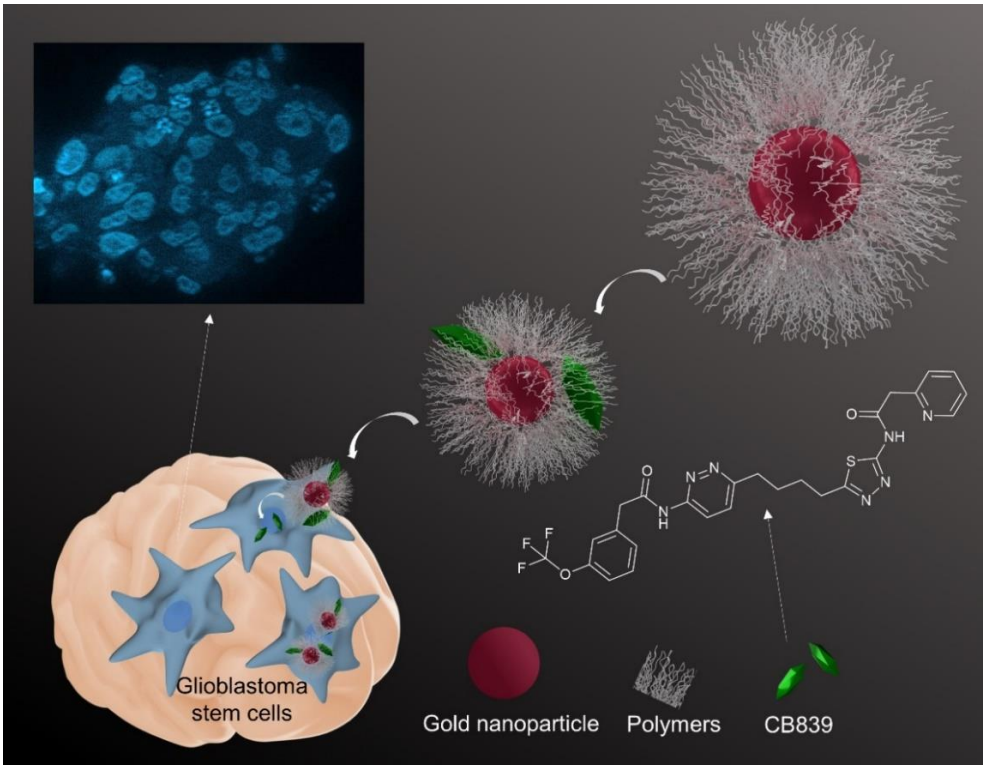

Figure 17. Graphical abstract from ref. 251. Au-polymer nanocarriers deliver the CB839 inhibitor for treatment of GSCs.

Summary:

Au NPs covered with citrate and four different biocompatible polymers were synthesized via one- or two-step routes as carriers for the promising drug candidate CB839. The size, morphology, elemental composition and physicochemical properties of the Au-polymer and Au-polymer-CB839 NPs were characterized using TEM, STEM, EDX, IR, UV-VIS, TGA and DLS analysis. Furthermore, qualitative investigations were performed with spectroscopic techniques to assure the presence of CB839 on the NP surface. The amount of CB839 loaded onto each nanocarrier was quantified by HPLC, developing and optimizing a method accordingly. The cytotoxicity effect of the Au-polymer-CB839 conjugates was investigated and compared to the results of pristine CB839 in GSCs. The therapeutic effect and penetration capabilities were assessed *in vitro* in 2D

and 3D models using two different assays, which do not require optical detection. By using the colony formation ability of the cells, false readouts in combination with the Au absorbance were avoided. Despite its chemical inertness and low water solubility, experiments showed a successful binding of CB839, especially to PVA-covered Au NPs, as well as an increased efficacy of Au-CB839 NPs compared to unmodified CB839.

Contributions to the work:

- Conceptualization and design of synthesis methods for Au-polymer NPs.
- Synthesis and optimization of AuCit, AuThioPEG, AuPVA, AuPEI and AuPVP NPs.
- Investigations regarding possible coupling methods of water insoluble drugs to Au NPs, optimization of Au-CB839 binding parameters. Experiments for enhancing the drug loading efficiency of CB839.
- Sample preparation and NP characterization.
- Acquirement and analysis of TEM, STEM images and EDX spectra.
- Further characterization via DLS, zeta potential, TGA, IR, UV-VIS and fluorescence spectroscopy studies.
- Incubation of GSCs with Au-CB839 NPs *in vitro* and completing colony forming assays with the help of Dr. Ann-Christin Nickel.
- Data curation, interpretation and validation of chemical and biological results.
- Compilation of all experimental results in form of a scientific article. Continuous corrections and improvements of the manuscript throughout the peer-review process. Execution of further required experiments and preparation of the revision document.
- Coordination of experiments done by external cooperation partners, as well as communication regarding the final manuscript.
- Cell cultures, maintenance of incubated cells and image acquirement using fluorescence microscopy were done by Dr. Ann-Christin Nickel.
- Support with TEM, STEM and EDX measurements and access to the facilities was provided by Dr. Juri Barthel from Forschungszentrum Jülich. Dr. Barthel also assisted with formal result analysis and manuscript review.
- Supervision and project administration were done by PD Dr. Ulf Kahlert and Prof. Dr. Christoph Janiak, as well as review and editing of the manuscript.
- Submission to the “Pharmaceutics” journal and final approval of the manuscript with Prof. Dr. Christoph Janiak.

pharmaceutics

MDPI

Article

Augmented Therapeutic Potential of Glutaminase Inhibitor CB839 in Glioblastoma Stem Cells Using Gold Nanoparticle Delivery

Beatriz Giesen [1], Ann-Christin Nickel [2], Juri Barthel [3], Ulf Dietrich Kahlert [2,4,*] and Christoph Janiak [1,*]

[1] Institut für Anorganische Chemie und Strukturchemie, Heinrich-Heine-Universität Düsseldorf, 40204 Düsseldorf, Germany; beatriz.giesen@uni-duesseldorf.de
[2] Klinik für Neurochirurgie, Medizinische Fakultät/Universitätsklinikum Düsseldorf, 40225 Düsseldorf, Germany; ann-christin.nickel@med.uni-duesseldorf.de
[3] Ernst Ruska-Centrum für Mikroskopie und Spektroskopie mit Elektronen (ER-C 2), Forschungszentrum Jülich GmbH, 52425 Jülich, Germany; ju.barthel@fz-juelich.de
[4] Deutsches Konsortium für Translationale Krebsforschung (DKTK), 40225 Essen/Düsseldorf, Germany
* Correspondence: ulf.kahlert@med.uni-duesseldorf.de (U.D.K.); janiak@uni-duesseldorf.de (C.J.)

Abstract: Gold nanoparticles (Au NPs) are studied as delivery systems to enhance the effect of the glutaminase1 inhibitor CB839, a promising drug candidate already in clinical trials for tumor treatments. Au NPs were synthesized using a bottom-up approach and covered with polymers able to bind CB839 as a Au-polymer-CB839 conjugate. The drug loading efficiency (DLE) was determined using high-performance liquid chromatography and characterization of the CB839-loaded NPs was done with various microscopic and spectroscopic methods. Despite the chemical inertness of CB839, Au NPs were efficient carriers with a DLE of up to 12%, depending on the polymer used. The therapeutic effect of CB839 with and without Au was assessed in vitro in 2D and 3D glioblastoma (GBM) cell models using different assays based on the colony formation ability of GBM stem cells (GSCs). To avoid readout disturbances from the Au metal, viability methods which do not require optical detection were hereby optimized. These showed that Au NP delivery increased the efficacy of CB839 in GSCs, compared to CB839 alone. Fluorescent microscopy proved successful NP penetration into the GSCs. With this first attempt to combine CB839 with Au nanotechnology, we hope to overcome delivery hurdles of this pharmacotherapy and increase bioavailability in target sites.

Keywords: glutaminase inhibition; gold nanoparticles; drug delivery; glioblastoma stem cells

Citation: Giesen, B.; Nickel, A.-C.; Barthel, J.; Kahlert, U.D.; Janiak, C. Augmented Therapeutic Potential of Glutaminase Inhibitor CB839 in Glioblastoma Stem Cells Using Gold Nanoparticle Delivery. *Pharmaceutics* **2021**, *13*, 295. https://doi.org/10.3390/pharmaceutics13020295

Academic Editor: Sabrina Pricl

Received: 25 January 2021
Accepted: 18 February 20121
Published: 23 February 2021

1. Introduction

The low survival rate of patients after diagnosis with glioblastoma (GBM), a highly aggressive brain cancer, is believed to rely on the invasive nature of the tumor, its innate recurrence and the high level of therapy resistance of the disease [1]. Moreover, the difficulty of therapeutics to sufficiently pass the blood–brain barrier (BBB) during treatment adds to the complexity of the management of patients with GBM [2,3]. A subpopulation of cells with enhanced stem characteristics (GBM stem-like cells, GSCs) have been the focus of new strategies to eradicate GBM, as they seem to be responsible for building therapy resistance due to their self-renewal properties and their ability to differentiate into a variety of cell types within the tumor [4–6].

In recent years, the increased glucose and glutamine uptake of tumors needed to maintain their metabolism has been exploited as a target in breast, prostate, glioma, lung, kidney, thyroid, and blood cancers [7–13]. Instead of converting glucose to pyruvate to produce adenosine triphosphate (ATP) like normal cells, cancer cells have been known to

utilize glutamine, an amino acid contained abundantly in plasma, as a nitrogen and carbon source to synthesize ATP and nucleotides [14]. During glutaminolysis, glutamine is hydrolyzed to glutamate and ammonia by the mitochondrial enzyme glutaminase1 (GLS1), a process needed to produce substrates for the citric acid cycle and subsequently supply the cells with vital proteins and other important metabolites [15]. Thus, by inhibiting the function of glutaminases, cell apoptosis and a slower tumor growth is expected and has already been observed in a variety of cases [16].

The compound *N*-[5-[4-[6-[[2-[3-(trifluoromethoxy)phenyl]-acetyl]amino]-3-pyridazinyl]butyl]-1,3,4-thiadiazol-2-yl]-2-pyridineacetamide (CB839) (Figure 1) shows great promise as a glutaminase inhibitor, with several clinical trials as cancer therapy underway [17,18]. Most recently, CB839—brand marked under the name Telaglenastat—is being investigated in a phase 2, randomized, multicenter, double-blind clinical study enrolling 120 lung cancer patients (NCT04265534). Treatment regime consists of orally administered CB839 as a supplement to food. Moreover, the tolerability of the drug in healthy adults dosing 800 mg (4 × 200 mg tablets) administered twice daily is currently being assessed in the phase 1 NCT04607512 trial.

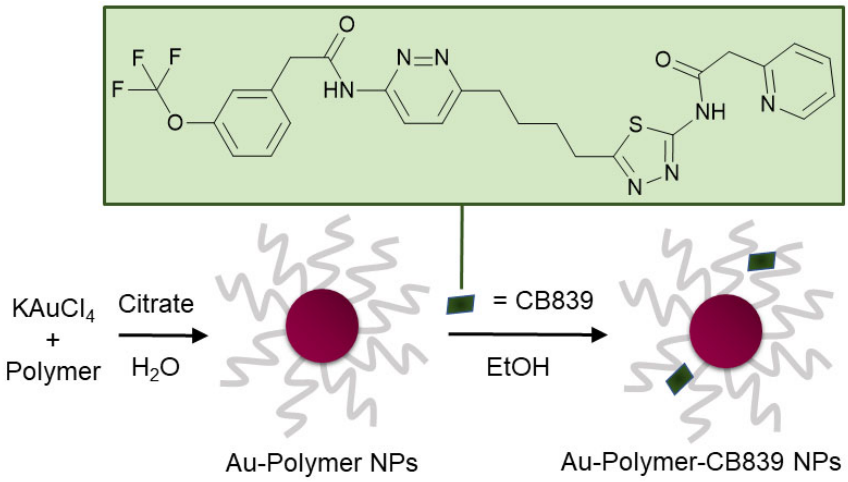

Figure 1. Schematic synthesis of polymer coated gold nanoparticles (Au NPs) carrying the CB839 inhibitor.

CB839 has good oral bioavailability and a potency independent from glutamine concentration about 13 times higher than its predecessor bis-2-(5-phenylacetamido-1,3,4-thia-diazol-2-yl)ethyl sulfide (BPTES) [19]. We and others have previously shown that pharmacological GLS inhibition (GLSi) is effective to combat GSCs [20,21] and GLSi candidate CB839 is the favorable strategy to do so, as it has superior target specificity [22]. In vivo therapy studies with this drug candidate, however, have shown that—in comparison to other tissues—the brain accumulation of CB839 is significantly hindered, most likely due to the challenge of passing the BBB [19]. Moreover, this in vivo trail enforces improving the general bioavailability of CB839 into the tumor sites, as oral treatment with the compound require severely high dosages to achieve therapy efficacy. Thus, new strategies to ensure more effective penetration of this promising drug candidate into tumor cells are urgently required.

The use of gold nanoparticles (Au NPs) as therapy carrier platform surges in recent biomedical applications due to their straight-forward synthesis and various, modifiable intrinsic functional properties [23]. Furthermore, nanoparticles present an enhanced permeation and retention (EPR) effect in tumors and can successfully transverse the cell membrane barrier of GSCs, as previously demonstrated [24,25]. In addition, Au NPs as

pharmacological carriers can be beneficial to overcome the obstacles of administrating poorly water-soluble compounds such as CB839, thereby reducing the required doses to be administered and possibly minimizing risks of side-effects in patients.

Unlike prior glutaminase inhibitors, new generation inhibitors such as BPTES or BPTES analogues like CB839 do not contain highly reactive functional groups in their structure [26]. While this is considered a biological advantage because the drug cannot form toxic intermediates with proteins, it complicates a possible binding to the surface of a NP. Because no covalent bonds can be easily formed between CB839 and NP capping ligands, the use of conventional drug-attachment methods such as *click*-reactions, 1-ethyl-3-(3-dimethylaminopropyl) carbodiimide hydrochloride/N-hydroxy succinimide (EDC/NHS) chemistry and cross-linkers (as seen for doxorubicin or anticancer taxanes such as paclitaxel or docetaxel) [27–29] is not possible without significant structure modification. Since such an alteration poses a high risk to influence the promising clinical effect known for this inhibitor, choosing a polymer as a surface ligand can provide the necessary matrix to load the CB839 molecules to the NPs. Through physical adsorption, polymers are capable of easily embedding drugs and macromolecules without the need for chemical modification, sometimes even achieving a higher loading than encapsulation techniques [30]. Moreover, polymers can increase the retention time of drugs, as well as their circulation in blood and are able to release them when the conjugate is exposed to endo- and exogeneous tumor stimuli [31].

In this work, a variety of biocompatible polymers were extensively examined regarding their ability to load CB839 onto the surface of the polymer-coated Au NPs (Figure S1, Supplementary Materials (SM)). After a fast preparation of Au-Polymer-CB839 NPs without the need of additional linkers (Figure 1), the efficacy of the CB839 inhibitor with and without the Au carriers was assessed in vitro using GBM neurospheres. These neurospheres are capable of reflecting the original tumor environment more closely due to their three-dimensional structure, compared to classical disease models using monolayer culturing technology [32]. For example, a hypoxic micro-environment could be formed in spheres from the outside to the inner core or the drug uptake can be slower for the inner cells than for the outlaying cells [33]. Since the low toxicity of the individual components of the conjugate (Au NPs, polymers and CB839 on non-tumor cells) is well known [22,34–36], we focused on the synthesis of novel Au-Polymer-CB839 NPs and the assessment of its therapeutic potential compared to the neat counterpart. Our results advocate Au NPs to effectively improve the therapeutic potential of anti-tumor metabolic therapies.

To our knowledge, CB839 has only been combined with purely polymeric NPs and liposomes to facilitate its administration [37,38] but this is the first time it is attached to Au NPs. Contrary to commonly used assays such as MTT, Cell-Titer-Glo® or Annexin A5, our focus lied further in the optimization of methods to assess the viability of the GSCs after treatment with Au-Polymer-CB839 NPs that do not rely on optical detection or addition of reagents. Au NPs may disturb assay readouts through their ability to absorb visible light, lumines, quench fluorescent signals or simply by interacting with assay components [39–41]. Thus, it is of high importance to have reliable and easy-to-apply methods to test the toxicity of drugs when using Au NPs.

2. Materials and Methods

2.1. Materials

Potassium tetrachloridoaurate (III), polyvinyl alcohol (PVA) Mowiol 4-88, M_w ~31,000 g/mol, poly(ethylene glycol) methyl ether thiol (ThioPEG), M_w ~800 g/mol, branched polyethylene imine (PEI) M_w ~25,000 g/mol, polyvinyl pyrrolidone (PVP), M_w ~3500 g/mol, fluorescein isothiocyanate (FITC), crystal violet, 4-nitro blue tetrazolium chloride, 4′,6-diamidino-2-phenyl-indol-dihydro-chloride (DAPI), Trypan Blue and Heparin (#H0878) were purchased from Sigma Aldrich, Darmstadt, Germany. Sodium citrate dihydrate was

from J.T. Baker Chemicals, Schwerte, Germany and dimethyl sulfoxide (DMSO, 99.7% purity) from Honeywell, Offenbach, Germany. Telaglenastat (CB839) was purchased from Adooq Bioscience, Irvine, CA, USA. Ethanol and methanol (Merck, Darmstadt, Germany) were of p.a. purity. Penicillin/Streptomycin (#P4333) was also from Merck, Darmstadt, Germany. Phosphate-buffered saline (PBS, Gibco #10010015), Dulbecco's Modified Eagle Medium without pyruvate (DMEM, Gibco #11965092), B27 supplement (Gibco #17504044), Ham's F12 Nutrient Mix (Gibco #11765047), Antibiotic-Antimycotic (Gibco #15240096), fetal bovine serum (FBS, Gibco #11965092), poly-D-lysine (Gibco #A3890401), agarose (Gibco #18300012) and slide mounting solution (eBioscience™ Fluoromount-G™, #00-4958-02) were from Thermo Fisher Scientific, Schwerte, Germany. Human epidermal growth factor (#AF-100-15) and human basic fibroblast growth factor (#AF-100-18B) were from Peprotech, Rocky Hill, NJ, USA and the tissue medium (#1620C) from KliniPath, Duiven, Netherlands. The Spectra/Por® dialysis membrane was purchased from Spectrum Laboratories, Schwerte, Germany. All materials were used without further purification. The Milli-Q® purification system was used to treat water for all reactions.

2.2. Methods

Transmission electron microscopy (TEM): 10 µL of each gold solution (in water for AuCit, AuThioPEG, AuPVP, AuPVA, and AuPEI; in ethanol for AuR-CB839 NPs) were dropped without dilution onto a 200 µm carbon-coated copper grid (from Electron Microscopy Sciences #CF200-CU, Munich, Germany), followed by drying in air. An FEI Tecnai G2 F20 electron microscope [42] operated at 200 kV accelerating voltage was used and TEM images were recorded with a Gatan UltraScan 1000P camera. Image calibration was done using Debye-Scherrer patterns recorded from a gold reference sample (S106, Plano GmbH, Wetzlar, Germany). To determine the NP size and size distribution, over 100 particles were counted using the Gatan Digital Micrograph software.

Scanning transmission electron microscopy (STEM) measurements were carried out using a high-angle annular dark-field (HAADF) detector combined with energy-dispersive X-ray (EDX) mapping. The sample preparation was the same as for TEM.

Fourier transform infrared (IR) spectra were recorded on a Bruker TENSOR 37 spectrometer in attenuated total reflection mode (Platinum ATR-QL, Diamond) between 550–4000 cm^{-1} after solvent removal from purified gold samples.

Ultraviolet–visible (UV-VIS) spectra were measured on a UV-2450 spectrometer (Shimadzu, Kyoto, Japan) using gold solutions and further analysis was done using the UVProbe software (Shimadzu).

Fluorescence spectroscopy: Gold solutions were diluted 1:10 in PBS, placed in quartz glass cuvettes and analyzed with an excitation of 490 nm on a FluoroMax-4 Spectrofluorometer from HORIBA Scientific, Irvine, CA, USA.

Thermogravimetric analysis (TGA) was carried out after solvent removal from purified gold samples on a Netzsch TG209 F3 Tarsus (Netzsch, Selb, Germany) under nitrogen atmosphere between 30 and 1000 °C at a heating rate of 5 K min^{-1}.

Dynamic light scattering (DLS): Hydrodynamic diameters were determined with a Malvern Nano S Zetasizer instrument with a HeNe laser at a wavelength of 633 nm by diluting the ethanolic AuPVA-CB839 sample 1:20 in H_2O or DMEM.

High-performance liquid chromatography (HPLC): Detection and quantification of CB839 in the supernatant samples was done using a Shimadzu LC 20AT prominence instrument with an SPD-M20A detector and a Luna C18(2) (250 × 4.60 mm, 5 micron) column from Phenomenex®. The sample loop volume was 20 µL and the absorbance was detected at a wavelength of 254 nm. The mobile phase consisted of 33% methanol and 67% H_2O with a flow rate of 1 mL/min. Before each measurement, the column was flushed with the MeOH/H_2O mixture for 30 min. The total run time per measurement was 13 min, whereas the CB839 peak could be found after approximately 9 min. Quantification of CB839 was done via peak integration after making a standard calibration curve.

2.3. Nanoparticle Synthesis

Citrate-coated gold nanoparticles (AuCit): 20 mg (53 μmol) of $KAuCl_4$ were dissolved in 200 mL of H_2O and the solution was heated to 100 °C while stirring at 250 rpm. After addition of 93 mg (319 μmol) of sodium citrate, the color changed to bright red. The AuCit NP suspension was washed with 200 mL of H_2O using centrifugation (22,000 rcf, 1 h, 4 °C) and resuspended in 200 mL of water before reaction with PEG and PVP or in ethanol before loading with CB839.

ThioPEG-coated gold nanoparticles (AuThioPEG) and PVP-coated gold nanoparticles (AuPVP): The aqueous AuCit NP solution (200 mL) was reacted with ThioPEG or PVP in excess (100 μmol) and stirred at room temperature for 24 h. After separation via centrifugation, the polymer-coated Au NPs AuThioPEG and AuPVP were resuspended in 200 mL of ethanol.

PVA-coated gold nanoparticles (AuPVA): 20 mg (53 μmol) of $KAuCl_4$ were added to a PVA solution (33 mg in 200 mL of H_2O) and heated to 90 °C. When the temperature was reached, 29 mg (100 μmol) of sodium citrate were added and the solution was continued to stir for 30 min until it turned dark red. After washing with 200 mL of water and centrifuging, the AuPVA NPs were resuspended in 200 mL of ethanol.

PEI-coated gold nanoparticles (AuPEI) were synthesized as described previously [25].

2.4. Loading of CB839 to Gold Nanoparticles (AuR-CB839, R: Cit, ThioPEG, PVP, PVA, PEI)

50 mL of the ethanolic solutions of AuCit, AuThioPEG, AuPVP, AuPVA and AuPEI NPs were combined with a 1 g/L CB839 stock in ethanol to obtain a final drug concentration of 0.05 g/L. The solutions were heated to 40 °C for 30 min and stirred for another 72 h at room temperature. After centrifugation for 1 h at 22,000 rcf and 4 °C, the supernatants were collected and used to quantify the unloaded amount of the drug which remained in solution via HPLC. Using the HPLC values, the mass of CB839 in the NPs was calculated by subtracting the CB839 amount used from the amount found in the supernatants. For each batch, the AuR-CB839 NPs pellets were resuspended with a specific volume of DMEM so that in each AuR-CB839 NP dispersion the concentration of CB839 was equivalent to 1μmol/L. Since each NP type loaded different amounts of CB839 (see Section 3.2.), the DMEM volume was adjusted depending on the sample. This procedure was repeated for each 50 mL NP batch synthesized, whereas HPLC results varied by about 1–6% between batches.

2.5. Synthesis of Fluorescent PVA Gold Nanoparticles (AuPVA-FITC)

FITC conjugated AuPVA nanoparticles were synthesized according to a two-step process based on our previously published reaction method [25]. In short, FITC was reacted with the pre-formed AuPVA NPs (synthesized as explained in Section 2.3). To increase the solubility of FITC, 50 mg (0.13 mmol) of the solid were dissolved in DMSO to form a FITC DMSO solution with a concentration of 4 g/L. This DMSO solution was then diluted to 0.05 g/L in water (FITC stock solution). Five milliliters of this stock solution were added to 50 mL of the aqueous AuPVA NP suspension, stirred at room temperature for 8 h and dialyzed through a 3.5 kDa Spectra/Por® membrane against PBS for 24 h. AuPVA-FITC NPs were washed with 50 mL of H_2O and redispersed in 50 mL of DMEM.

2.6. Cell Cultures

JHH520 cells were provided by G. Riggins (Baltimore, MD, USA), GBM1 by A. Vescovi (Milan, Italy) and BTSC407 by M.S. Carro (Freiburg, Germany). GBM neurospheres were cultured in DMEM without pyruvate, 2% B27 supplement, 30% Ham's F12 Nutrient Mix, 20 ng/mL human epidermal growth factor, 20 ng/mL human basic fibroblast growth factor, 5 μg/mL heparin and antibiotic-antimycotic solution. U87 cells, kindly provided by A. Weyerbrock (University Freiburg, Freiburg, Germany), were cultured adherently in DMEM medium supplemented with 10% FBS. All cells were

cultured in the presence of 1% Penicillin/Streptomycin. The absence of mycoplasma contamination was tested for all cells and their genetic identity was validated using short tandem repeat analysis as previously published [43]. Ethical approval for the use of the cell models to study brain cancer biology was from the ethical commission of the medical faculty of Heinrich-Heine University (study ID 5841R, initial approval 31March 2017, revised and renewed 16 September 2019). For all the functional assays we applied the following treatment conditions: Volume adjusted media treatment (control); 1 μmol/L CB839 or Au NP suspension containing 1 μmol/L CB839. CB839 was dissolved in ethanol and for a 3 mL well, 1.7 μL of this stock solution was added. We chose 1 μmol/L as our standard in vitro substance treatment condition as this concentration is generally considered sufficient to achieve a corresponding peak serum level in clinical testing [44]. Moreover, our group previously showed that this concentration of CB839 is a suitable parameter setting to conduct meaningful assays using the same preclinical models [22].

2.7. Colony Formation Assays

Poly-D-Lysine method: A solution of 0.1 g/L of poly-D-lysine was diluted with sterile PBS to a concentration of 50 μg/mL and used to coat six-well flat-bottom plates. After 1 h of incubation at room temperature, the solution was removed and the plates were washed 3-times with sterile H_2O and left to dry on a sterile bench for 2 h. Subsequently, 500 suspension cells (GSCs) were seeded successfully attaching completely within 24 h. After that, the culture medium was replaced with fresh medium containing CB839 or AuR-CB839 NPs in DMEM with a final drug concentration of 1 μmol/L per well. After a 72 h incubation period at 37 °C, the NP-medium was removed and new culture medium was added every 3 days for 3 weeks. Finally, the plates were washed with PBS and the colonies were fixed using ice-cold methanol. Prior to counting the colonies, these were stained with a 0.5 vol.% crystal violet solution in methanol, washed with water and air-dried. Due to the nature of intrinsic adherent growth of U87 cells, these plates were not coated with poly-D-lysine.

Agarose method [45]: Prior to embedding the cells into the soft-agar-medium dilution, the cells were incubated with CB839 or AuR-CB839 NPs in DMEM (1 μmol/L) for 72 h. Six-well flat-bottom plates were coated with 1.5 mL of neurosphere medium containing 1 vol.% of melted agarose at 70 °C for 1 h. 2 mL of the treated cell suspension (1000 cells/well) with 0.6 vol.% agarose were added and incubated for 1 h at room temperature before adding 2 mL medium on top. After this time, the medium on the top layer was replaced with 2 mL fresh medium every 3 days for 3 weeks. At last, the top layer was removed and the plates were incubated overnight at 37 °C with 1 mL of a 1 g/L 4-nitro blue tetrazolium chloride solution in PBS before counting the formed colonies.

All experiments with both methods were done in triplicates and the results were expressed as mean values accompanied by standard deviations.

2.8. Fluorescent Microscopy

After synthesis, AuPVA-FITC NPs were dialyzed, centrifuged and resuspended in 50 mL of DMEM (see Section 2.5). In Equation (4) (Section 3.2), we estimate the number of AuPVA NPs per batch to 5×10^{17}, thus giving a concentration of 5×10^{17} NPs/50 mL or 10^{19} NPs/L. From the Au-FITC-DMEM dispersion, 5 μL were added to a 1 mL-well containing 100,000 GBM cells. Subsequently, we estimate the concentration of AuPVA-FITC NPs to be 5×10^{13} NPs/mL (or the ratio 5×10^{8} NPs/cell), based on the amount of gold precursor used for each synthesis batch and assuming a 100% conversion (cf. Equation (4)). GBM cells were grown in spheroid culture (70–150 μm) and incubated with AuPVA-FITC NPs for 1 h. At the end of the incubation, the spheroids were washed three times with PBS and fixed with 70% methanol for 15 minutes. Then the fixed spheres were processed for frozen sections. Briefly, the spheres were embedded into frozen tissue medium and frozen/stored at −20 °C until they were processed for sectioning. The specimens were cut into 5–7 μm sections using a CM1900 Cryostat (Leica, Nussloch,

Germany). For the staining process, the sections were rinsed 3-times with PBS and incubated with a DAPI solution (0.1 μg/mL in PBS) for 2 min. After rinsing the slides with PBS, the specimens were either directly mounted in slide mounting solution and covered with a coverslip or were further treated with Trypan Blue to quench extracellular fluorescence. A 0.1 vol.% Trypan Blue solution was added to the section, followed by direct mounting and covering the sample. The slides were analyzed using a Zeiss Axiovision Apotome.2 confocal microscope (Zeiss, Oberkochen, Germany) and the software ZEN Blue (2.3, SP1, black, 64 bit, release version 14.0.0.0 also from Zeiss).

3. Results and Discussion

3.1. Synthesis and Characterization of Au NPs

In order to bind CB839 to a nanocarrier, several polymeric capping ligands with different reactive groups were deposited on the surface of Au NPs as anchors. The synthesis of these gold "nanovehicles" consisted mainly of a reduction of an equal amount of gold(III) salt $KAuCl_4$, using sodium citrate as a reducing agent. Starting from citrate coated gold (AuCit) NPs, made with a modification of the *Turkevich* method [46], spherical monodisperse particles were synthesized (vide infra), which were later used in a ligand exchange reaction to obtain polymer coated NPs, e.g., with poly(ethylene glycol) methyl ether thiol (AuThioPEG NPs) and with polyvinyl pyrrolidone (AuPVP NPs), respectively. Polyvinyl alcohol-coated gold (AuPVA) NPs were synthesized in a straight-forward *one-pot* reaction. The polymers ThioPEG, PVA, PVP, and PEI were chosen due to their known biocompatibility and their affinity for gold, as well as to provide a variety of different functional groups, which might successfully load CB839 onto the nanocarriers. Additionally, AuCit NPs were also included to see if Au presents any interaction with CB839 before any ligand exchange reaction with polymers.

TEM investigations of these samples show an overall spherical morphology of the Au NPs with almost no degree of agglomeration (Figure 2) and NP sizes between 8 and 15 nm (Figure S2, Supplementary Materials (SM)). While citrate NPs had a size of 15 ± 2 nm (Figure 2a), a subsequent citrate-to-polymer exchange with ThioPEG resulted in NPs with an unchanged size of 15 ± 2 nm (Figure 2b) and with PVP gave NPs with 11 ± 2 nm average size (Figure 2c). By using the same amounts of gold precursor in the presence of PVA, spherical AuPVA NPs with a size of 8 ± 2 nm (Figure 2d) and with PEI smaller-sized 4 nm AuPEI NPs [25] were synthesized and evaluated as potential drug delivery systems.

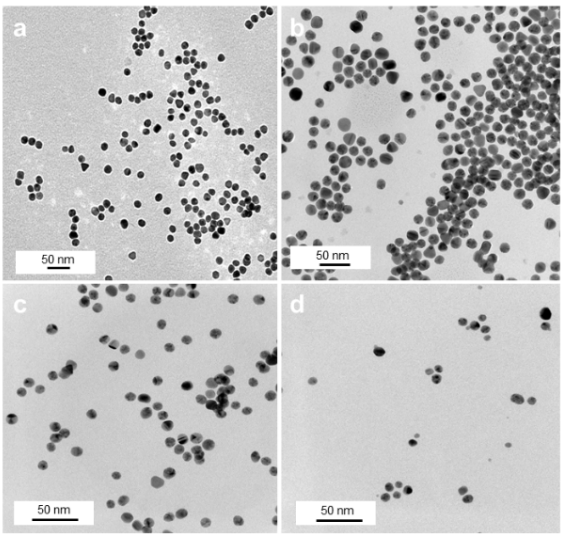

Figure 2. TEM images of AuCit (**a**), AuThioPEG (**b**), AuPVP (**c**), and AuPVA (**d**) NPs, captured at 50,000× (**a**), 100,000× (**b**), and 150,000× (**c**,**d**) magnification.

After reacting the various Au-Polymer NPs with CB839, no apparent size increase was observed for any of the NP types except for AuPEI (Figure S3, SM). There was however a slight reorganization between the Au cores, especially in the case of AuPVA and AuPVP NPs (Figure S3c,d, SM), most likely due to an alteration in surface chemistry and charge after interaction of the polymers with CB839.

3.2. Quantification of CB839 Loading

Subsequently, the amount of CB839 attached to the NPs was examined by collecting supernatants of all samples after centrifugation and quantifying the not adsorbed, remaining drug concentration via HPLC analysis. For this purpose, a method capable of efficiently separating CB839 in all NP samples was developed and optimized. By using a mixture of methanol and water as mobile phase, CB839 could be identified after a retention time of only 9 min and its concentration could be calculated with a standard calibration curve (Figure S4, SM). The drug loading efficiency (DLE) of AuCit, AuThioPEG, AuPVA, AuPVP and AuPEI NPs was calculated according to Equation (1) and results are displayed in Table 1.

$$\begin{aligned} &Drug\ Loading\ Efficiency\ (\%) \\ &= \frac{Total\ amount\ of\ CB839\ used - remaining\ CB839\ amount\ in\ supernatant}{Total\ amount\ of\ CB839\ used} \times 100\% \\ &= \frac{Amount\ of\ loaded\ CB839}{Total\ amount\ of\ CB839\ used} \times 100\% \end{aligned} \quad (1)$$

From all five ligands used to cover the gold NPs (Figure S1, SM), PVA seems to be the most effective in loading up to 12% CB839 on the surface of NPs. This finding can probably be explained by the strong interaction of the amide group in CB839 with the numerous hydroxyl groups in the PVA chains, which has been previously exploited to bind or stabilize hormones, proteins and other pharmaceuticals [47,48]. Here, the hypothesis is that the OH groups of PVA can act both as hydrogen bond acceptors from the amide-NH groups of CB839 and donors to the aromatic nitrogen atoms and to the amide C=O groups of CB839, which leads to stronger supramolecular interactions with CB839, compared to the other polymers. Similarly, the different properties between NP types such as core size, polymeric shell and surface charge can affect the loading efficiency of each Au NP. The small size and positive charge of AuPEI NPs [25] seem to be counterproductive to load CB839. Larger 15 nm AuCit NPs show the second highest DLE after AuPVA NPs, due to possible electrostatic interactions with CB839. Aside from NP size and surface charge, the chemical nature of the polymer shell used for Au NPs can also play an important role on the DLE. Citrate and PVA feature strong hydrogen bond donor and acceptor OH groups. The NH and NH_2 groups in PEI are already weaker H bond donors and acceptors, with the latter getting lost upon protonation. Also, upon protonation, the H bond donor function of the NH_2^+ and NH_3^+ groups will then be engaged by the counter anion. PVP is no H donor but only a week acceptor, while ThioPEG has no H bonding capabilities. Even though in theory a stronger CB839 binding capability was expected from PVP due its hydrogen bond accepting C=O groups, AuThioPEG showed a higher DLE (Table 1). A reason for this counterintuitive behavior might have to do with the polymer chain arrangement around the Au NPs. ThioPEG with M_w ~800 g/mol has shorter chain lengths than polyvinyl pyrrolidone (PVP) with M_w ~3500 g/mol. Shorter polymer chains cannot form a dense polymer layer as longer ones can. Thus, shorter polymer chains will be more amenable to embed guest molecules.

Table 1. Drug loading efficiency of Au NPs. [a]

Au NPs	Drug Loading Efficiency (%)
AuCit	8
AuThioPEG	4
AuPVA	12
AuPVP	0
AuPEI	1

[a] From HPLC determination in supernatant solution according to Equation (1).

Even though DLE results give an overall impression of the loading success among samples, they are dependent of the concentration of CB839 used and thus only describe the efficiency of each specific reaction. For better interpretation of the experiments and the later application of the CB839-NPs, calculating the amount of CB839 molecules that are loaded per NP might be more relevant. This was done taking AuPVA-CB839 NPs as an example.

Based on the spherical shape and the radius of Au NPs (e.g., $r = 4$ nm) determined by TEM measurements, the volume of a single NP can be calculated by Equation (2):

$$V_{NP} = \frac{4}{3} \cdot \pi \cdot r^3 = 268\, nm^3 \quad (2)$$

and its mass with Equation (3) (density of Au, $\rho_{Au} = 19.32$ g/cm^3):

$$m_{NP} = \rho \cdot V = 5.18 \cdot 10^{-18}\, g. \quad (3)$$

Since 5 mg $KAuCl_4$ were used in the reaction, the mass of Au in the salt ($m_{Au} = 2.6$ mg), assuming a 100% conversion from $KAuCl_4$ to Au NPs, can be used to determine the total number of Au NPs (N_{NPs}) in the sample:

$$N_{NPs} = \frac{m_{Au}}{m_{NP}} = 5 \cdot 10^{17}. \quad (4)$$

From the molar amount of CB839 applied in the synthesis of AuPVA-CB839 NPs, the number of CB839 molecules can be calculated as:

$$N_{CB839} = n_{CB839} \cdot N_A = 2.6 \cdot 10^{18} \quad (5)$$

$n_{CB839} = 4.4 \cdot 10^{-6}$ mol, $N_A = 6.022 \cdot 10^{23}$ mol^{-1} (Avogadro constant).

Since the AuPVA NPs loaded 12% of the added CB839, according to the DLE results, the number of CB839 molecules loaded onto the NPs ($N_{CB839loaded}$) is:

$$N_{CB839loaded} = N_{CB839} \cdot 0.12 = 3.2 \cdot 10^{17}\ molecules. \quad (6)$$

Finally, the number CB839 molecules loaded per NP ("Loading yield") can be calculated using Equation (7):

$$\text{Loading yield} = \frac{N_{CB839loaded}}{N_{NP}} = 0.6. \quad (7)$$

Thus, we conclude that approximately 60% of AuPVA NPs carry one drug molecule. Since this estimation was made based on the ideal 100% NP formation from the gold precursor, this value represents the lowest possible loading of CB839 onto AuPVA NPs and might be higher in reality.

To further evaluate this result, the size of the CB839 molecule was compared to the size of a NP. With help of a crystal structure published by Huang et al. [49], we estimated the length of the CB839 molecule in its folded conformations to be approximately 2 × 0.8 nm, and in its linear form 2.9 × 0.75 nm, taking the van der Waals radii into account (Figures 3 and S5, SM). Therefore, since the size of CB839 is in the same order of magnitude as the size of a NP, it would be difficult to achieve a much higher CB839 loading with NPs of this small size. Even though we believe 60% to be a good result, improvement of the loaded amount might be possible by adjusting reaction parameters

or using larger NP sizes. While these DLE values are the result of experiments using a single CB839 molar amount of n_{CB839}= 4.4 × 10^{-6} mol, we will continue trying to improve the DLE of AuPVA NPs in the future by testing additional CB839 concentrations in the reaction.

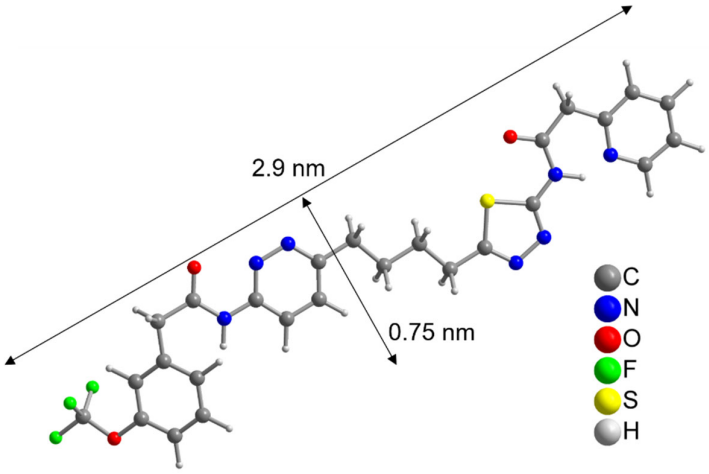

Figure 3. Linearized structure of the CB839 molecule. For the folded conformations in the glutaminase C complex, see Figure S5, SM.

3.3. Physicochemical Characterization of AuPVA-CB839 NPs

Prior to its application in cells, the physicochemical properties AuPVA-CB838 NPs, the NP type with highest CB839 loading, were investigated in-depth. Besides quantifying the amount of CB839 bound to the NPs, the immobilization of the drug on the surface of the AuPVA NPs was confirmed through various spectroscopic methods. IR spectroscopy of the dried NP-drug conjugate showed characteristic C-F stretching (1142 cm^{-1}) and bending (735 cm^{-1}) vibrations of the CF_3 group of CB839, as well as the N-H band of its amide group (1534 cm^{-1}) and the aromatic C-H bending (703 cm^{-1}) vibration (Figure S6, SM).

Moreover, UV-VIS spectroscopy of the AuPVA-CB839 NPs showed an additional absorbance maximum at 240 nm corresponding to CB839 compared to the AuPVA NPs, which only showed the characteristic plasmonic band at 550 nm (Figure 4). These spectra also show no visible size increase or agglomeration of the AuPVA NPs after reaction with CB839, since the 550 nm absorbance signal of AuPVA-CB839 NPs did not shift to larger wavelengths.

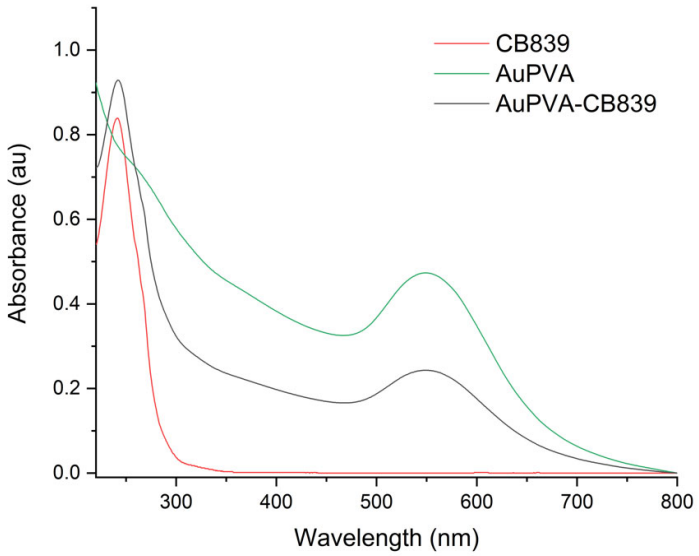

Figure 4. UV-VIS spectra of CB839 (red), AuPVA (green), and AuPVA-CB839 NPs (black).

Using energy-dispersive X-ray spectroscopy (EDX), elemental maps of AuPVA-CB839 NPs were collected on a scanning transmission electron microscope (STEM). The elements gold, corresponding to the AuPVA NPs and fluorine from CB839 are displayed in maps in Figure 5. Here, fluorine appears to be in the same area as gold and to form similar circular patterns correlated with the Au map. Since electrons scatter strongly from Au, the contrast in the fluorine (F-K) X-ray map is likely caused by an increase in the Bremsstrahlung background. In order to confirm the presence of F in the vicinity of Au NPs and to observe the influence of background radiation, X-ray spectra taken on Au NPs were compared against such taken from surrounding areas (Figure S7, SM).

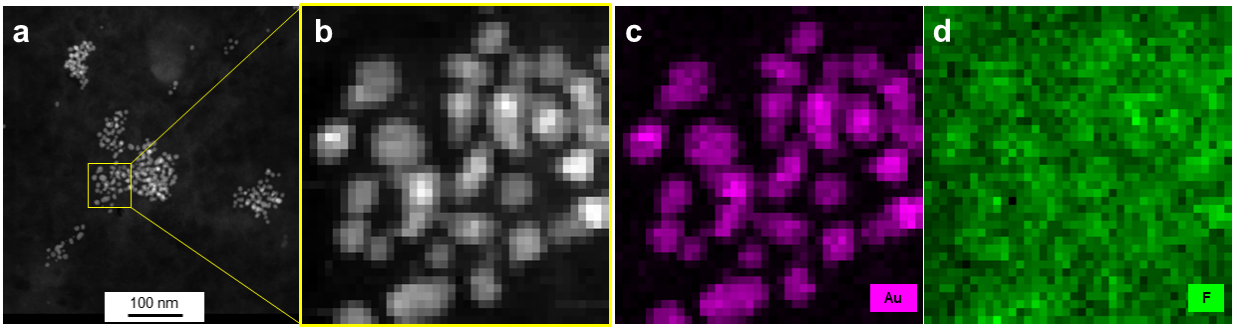

Figure 5. HAADF-STEM images (**a**,**b**) and EDX elemental mapping (**c**,**d**) of AuPVA-CB839 NPs. Gold, corresponding to the NPs is shown in pink and fluorine contained in CB839 in green.

From the Au-Mα_1 elemental map (Figure S7a, SM), the inner areas and the edges of NPs were carefully selected (Figure S7b, SM) and three EDX spectra from these scan point subsets were created by averaging all points of a subset (Figure S7c, SM). Since the Au-Mα_1 signal at 2123 eV (red dot, Figure S7c, SM) is strongest on the particles, weaker at edges and absent next to the particles, we believe the threshold values for the assignment to edge and particle interior were chosen correctly. There is no denying that stronger Bremsstrahlung occurs when the electron beam passes through the strongly scattering Au particles, as can be seen in the pure background regions of the spectra, e.g., at 1200–1500 eV. However, all spectra show a slight elevation of the EDX signal at 677 eV (F-K peak, black dot, Figure S7c, SM), independent of location. As AuPVA NPs are surrounded

by a large-sized surface polymer able to bind CB839 molecules, a F-K emission around the NPs (black scan area on Figure S7b, SM) can also be expected. Thus, we conclude that even though the discovery of a low amount of F atoms on Au NPs present upon loading CB839 is difficult due to the detection limits of the equipment, CB839 is found near the Au NPs.

Thermogravimetric analysis (TGA, Figure S8, SM) showed that the AuPVA-CB839 conjugates are stable to about 200 °C.

The colloidal properties of AuPVA-CB839 NPs were also investigated using DLS measurements (Figure S9, SM). In water, the hydrodynamic diameter of AuPVA-CB839 NPs was approximately 20 nm, while in culture media (DMEM) their size increased to 80 nm. This larger NP size in DMEM is to be expected, due to the formation of a protein corona around the surface of NPs as they interact with several proteins contained in cell culture media [50].

3.4. In Vitro Effect of AuPVA-CB839 NPs in GSCs

Following these investigations, the first in vitro tests in classical cell models of adherently grown U87 cells were conducted with AuPVA, AuCit, and AuThioPEG NPs (Figure S10, SM). We followed in our analysis the previously recommended use of quantifying cell colony formation efficiency (CFE) to functionally assess the cytotoxicity of nanomaterials [41].

Because the ability of Au NPs to absorb visible light can lead to false positive results when using a photometer to determine cell viability (Figure S11, SM), a quantification with the CFE method is most suitable for our study. This assay avoids any interference of metals, in our case Au, with other test components or optical detection methods thus minimizing signal disturbance and false recordings. The biological assessment was performed in a robust in vitro platform of $n = 4$ different glioma models featuring $n = 3$ glioma stem cell systems. For each model, we quantified the ability to form monolayer and spheroidic colonies in the presence of different treatment conditions.

Given that JHH520, GBM1, and BTSC407 GSCs are not adherent, the CFE assay was modified using poly-D-lysine, a polycationic amino acid polymer, which is able to interact with anionic parts of neural cells, thus effectively attaching them to a surface. As Figure S12, SM shows, this attachment endured the NP and staining treatments of GBM cells and allowed for data interpretation by counting the colonies formed due to the ability of GSCs of making colonies from single cells [22]. The less colony formation, the more effective the drug treatment. Our tests reveal that treating the cells with AuPVA-CB839 NPs containing 1 μmol/L CB839 impaired tumor cell growth, as benchmarked to treatment with 1 μmol/L CB839 only (Figure 6). The differences in the amount of reduction on CFE between the 2D (poly-D-lysine) vs. 3D (agarose) assay could be explained by the different susceptibly of the cells when grown in different conditions, whereby 3D more closely recapitulated the actual tumor physiology [32]. In addition, the variations in experimental handling sequence could result in different error introduction into the assays (pretreatment of cells for setting the Agarose assay, washing steps in 2D poly-D-lysine assay). Importantly however, the general trend of augmented therapeutic potential of our nano-delivered CB839 as compared to the unmodified substance is shown in all tested cell models with both assays, thereby supporting our technology for the development of an anti-metabolic therapy potentially able to eradicate tumors with stem cell properties.

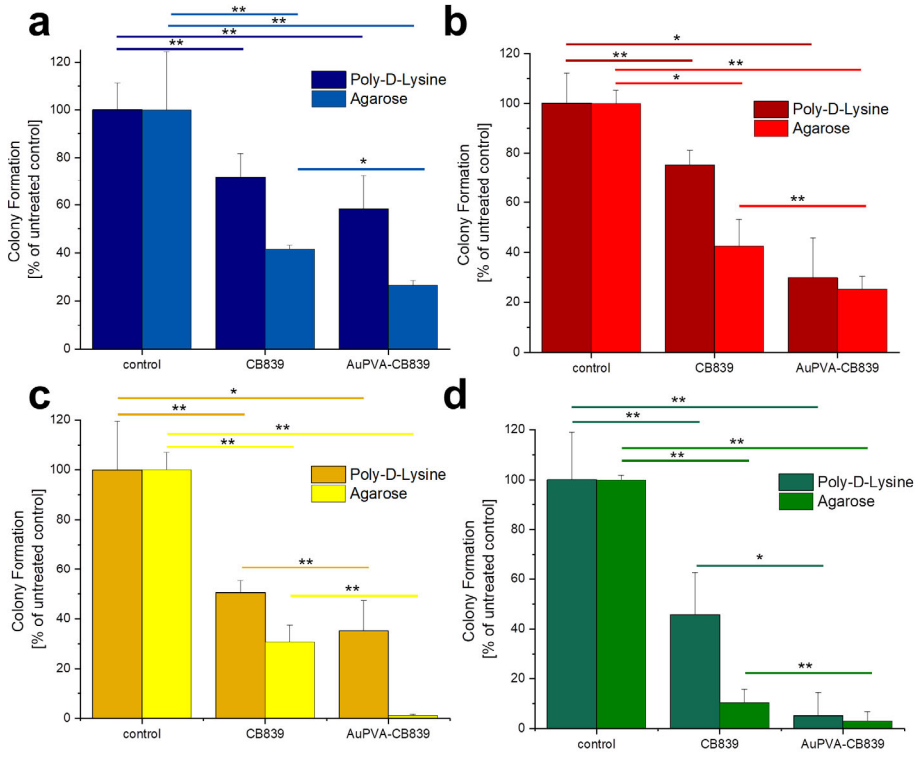

Figure 6. Colony Formation of U87 (**a**), JHH520 (**b**), GBM1 (**c**), and BTSC407 (**d**) cells after incubation with AuPVA-CB839 NPs, using both the 2D poly-D-lysine and the 3D agarose method. Dark columns in (**a**) are labelled as poly-D-lysine for comparison, even though no adhesion polymer was used since cell model U87 grows adherent already. A two-sample t-test was performed using Origin 8 software and significances are indicated: * $p > 0.05$, ** $p > 0.03$.

The percentage of colony formation in U87 cells with CB839 alone and with AuPVA-CB839 NPs differed only slightly when comparing both incubation methods (Figure 6a). JHH520 cells (Figure 6b) presented a similar reaction than GBM1 cells (Figure 6c), as they are both glutaminase-high expressing lines [22]. Interestingly, the in vitro clonogenicity of BTSC407 cells (Figure 6d) after treatment with AuPVA-CB839 NPs in agarose was only about 1%, compared to 30% with a CB839 treatment without NPs (relative to the control set at 100%), which speaks for the NP potential to enhance the drug effect, even in cell lines thought to be resistant due to lower GLS1 activation levels [22]. Based on our previously conducted functional assays with CB839 and other pharmacological GLS inhibitor C-968, using the same cell models as in this study, we believe that the total GLS1 protein abundancy predicts for the sensitivity of GBM cells to anti-GLS1 directed drugs. The fact that U87 and BTSC407 cells have comparably low GLS1 expression as opposed to GBM1 and JHH520 not only shows that our applied disease modeling technology can recapitulate the variation of target activity found in patients [21,22], but also reflects the molecular heterogeneous nature of this disease. Thus, this inter- and intratumoral cell metabolic heterogeneity may limit the durable effects of such monotherapies and the differences in saturation of GLS1 blockage could be a reason for the observed differences. Moreover, compared to serum-free spheroid models, the serum-containing in vitro growth conditions of the U87 cell line, known to dampen the effects of pharmaco interventions [51], can also be a reason for higher GLSi resistance. Acknowledging that this is rather a technical limitation than a translational relevant reason for possible source of therapy resistance, we added three spheroid, serum-free models (JHH520, BTSC407, and GBM1), in our project.

To our best knowledge, this is the first report of functionalizing the most promising GLSi compound CB839 to inorganic nanocarriers and performing bio validation. Our technology accompanies a previous report on BPTES-loaded poly(lactic)-glycolic acid NPs [52] and confirms the observation that application of nanotechnology is a powerful strategy to improve the therapeutic capacity of this drug class.

While the effect of CB839-loaded Au NPs on colony formation is shown, tests regarding quantification of the amount of inhibitor delivered into cells for each case are underway. Similarly, enzyme activity inhibition studies like those made in GSCs for CB839 [22] are pending for Au-CB839 NPs to gain additional knowledge about how they affect the target, as well as their intracellular delivery and release. Even though we recently benchmarked the phenotypic effects of CB839 against the absence of effects when applying DMSO in the same cell models as in the current study [22], we acknowledge that the repetition of these control experiments using ethanol solvent would be beneficial to further support some conclusions of this work. In the future, we will also include our CB839-loaded Au NPs in further screening assays in order to characterize their effect and toxicity more comprehensively in a high-throughput manner [53].

While the blood–brain barrier permeability of CB839 is challenging, as described in several in vitro studies [19,54], its specificity to inhibit GLS1 and the connection between response and IDH1 DNA mutation status of cancer patients [9] makes it a promising candidate for precision cancer therapy. Although an increased diffusion through the barrier is expected when attaching the small molecule to Au NPs [55–57], CB839 could also be part of an intraventrical, intrathecal, or localized intracranial chemotherapy. For intracranial chemotherapy, the BBB problematic could even be avoided because the drug is directly applied to the tumor cavity during tumor resection [58,59]. As has been well described in the literature for the study of GBM in vivo [60–63], we suggest a xenograft approach of human tumor stem cell models in rodent carriers, ideally in immune-tolerant models [64], to investigate the immune relevance of the applied intervention using nanocarried-CB839 in the future. Such an immunocompetent mouse model for human GBM cells—which has also been recently used for testing additional disease types [65]—would also help to study the effects of Au-CB839 NPs on the immune microenvironment of the tumor. Given the emergence of immune therapies as effective cancer treatments, the inclusion of such assays in future drug development projects are desirable to increase translational relevance.

3.5. Cell Internalization

To visualize the GSCs penetration potential by the Au-Polymer CB839 conjugate, fluorescent labelling of our NPs and our tumor models was used to investigate the NP internalization in GBM cells (Figure 7). For this purpose, AuPVA NPs were functionalized with FITC, resulting in AuPVA-FITC NPs. These fluorescent AuPVA NPs are used as a proof-of-concept to demonstrate that the PVA coated Au NPs are able to penetrate GSCs. We have only fluorescent-stained the AuPVA NPs with FITC because these NPs had the highest DLE. From our previous work [25], we realized the importance of the surface ligand on the degree of NP internalization and had discovered differences when testing the same NPs in different GBM cell lines. Thus, we wanted to make sure that AuPVA NPs were able to penetrate GSCs if they are later to be loaded with CB839.

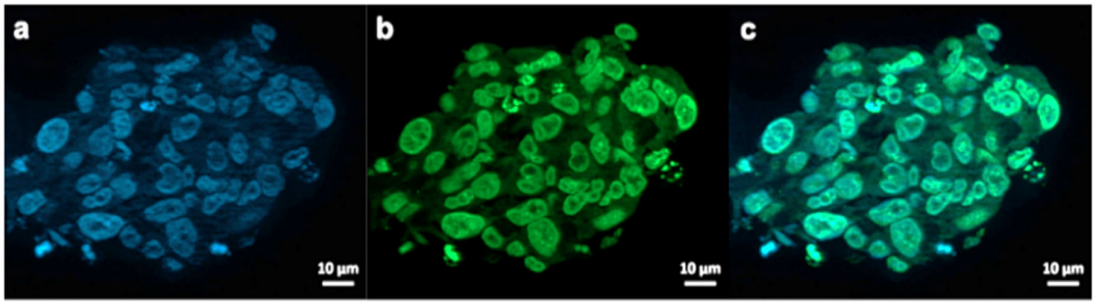

Figure 7. Exemplary fluorescence microscopy images of JHH520 cells after incubation with AuPVA-FITC NPs. Image (**a**) shows DAPI signals of cell DNA, image (**b**) FITC signals corresponding to AuPVA-FITC NPs and (**c**) a combined DAPI and FITC image.

The successful attachment of FITC to the Au NPs relies on the presence of a sulfur atom in the isothiocyanate group of the fluorophore. Given the strong affinity of gold for sulfur, FITC is able to coordinatively bind to Au NPs though relatively stable bonds [66,67]. Free FITC with its isothiocyanato, -NCS group is able to form Au-S bonds on the gold metal surface, requiring only minimal reaction time [68,69]. This attachment was confirmed by fluorescence spectroscopy (Figure S13, SM), which showed a quenched but still present fluorescence signal of AuPVA-FITC compared to FITC due to the interaction of the fluorophore with Au [70]. Moreover, the stretching band of the C=O group of the lactone in FITC was visible at 1728 cm^{-1} in IR spectra taken from AuPVA-FITC NPs (Figure S14, SM), as well as stretching vibrations from the benzene ring at 1601 and 1435 cm^{-1}. The FITC loading efficiency of AuPVA-FITC NPs (see Equation (S1) in the SM) was calculated using UV-VIS spectroscopy (Figure S15, SM). By comparing the absorbance intensity of the supernatant recovered after NP centrifugation (unloaded FITC) and the absorbance of total FITC used for the reaction, the loading was estimated to be approximately 23%. According to zeta potential measurements, AuPVA-FITC NPs remain stable in water for at least one hour at room temperature (Figure S16, SM). After this time, the surface charge of the NPs (−16 mV at 0 min) continues to decrease until reaching a zeta value of −27 mV, similar to the value of AuPVA NPs without FITC. Therefore, only freshly-prepared AuPVA-FITC NPs were used for further experiments in order to guarantee that a sufficient amount of FITC was still present on the NPs.

AuPVA-FITC NPs were added to the cells and sphere sections were studied under a fluorescence microscope. After staining cell DNA (Figure 7a), a green FITC signal (Figure 7b) corresponding to the NPs were visible in the same area (Figure 7c). Thus, we conclude that PVA is a suitable capping ligand for Au NPs, as it also allows their internalization, which is visualized after quenching extracellular fluorescence using Trypan Blue (Figure S17, SM).

Even though it has been demonstrated that Au NPs can be internalized through various endocytosis-based pathways or by direct cytoplasmic uptake [71], additional experiments are needed to determine the internalization mechanism of Au-CB839 NPs.

4. Conclusions

The synthesis of five Au NP types (four with polymer ligands and one with citrate) resulted in particles of 8–15 nm in size with different polymeric capping ligands. Despite the lack of functional groups with high chemical reactivity and a significant steric hindrance from its large size, the CB839 molecule could be immobilized on the surface of Au NPs through physical adsorption and electrostatic interactions with the polymers. AuPVA NPs were able to immobilize the highest amount of CB839, displaying a DLE of 12%. Calculations estimated that at least 60% of all AuPVA NPs carry one CB839 molecule. Even though characterization and quantification of CB838 loading using chromatographic and spectroscopic methods is challenging, AuPVA-CB839 NPs demonstrated improved

biological results. In vitro experiments in GSCs showed an enhanced effect of CB839 when delivered by Au NPs as compared to the neat drug solution. As expected due to the cellular and molecular heterogeneity of GBM, the therapy effect varied depending on the cell lines used. Our study presents and compares two suitable bioassays to test the effect of CB839-loaded Au nanocarriers. While 3D cell cultures are better models to mimic in vivo conditions, 2D cultures greatly facilitate a treatment with nanomaterials. Although human cell assays emerge as the preferred option to assess therapy efficacy and toxicology risk, current Au-drug development projects require testing in humanized animal models to enhance clinical prediction. Given the previously unmet need of treating GBM with effective, long-lasting therapies, our work raises hope to improve future care of patients using anti-cell metabolism directed approaches. Moreover, exploiting the unique optical and magnetic properties of Au NPs as theranostic devices are underway, thereby further extending the list of options how inorganic chemistry has the potential to improve neuro-oncology care, including clinical applied strategies such as photo- or hyperthermal therapy.

Supplementary Materials: The following are available online at www.mdpi.com/1999-4923/13/2/295/s1, Figure S1: Structural formula of citric acid (H_3Cit) and of the repeat units of the polymers poly(ethylene glycol) methyl ether thiol (ThioPEG), polyvinyl alcohol (PVA), polyvinyl pyrrolidone (PVP) and branched polyethylene imine (PEI), Figure S2: Histograms of Au-citrate (AuCit) (a), AuThioPEG (b), AuPVA (c) and AuPVP (d) nanoparticles (NPs). ThioPEG = poly(ethylene glycol) methyl ether thiol, PVA = polyvinyl alcohol, PVP = polyvinyl pyrrolidone., Figure S3: TEM images and histograms of AuCit-CB839 (a,f), AuThioPEG-CB839 (b,g), AuPVA-CB839 (c,h), AuPVP-CB839 (d,i) and AuPEI-CB839 (e,j) NPs. Images were captured at 200,000× (a), 100,000× (b) and 150,000× (c,d,e) magnification, Figure S4: HPLC chromatogram (a) and standard calibration curve (b) used for CB839 quantification., Figure S5: Structures of the two CB839 molecules, extracted from "glutaminase C in complex with inhibitor CB-839" (PBD ID: 5HL1, MMDB ID: 142270) [1]. Hydrogen atoms were added with Mercury [2], Figure S6: IR spectra of AuPVA-CB839 NPs (in black), CB839 (in red) and AuPVA NPs (in green), Figure S7: STEM EDX analysis of AuPVA-CB839 NPs. Elemental maps from the Au-Mα_1 intensity at 2123 ± 60 eV (a), NP inner and edge area selection ((b), all scan points assigned to edges are red, all those assigned to NP interiors are yellow and all other points are black) and corresponding EDX spectra of the three areas (c). Note: In (a) image pixels represent points where the electron probe was placed. A scan of 40 × 40 pixels was performed so, Figure S7a is shown at raw data resolution, Figure S7b is a mask applied to spectroscopic images at the resolution of the measurement, Figure S8: TGA curve for the decomposition of AuPVA-CB839 NPs (in black), CB839 (in red) and PVA (in blue), Figure S9: DLS measurements of AuPVA-CB839 NPs in water(a) and in DMEM (b), Figure S10: Colony Formation after treatment of U87 cells with CB839, AuThioPEG-CB839, AuCit-CB839 and AuPVA-CB839 NPs. Untreated cells were used as control, Figure S11: Absorbance measurements after incubation of GBM1 cells with culture medium (Control), AuPVA and AuPVA-CB839 NPs. These values were measured after performing the MTT Assay, as described previously [3]. Even though the MTT absorbance should be highest at the control (highest possible cell viability under the chosen conditions), wells treated with Au NPs show superior absorbance values even after several washing steps to remove NPs. This observation stresses the importance of choosing label-free non-optical methods to assess the toxicity of compounds accompanied by metal NPs, Figure S12: BTSC407 colonies after incubation with CB839 (wells 1–3) and with AuPVA-CB839 NPs (wells 4–6) using poly-D-lysine, Figure S13: Fluorescence spectra of AuPVA-FITC NPs (red line) and FITC (green line), Figure S14: IR spectra of AuPVA-FITC NPs (in brown), FITC (in purple) and AuPVA NPs (in green), Figure S15: UV-VIS spectra used to determine the loading efficiency of FITC for AuPVA-FITC NPs. The purple (upper) line (FITC) indicates the absorbance of total FITC added to the reaction. The brown (lower) line (sup. AuPVA-FITC) corresponds to the absorbance of FITC, which was not loaded onto AuPVA NPs and was obtained from the supernatant after centrifugation of the AuPVA-FITC product, Figure S16: Zeta potential measurements of AuPVA-FITC NPs. (a): Comparison of zeta potential of AuPVA NPs (in red) and freshly-prepared AuPVA-FITC NPs (in green). (b): Time-dependent zeta potential values of AuPVA-FITC NPs in water at room temperature, Figure S17: Microscopic images of JHH520 cells with AuPVA-FITC NPs after Trypan Blue quenching of extracellular fluorescence. (a) shows DAPI staining of cell nuclei, (b) shows the fluorescent AuPVA-FITC NPs inside the cells and (c) is a combination of (a) and (b).

Author Contributions: Conceptualization, B.G., U.D.K., and C.J.; methodology, B.G., A.C.N.; software, B.G., A.C.N.; validation, B.G.; formal analysis, B.G., A.C.N., and J.B.; investigation, B.G. and A.C.N.; resources, C.J. and U.D.K.; data curation, B.G.; writing—original draft preparation, B.G.; writing—review and editing, B.G., J.B., U.D.K., and C.J.; visualization, B.G.; supervision, U.D.K. and C.J.; project administration, U.D.K. and C.J.; funding acquisition, U.D.K. and C.J. All authors have read and agreed to the published version of the manuscript.

Funding: The work of Ulf Dietrich Kahlert is supported by the Federal Ministry of Education and Research (BMBF KZ 03VP03791), the Volkswagen Stiftung, the Hempel Family Foundation, the Brigitte-and Dr. Konstanze Wegener Foundation and the Sino-German Center for Science Promotion.

Institutional Review Board Statement: Ethical approval for the use of the cell models to study brain cancer biology was from the ethical commission of the medical faculty of Heinrich-Heine University (study ID 5841R, initial approval 31 March 2017, revised and renewed 16 September 2019).

Informed Consent Statement: Not applicable.

Data Availability Statement: The data presented in this study is contained within this article and its supplementary materials.

Acknowledgments: The authors thank the Ernst Ruska-Center, Forschungszentrum Jülich GmbH, Germany for access to the TEM facility under project number ER-C A-060. We acknowledge Constanze Uhlmann, Alexa Schmitz and Agustín Penagos for their support with this project. This article/publication is based upon work from COST Action CA 17140 "Cancer Nanomedicine from the Bench to the Bedside" supported by COST (European Cooperation in Science and Technology). Ulf Dietrich Kahlert thanks Hans-Jakob Steiger and Daniel Hänggi for their continuous support.

Conflicts of Interest: The authors declare no conflict of interest.

References

1. Yang, Y.; Hsieh, I.-Y.; Huang, X.; Li, J.; Zhao, W. Glioblastoma Stem-Like Cells: Characteristics, Microenvironment and Therapy. *Front. Pharmacol.* **2016**, *7*, 477.
2. Kahlert, U.D.; Mooney, S.M.; Natsumeda, M.; Steiger, H.-J.; Maciaczyk, J. Targeting cancer stem-like cells in glioblastoma and colorectal cancer through metabolic pathways. *Int. J. Cancer* **2017**, *140*, 10–22.
3. Harder, B.G.; Blomquist, M.R.; Wang, J.; Kim, A.J.; Woodworth, G.F.; Winkles, J.A.; Loftus, J.C.; Tran, N.L. Developments in Blood-Brain Barrier Penetrance and Drug Repurposing for Improved Treatment of Glioblastoma. *Front. Oncol.* **2018**, *8*, 462.
4. Garnier, D.; Renoult, O.; Alves-Guerra, M.-C.; Paris, F.; Pecqueur, C. Glioblastoma Stem-Like Cells, Metabolic Strategy to Kill a Challenging Target. *Front. Oncol.* **2019**, *9*, 118.
5. Cheng, L.; Wu, Q.; Guryanova, O.; Huang, Z.; Huang, Q.; Rich, J.N.; Bao, S. Elevated invasive potential of glioblastoma stem cells. *Biochem. Biophys. Res. Commun.* **2011**, *406*, 643–648.
6. Singh, S.K.; Clarke, I.D.; Terasaki, M.; Bonn, V.E.; Hawkins, C.; Squire, J.; Dirks, P.B. Identification of a cancer stem cell in human brain tumors. *Cancer Res.* **2003**, *63*, 5821–5828.
7. Singleton, D.C.; Dechaume, A.-L.; Murray, P.M.; Katt, W.P.; Baguley, B.C.; Leung, E.Y. Pyruvate anaplerosis is a mechanism of resistance to pharmacological glutaminase inhibition in triple-receptor negative breast cancer. *BMC Cancer* **2020**, *20*, 470.
8. Zhang, J.; Mao, S.; Guo, Y.; Wu, Y.; Yao, X.; Huang, Y. Inhibition of GLS suppresses proliferation and promotes apoptosis in prostate cancer. *Biosci. Rep.* **2019**, *39*, doi:10.1042/BSR20181826.
9. Seltzer, M.J.; Bennett, B.D.; Joshi, A.D.; Gao, P.; Thomas, A.G.; Ferraris, D.V.; Tsukamoto, T.; Rojas, C.J.; Slusher, B.S.; Rabinowitz, J.D.; et al. Inhibition of glutaminase preferentially slows growth of glioma cells with mutant IDH1. *Cancer Res.* **2010**, *70*, 8981–8987.
10. Choudhury, M.; Yin, X.; Schaefbauer, K.J.; Kang, J.-H.; Roy, B.; Kottom, T.J.; Limper, A.H.; Leof, E. SIRT7-mediated modulation of glutaminase 1 regulates TGF-β-induced pulmonary fibrosis. *FASEB J.* **2020**, *34*, 8920–8940.
11. Hoerner, C.R.; Chen, V.J.; Fan, A.C. The 'Achilles Heel' of Metabolism in Renal Cell Carcinoma: Glutaminase Inhibition as a Rational Treatment Strategy. *Kidney Cancer* ***2019***, *3*, 5–29.
12. Yu, Y.; Yu, X.; Fan, C.; Wang, H.; Wang, R.; Feng, C.; Guan, H. Targeting glutaminase-mediated glutamine dependence in papillary thyroid cancer. *J. Mol. Med.* **2018**, *96*, 777–790.
13. Zacharias, N.M.; Baran, N.; Shanmugavelandy, S.S.; Lee, J.; Lujan, J.V.; Dutta, P.; Millward, S.W.; Cai, T.; Wood, C.G.; Piwnica-Worms, D.; et al. Assessing metabolic intervention with a glutaminase inhibitor in real-time by hyperpolarized magnetic resonance in acute myeloid leukemia. *Mol. Cancer* **2019**, *18*, 1937–1946.
14. Reckzeh, E.S.; Karageorgis, G.; Schwalfenberg, M.; Ceballos, J.; Nowacki, J.; Stroet, M.C.M.; Binici, A.; Knauer, L.; Brand, S.; Choidas, A.; et al. Inhibition of Glucose Transporters and Glutaminase Synergistically Impairs Tumor Cell Growth. *Cell Chem. Biol.* **2019**, *26*, 1214–1228.

15. De Lartigue, J. Hallmark tumor metabolism becomes a validated therapeutic target. *J. Community Support. Oncol.* **2018**, *16*, e47–e52.
16. Lukey, M.L.; Cerione, R.A. Starving the Devourer: Cutting Cancer Off from Its Favorite Foods. *Cell Chem. Biol.* **2019**, *26*, 1197–1199.
17. Study of CB-839 in Combination w/ Paclitaxel in Patients of African Ancestry and Non-African Ancestry With Advanced TNBC (Clinical Trial ID: NCT03057600). Available online: https://clinicaltrials.gov/ct2/show/NCT03057600 (accessed on 15 February 2021).
18. Bennett, M.K.; Gross, M.I.; Bromley, S.D.; Li, J.; Chen, L.; Goyal, B.; Laidig, G.; Stanton, T.F.; Sjogren, E.B. Calithera Biosciences, Inc. Treatment of cancer with heterocyclic inhibitors of glutaminase. International Publication No. WO2014/089048 Al, International Application No. PCT/US2013/072830, 12 June 2014.
19. Gross, M.I.; Demo, S.D.; Dennison, J.B.; Chen, L.; Chernov-Rogan, T.; Goyal, B.; Janes, J.R.; Laidig, G.J.; Lewis, E.R.; Li, J.; et al. Antitumor Activity of the Glutaminase Inhibitor CB-839 in Triple-Negative Breast Cancer. *Mol. Cancer Ther*. **2014**, *13*, 890–901.
20. Restall, I.J.; Cseh, O.; Richards, L.M.; Pugh, T.J.; Luchman, H.A.; Weiss, S. Brain Tumor Stem Cell Dependence on Glutaminase Reveals a Metabolic Vulnerability through the Amino Acid Deprivation Response Pathway. *Cancer Res.* **2020**, *80*, 5478–5490.
21. Kahlert, U.D.; Cheng, M.; Koch, K.; Marchionni, L.; Fan, X.; Raabe, E.H.; Maciaczyk, J.; Glunde, K.; Eberhart, C.G. Alterations in cellular metabolome after pharmacological inhibition of Notch in glioblastoma cells. *Int. J. Cancer* **2016**, *138*, 1246–1255.
22. Koch, K.; Hartmann, R.; Tsiampali, J.; Uhlmann, C.; Nickel, A.-C.; He, X.; Kamp, M.; Sabel, M.; Barker, R.; Steiger, H.-J.; et al. A comparative pharmaco-metabolomic study of glutaminase inhibitors in glioma stem-like cells confirms biological effectiveness but reveals differences in target-specificity. *Cell Death Discov*. **2020**, *6*, 20.
23. Hu, X.; Zhang, Y.; Ding, T.; Liu, J.; Zhao, H. Multifunctional Gold Nanoparticles: A Novel Nanomaterial for Various Medical Applications and Biological Activities. *Front. Bioeng. Biotechnol.* **2020**, doi:10.3389/fbioe.2020.00990.
24. Maeda, H.; Nakamura, H.; Fang, J. The EPR effect for macromolecular drug delivery to solid tumors: Improvement of tumor uptake, lowering of systemic toxicity, and distinct tumor imaging in vivo. *Adv. Drug Deliv. Rev.* **2013**, *65*, 71–79.
25. Giesen, B.; Nickel, A.-C.; Garzón-Manjón, A.; Vargas-Toscano, A.; Scheu, C.; Kahlert, U.D.; Janiak, C. Influence of synthesis methods on the internalization of fluorescent gold nanoparticles into glioblastoma stem-like cells. *J. Inorg. Biochem.* **2020**, *203*, 110952.
26. Zimmermann, S.C.; Wolf, E.F.; Luu, A.; Thomas, A.G.; Stathis, M.; Poore, B.; Nguyen, C.; Le, A.; Rojas, C.; Slusher, B.S.; et al. Allosteric Glutaminase Inhibitors Based on a 1,4-Di(5-amino-1,3,4-thiadiazol-2-yl)butane Scaffold. *ACS Med. Chem. Lett.* **2016**, *7*, 520–524.
27. Mao, W.; Kim, H.S.; Son, Y.J.; Kim, S.R.; Yoo, H.S. Doxorubicin encapsulated clicked gold nanoparticle clusters exhibiting tumor-specific disassembly for enhanced tumor localization and computerized tomographic imaging. *J. Control. Release* **2018**, *269*, 52–62.
28. Ruan, S.; Yuan, M.; Zhang, L.; Hu, G.; Chen, J.; Cun, X.; Zhang, Q.; Yang, Y.; He, Q.; Gao, H. Tumor microenvironment sensitive doxorubicin delivery and release to glioma using angiopep-2 decorated gold nanoparticles. *Biomaterials* **2015**, *37*, 425–435.
29. Fu, Y.; Feng, Q.; Chen, Y.; Shen, Y.; Su, Q.; Zhang, Y.; Zhou, X.; Cheng, Y. Comparison of Two Approaches for the Attachment of a Drug to Gold Nanoparticles and Their Anticancer Activities. *Mol. Pharm.* **2016**, *13*, 3308–3317.
30. Zhao, H.; Lin, Z.Y.; Yildirimer, L.; Dhinakar, A.; Zhao, X.; Wu, J. Polymer-based nanoparticles for protein delivery: Design, strategies and applications. *J. Mater. Chem. B* **2016**, *4*, 4060–4071.
31. Qin, X.; Li, Y. Strategies to Design and Synthesize Polymer-Based Stimuli-Responsive Drug-Delivery Nanosystems. *ChemBioChem* **2020**, *21*, 1236–1253.
32. Negron, K.; Khalasawi, N.; Lu, B.; Ho, C.-Y.; Lee, J.; Shenoy, S.; Mao, H.-Q.; Wang, T.-H.; Hanes, J.; Suk, J.S. Widespread gene transfer to malignant gliomas with In vitro-to-In vivo correlation. *J. Control. Release* **2019**, *303*, 1–11.
33. Lee, J.M.; Mhawech-Fauceglia, P.; Lee, N.; Parsanian, L.C.; Lin, Y.G.; Gayther, S.A.; Lawrenson, K. A three-dimensional microenvironment alters protein expression and chemosensitivity of epithelial ovarian cancer cells in vitro. *Lab. Investig.* **2013**, *93*, 528–542.
34. Kang, M.S.; Lee, S.Y.; Kim, K.S.; Han, D.-W. State of the Art Biocompatible Gold Nanoparticles for Cancer Theragnosis. *Pharmaceutics* **2020**, *12*, 701.
35. Zhang, X.D.; Wu, D.; Shen, X.; Liu, P.X.; Yang, N.; Zhao, B.; Zhang, H.; Sun, Y.M.; Zhang, L.A.; & Fan, F.Y. Size-dependent in vivo toxicity of PEG-coated gold nanoparticles. *Int. J. Nanomed.* **2011**, *6*, 2071–2081.
36. Paradossi, G.; Cavalieri, F.; Chiessi, E.; Spagnoli, C.; Cowman, M.K.; Poly(vinyl alcohol) as versatile biomaterial for potential biomedical applications. *J. Mater. Sci. Mater. Med.* **2003**, *14*, 687–691.
37. Acharya, A.P.; Chan, S.Y.W.; LITTLE, S.R. University of Pittsburgh of the commonwealth system of higher education. Compositions and methods for administering a YAP1/WWRT1 inhibiting composition and a GLS1 inhibiting composition. International Publication No. WO2019/104038 Al, International Application No. PCT/US2018/062013, 31 May 2019.
38. Ruan, B.; Ruan, J. Faming Zhuanli Shenqing. Liposome containing glutamine metabolism inhibitor and pharmaceutical composition and use thereof. Patent No. CN107714650, 23 February 2018.
39. Adewale, O.B.; Davids, H.; Cairncross, L.; Roux, S. Toxicological Behavior of Gold Nanoparticles on Various Models: Influence of Physicochemical Properties and Other Factors. *Int. J. Toxicol.* **2019**, *38*, 357–384.
40. Sanabria, N.M.; Gulumian, M. The presence of residual gold nanoparticles in samples interferes with the RT-qPCR assay used for gene expression profiling. *J. Nanobiotechnol*. **2017**, *15*, 1–26.

41. Ponti, J.; Kinsner-Ovaskainen, A.; Norlen, H.; Altmeyer, S.; Cristina, A.; Bogni, A. *Interlaboratory Comparison Study of the Colony Forming Efficiency Assay for Assessing Cytotoxicity of Nanomaterials. EUR—Scientific and Technical Research Reports;* Report No. 978-92-79-44677-1; Publications Office of the European Union: Luxembourg, 2014.
42. Ernst Ruska-Centre for Microscopy and Spectroscopy with Electrons, FEI Tecnai G2 F20, *J. Large-Scale Res. Facil.* **2016**, *2*, 77, doi:10.17815/jlsrf-2-138.
43. Kahlert, U.D.; Suwala, A.K.; Raabe, E.H.; Siebzehnrubl, F.A.; Suarez, M.J.; Orr, B.A.; Bar, E.E.; Maciaczyk, J.; Eberhart, C.G. ZEB1 promotes invasion in human fetal neural stem cells and hypoxic glioma neurospheres. *Brain Pathol.* **2015**, *25*, 724–732.
44. Liston, D.R.; Davis, M. Clinically Relevant Concentrations of Anticancer Drugs: A Guide for Nonclinical Studies. *Clin. Cancer Res.* **2017**, *23*, 3489–3498.
45. Tsiampali, J.; Neumann, S.; Giesen, B.; Koch, K.; Maciaczyk, D.; Janiak, C.; Hänggi, D.; Maciaczyk, J. Enzymatic Activity of CD73 Modulates Invasion of Gliomas via Epithelial-Mesenchymal Transition-Like Reprogramming. *Pharmaceutics* **2020**, *13*, 378.
46. Turkevich, J.; Stevenson, P.C.; Hillier, J. A study of the nucleation and growth processes in the synthesis of colloidal gold. *Discuss. Faraday Soc.* **1951**, *11*, 55–75.
47. Zhang, H.; Ren, P.; Yang, F.; Chen, J.; Wang, C.; Zhou, Y.; Fu, J. Biomimetic epidermal sensors assembled from polydopamine-modified reduced graphene oxide/polyvinyl alcohol hydrogels for the real-time monitoring of human motions. *J. Mater. Chem. B* **2020**, *8*, 10549.
48. McHugh, K.; Jing, L.; Severt, S.Y.; Cruz, M.; Sarmadi, M.; Jayawardena, H.S.N.; Perkinson, C.F.; Larusson, F.; Rose, S.; Tomasic, S.; et al. Biocompatible near- infrared quantum dots delivered to the skin by microneedle patches record vaccination. *Sci. Transl. Med.* **2019**, *11*, e7162.
49. Huang, Q.; Stalnecker, C.; Zhang, C.; McDermott, L.A.; Iyer, P.; O'Neill, J.; Reimer, S.; Cerione, R.A.; Katt, W.P. Characterization of the interactions of potent allosteric inhibitors with glutaminase C, a key enzyme in cancer cell glutamine metabolism. *J. Biol. Chem.* **2018**, *293*, 3535–3545.
50. Cheng, X.; Tian, X.; Wu, A.; Li, J.; Tian, J.; Chong, Y.; Chai, Z.; Zhao, Y.; Chen, C.; Ge, C. Protein Corona Influences Cellular Uptake of Gold Nanoparticles by Phagocytic; Nonphagocytic Cells in a Size-Dependent Manner. *ACS Appl. Mater. Interfaces* **2015**, *7*, 20568–20575.
51. Larsson, P.; Engqvist, H.; Biermann, J.; Rönnerman, E.W.; Forssell-Aronsson, E.; Kovács, A.; Karlsson, P.; Helou, K.; Parris, T.Z. Optimization of cell viability assays to improve replicability and reproducibility of cancer drug sensitivity screens. *Sci. Rep.* **2020**, *10*, 5798.
52. Elgogary, A.; Xu, Q.; Poore, B.; Alt, J.; Zimmermann, S.C.; Zhao, L.; Fu, J.; Chen, B.; Xia, S.; Liu, Y.; et al. Combination therapy with BPTES nanoparticles and metformin targets the metabolic heterogeneity of pancreatic cancer. *Proc. Natl. Acad. Sci. USA* **2016**, *113*, e5328–e5336.
53. Fischer, I.; Nickel, A.-C.; Qin, N.; Taban, K.; Pauck, D.; Steiger, H.-J.; Kamp, M.; Muhammad, S.; Hänggi, D.; Fritsche, E.; et al. Different Calculation Strategies Are Congruent in Determining Chemotherapy Resistance of Brain Tumors In Vitro. *Cells* **2020**, *9*, 2689.
54. Khadka, S.; Arthur, K.; Washington, M.; Barekatain, Y.; Ackroyd, J.; Behr, E.; Suriyamongkol, P.; Lin, Y.-H.; Crowley, K.; Pham, C.D.; et al. Impaired Anaplerosis Is a Major Contributor to Glycolysis Inhibitor Toxicity in Glioma. *PREPRINT* **2020**, doi:10.21203/rs.3.rs-125147/v1.
55. Sokolova, V.; Mekky, G.; van der Meer. S. B.; Seeds, M.C.; Atala, A.J.; Epple, M. Transport of ultrasmall gold nanoparticles (2 nm) across the blood-brain barrier in a six-cell brain spheroid model. *Sci. Rep.* **2020**, *10*, 18033.
56. Khongkow, M.; Yata, T.; Boonrungsiman, S.; Ruktanonchai, U.R.; Graham, D.; Namdee, K. Surface modification of gold nanoparticles with neuron-targeted exosome for enhanced blood-brain barrier penetration. *Sci. Rep.* **2019**, *9*, 8278.
57. Cheng, Y.; Dai, Q.; Morshed, R.A.; Fan, X.; Wegscheid, M.L.; Wainwright, D.A.; Han, Y.; Zhang, L.; Auffinger, B.; Tobias, A.L.; et al. Blood-brain barrier permeable gold nanoparticles: An efficient delivery plat-form for enhanced malignant glioma therapy and imaging. *Small* **2014**, *10*, 5137–5150.
58. Sheleg, S.V.; Korotkevich, E.A.; Zhavrid, E.A.; Muravskaya, G.V.; Smeyanovich, A.F.; Shanko, Y.G.; Yurkshtovich, T.L.; Bychkovsky, P.B.; Belyaev, S.A. Local chemotherapy with cisplatin-depot for glioblastoma multiforme. *J. Neurooncol.* **2002**, *60*, 53–59.
59. Nam, L.; Coll, C.; Erthal, L.C.S.; de la Torre, C.; Serrano, D.; Martínez-Máñez, R.; Santos-Martínez, M.J.; Ruiz-Hernández, E. Drug Delivery Nanosystems for the Localized Treatment of Glioblastoma Multiforme. *Materials* **2018**, *11*, 779.
60. Lenting, K.; Verhaak, R.; Ter Laan, M.; Wesseling, P.; Leenders, W. Glioma: Experimental models and reality. *Acta Neuropathol.* **2017**, *133*, 263–282.
61. Huszthy, P.C.; Daphu, I.; Niclou, S.P.; Stieber, D.; Nigro, J.M.; Sakariassen, P.; Miletic, H.; Thorsen, F.; Bjerkvig, R. In vivo models of primary brain tumors: Pitfalls and perspectives. *Neuro. Oncol.* **2012**, *14*, 979–993.
62. Robertson, F.L.; Marqués-Torrejón, M.A.; Morrison, G.M.; Pollard, S.M. Experimental models and tools to tackle glioblastoma. *Dis. Models Mech.* **2019**, *12*, doi:10.1242/dmm.040386.
63. Upadhyay, U.M.; Tyler, B.; Patta, Y.; Wicks, R.; Spencer, K.; Scott, A.; Masi, B.; Hwang, L.; Grossman, R.; Cima, M.; et al. Intracranial microcapsule chemotherapy delivery for the localized treatment of rodent metastatic breast adenocarcinoma in the brain. *Proc. Natl. Acad. Sci. USA* **2014**, *111*, 16071–16076.
64. Semenkow, S.; Li, S.; Kahlert, U.D.; Raabe, E.H.; Xu, J.; Arnold, A.; Janowski, M.; Oh, B.C.; Brandacher, G.; Bulte, J.W.M.; et al. An immunocompetent mouse model of human glioblastoma. *Oncotarget* **2017**, *8*, 61072–61082.

65. Lan, X.; Kedziorek, D.A.; Chu, C.; Jablonska, A.; Li, S.; Kai, M.; Liang, Y.; Janowski, M.; Walczak, P. Modeling human pediatric and adult gliomas in immunocompetent mice through costimulatory blockade. *Oncoimmunology* **2020**, *9*, 1776577.
66. Wei, S.-C.; Hsu, P.-H.; Lee, Y.-F.; Lin, Y.-W.; Huang, C.-C. Selective Detection of Iodide and Cyanide Anions Using Gold-Nanoparticle-Based Fluorescent Probes. *ACS Appl. Mater. Interfaces* **2012**, *4*, 2652–2658.
67. Zhao, P.; Li, N.; Astruc, D. State of the art in gold nanoparticle synthesis. *Coord. Chem. Rev.* **2013**, *257*, 638–665.
68. Boles, M.; Ling, D.; Hyeon, T.; Talapin, D.V. The surface science of nanocrystals. *Nat. Mater.* **2016**, *15*, 141–153.
69. Xue, Y.; Li, X.; Li, H.; Zhang, W. Quantifying thiol–gold interactions towards the efficient strength control. *Nat. Commun.* **2014**, *5*, 4348.
70. Wang, S.; Wang, X.; Zhang, Z.; Chen, L. Highly sensitive fluorescence detection of copper ion based on its catalytic oxidation to cysteine indicated by fluorescein isothiocyanate functionalized gold nanoparticles. *Colloids Surf. A Physicochem. Eng. Asp.* **2015**, *468*, 333–338.
71. Donahue, N.D.; Acar, H.; Wilhelm, S. Concepts of nanoparticle cellular uptake, intracellular trafficking, and kinetics in nanomedicine. *Adv. Drug Deliv. Rev.* **2019**, *143*, 68–96.

pharmaceutics

Supplementary Materials: Augmented Therapeutic Potential of Glutaminase Inhibitor CB839 in Glioblastoma Stem Cells Using Gold Nanoparticle Delivery

Beatriz Giesen, Ann-Christin Nickel, Juri Barthel, Ulf Dietrich Kahlert and Christoph Janiak

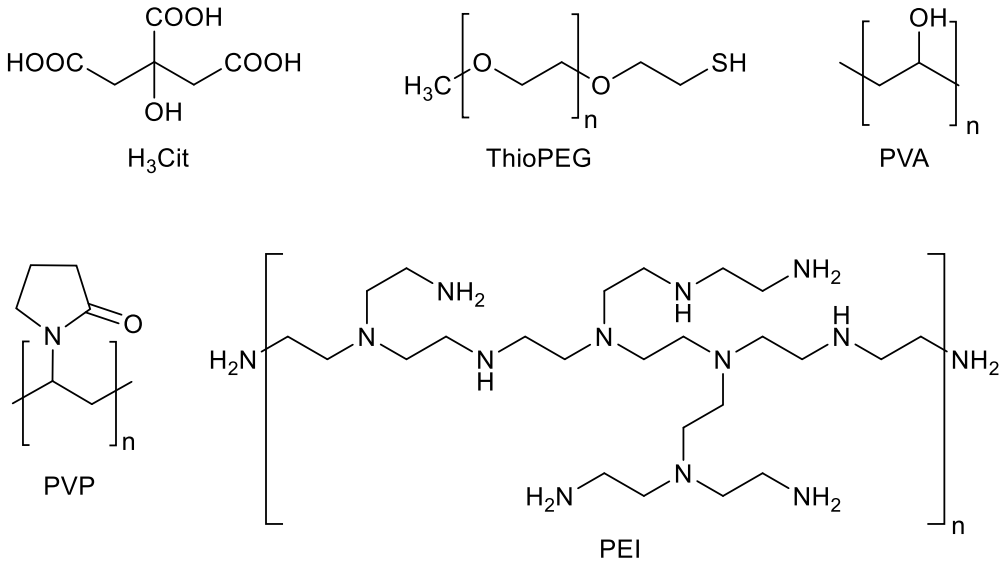

Figure S1. Structural formula of citric acid (H_3Cit) and of the repeat units of the polymers poly(ethylene glycol) methyl ether thiol (ThioPEG), polyvinyl alcohol (PVA), polyvinyl pyrrolidone (PVP) and branched polyethylene imine (PEI).

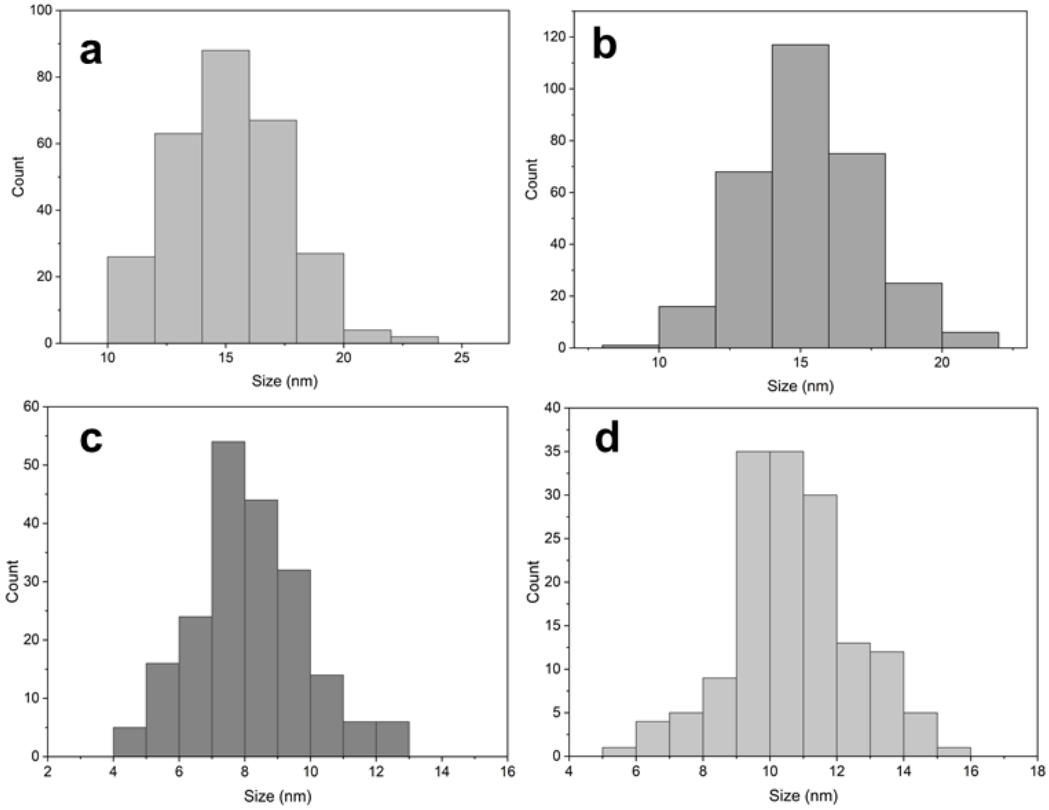

Figure S2. Histograms of Au-citrate (AuCit) (**a**), AuThioPEG (**b**), AuPVA (**c**) and AuPVP (**d**) nanoparticles (NPs). ThioPEG = poly(ethylene glycol) methyl ether thiol, PVA = polyvinyl alcohol, PVP = polyvinyl pyrrolidone.

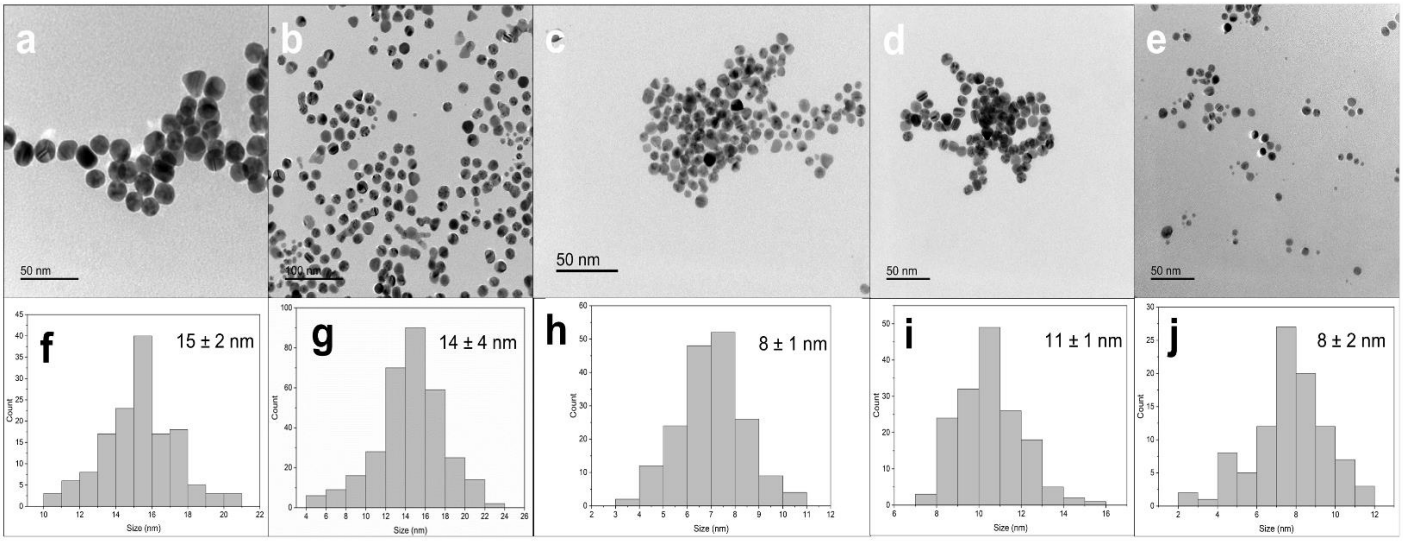

Figure S3. TEM images and histograms of AuCit-CB839 (**a**,**f**), AuThioPEG-CB839 (**b**,**g**), AuPVA-CB839 (**c**,**h**), AuPVP-CB839 (**d**,**i**) and AuPEI-CB839 (**e**,**j**) NPs. Images were captured at 200,000× (**a**), 100,000× (**b**) and 150,000× (**c**,**d**,**e**) magnification.

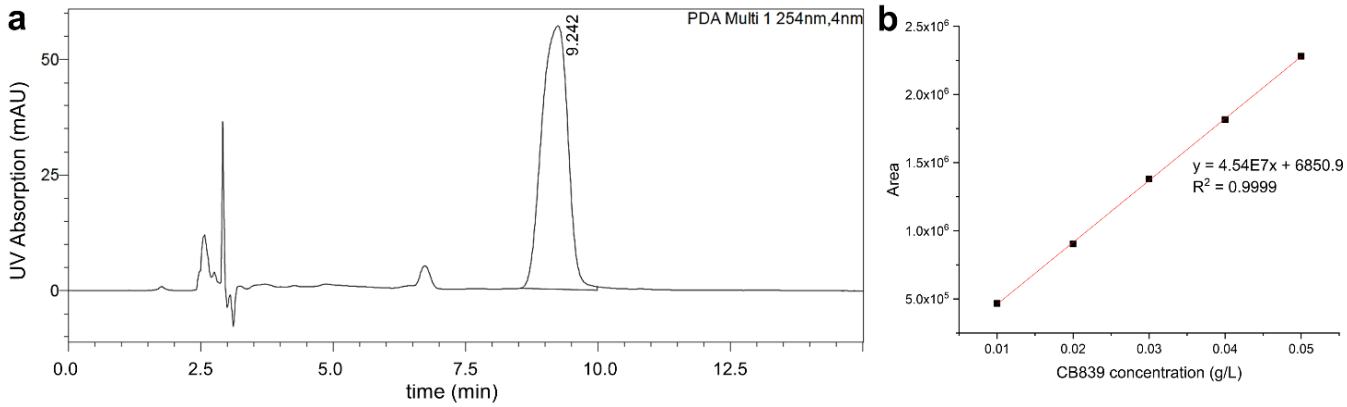

Figure S4. HPLC chromatogram (**a**) and standard calibration curve (**b**) used for CB839 quantification.

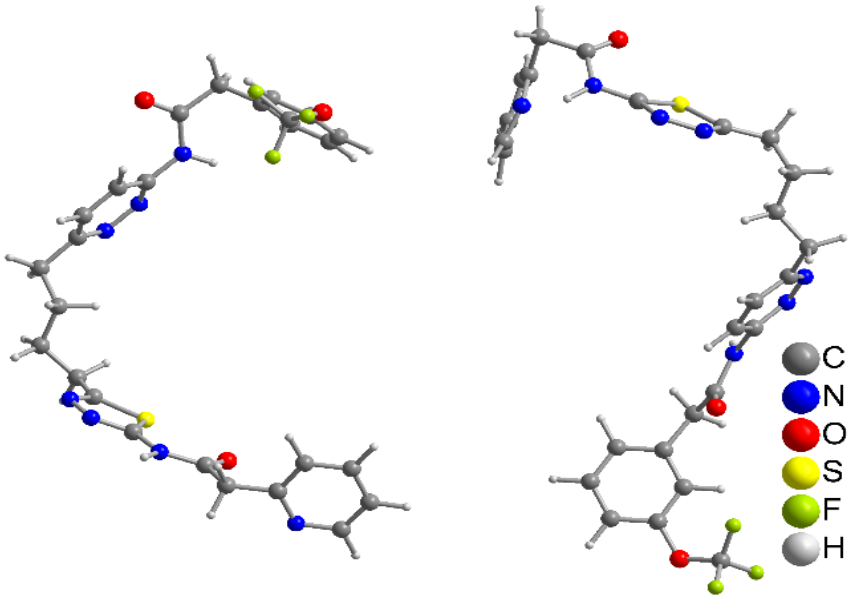

Figure S5. Structures of the two CB839 molecules, extracted from "glutaminase C in complex with inhibitor CB-839" (PBD ID: 5HL1, MMDB ID: 142270) [1]. Hydrogen atoms were added with Mercury [2].

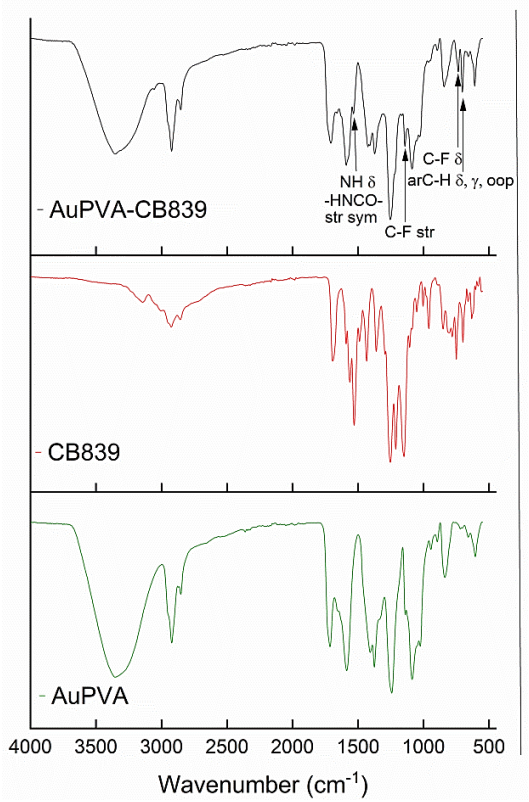

Figure S6. IR spectra of AuPVA-CB839 NPs (in black), CB839 (in red) and AuPVA NPs (in green).

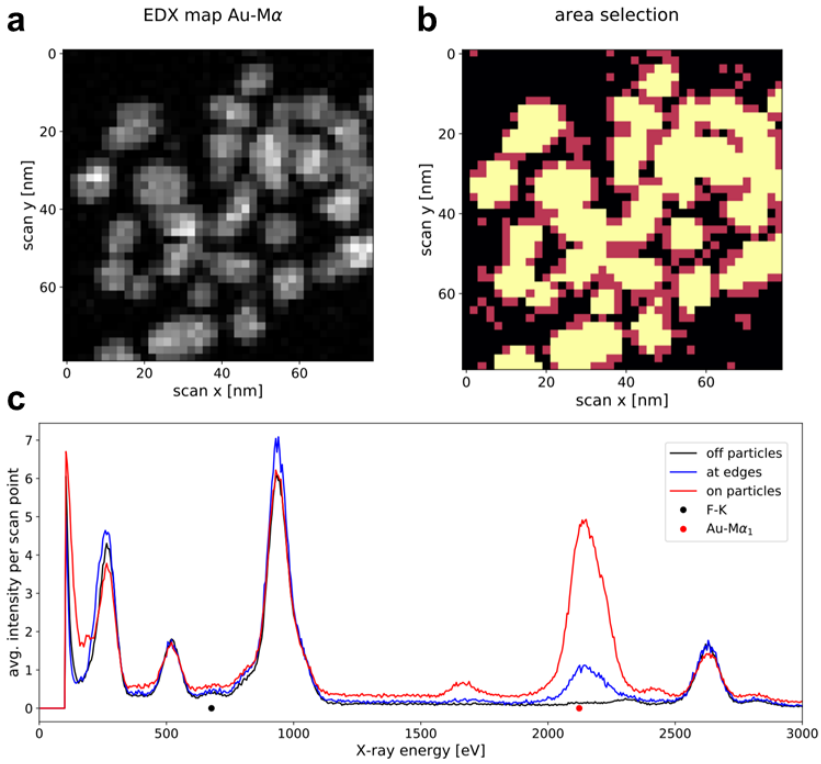

Figure S7. STEM EDX analysis of AuPVA-CB839 NPs. Elemental maps from the Au-Mα1 intensity at 2123 ± 60 eV (**a**), NP inner and edge area selection ((**b**), all scan points assigned to edges are red, all those assigned to NP interiors are yellow and all other points are black) and corresponding EDX spectra of the three areas (**c**). Note: In (a) image pixels represent points where the electron probe was placed. A scan of 40 × 40 pixels was performed so, Figure S7a is shown at raw data resolution, Figure S7b is a mask applied to spectroscopic images at the resolution of the measurement.

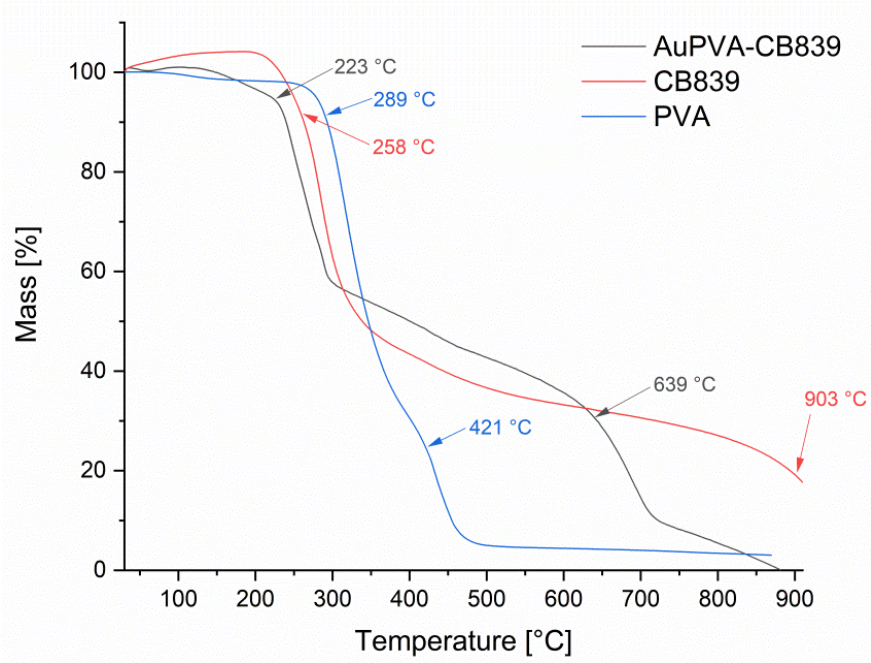

Figure S8. TGA curve for the decomposition of AuPVA-CB839 NPs (in black), CB839 (in red) and PVA (in blue).

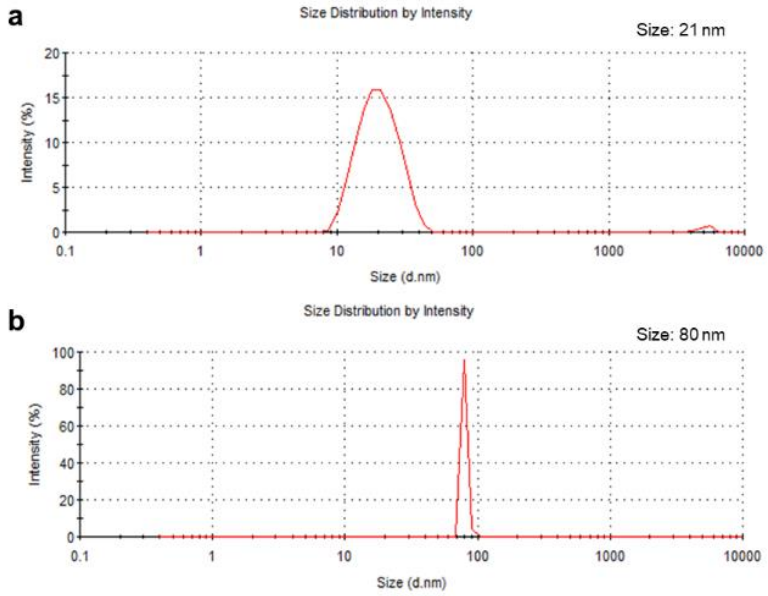

Figure S9. DLS measurements of AuPVA-CB839 NPs in water(**a**) and in DMEM (**b**).

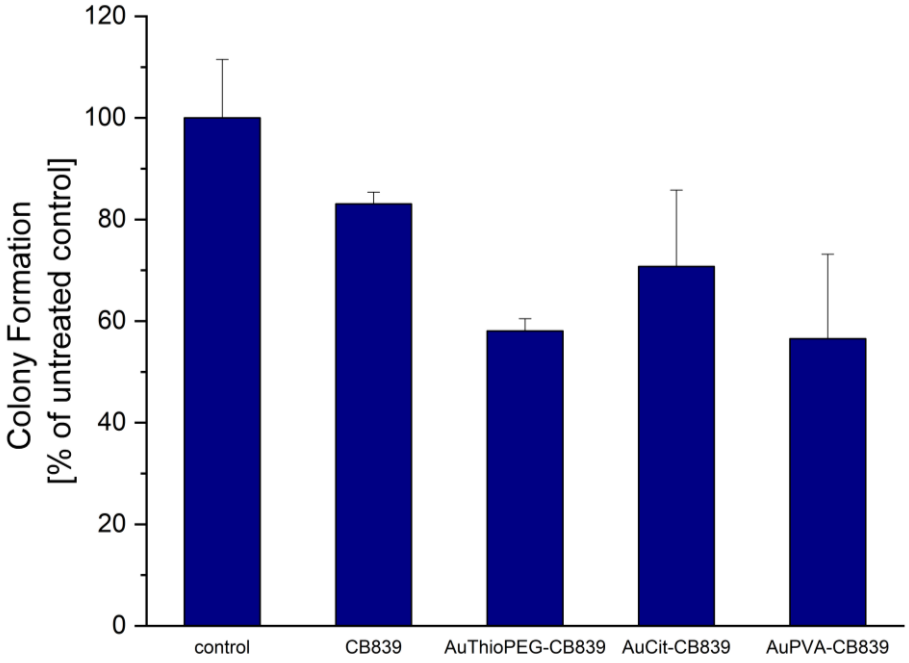

Figure S10. Colony Formation after treatment of U87 cells with CB839, AuThioPEG-CB839, AuCit-CB839 and AuPVA-CB839 NPs. Untreated cells were used as control.

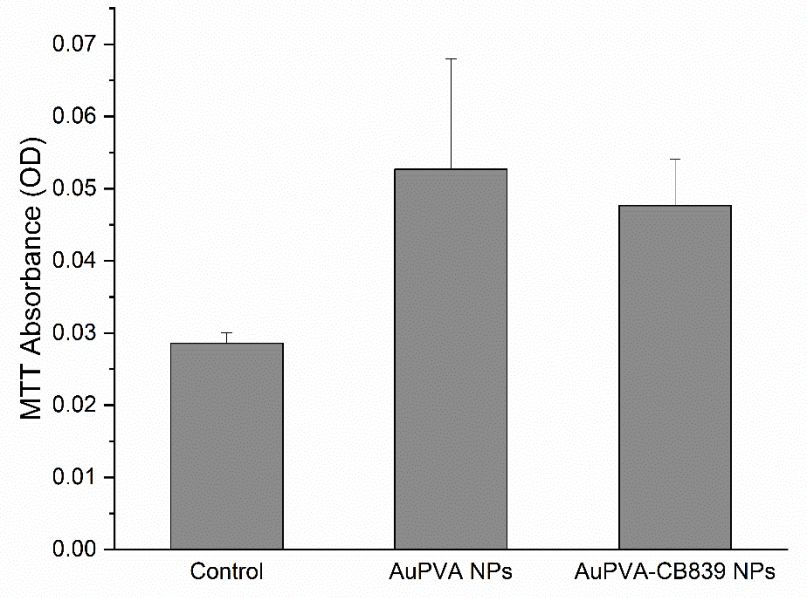

Figure S11. Absorbance measurements after incubation of GBM1 cells with culture medium (Control), AuPVA and AuPVA-CB839 NPs. These values were measured after performing the MTT Assay, as described previously [3]. Even though the MTT absorbance should be highest at the control (highest possible cell viability under the chosen conditions), wells treated with Au NPs show superior absorbance values even after several washing steps to remove NPs. This observation stresses the importance of choosing label-free non-optical methods to assess the toxicity of compounds accompanied by metal NPs.

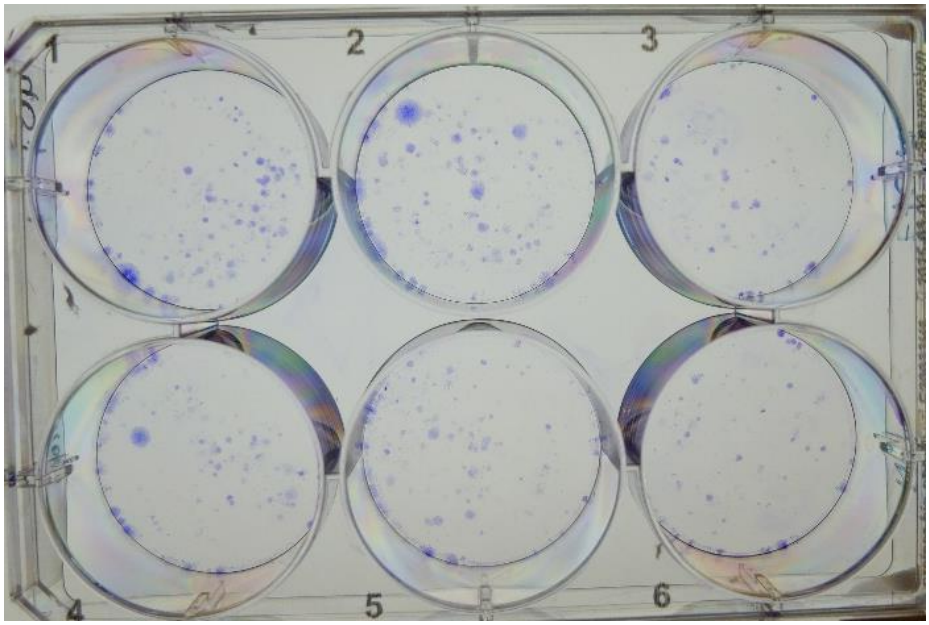

Figure S12. BTSC407 colonies after incubation with CB839 (wells 1–3) and with AuPVA-CB839 NPs (wells 4–6) using poly-D-lysine.

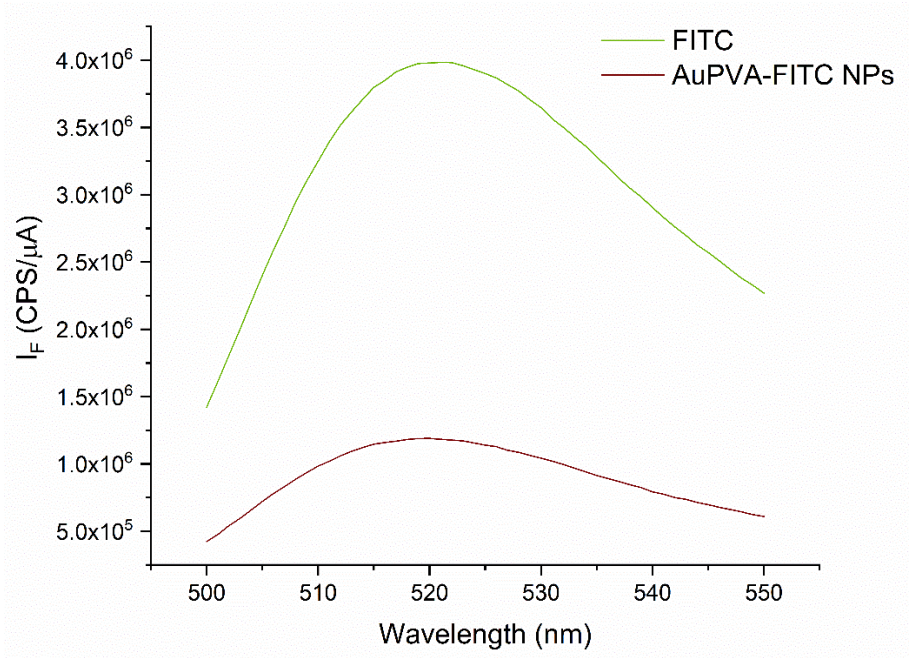

Figure S13. Fluorescence spectra of AuPVA-FITC NPs (red line) and FITC (green line).

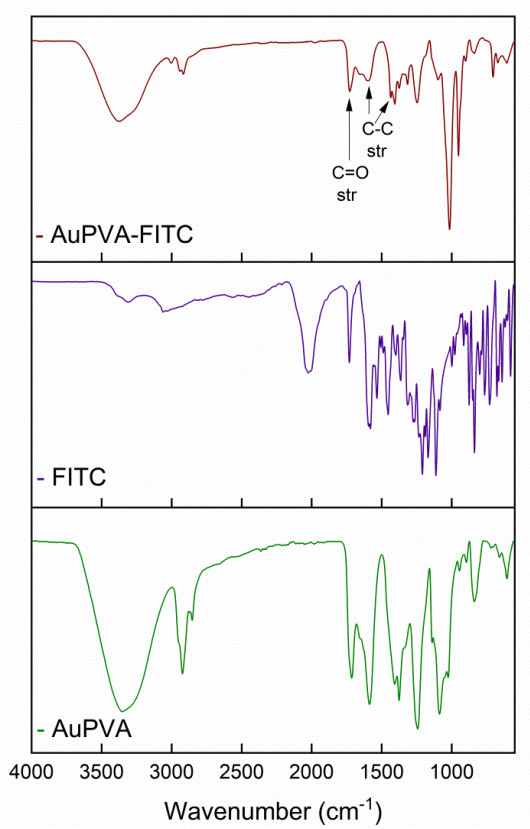

Figure S14. IR spectra of AuPVA-FITC NPs (in brown), FITC (in purple) and AuPVA NPs (in green).

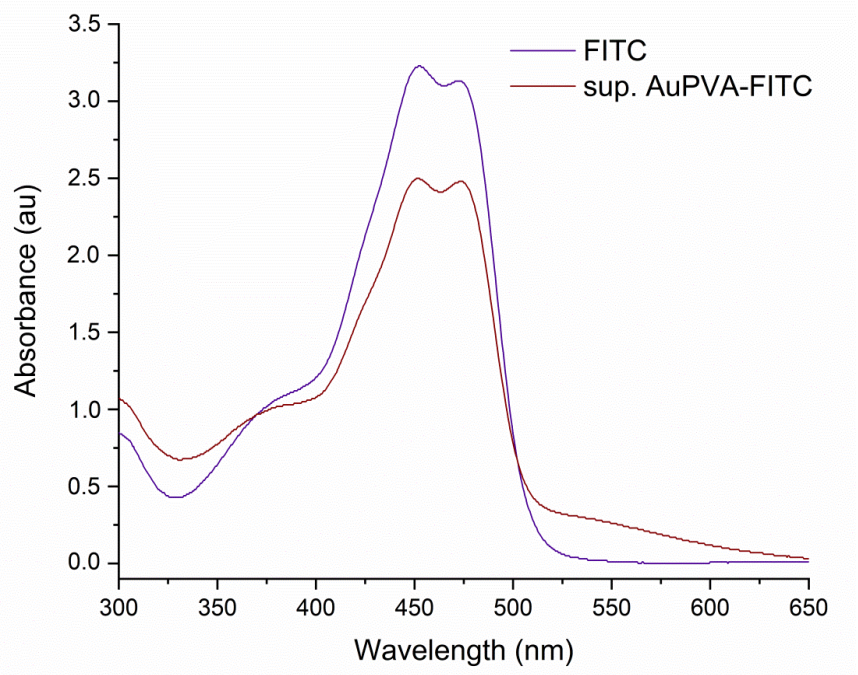

Figure S15. UV-VIS spectra used to determine the loading efficiency of FITC for AuPVA-FITC NPs. The purple (upper) line (FITC) indicates the absorbance of total FITC added to the reaction. The brown (lower) line (sup. AuPVA-FITC) corresponds to the absorbance of FITC, which was not loaded onto AuPVA NPs and was obtained from the supernatant after centrifugation of the AuPVA-FITC product.

$$FITC\ Loading\ Efficiency\ (\%) = \frac{Absorbance\ FITC\ (450\ nm) - \text{absorbance sup. AuPVA} - \text{FITC (450 nm)}}{Absorbance\ FITC\ (450\ nm)} \times 100\%$$

$$= \frac{3.23 - 2.5}{3.23} \times 100\% = 23\% \quad \text{(S1)}$$

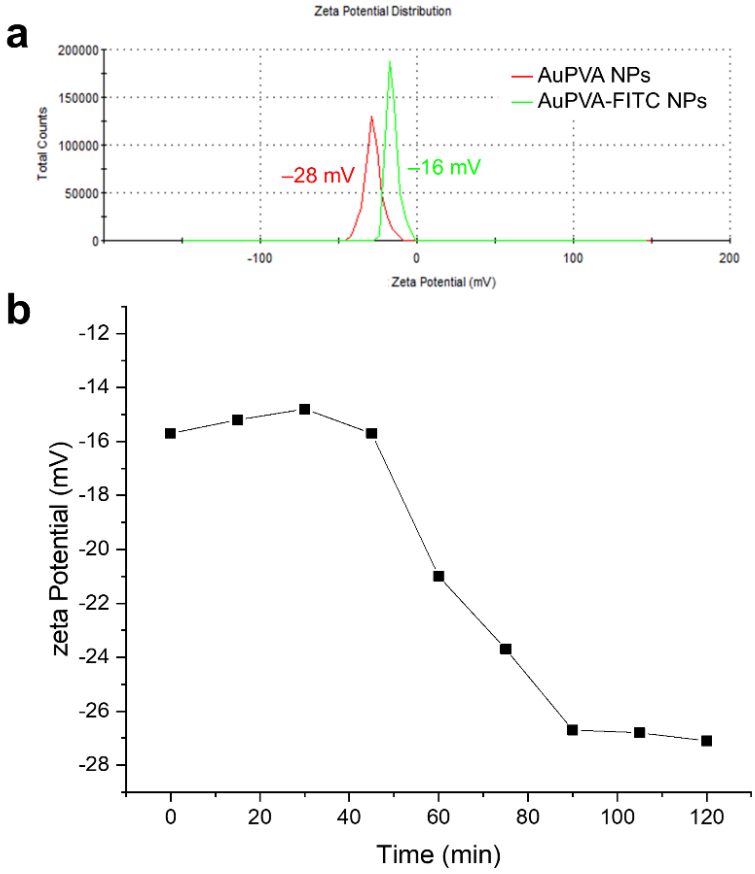

Figure S16. Zeta potential measurements of AuPVA-FITC NPs. (**a**): Comparison of zeta potential of AuPVA NPs (in red) and freshly-prepared AuPVA-FITC NPs (in green). (**b**): Time-dependent zeta potential values of AuPVA-FITC NPs in water at room temperature.

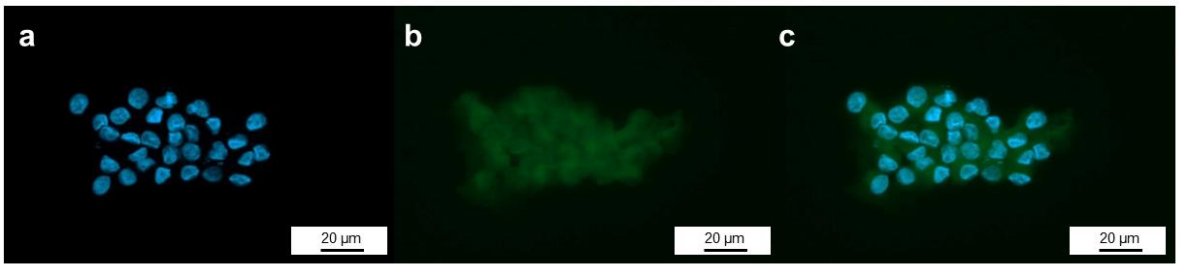

Figure S17. Microscopic images of JHH520 cells with AuPVA-FITC NPs after Trypan Blue quenching of extracellular fluorescence. (**a**) shows DAPI staining of cell nuclei, (**b**) shows the fluorescent AuPVA-FITC NPs inside the cells and (**c**) is a combination of (**a**) and (**b**).

References

1. Huang, Q., Stalnecker, C., Zhang, C., McDermott, L. A., Iyer, P., O'Neill, J., Reimer, S., Cerione, R. A. and Katt, W. P. Characterization of the interactions of potent allosteric inhibitors with glutaminase C, a key enzyme in cancer cell glutamine metabolism. *J. Biol. Chem*. **2018**, 293, 3535–3545.
2. Mercury 2020.2.0, Copyright © CCDC, 2001–2020, http://www.ccdc.cam.ac.uk/
3. Giesen, B., Nickel, A.-C., Garzón-Manjón, A., Vargas-Toscano, A., Scheu, C., Kahlert, U. D. and Janiak, C. Influence of synthesis methods on the internalization of fluorescent gold nanoparticles into glioblastoma stem-like cells. *J. Inorg. Biochem.* **2020**, 203, 110952.

3.3. Co-author Publications

Co-author publications are listed with the respective own contributions. A short summary and a description of the contribution to the respective publication are shown.

3.3.1. Enzymatic Activity of CD73 Modulates Invasion of Gliomas via Epithelial-Mesenchymal Transition-Like Reprogramming

J. Tsiampali, S. Neumann, B. Giesen, K. Koch, D. Maciaczyk, C. Janiak, D. Hänggi, J. Maciaczyk,

Pharmaceuticals **2020**, 13, 378.

DOI: 10.3390/ph13110378, reprinted under the Creative Commons Attribution License from reference 252, published by MDPI.

Summary:

The propagation of GB cells depends on the molecular reprogramming associated with an EMT-like process (section 1.6). The cell surface protein CD73 has been known to regulate EMT, presenting both enzymatic and non-enzymatic activity. As an enzyme, CD73 catalyzes the conversion of adenosine monophosphate (AMP) to adenosine (ADO) (Figure 18), which is implicated in the immune escape of tumors such as GB. Additionally, CD73 can serve as an adhesive molecule by controlling interactions between cells and extracellular matrix components. In this work, the effect of CD73 on GSC growth was investigated as a potential target for GB treatment. The inhibition of the enzymatic activity of CD73 was investigated by pharmacological treatment of GSCs with adenosine 5'-(α,β-methylene)diphosphate (APCP) or with the phosphodiesterase inhibitor Pentoxifylline (PTX). CD73 enzymatic activity was determined by HPLC. A reduction of CD73 resulted in significant suppression of GSC viability, proliferation and clonogenicity, while the CD73 enzymatic activity exhibited negative effects on cell invasion due to impaired downstream ADO signaling.

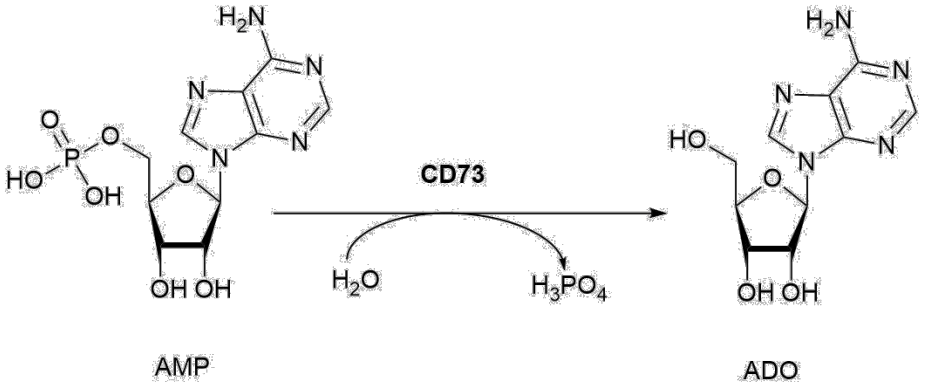

Figure 18. Enzymatic conversion of AMP to ADO by CD73.

Contributions to the work:

- Measurement of changes in the conversion of AMP to ADO upon genetic and pharmacological inhibition of CD73 using HPLC.
- Literature search, development and optimization of the HPLC method used to quantify the enzymatic activity of CD73.
- Identification of peaks corresponding to AMP and ADO in water (Figure 19a) and in DMEM medium (Figure 19b).
- Simultaneous quantification of AMP and ADO through a calibration curve of both standards and subsequent peak integration.
- Analysis, curation and illustration of HPLC results.
- Display of chemical structures and HPLC chromatogram (Figure 18, Figure 19) for the manuscript.
- Corrections during the peer-review process.
- Revision and modification of the final manuscript as co-author.

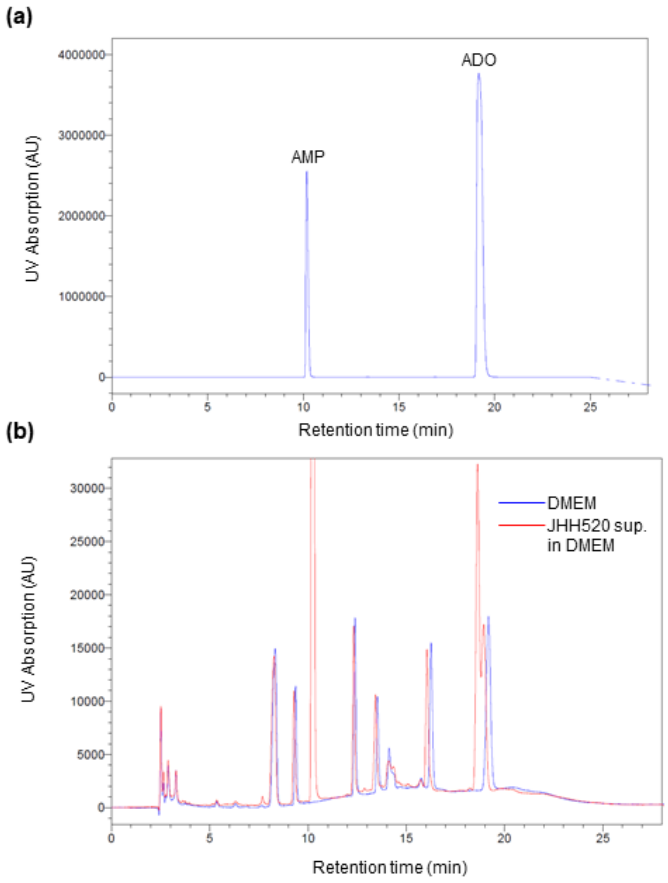

Figure 19. HPLC chromatograms of AMP and ADO standards (a) and of supernatant of JHH520 cells after incubation with AMP (b) are shown.

3.3.2. Nickel Nanoparticles Supported on a Covalent Triazine Framework as Electrocatalyst for Oxygen Evolution Reaction and Oxygen Reduction Reactions

S. Öztürk, Y. X. Xiao, D. Dietrich, B. Giesen, J. Barthel, J. Ying, X. Y. Yang, C. Janiak,

Beilstein Journal of Nanotechnology **2020**, 11, 770-781.

DOI: 10.3762/bjnano.11.62, reprinted under the terms of the Creative Commons Attribution License from reference 253, published by Beilstein Institut.

Summary:

Due to the increasing energy demand and the environmental issues triggered by fossil fuel combustion, more efficient and cost-effective catalysts for sustainable conversion and storage of energy are in urgent need. To this end, nickel nanoparticles (Ni NPs) supported on covalent

triazine frameworks (CTFs) were synthesized using bis(cycloocta-1,5-diene)nickel ($Ni(COD)_2$) and the ionic liquid (IL) 1-butyl-3-methylimidazolium bis(trifluoromethylsulfonyl)imide ([BMIm][NTf_2]) as novel electrocatalysts for water splitting reactions. The effects of alterations in the synthesis parameters - such as precursor amount and temperature - on the resulting composite materials were investigated using PXRD, AAS, nitrogen sorption and XPS analysis. Furthermore, the size, morphology, elemental composition and crystalline phase of the NPs was studied with SEM, TEM, STEM and EDX. Finally, the catalytic activity of the CTF-supported Ni NPs was investigated for the oxygen evolution reaction (OER) and oxygen reduction reaction (ORR). The composite synthesized at 600 °C (Ni/CTF-1-600) presented an OER catalytic activity comparable to other nickel-based electrocatalysts, yet outperformed the benchmark catalyst RuO_2. Furthermore, this material demonstrated high stability with negligible decrease in activity towards OER and ORR.

Contributions to the work:

- Extensive TEM, HR-TEM and STEM measurements of the materials Ni/CTF-1-600-33, Ni/CTF-1-600-22, Ni/CTF-1-400-35 and Ni/CTF-1-400-20 (Figure 20). EDX spectroscopy analysis including spectra generation and elemental mapping (Figure 21).
- Assistance with sample preparation and purification at time of material deposition onto a TEM grid.
- Introduction to NP size determination method and use of the Gatan Microscopy software.
- Support with interpretation of microscopy and EDX results.
- Illustration and display of STEM-EDX elemental maps for the manuscript (Figure 21, as well as Figure S12 and S13 in reference 253).
- Confirmation of the presence of particles on the CTF surface using TEM images. Figure 20b shows some Ni NPs sticking out over the edge of the CTF (red circle).
- Assistance in all TEM-related questions during the peer-review process and improvement of the manuscript accordingly.
- Review and correction of the final manuscript as co-author.

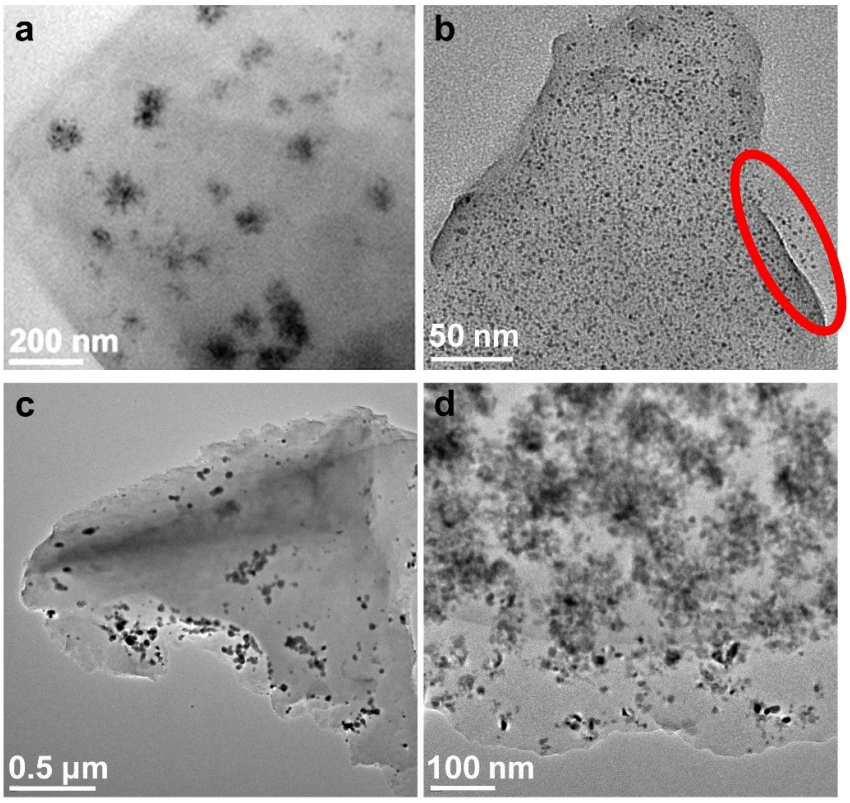

Figure 20. TEM images of Ni/CTF-1-600-22 (a), Ni/CTF-1-600-33 (b), Ni/CTF-1-400-20 (c) and Ni/CTF-1-400-35 (d), showing Ni NPs supported on CTF. The red circle in (b) indicates the presence of "washed-off" Ni NPs on the surface.

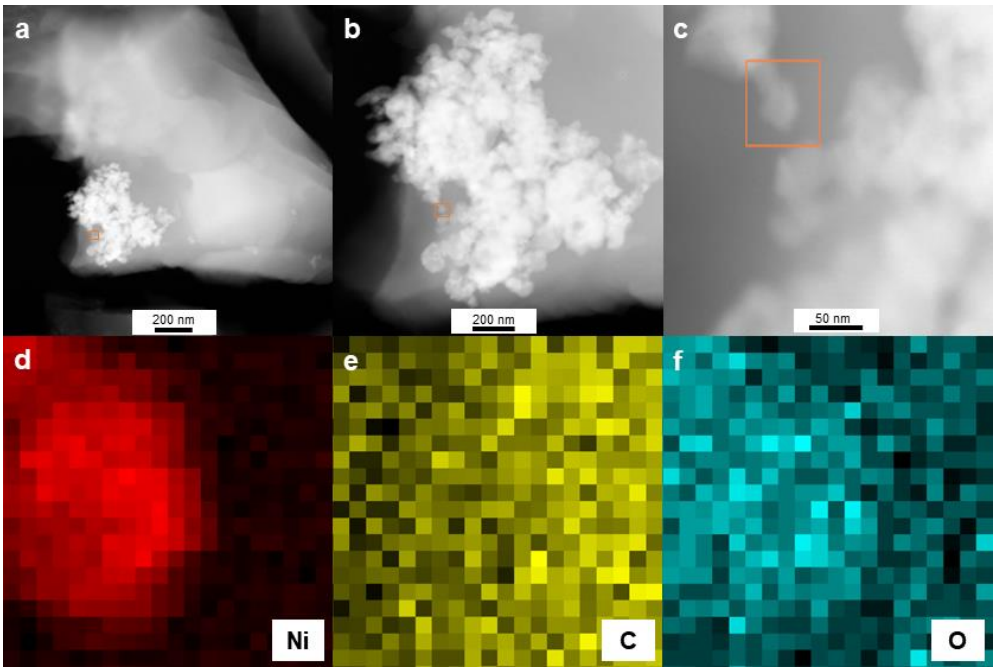

Figure 21. STEM images of Ni/CTF1-1-600-22 and EDX elemental maps of Ni, C and O taken from the area inside the orange square.

3.3.3. Synthesis of Plasmonic Fe/Al Nanoparticles in Ionic Liquids

A. Schmitz, H. Meyer, M. Meischein, A. Garzón-Manjón, L. Schmolke, B. Giesen, C. Schlüsener, P. Simon, Y. Grin, R. A. Fischer, C. Scheu, A. Ludwig, C. Janiak,

RSC Advances **2020**, 10, 12891-12899.

DOI: 10.1039/D0RA01111H, reprinted under a Creative Commons Attribution-NonCommercial 3.0 Unported Licence from reference 254, published by The Royal Society of Chemistry.

Summary:

Non-noble bimetallic Fe/Al NPs were synthesized using bottom-up and top-down approaches as potential low-cost nano catalysts and alternatives for the commonly used Pd benchmark. Fe/Al NPs synthesized in three different ILs under mild conditions were characterized using PXRD, XPS, AAS, SEM, TEM and SAED analysis. The bottom-up approaches resulted in crystalline FeAl NPs on an amorphous background, while the top-down approach revealed small Fe_4Al_{13} NPs. Interestingly, Fe_4Al_{13} NPs in the IL 1-octylpyridinium bis(trifuoromethylsulfonyl)imide ([OPy][NTf_2]) displayed two absorption bands in the green-blue to green spectral region (475 and 520 nm), which give rise to a complementary red color, similar to the one known for Au NPs.

Contributions to the work:

- TEM, EDX and SAED measurements of the NP samples synthesized by bottom-up approaches (Figure 22 and Figures S3, S7, S9 and S11 in reference 254).
- Review and correction of the final manuscript as co-author.

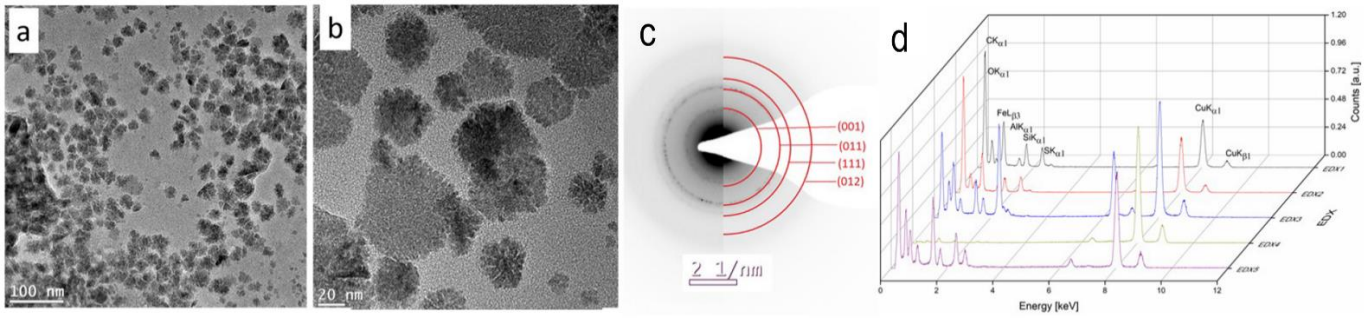

Figure 22. TEM images (a, b), SAED (c) and EDX spectra (d) of Fe/Al NPs from [LiFe(bis(trimethylsilyl)amido)$_3$] and $LiAlH_4$ in [OPy][NTf_2].

3.3.4. Probing the Limits of Linker Substitution in Aluminum MOFs through Water Vapor Sorption Studies: Mixed-MOFs Instead of Mixed-linker CAU-23 and MIL 160 Materials

C. Schlüsener, D. N. Jordan, M. Xhinovci, T. J. Matemb Ma Ntep, A. Schmitz, B. Giesen, C. Janiak,

Dalton Transactions **2020**, 49, 7373-7383.

DOI: 10.1039/D0DT01044H, reprinted from reference 255 by permission of The Royal Society of Chemistry.

Summary:

Efforts to synthesize mixed-linker metal-organic frameworks (MOFs) from the linkers 2,5-thiophenedicarboxylate (TDC) and 2,5-furandicarboxylate (FDC) resulted in the formation of mixed phases of the MOFs known as CAU-23 and MIL-160. Since PXRD, IR and nitrogen sorption analysis failed to distinguish between mixed MOFs and mixed-linker phases, measurements of water vapor sorption isotherms were introduced to characterize the materials. The synthetized MOF combinations with TDC:FDC ratios from 38:62 to 82:18 revealed two or three uptake steps in the water sorption isotherm, corresponding to both CAU-23 and MIL-160, as well as to the formation of the MOF MIL-53-TDC, a polymorph of CAU-23. Furthermore, the existence of different phases was verified using STEM by acquiring point EDX spectra of MOFs with different morphologies. For the material with TDC:FDC 53:47, different aluminum and sulfur amounts were found among the more crystalline rod-like particles and the diffuse particle regions (Figure 23).

Contributions to the work:

- STEM and EDX measurements of the TDC:FDC 53:47 MOF.
- Review and correction of the final manuscript as co-author.

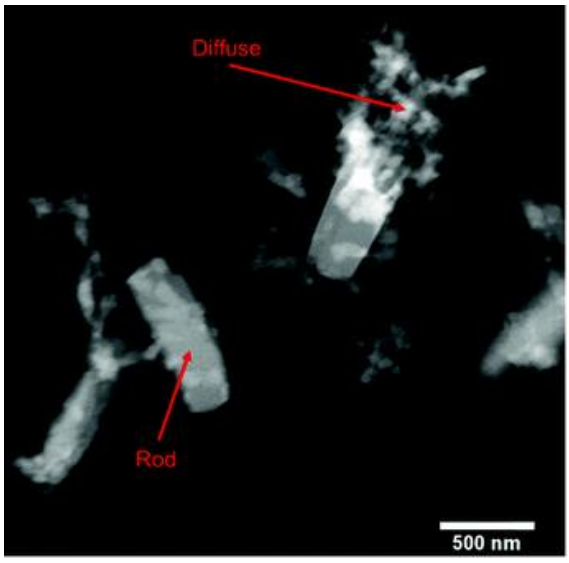

Figure 23. STEM image of MOF with a TDC:FDC ratio of 53:47. The area indicated by the red arrows was used to perform point EDX measurements of the rod and diffuse particles.

3.3.5. Acylselenoureato Bis(chelates) of Lead: Synthesis, Structural Characterization and Microwave-assisted Formation of PbSe Nano- and Microstructures

K. Klauke, A. Schmitz, A. C. Swertz, B. B. Beele, B. Giesen, C. Schlüsener, C. Janiak, F. Mohr,

New Journal of Chemistry **2020**, 44, 7719-7726.

DOI: 10.1039/D0NJ01433H, reprinted under a Creative Commons Attribution-NonCommercial 3.0 Unported Licence from reference 256, published by The Royal Society of Chemistry.

Summary:

Three lead(II) bis(acylselenoureato) complexes were synthesized and confirmed using NMR spectroscopy, elemental analysis and single crystal XRD. A lead(II) complex was used as a single-source precursor for PbSe NPs, synthesized by a microwave-assisted method. For this purpose, propylene carbonate (PC) and the IL [BMIm][NTf_2] were used, as well as mixtures of trioctylphosphine (TOP), octadecene (ODC) and [BMIm][NTf_2] or [BMIm][NTf_2] and PC. Depending on the stabilizer used, small 19 nm PbSe NPs or PbSe cubes between 178 nm and 366 nm were obtained. The PbSe particle suspensions were characterized by PXRD, TEM, EDX and SAED.

Contributions to the work:

- TEM, STEM and SAED measurements of the NP samples (Figure 24, as well as Figures S2, S3, S4, S5 and S6 in reference 256).
- EDX spectroscopy analysis including spectra generation and elemental mapping (Figure 25).
- Review and correction of the final manuscript as co-author.

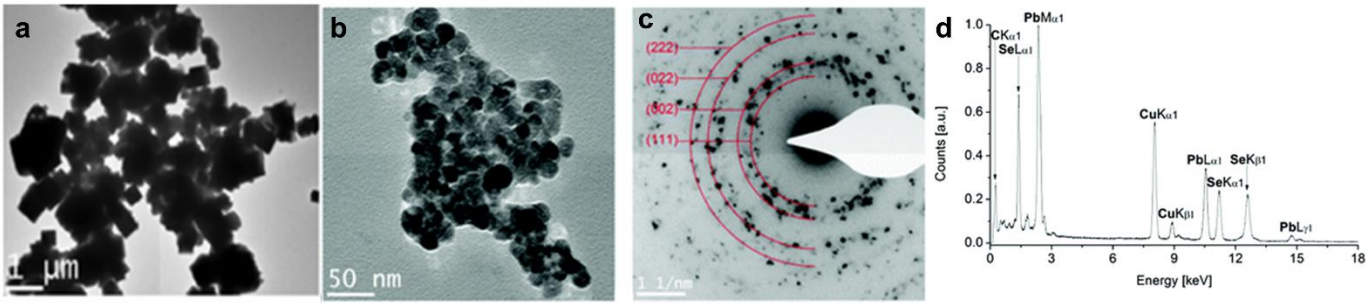

Figure 24. TEM images of PbSe cubes in PC(a) and NPs in ODC/TOP and [BMIm][NTf_2] (b). SAED (c) and EDX spectrum (d) of PbSe NPs.

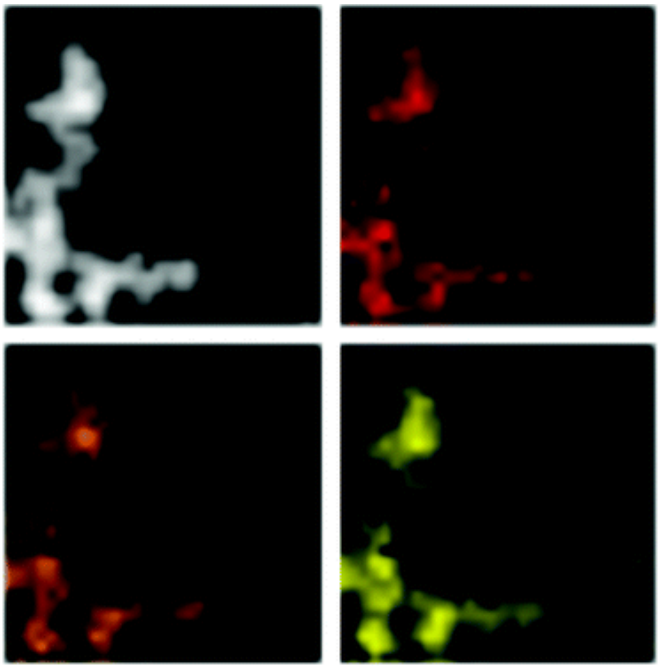

Figure 25. STEM-EDX elemental maps of PbSe particles in [BMIm][NTf_2]. White: HAADF-STEM image, red: Se, orange: Pb L-shell, yellow: Pb M-shell.

3.3.6. Bimetallic Co/Al Nanoparticles in an Ionic Liquid: Synthesis and Application in Alkyne Hydrogenation

L. Schmolke, B. Gregori, B. Giesen, A. Schmitz, J. Barthel, L. Staiger, R. A. Fischer, A. J. von Wangelin, C. Janiak,

New Journal of Chemistry **2019**, 43, 16583-16594.

DOI: 10.1039/C9NJ03622A, reprinted from reference 257 by permission of The Royal Society of Chemistry (RSC) on behalf of the Centre National de la Recherche Scientifique (CNRS) and the RSC.

Summary:

Cobalt/aluminium nanoalloys with different molar Co/Al ratios were synthesized via microwave-induced decomposition of different organometallic precursors in [BMIm]NTf_2. Dual-source precursor routes were followed by reacting dicobalt octacarbonyl ($Co_2(CO)_8$) and pentamethylcyclopentadienyl aluminum ($[AlCp^*]_4$), as well as Co amidinate ($[Co(^iPr_2\text{-MeAMD})_2]$) and Al amidinate ($[Me_2Al(^iPr_2\text{-MeAMD})]$). While none of the methods resulted in phase-pure Co/Al NPs, the first combination yielded CoAl NPs with a molar Co/Al ratio of 1:1 and a size of 3 nm. The second reaction using 1:1 and 3:1 ratios afforded CoAl and Co_3Al NPs with an average diameter of 3 and 2 nm, respectively. After characterization with TEM, EDX, SAED, STEM and XPS, the Co/Al nanoalloys were investigated as potential non-noble catalysts in hydrogenation reactions. The Co/Al NPs showed a higher catalytic activity in the hydrogenation of phenylacetylene, compared to monometallic Co NPs, with a without the addition of an activating co-catalyst.

Contributions to the work:

- TEM, STEM and SAED measurements of the NP samples (Figure 26, as well as Figures S8, S9, S12, S15, S18, S19, S21, S22, S24 and S27 in reference 257).
- EDX spectroscopy analysis including spectra generation and elemental mapping (Figure 27, as well as Figures S10, S13, S16, S20, S23, S25, S26 and S28 in reference 257).
- Review and correction of the final manuscript as co-author.

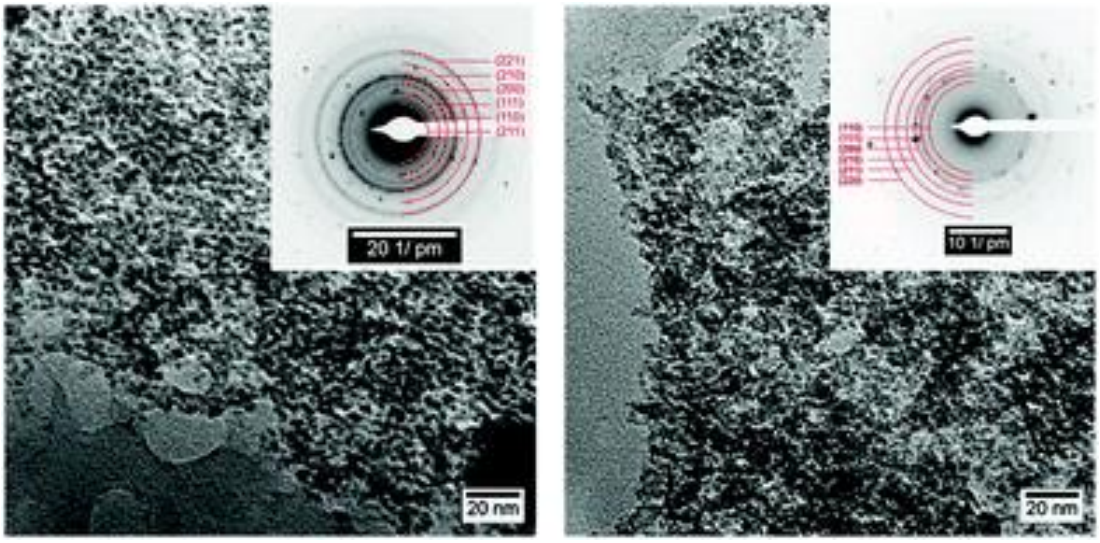

Figure 26. TEM images and SAEDs of fcc CoAl (left) and fcc Co_3Al NPs (right) from the reaction of [Co(^{i}Pr2-MeAMD)$_2$] and [$Me_2Al(^iPr_2$-MeAMD)] in [BMIm]NTf_2.

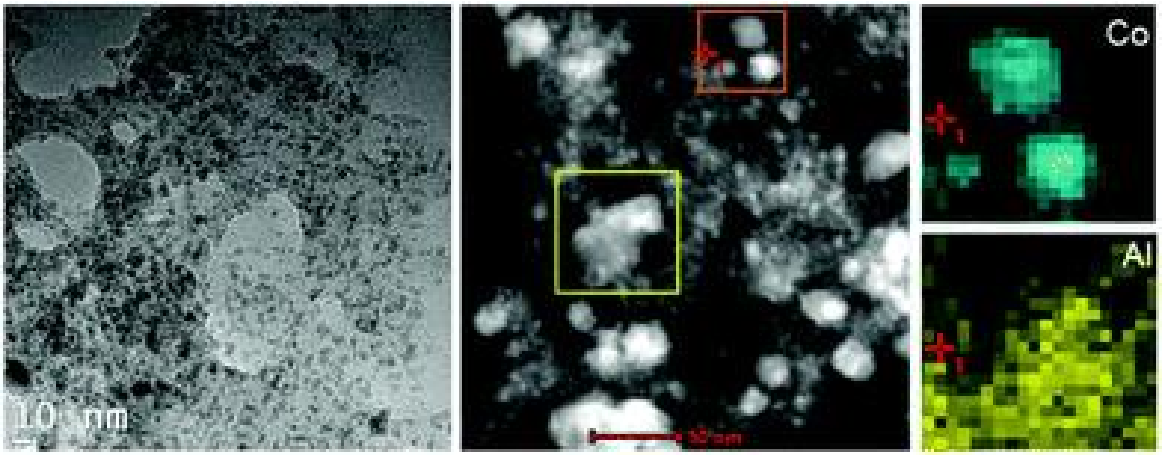

Figure 27. TEM image (left), STEM image (middle) and EDX mapping (right) showing cobalt (green) and aluminum (yellow) of the NPs obtained from the $Co_2(CO)_8$ and $[AlCp^*]_4$ decomposition in [BMIm]NTf_2. Elemental maps were acquired from the area marked by the orange window and using the yellow window as reference.

4. Additional Results

In this chapter, further results which have not yet been published in scientific journals will be described. These experiments were conducted as complementary studies and side projects during this dissertation.

4.1. Synthesis and Surface Modification of Au NPs

4.1.1. Au NPs with thiol-terminated polyethylenimine (Au-ThioPEI)

Given the known affinity of sulfur for gold, the surface functionalization of Au NPs with a thiol-containing capping ligand could bring additional advantages for the synthesis of Au nanomaterials. Compared to using a “sulfur-free” ligand, a thiolation would result in a stronger bond between the surface coating and the Au NP (see chapter 1.3.1). Therefore, after exploring the great stabilization potential of the PEI polymer for Au NPs in chapter 3.1, a ThioPEI ligand was synthesized according to Figure 28:

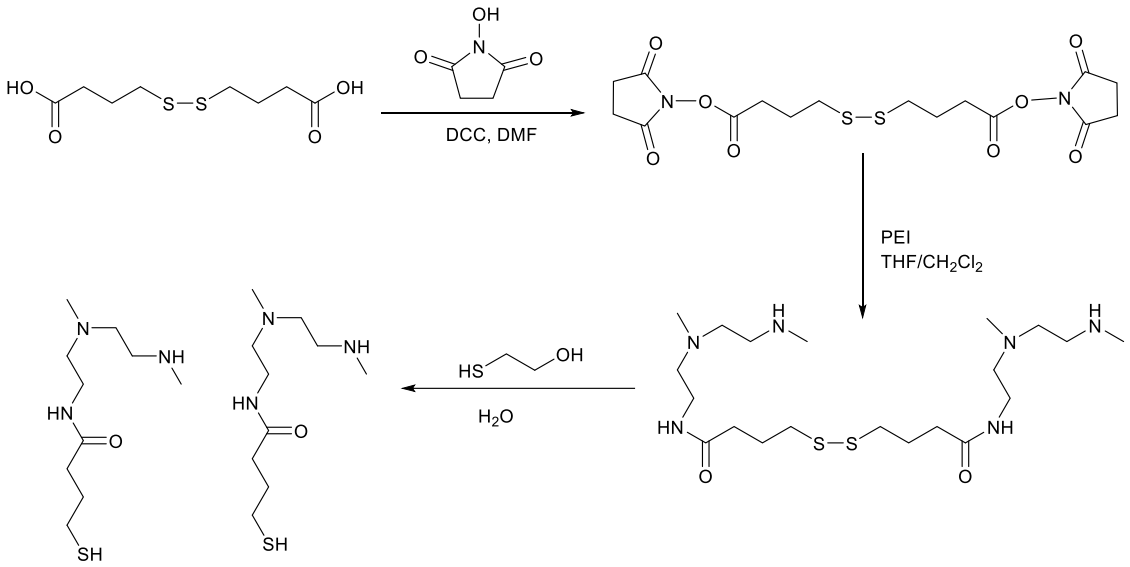

Figure 28. Synthesis of ThioPEI, modified from the route described by *Thomas et al.*[258] DCC: N,N′-Dicyclohexylcarbodiimide, DMF: dimethylformamide, PEI: polyethylenimine (displayed with simplified polymeric chains), THF: tetrahydrofuran.

The product ThioPEI was analyzed by ^{1}H-NMR spectroscopy, as shown in Figure 29. Both methylene protons from PEI (**7** in Figure 29) were located at 3.8 ppm, as well as the ones next to the carbonyl group (**9** in Figure 29) at 3.6 ppm, which formed a triplet. Protons from the CH_2 groups (**3** and **4** in Figure 29) overlap at 3.0 ppm, as well as those adjacent to the thiol group (**9** in Figure 29). Singlets expected for the methyl protons of PEI (**1** and **5** in Figure 29) also overlap in a large multiplet starting at 2.9 ppm. Even though large residual solvent signals from dimethylformamide used in the reaction were still present in the solution, the spectrum shows characteristic peaks corresponding to ThioPEI. For a more accurate NMR characterization of ThioPEI, additional efforts in sample preparation are needed, preferably accompanied by mass spectral analysis.

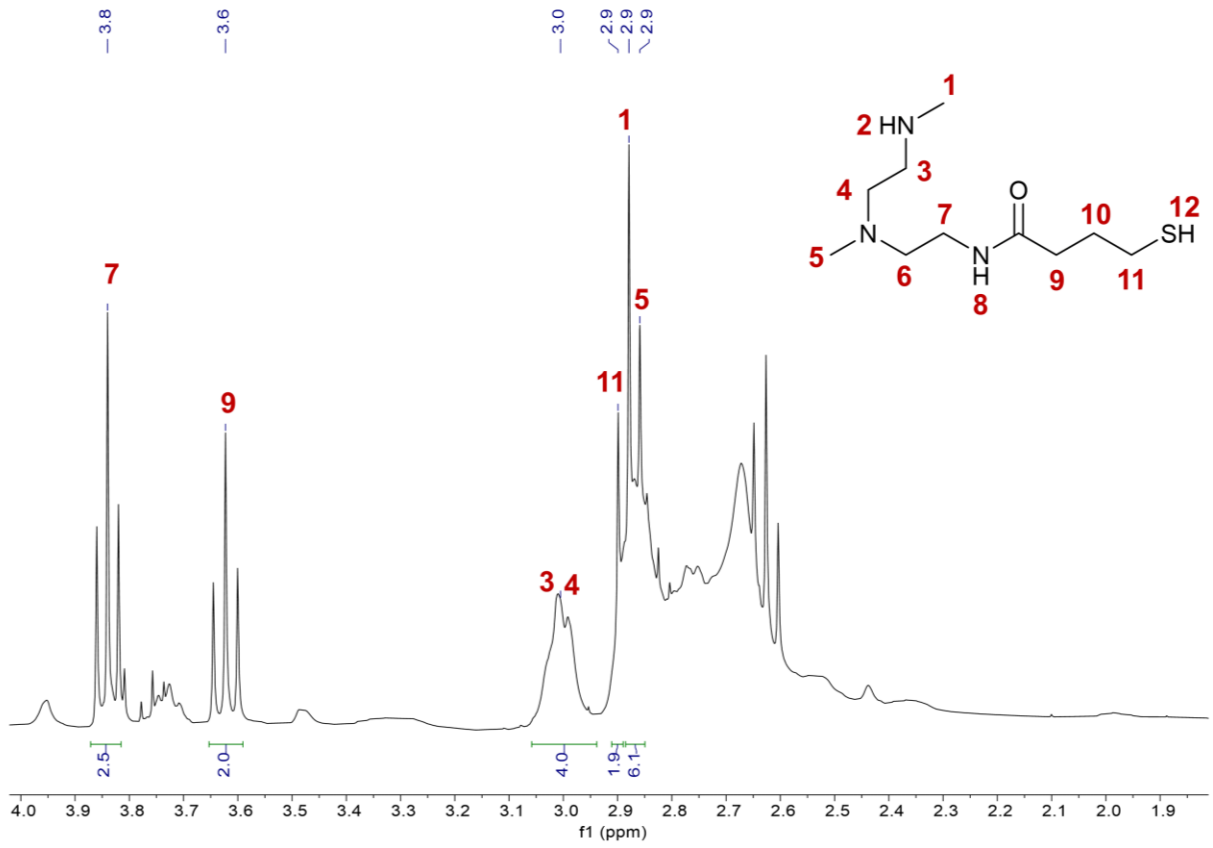

Figure 29. ^{1}H-NMR spectrum of ThioPEI in D_2O.

The ThioPEI ligand was used to synthesize Au NPs by reduction of the $KAuCl_4$ salt with $NaBH_4$:

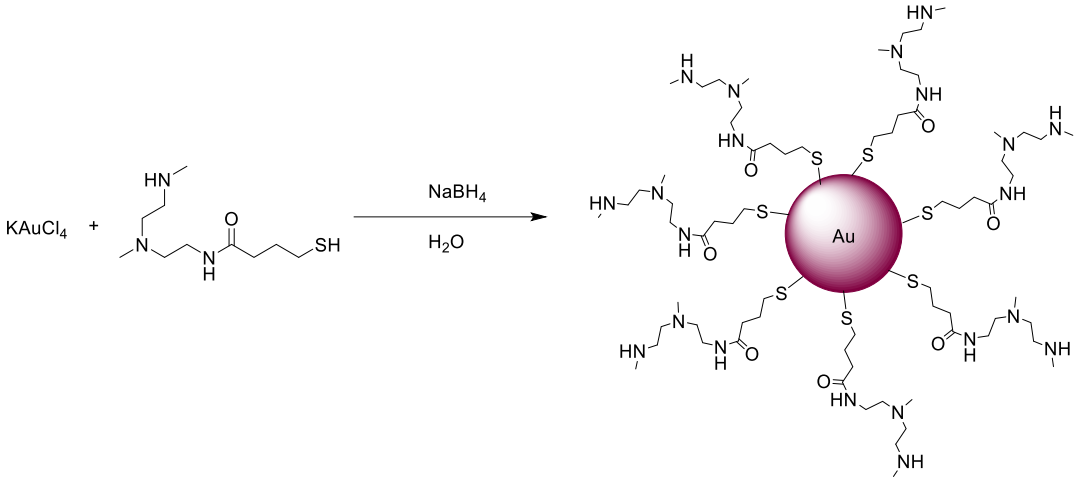

Figure 30. Synthesis of Au-ThioPEI NPs.

TEM investigations of the product from Figure 30 revealed the formation of spheric Au-ThioPEI NPs with a monodisperse distribution and an average size of 12 ± 3 nm (Figure 31a, b). DLS measurements showed a hydrodynamic diameter of approximately 21 nm for AuThioPEI NPs (Figure 31c).

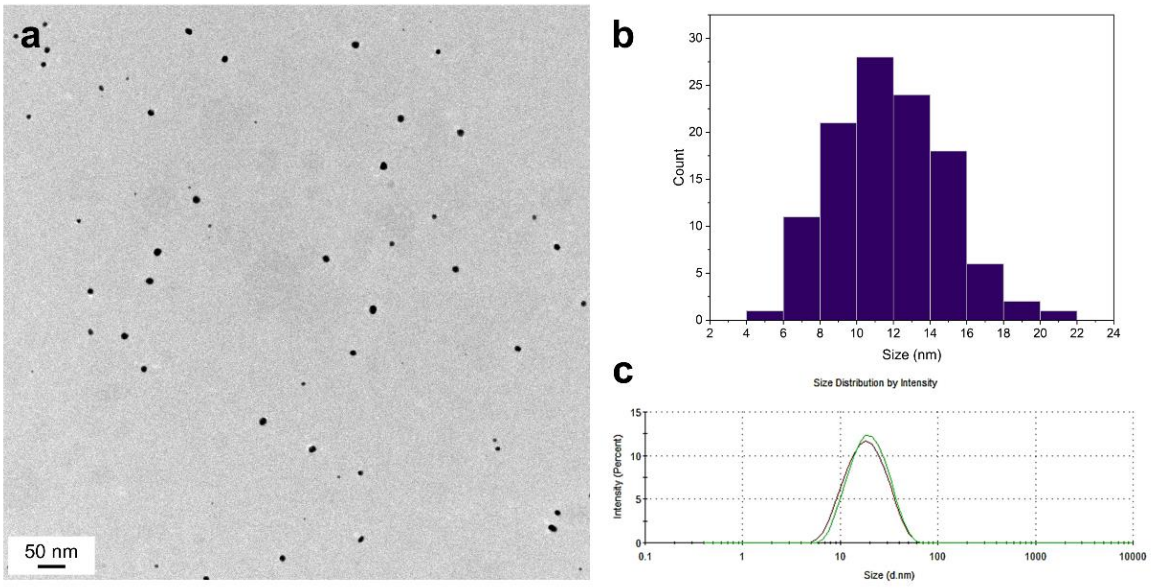

Figure 31. TEM image (a), size distribution (b) and DLS measurements (c) of Au-ThioPEI NPs.

4.1.2. Au NPs with polyethylene glycol (Au-PEG)

The polymer polyethylene glycol (PEG) is also widely used as a Au NP capping ligand in biotechnology applications to enhance their stability and water solubility. PEG is non-toxic, biocompatible and can provide a longer blood circulation time of NPs, thus improving their cell internalization potential.[259] Thus, Au NPs coated with PEG were synthesized both using a “one-pot” method or by a post-synthetic modification of citrate capped NPs.

In the first approach, $KAuCl_4$ was reduced with sodium citrate and combined with PEG in a microwave-assisted reaction, yielding spheric Au NPs with a core size of 9 ± 1 nm and a hydrodynamic diameter of approximately 34 nm (Figure 32). DLS measurements additionally showed a formation of agglomerates with sizes over 1000 nm (Figure 32c).

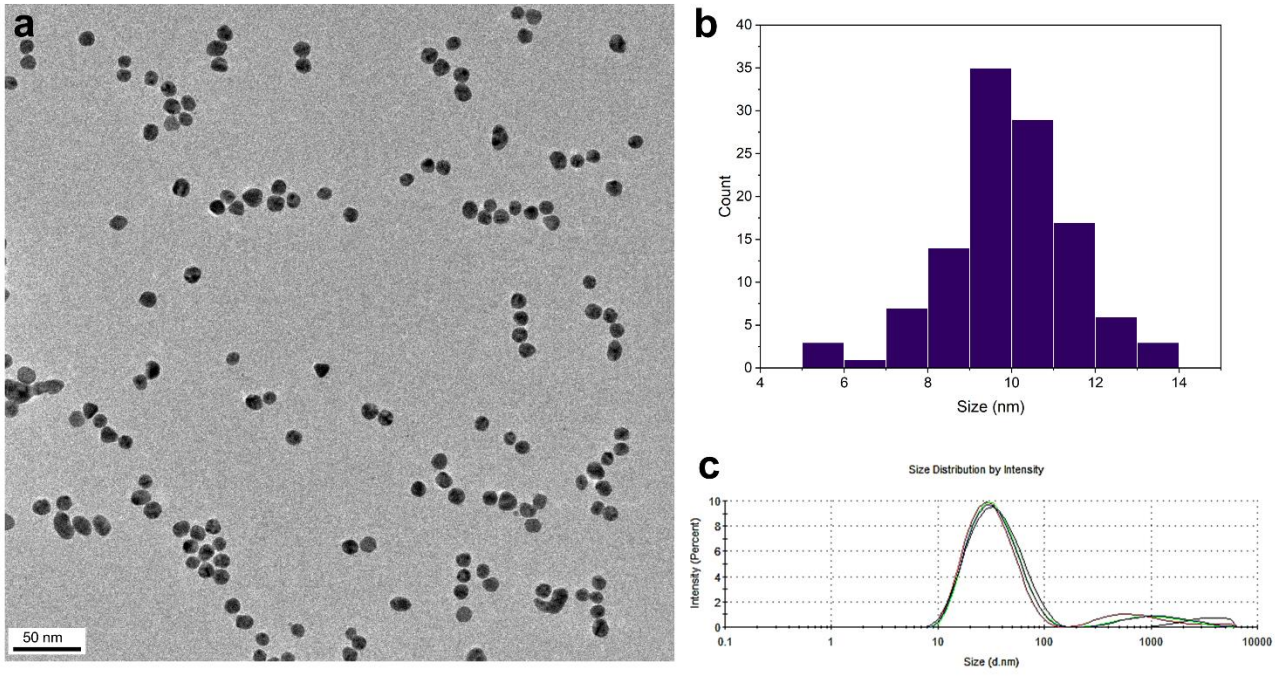

Figure 32. TEM image (a), size distribution (b) and DLS measurements (c) of Au-PEG NPs via "one-pot" synthesis.

For the second approach, Au-Citrate NPs with a core size of 15 ± 2 nm and a diameter of 24 nm were synthesized according to the *Turkevich* method[54] (Figure 33). UV-VIS spectra of Au-Citrate NPs revealed an absorbance at 520 nm, corresponding to the characteristic surface plasmon peak (SPR) of Au NPs (Figure 33d).

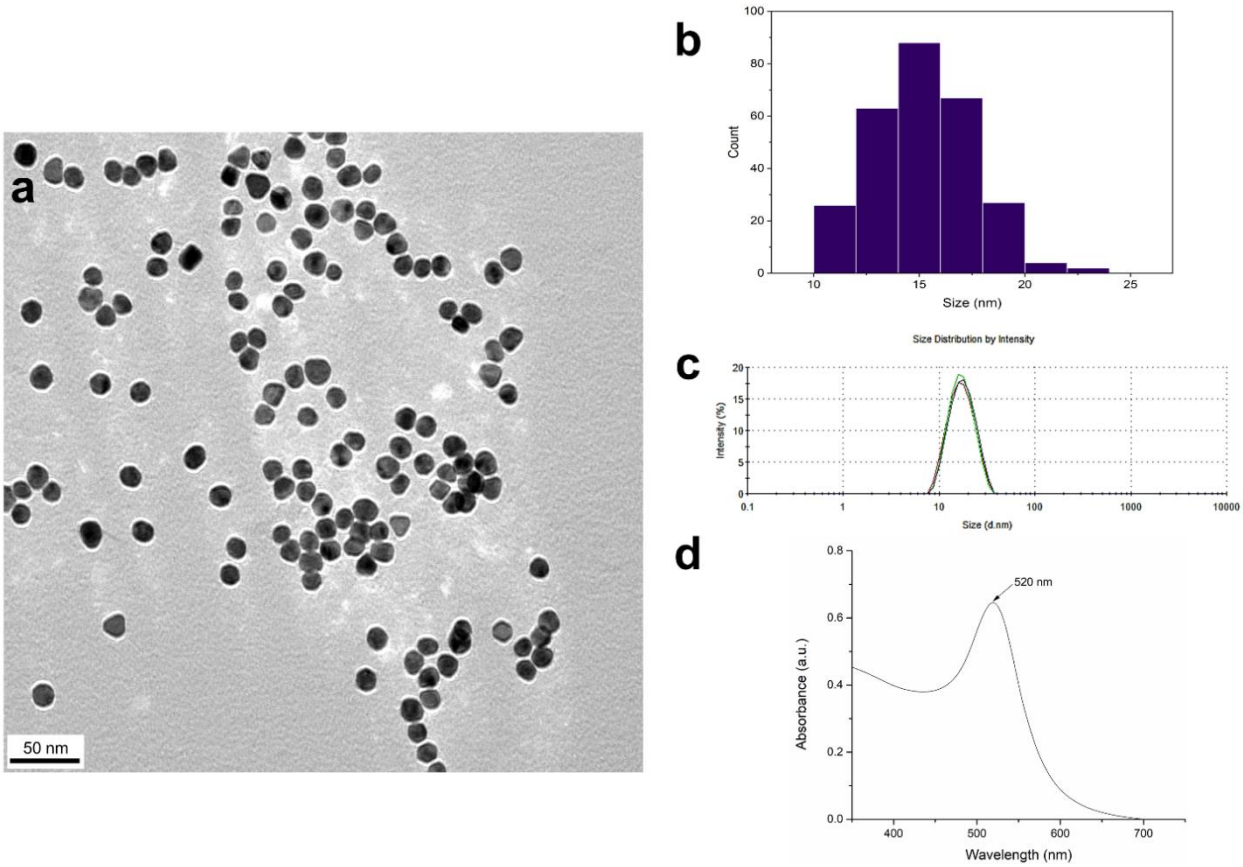

Figure 33. TEM image (a), size distribution (b), DLS measurements (c) and UV-VIS spectrum (d) of Au-Citrate NPs.

In order to confirm the PEGylation of Au-citrate NPs, their hydrodynamic diameter, zeta potential and UV-VIS absorbance was studied before and after reaction with PEG. As Table 1 displays, the overall size of Au-citrate NPs significantly increased after reaction with the PEG polymer from 24 to 296 nm. Moreover, the negative surface charge of citrate slightly decreased after PEGylation, while the SPR peak of Au-PEG NPs remained similar to that of Au-citrate NPs, according to UV-VIS measurements. Although both the “one-pot” and two-step method can be used for synthesis of Au-PEG NPs with sizes between 9 and 15 nm, additional purification steps are needed to separate agglomerates and unreacted polymers from the final NP solution.

Table 1. DLS, zeta potential and UV-VIS spectra comparison of Au-citrate and Au-PEG NPs synthesized using the two-step method.

	Au-citrate NPs	Au-PEG NPs
Hydrodynamic Diameter (nm)	24	296
Zeta Potential (mV)	-45	-38
SPR peak (nm)	520	521

4.1.3. Au NPs with thiol-terminated polyethylene glycol (Au-ThioPEG)

The *in-situ* formation of Au NPs coated by a thiol-functionalized PEG polymer was attempted based on the synthesis route published by *Joh et al*.[260] Through reduction of $KAuCl_4$ with sodium citrate in the presence of methoxy-terminated PEG thiol, Au NPs of two different sizes (31 ± 7 nm and 8 ± 2 nm) were formed as seen in Figure 34. The presence of the two separate NP species was also evident through DLS measurements in solution, with sizes of approximately 3 nm and 68 nm.

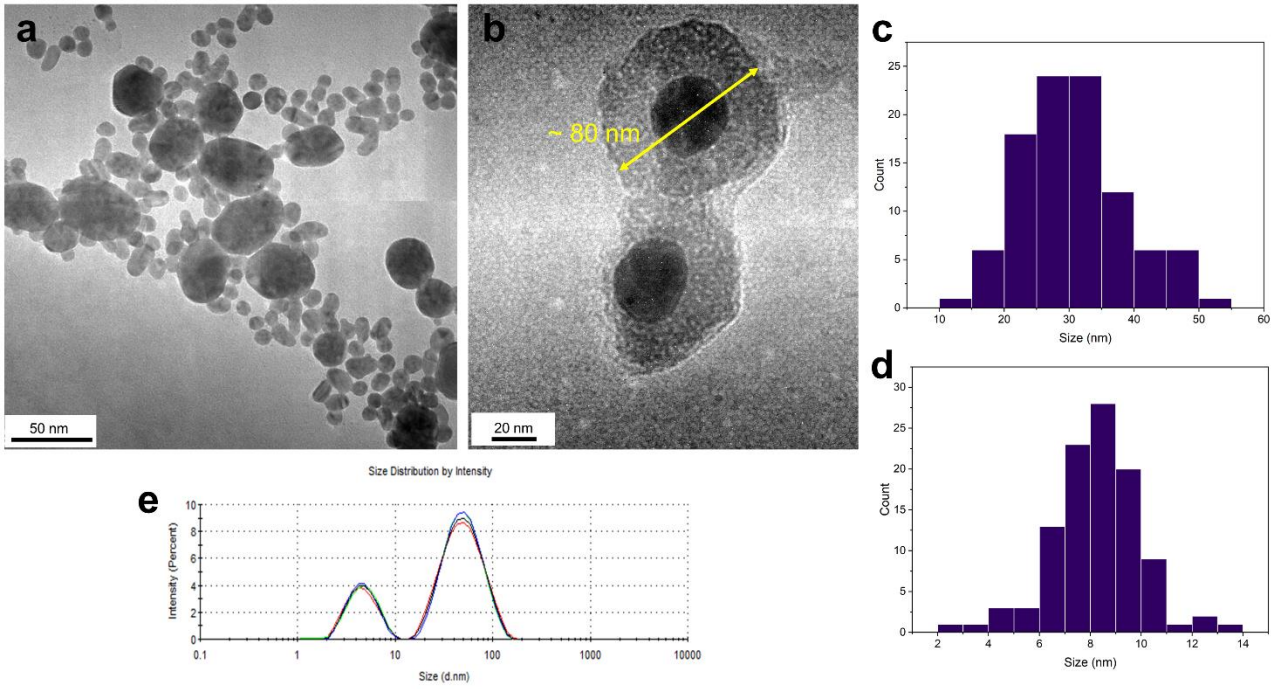

Figure 34. TEM images (a, b), size distribution (c, d) and DLS measurements (d) of Au-ThioPEG NPs.

While organic surface coatings are generally not visible from TEM measurements at 200 kV, an HR-TEM image made of two isolated Au-ThioPEG NPs (Figure 34b) was able to capture the Au cores of ~ 31 nm NPs surrounded by polymer shells. Using this image, the diameter of the core and ligand, was estimated to be approximately 80 nm, in agreement with DLS measurements made of the Au-ThioPEG NP solution. Hence, it can be possible to capture a glimpse of the surface of Au NPs by using the appropriate high-resolution electron microscope and a fast handling when acquiring the image. This allows further understanding of the NP nature without compromising the image resolution of the metal core by lowering the electron current of the microscope.

4.1.4. Au NPs with thiol-terminated polyethylene glycol and polyethylenimine (Au-PEI-ThioPEG)

To combine the advantages of using both PEI and PEG polymers, Au-PEI NPs (see AuPEI6 in publication from chapter 3.1) were reacted with methoxy PEG thiol in aqueous medium (Figure 35). After purification using dialysis, at least two different sized NP species were detected in DLS measurements. The average NP core size was 5 ± 1 nm, similar to AuPEI6 NPs.

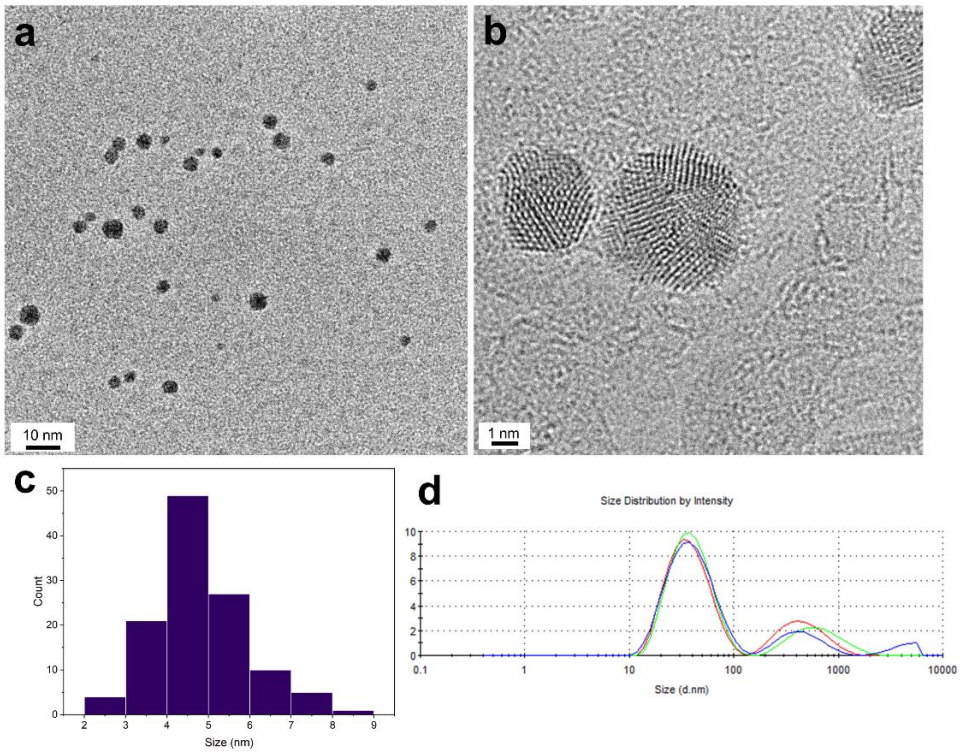

Figure 35. TEM images (a, b), size distribution (c) and DLS measurements (d) of Au-PEI-ThioPEG NPs.

4.1.5. Au NPs with polyethylenimine and fluorescein isothiocyanate (Au-PEI-FITC)

Further TEM studies of Au-PEI NPs functionalized with fluorescein isothiocyanate (AuPEI-FITC2 in publication from chapter 3.1) revealed the formation of unique leaf-like structures after the NP solution is dropped onto the copper carbon grid (Figure 36a). This network is most likely formed due to the interaction of FITC with the polymer and does not affect the size or agglomeration degree of the AuPEI-FITC NPs, compared to their size prior to the reaction with FITC (Figure 36, Fig. 5b from publication in chapter 3.1). While most NPs were found embedded into the network (Figure 36b), some “free” particles are visible in Figure 36c.

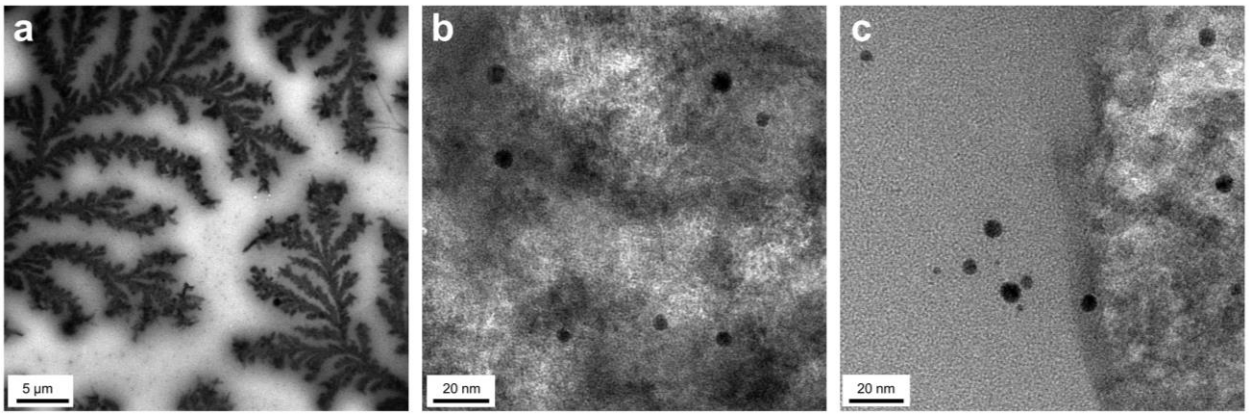

Figure 36. TEM images of Au-PEI-FITC NPs.

4.1.6. Au Nanorods

Besides spherical particles, Au nanomaterials with a rod-like morphology have also been exploited in the fields of biodiagnostics and photothermal therapy due to their additional surface plasmon resonance (SPR) in longitudinal mode.[261] This second resonance occurring at longer wavelengths than the transverse signal due to electron oscillation in the length direction of the rod may enhance the extinction coefficient and light absorption of the material, compared to that of Au nanospheres with a single SPR at ~520 nm.[262,263]

Au nanorods (Au-NRs) were synthesized with cetyltrimethylammonium bromide (CTAB) using seed-mediated growth *via* underpotential deposition with Ag^+ (Figure 37).[264]

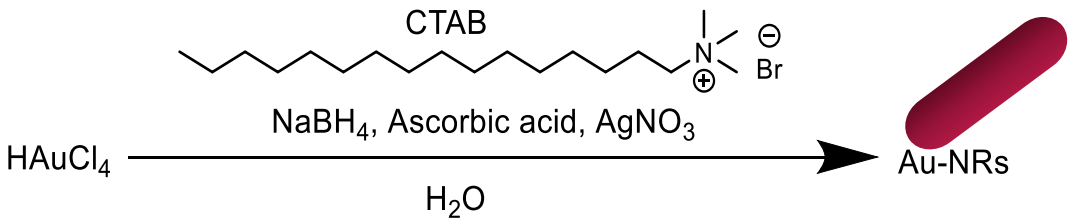

Figure 37. Synthesis reaction of Au-NRs.

After UV-VIS analysis of the solution, the transversal absorbance maximum was found at 536 nm and the longitudinal at 745 nm, which corresponds to an Au-NR length of approximately 50 nm[265] (Figure 38). Besides these two expected signals, an additional absorbance was detected at 580 nm, which could mean a possible formation of further morphologies such as Au spheres, cubes or prisms.[266] Thus, TEM studies and optimization of the reaction parameters are needed before using these Au-NRs in further applications.

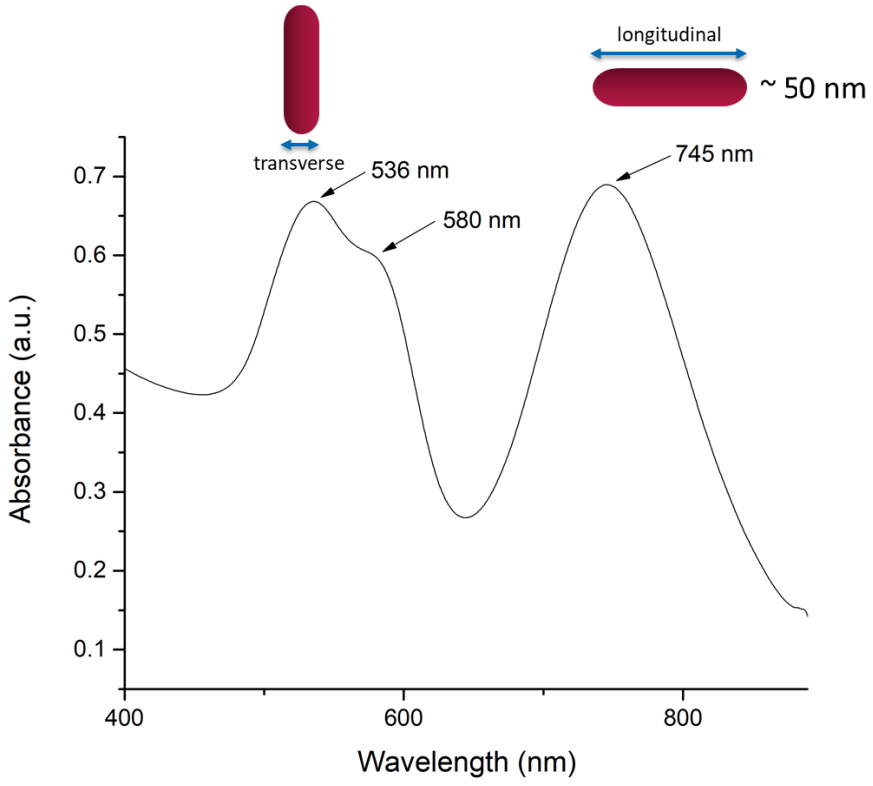

Figure 38. UV-VIS spectrum of Au-NRs.

4.2. Au NPs as Gene Carriers

Due to its high cationic charge density, PEI is an ideal capping ligand to attach negatively charged nucleic acids on the surface of Au NPs (see chapter 1.4.3.1.2.). This ability to bind DNA molecules through electrostatic interactions was studied using Au-PEI NPs (AuPEI6 in publication from chapter 3.1) and a plasmid containing a green fluorescent protein (GFP) (Figure 39). If attached to Au, this protein can be used as a reporter gene to monitor the successful NP transfection into eukaryotic cells, as it can be easily identified and measured through fluorescence assays after exposure to blue UV light.[267] Additionally, the use of NPs as transfection agents can overcome the disadvantages of other gene carriers such as their increased cytotoxicity, non-special interaction and aggregation in cells.[268,269]

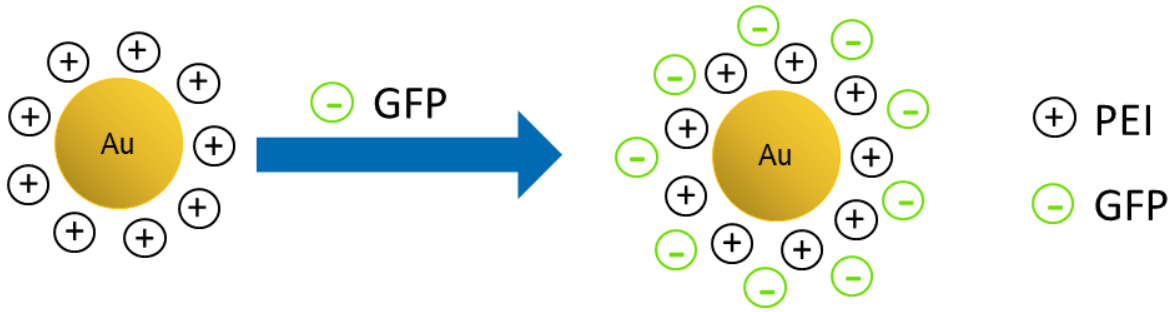

Figure 39. Schematic representation of the attachment of a GFP plasmid on the surface of Au-PEI NPs through electrostatic interactions.

Experiments were done combining Au-PEI NPs and GFP at weight ratios w(AuPEI):w(GFP) 4:1, 3:1 and 2:1. After purification via centrifugation, the AuPEI-GFP products were subjected to zeta potential measurements (Figure 40). As expected, the surface charge of the buffered Au-PEI control (Figure 40, black bar) changed from positive to negative after reaction with the plasmid, signalizing a successful GFP attachment to the NP surface. The increase of negative charge was proportional to the amount of GFP added to the sample, as seen for the 2:1 NPs (Au-PEI-GFP2) with the highest negative surface charge of -17 mV (Figure 40, purple bar). The size and morphology of the Au-PEI-GFP2 NPs was investigated with TEM analysis, which showed an increase in sizes from 4 ± 1 nm (Au-PEI NPs) to 16 ± 3 nm after addition of GFP to the Au solution (Figure 41). This increase was also evident by a color change of the solution from light red to purple (Figure 41c).

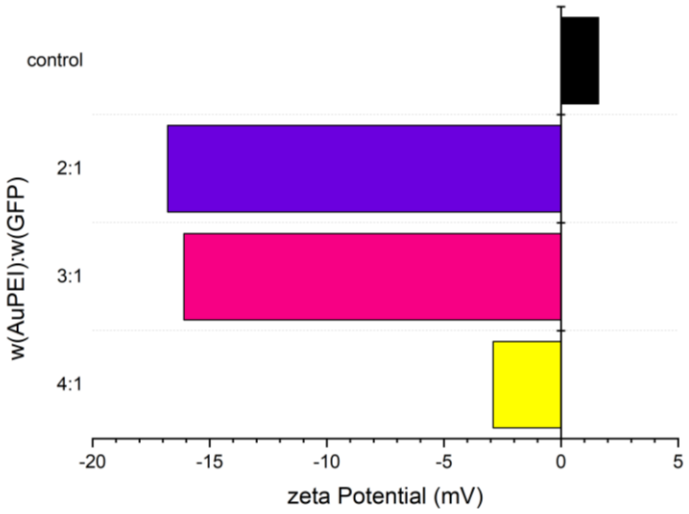

Figure 40. Zeta potential measurements of Au-PEI NPs (control) and Au-PEI-GFP NPs at different ratios.

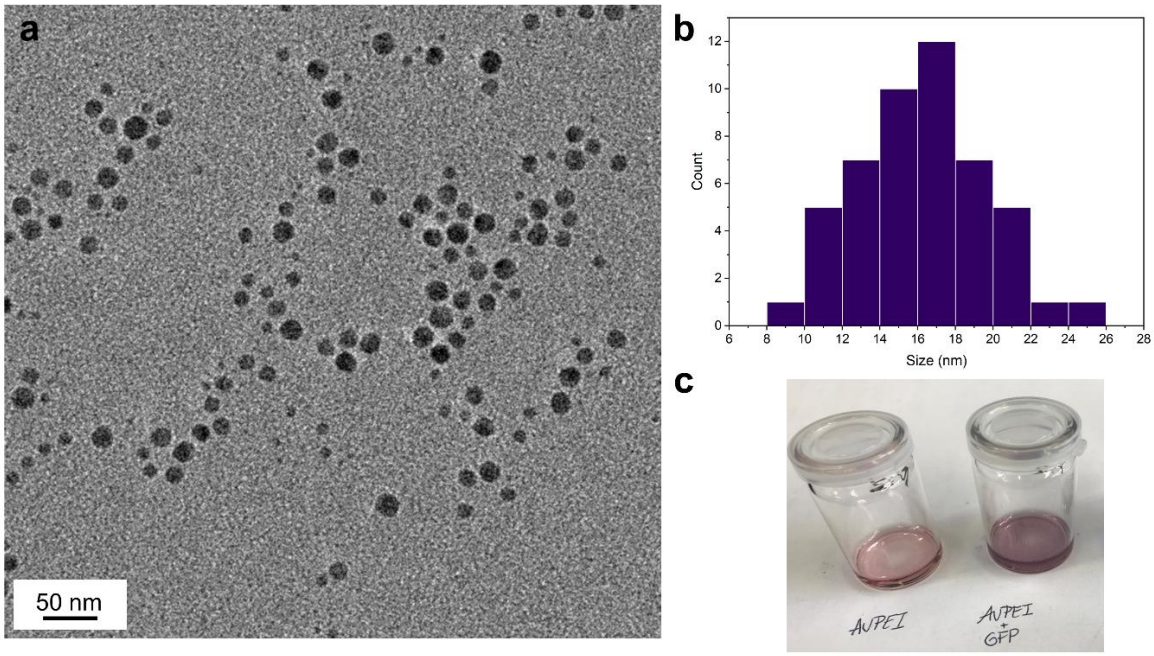

Figure 41. TEM image (a) and size distribution of Au-PEI-GFP2 NPs (b). Color change of Au-PEI NPs after addition of GFP (c).

The transfection of the AuPEI-GFP2 NPs into GSCS was investigated by incubation in different cell lines, followed by a qualitative analysis using bright-field and fluorescence microscopy (Figure 42). Results summarized in Table 2 reveal that a successful transfection of Au-PEI-GFP2 NPs - visible by a fluorescent signal inside the cells - is dependant on the cell line used. Although Au-

PEI-GFP2 NPs are transfected into most cell types, (BTSC)407 cells show almost no effect after treatment with NPs. Similar observations were made when the (BTSC)407 cell line was treated with AuPEI-FITC and AuPVA NPs (publications from chapters 3.1 and 3.2).

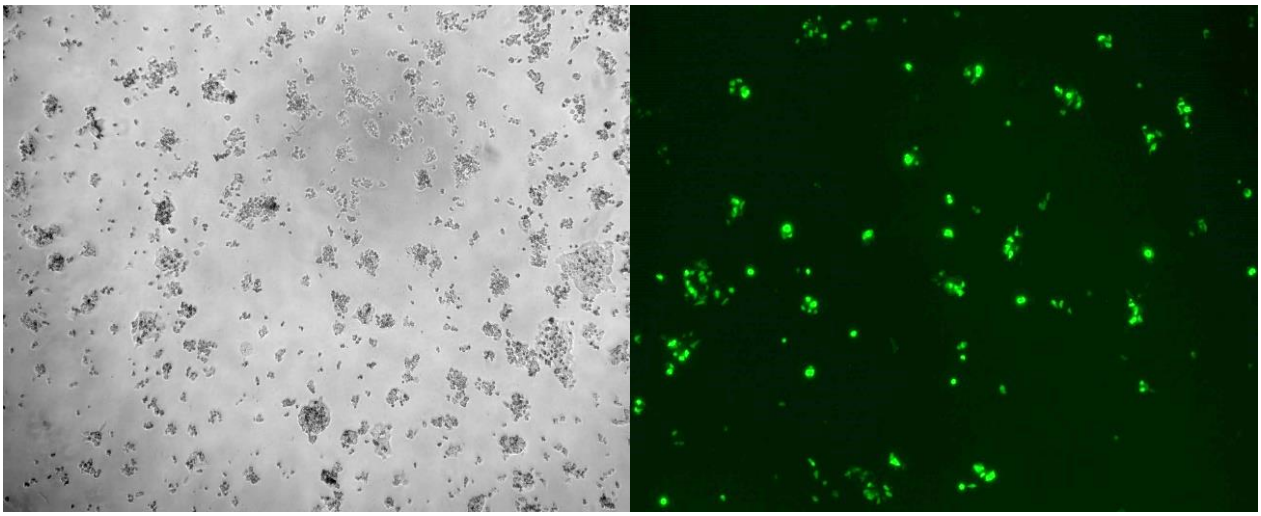

Figure 42. Bright-field (left) and fluorescent microscopic images (right) of HEK cells incubated with AuPEI-GFP2 NPs.

Because a negative surface charge of the NPs can result in low cellular uptake in GSCs, functionalization with an additional capping ligand (*e.g.* PEG or SiO_2) should be performed on Au-PEI-GFP NPs to obtain an optimal "weakly positive" surface. Furthermore, the incorporation of a specific receptor-mediated binding should enhance the internalization and transfection of AuPEI-GFP NPs.[269]

Table 2. Qualitative studies indicating transfection of Au-PEI-GFP2 NPs into cells based on visible fluorescence under the microscope. Green tick: fluorescence signal was detected, red ex: no fluorescence visible.

Cell line	**HEK**	**JHH520**	**RAV19**	**233**	**Sf188**	**BTSC407**
Visible fluorescence	✓	✓	✓	x	✓	x

4.3. Au-Cyclodextrin NPs for Drug Delivery

As stated in chapter 1.4.3.1, host-guest system such as cyclodextrins can be combined with NPs to efficiently attach and release water insoluble drugs in a non-covalent matter. To this end, an *in situ* Au NPs formation and simultaneous functionalization with cyclodextrin was attempted based on five different synthesis routes described in the literature.[270-273] The synthesis parameters used for each reaction and results of DLS measurements are displayed in Table 3. For all reactions, $KAuCl_4$ was used instead of chloroauric acid ($HAuCl_4$), as a more affordable solid precursor. From all synthesis methods, the reduction of $KAuCl_4$ using $NaBH_4$, based on the work of *Brugnerotto et al*.[272] yielded the most monodisperse solution with a single NP species of approximately 159 nm (Table 3, entry 3). The other NP solutions (Table 3, entries 1, 2, 4 and 5) presented two or three different sized NPs, most likely due to the effect of the parameter changes made on the final result, and were not used for further applications.

Table 3. Synthesis of cyclodextrin-modified Au NPs. Size and size distribution were determined via DLS measurements of aqueous solutions after purification.

Entry	Reaction parameters	Size (nm)	Size distribution y scale: Intensity (%), x scale: Size (nm)
1	$KAuCl_4$ —(ß-Cyclodextrin, pH 7.4; H_2O, 100°C, 30 min)→ Au-Cyclodextrin NPs	66, 263	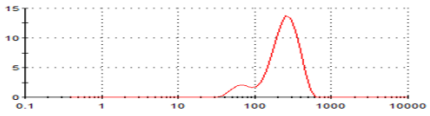
2	$KAuCl_4$ —(ß-Cyclodextrin, NaOH; H_2O, 70°C, 20 min)→ Au-Cyclodextrin NPs	12, 61, 246	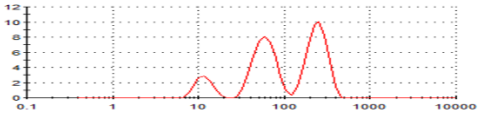
3	$KAuCl_4$ —(ß-Cyclodextrin, $NaBH_4$; H_2O, rt, 12h)→ Au-Cyclodextrin NPs	159	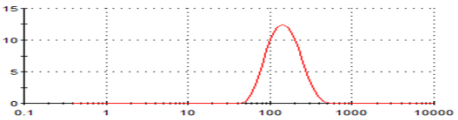
4	$KAuCl_4$ —(ß-Cyclodextrin, Na-Citrate; H_2O, 100°C, 1 h)→ Au-Cyclodextrin NPs	330, 5062	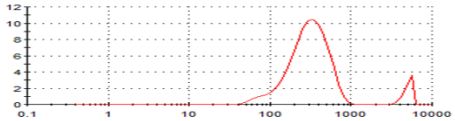
5	$KAuCl_4$ —(ß-Cyclodextrin, $NaBH_4$; H_2O, rt, 18h)→ Au-Cyclodextrin NPs	43, 205, 5662	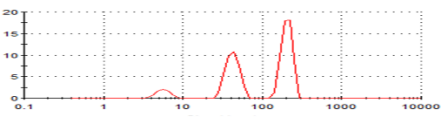

The most monodisperse Au-Cyclodextrin NPs (Table 3, entry 3) were examined with TEM analysis, which showed the formation of flower-like Au nanostructures of approximately

60 ± 16 nm (Figure 43), instead of the expected spherical morphology. To test their ability as drug delivery probes, these nanostructures were later reacted with the GLS1 inhibitor CB839 (see section 1.6.2). In accordance with the method described in the publication in chapter 3.2, the unreacted drug was separated from the NP-drug product using centrifugation and the amount of CB839 in the supernatant was quantified using HPLC. As Figure 44 shows, the HPLC chromatogram of the supernatant from the reaction of Au-Cyclodextrin NPs with CB839 displayed the peak corresponding to CB839 after a retention time of 9 min, as seen for Au-polymer NPs (chapter 3.2). Additionally, a new peak of lower intensity was found after 12 min. A possible explanation for this new detected signal may be that the cyclodextrin-CB839 complex can detach from the Au "nanoflower" and is collected in the supernatant after centrifugation. However, further studies are needed to identify the substance detected at 12 min and prove this hypothesis.

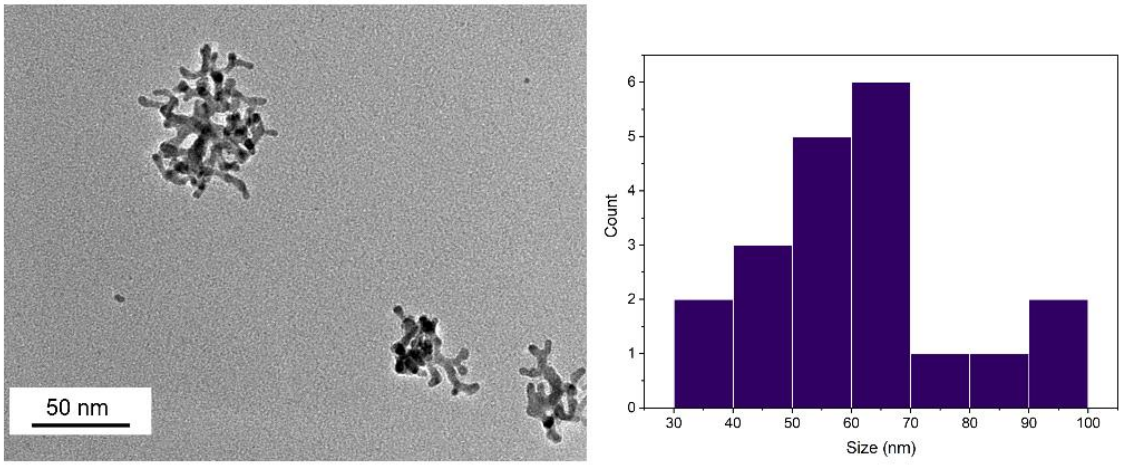

Figure 43. TEM image and size distribution of Au-Cyclodextrin nanostructures.

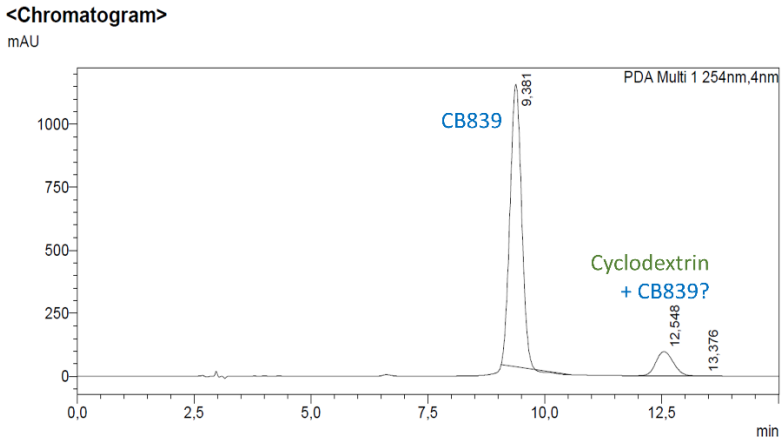

Figure 44. HPLC chromatogram of the supernatant of the reaction of Au-Cyclodextrin NPs and CB839.

With the purpose of forming a stronger bond between Au NPs and cyclodextrin, a thiol function was incorporated to the latter by replacing its terminal -OH groups with -SH ones (Figure 45).

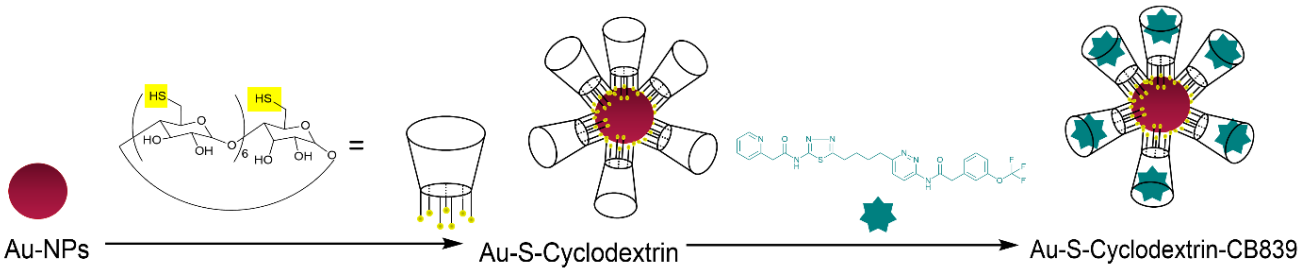

Figure 45. Schematic representation of Au NPs functionalized with thio-cyclodextrins for delivery of CB839.

Furthermore, pre-formed Au NPs of known stability and drug loading capacity can be employed in a ligand combination strategy to increase the loading efficiency of the nanocarrier. This approach was tested using AuPVA NPs, which were able to load the highest amount of CB839 on its surface of all Au-polymer NPs tested (see publication, chapter 3.2). After the reaction of AuPVA NPs with heptakis(6-deoxy-6-thio)-β-cyclodextrin (SH-cyclodextrin, resulting in AuPVA-S-Cyclodextrin NPs), the NP size increased from 21 to 290 nm, which was visible from the solution color change from red to deep purple (Figure 46 a,b). After measuring the absorbance of CB839 at the same concentration used for the synthesis of AuPVA-S-Cyclodextrin-CB839 NPs and that of the supernatant collected, the drug loading efficiency was estimated to be around 60% (Figure 46c, for calculation details see publication, chapter 3.2). While repetitions and additional analysis using HPLC are needed for an exact quantification, this value represents the potential of ligand combination approaches to increase the drug loading capabilities of nanocarriers. Since the agglomeration state of NPs can have a significant effect on their reactivity and toxicity *in vivo* (see chapter 1.5.2), their dispersity and size have to be closely monitored after each functionalization step.

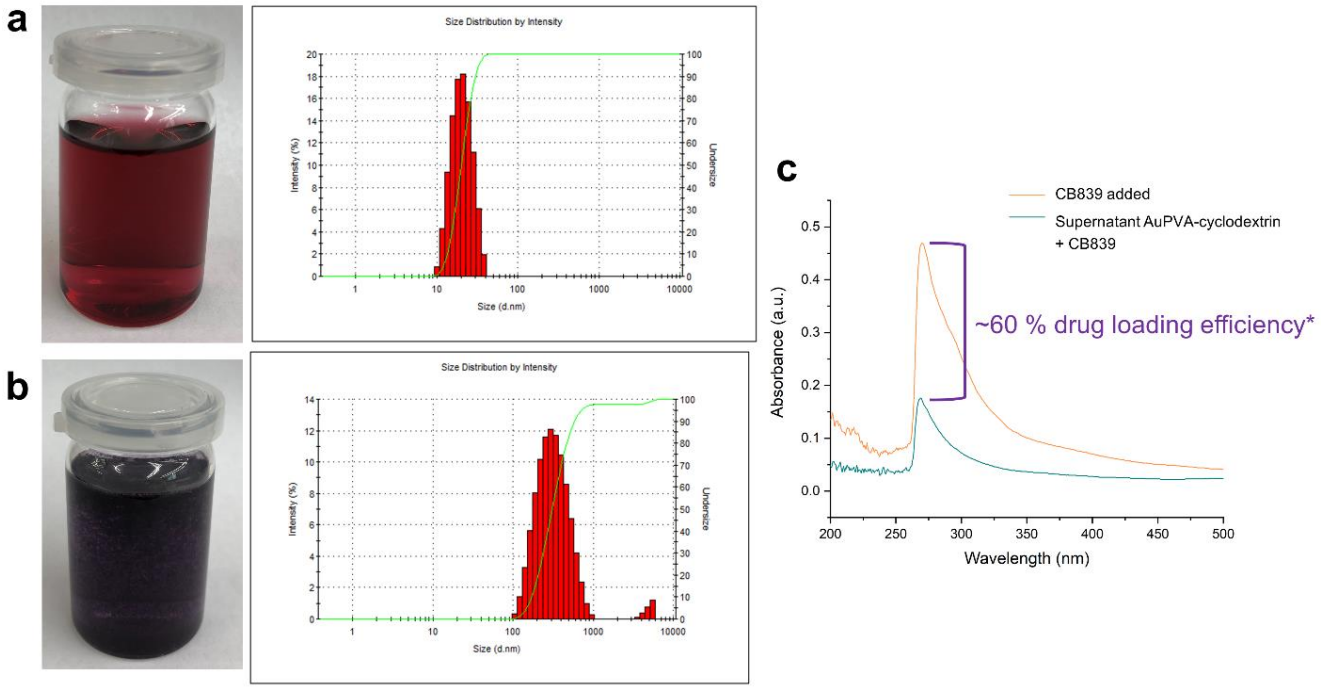

Figure 46. Reaction of AuPVA NPs with SH-Cyclodextrin and CB839. Solution and DLS size distribution of AuPVA NPs (a) and AuPVA-S-Cyclodextrin NPs (b). UV-VIS spectra of CB839 and of supernatant collected after reaction of AuPVA-S-Cyclodextrin NPs with CB839 (c). * Drug loading efficiency was estimated from the absorbance of the CB839 added to the reaction, compared to the absorbance of the supernatant.

4.4. Au NPs for Photodynamic Therapy

Photodynamic therapy, a promising minimally invasive strategy to treat cancer, consists of administering a photosensitive drug (also called photosensitizer) to tumor tissues, which are later destroyed through reactive oxygen species produced by irradiation with an external light source.[274] 5-Aminolevulinic acid (5-ALA) is an example of a photosensitizer widely used in clinical applications. Even though 5-ALA has good biocompatibility, its zwitterionic nature hinders efficient penetration into cell membranes and therefore a sufficient accumulation in tumors.[275] The use of 5-ALA-conjugated Au NPs have already demonstrated to specifically accumulate in tumor vasculature, resulting in an enhanced ROS formation and high destruction efficacy of cancer cells with minimal damage to healthy cells.[276]

Using the previously described AuPEI NPs (AuPEI6 in publication from chapter 3.1), 5-ALA can be immobilized on the surface of the positively charged nanocarriers using electrostatic interactions. Based on the synthesis published by *Oo et al.*,[276] 5-ALA was combined with AuPEI NPs at a concentration of 1 mmol/L in Dulbecco's Modified Eagle Medium (DMEM).

UV-VIS spectroscopy measurements (Figure 47) showed no apparent shift in the absorption peak of AuPEI NPs at 520 nm, and thus no NP agglomeration after conjugation with 5-ALA:

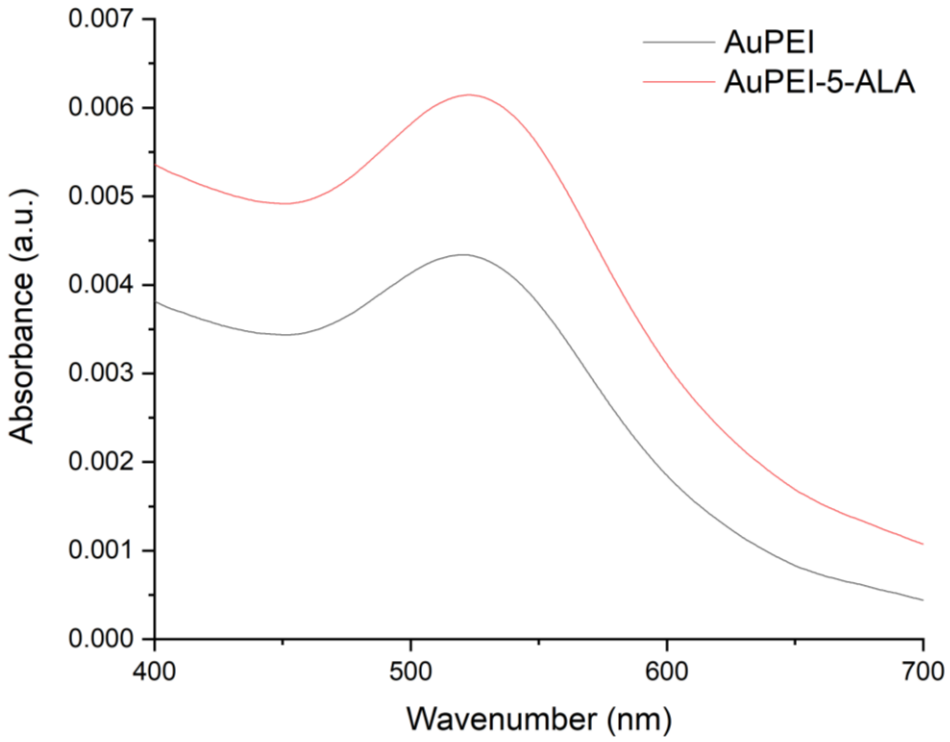

Figure 47. UV-VIS measurements of AuPEI (grey line) and AuPEI-5-ALA (red line) NPs.

DLS measurements of AuPEI in DMEM (Figure 48, red line) showed NPs of two different sizes, most likely corresponding to “bare” AuPEI NPs (smaller size of ~15 nm) and AuPEI NPs presenting an additional protein corona formed after the NPs come in contact with the different proteins contained in the medium[164](~ 83 nm). After conjugation with 5-ALA, the hydrodynamic diameter of AuPEI NPs increased from 83 nm to approximately 134 nm (Figure 48, green line), which speaks for a successful addition of 5-ALA to the gold surface.

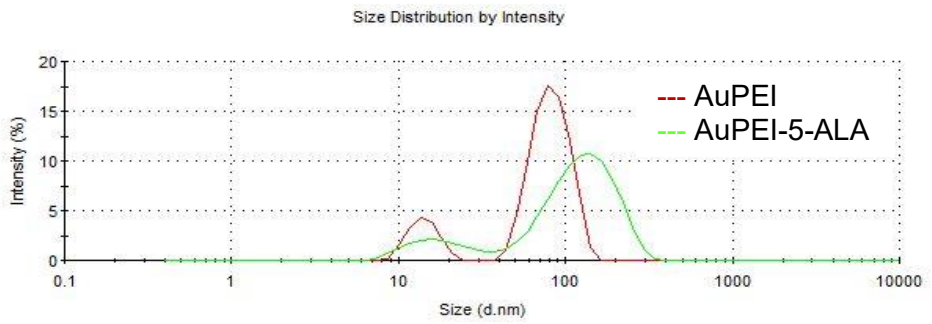

Figure 48. DLS measurements of AuPEI (red line) and AuPEI-5-ALA (green line) NPs.

TEM investigations of the AuPEI-5-ALA NPs revealed a slight size increase in some cases from the starting 4 ± 1 nm (AuPEI NPs) to an average of 7 ± 2 nm after reaction with 5-ALA (Figure 49). The functionalization of the Au nanospheres with a PEI-5-ALA surface shell was also visible in high resolution images (Figure 49b) of AuPEI-5-ALA NPs.

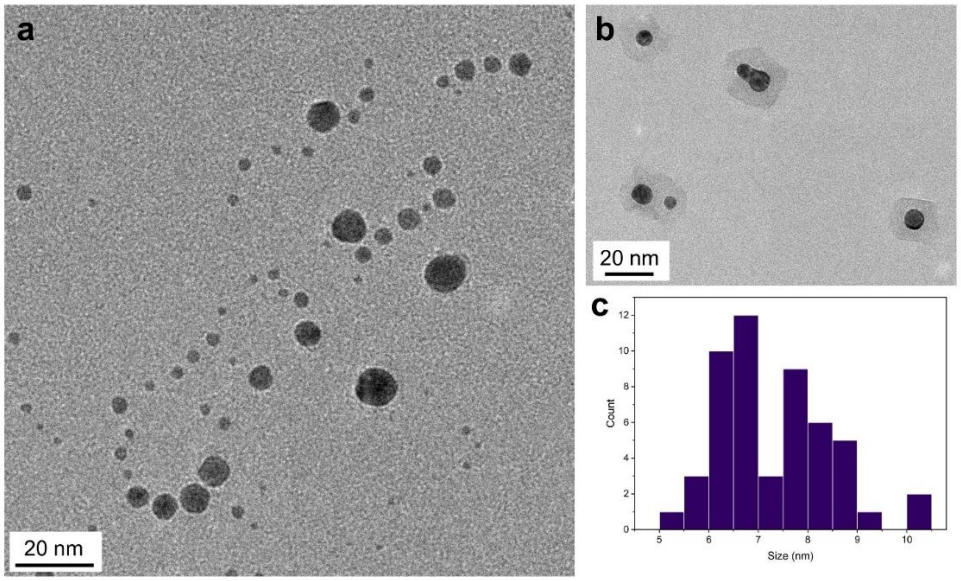

Figure 49. TEM images (a, b) and size distribution (c) of AuPEI-5-ALA NPs.

Experiments to test the effect of AuPEI-5-ALA NPs in combination with photodynamic therapy for the treatment of cancerous cells are underway.

4.5. Loading of Other Anticancer Drugs onto Au NPs

Besides loading of the GLS1 inhibitor CB839 onto Au NPs (publication in chapter 3.2), additional efforts were made to immobilize other anticancer therapeutic agents onto Au nanocarriers. Due to the favorable results involving the decrease of cell proliferation and migration mechanism in GB cells, experiments were conducted with the compounds known as MSAB and LGK974. Both molecules are inhibitors of the Wingless (Wnt) signaling pathway, which is thought to be responsible for promoting stem cell properties and resistance to both radio- and chemotherapy in GB.[277,278]

3-[[(4-Methylphenyl)sulfonyl]amino]-benzoic acid methyl ester (MSAB) can be synthesized in an one-step reaction forming N−S bonds from the direct coupling of sodium p-toluenesulfunic acid with methyl-3-nitrobenzoate (Figure 50). In this Fe^{2+} catalyzed reaction, $NaHSO_3$ acts as a reductant and DMDACH as an additive to provide MSAB in good yields under mild conditions.[279]

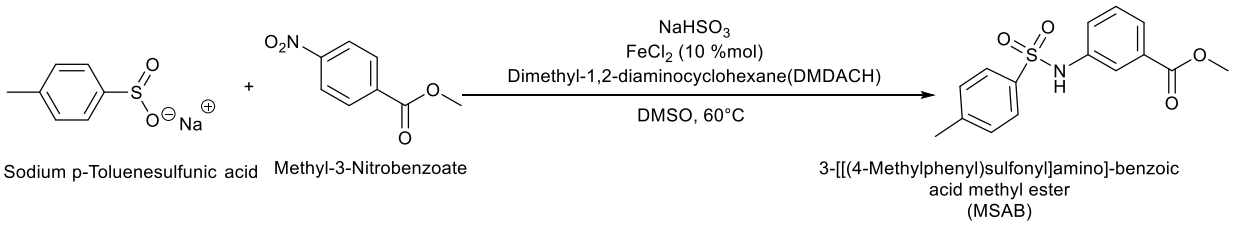

Figure 50. Synthesis reaction of MSAB, based on ref. 279.

MSAB formation was confirmed using ^{1}H-NMR spectroscopy (Figure 51), which showed the methylene protons of the -CH_3 group at 2.3 ppm (**1** in Figure 51), as well as aromatic protons at 7.4 ppm (**2** in Figure 51). The single proton of the sulfoamide group was located at 3.3 ppm (**3** in Figure 51). Methine protons with chemical shifts of 10.5, 7.6 and 7.6 ppm correspond to number **4**, **5** and **6** in Figure 51. Lastly, the methylene protons of the ester groups, with an integral of three, appeared at 3.8 ppm (**7** in Figure 51).

Besides the expected signals corresponding to the product, unidentified peaks were also found in the spectrum. Therefore, optimization of the synthesis parameters and of the flash chromatography purification method is needed before combining the MSAB product with Au NPs.

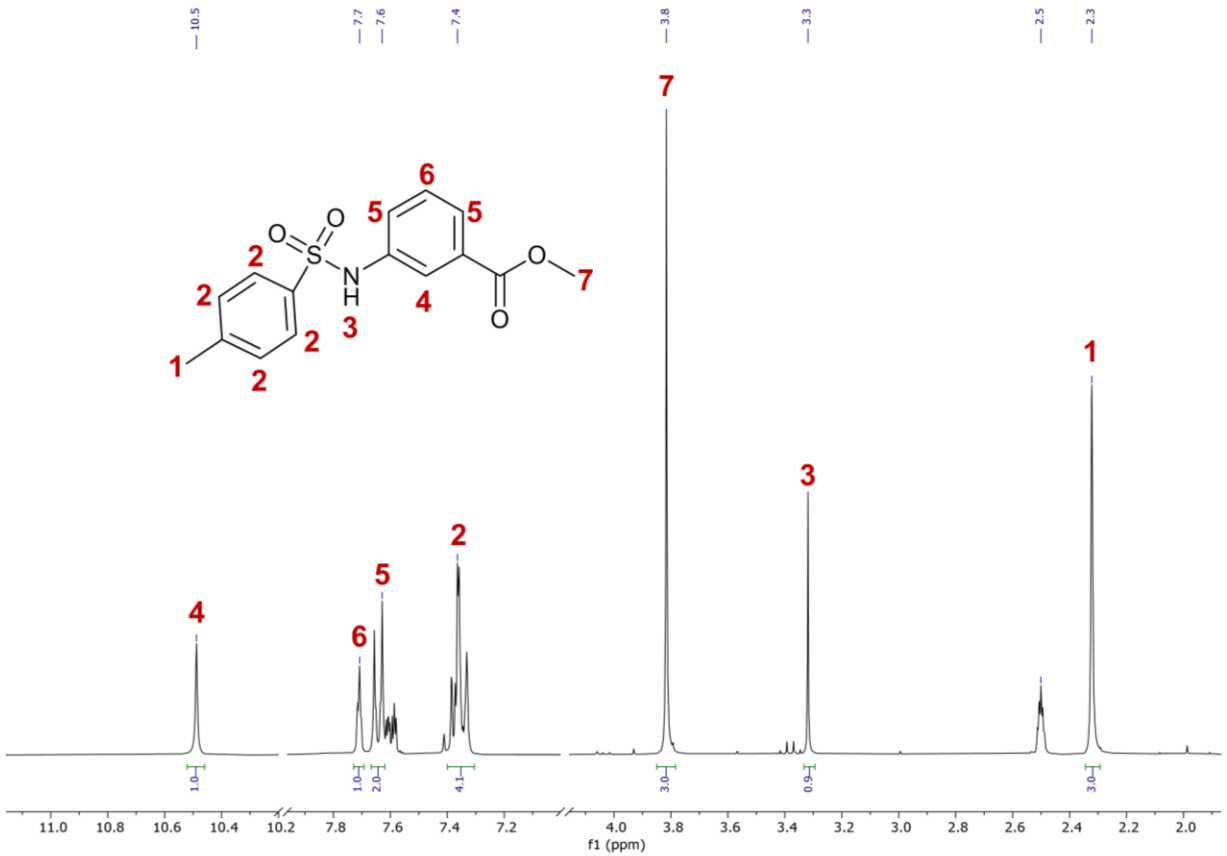

Figure 51. ^{1}H-NMR spectrum of MSAB in DMSO-d6.

For the reaction of LGK974 with Au NPs, a stock of the inhibitor dissolved in DMSO was added to the aqueous solution of previously prepared Au-Citrate NPs (described in chapter 4.1.2), according to Figure 52a. TEM investigations of the product suspension revealed the appearance of elongated structures, most likely corresponding to the LGK974 stock, after depositing the water-DMSO mixture onto the TEM grid. As the images b-d (Figure 52) show, the Au NPs are not homogeneously dispersed anymore (as seen in Figure 33) but seem to be gathered around these “bars”, which could be a sign of insufficient miscibility of the DMSO stock with the rest of the water solution.

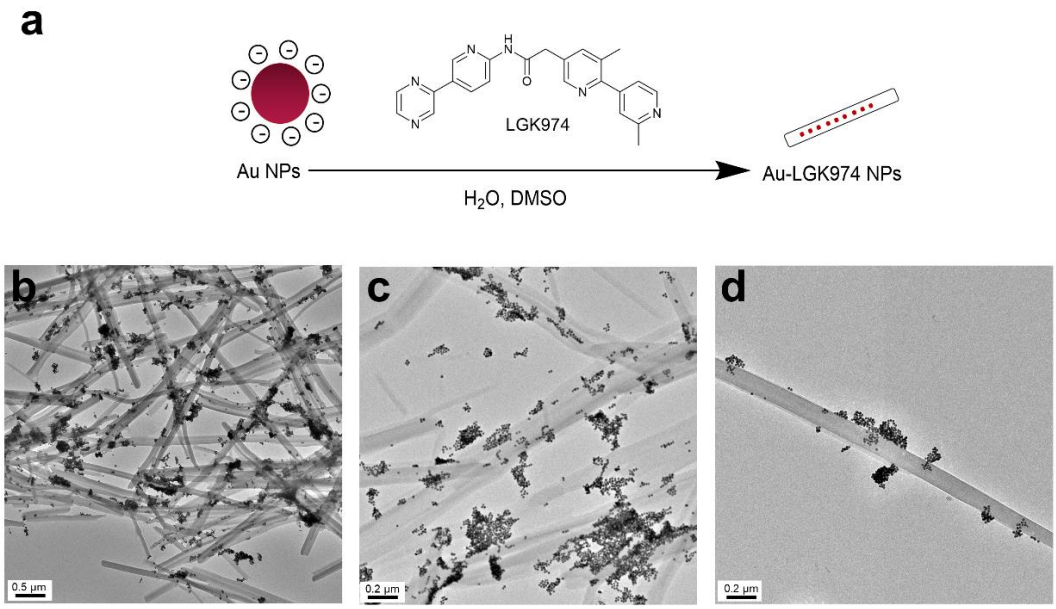

Figure 52. Reaction of LGK974 and Au-Citrate NPs. Synthesis scheme (a) and TEM images (b-d).

Subsequently, the Au-LGK974 NPs were isolated from the solvent mixture via centrifugation, washed and resuspended with DMSO to remove unreacted LGK974 and studied again with IR spectroscopy and TEM. The characteristic IR bands of the LGK974 (Figure 53, blue line) are only visible to some extent in the spectrum of Au-LGK974 NPs (Figure 53, black line), showing only the C=O stretch at 1685 cm^{-1} and the C-N stretch (1536 cm^{-1})[280] with low transmittance.

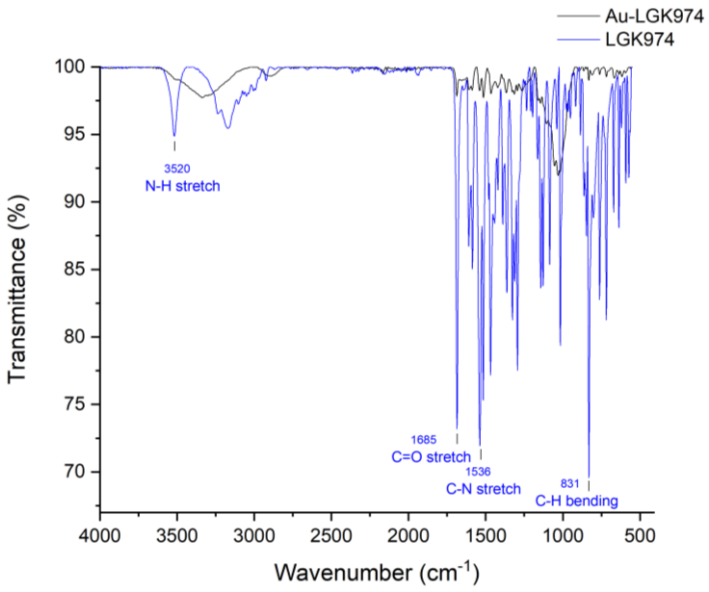

Figure 53. IR spectra of LGK974 (blue line) and Au-LGK974 NPs (black line).

The solvent change of the NPs from water to DMSO caused the Au-LGK974 NPs to agglomerate, as displayed in Figure 54a. This agglomeration effect when using DMSO was also found in the reaction of MSAB and CB839 with Au-Citrate NPs (Figure 54b,c), which is why further experiments were done dissolving inhibitors in ethanol (as described in the publication of chapter 3.2). Thus, even though the solubility of MSAB, LGK974 and CB839 is higher in DMSO, an ethanol stock of lower concentration is more suitable for reactions with Au NPs to avoid losing the intrinsic properties of the nanomaterials.

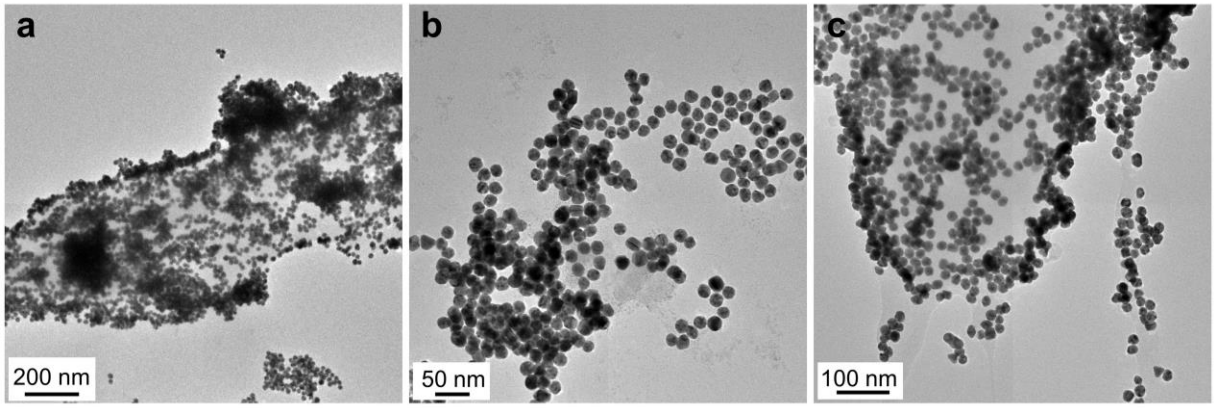

Figure 54. TEM images of Au-Citrate NPs reacted with DMSO stocks of LGK974 (a), MSAB (b) and CB839 (c).

5. Summary and Outlook

The aim of this work was the synthesis of biocompatible Au NPs to efficiently deliver pharmacological therapeutics and enhance their effect for the treatment of GB, particularly eradicating the most therapy resistant cell population of tumor stem cells.

This task was initially approached by developing rapid and straight-forward reaction routes able to produce monodisperse small-sized Au nanospheres in aqueous solutions. A microwave-assisted method was selected as a time-efficient and energy-saving alternative compared to conventional decomposition methods, as it allows the simultaneous optimization of different reaction parameters through fast serial experiments. Using this technique, “hot spots” surpassing the boiling point of water and minimizing the heating phase of the solution[281,282] were exploited to create Au NPs with a narrow size distribution. This microwave “superheating effect” supported the efficient reduction of the precursor $KAuCl_4$ after only 2 min. The PEI polymer was added to the reaction to serve as a capping ligand to the formed NPs, able to protect them against agglomeration and potentially serve as a surface matrix to conjugate therapeutic compounds, as commonly seen in gene therapy.[149] Additionally, PEI served as a reducing agent in the synthesis through a redox reaction involving the oxidation of the alpha carbon of its amine group and the reduction of the Au^{III} salt to Au^0.

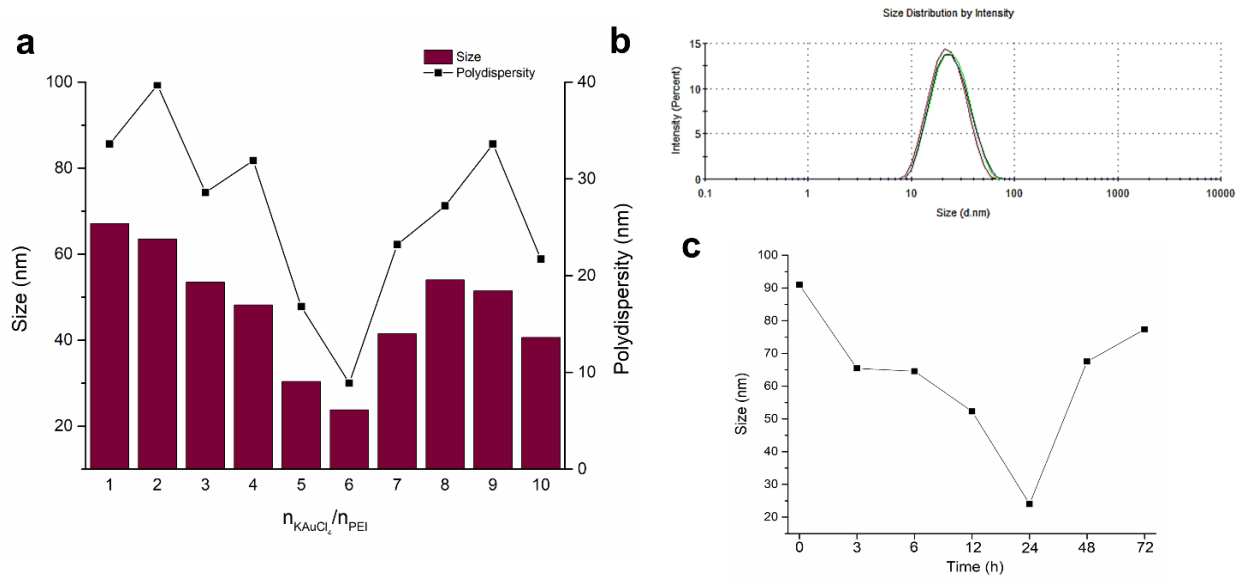

Figure 55. Synthesis of AuPEI NPs. Size and polydispersity depending on $KAuCl_4$:PEI ratio (a), size distribution of AuPEI6 NPs (b) and size increase of AuPEI6 NPs depending on dialysis time (c).

Even though the alteration of precursor-to-ligand ratio can provide moderate size control in the formation of Au NPs, the experiments done with $KAuCl_4$ and PEI showed that a stochiometric variation not only affected the NP size distribution but also their polydispersity. DLS measurements of the Au NPs synthesized with the n_{KAuCl4}/n_{PEI} molar ratios of 1 to 10 resulted in diameters between 24 and 67 nm (Figure 55a) with the lowest polydispersity and smallest size of the AuPEI corresponding to $n_{KAuCl4}/n_{PEI} = 6$ (AuPEI6 NPs, Figure 55b). Furthermore, the dialysis purification process to remove unbound PEI also played an important role on the size of AuPEI NPs, causing agglomeration of the Au cores if 24 h were exceeded (Figure 55c).

Investigations about a possible uptake of these Au NPs by GSCs were possible by binding the fluorescent marker FITC on the NP surface. The labelling of the AuPEI NPs with FITC proceeded by following four different routes, which resulted in fluorescent AuPEI-FITC NPs with sizes between 3 and 6 nm (Figure 56), as investigated using TEM analysis. Gold and sulfur STEM-EDX elemental mapping confirmed the attachment of FITC to every NP type, as expected based on the strong interactions of its isothiocyanate group with the Au metal.[101] While this attachment was stable in physiologically relevant pH values 6-8 and even after being taken up by cells, the amount of bound FITC variated between samples as fluorescence measurements of AuPEI-FITC NPs showed. A comparison between the fluorescence of “free” FITC and the lower intensities found for the NPs demonstrated the fluorescence quenching abilities of Au. The ratio of fluorescent NPs was estimated to be at least 50%.

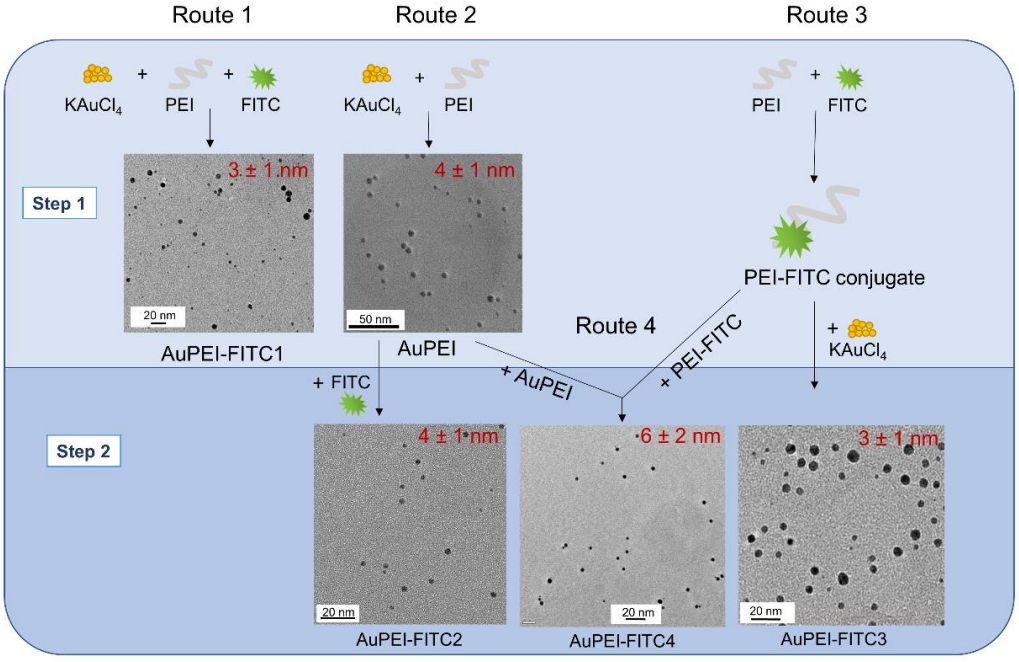

Figure 56. Synthesis of AuPEI-FITC NPs using four different reaction routes.

Qualitative studies about the NP uptake were made after incubating three spheroid GSC lines – known to adequately recapitulate tumor pathophysiology and being able to create tumors in mice[227,277,283] – with the AuPEI-FITC NPs and acquiring several images with a fluorescence microscope. Among the plated cells, almost all neurospheres displayed a green fluorescence on their inside, corresponding to internalized AuPEI-FITC NPs. Still, for drug delivery purposes, it is important to distinguish between NPs which are only bound to the surface of cells ("adsorbed") and the ones which are truly internalized. This differentiation was done using Trypan Blue dye, which is able to quench all extracellular fluorescence after being applied to the cell suspensions. Quantification experiments using FACS and Trypan Blue quenching revealed that the percentage of internalized NPs is highly dependent on the NP type and thus the route with which it was synthesized, as well as on the cell line in which it was tested (Table 4).

Out of all the NP types, AuPEI-FITC1 NPs, synthesized via a novel one-pot reaction (Figure 56, Route 1), presented the highest internalization after only an hour (~ 53%), making them the most suitable vector for drug delivery into GSCs out of the four synthesized AuPEI-FITC NPs. While the difficulty of internalizing NPs into these cells remains, the simple reaction yielding AuPEI-FITC1 NPs allowed for at least half of the cells of each cell line to get transfected.

Table 4. Fraction of cells with adsorbed and internalized vs. internalized AuPEI-FITC NPs in different GB cell lines.

Cell line	AuPEI-FITC1		AuPEI-FITC2		AuPEI-FITC3		AuPEI-FITC4	
	Adsorbed+ internalized (%)	Internalized (%)	Adsorbed+ internalized (%)	Internalized (%)	Adsorbed+ internalized (%)	Internalized (%)	Adsorbed+ internalized (%)	Internalized (%)
GBM1	63	61	56	29	52	7	65	9
JHH520	60	51	75	44	77	39	76	7
407	49	47	53	33	60	9	54	5
Average (all)	57	**53**	61	**35**	63	**18**	65	**7**

A relatively low cytotoxicity at concentrations of 0.25 to 2 mg/L and incubation times shorter than 24 h was found for AuPEI-FITC NPs using the MTT assay. This is a positive result given that Au NPs should serve as carriers for more specific tumor-killing compounds. Special characterization of the NPs is needed after their internalization into cells, since pH changes, formation of protein coronas with medium proteins, polymer degradation and other ionic interactions happening during uptake processes contribute to NP agglomeration, toxicity and loss of their special properties.

Given the unsatisfactory current treatment of GB with temozolomide, further pharmacotherapies which could be delivered by GSC-penetrating Au NPs were examined in this work. Besides short investigations with the promising cancer-drug candidates MSAB[278] and LGK974,[284] special focus was given to the inhibitor CB839. CB839 is a clinically investigated small molecular inhibitor of the metabolic enzyme GLS1, known to play crucial roles in GSC biology and glutamine addiction of rapid growing cancers in general.[228] The difficulty of an immobilization of CB839 on the surface of Au NPs lied in its relatively large size, poor water solubility and chemical inertness. Since the superior efficacy of this drug candidate has currently been tested in several clinical trials, a CB839 loading should ideally not involve any structure modification, which could jeopardize its action. Consequently, polymers were chosen again as non-covalent drug binding moieties and stabilizing agents for Au NPs.

In addition to PEI, Au NPs were functionalized with citrate, PEG, PVA and PVP to provide further functional groups possibly able to couple CB839 by physical adsorption or other attractive forces. The Au-polymer NPs were synthesized either through one-pot routes or ligand-exchange reactions starting from Au-citrate NPs. As seen by TEM, the reaction of these NPs with CB839 dissolved in ethanol did not cause any significant NP agglomeration and the Au core sizes remained between 8 and 15 nm (Figure 57), depending on the surface ligand.

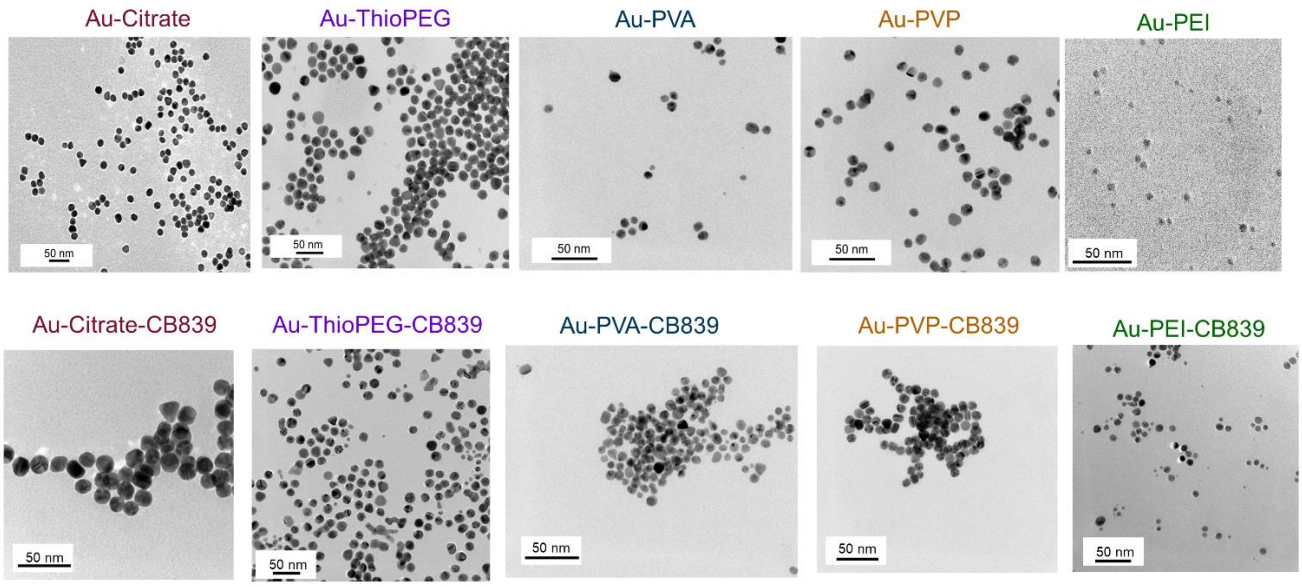

Figure 57. TEM images of Au-citrate and Au-polymer NPs before (upper row) and after reaction with CB839 (lower row).

Since no detailed information had been published regarding quantification procedures for CB839, a new HPLC method was developed by testing several ratios of water and methanol as the mobile phase and a reversed phase C18 column as the stationary phase. An adequate separation of the compound was attained after a retention time of 9 min with 33% of methanol, 67% of H_2O and a flow rate of 1 mL/min. The UV absorbance detected at 254 nm was used to create a calibration curve with CB839 standards of different concentrations and subsequently determine the amount of CB839 embedded to each NP sample.

The AuPVA NPs had the highest loading of CB839 with an efficiency of 12%, compared to the Au-Citrate (8%), AuThioPEG (4%), AuPEI (1%) and AuPVP NPs (0%). We postulate that the hydroxyl groups of the PVA chains accept hydrogen bonds from the amide-NH groups of CB839 but are also donors to the aromatic nitrogen atoms and to the amide C=O groups of CB839. The AuPEI NPs were poor carriers for CB839, most likely because both components have similar sizes (4 nm NPs and ~3 nm long CB839 molecule). Besides the H-bond capabilities and NP size, other parameters such as chain length and surface arrangement of the polymers might play a role in the drug loading efficiency. Mathematical calculations considering the drug loading efficiency and the number of Au NPs and CB839 molecules in the sample were used to estimate that approximately 60% of the AuPVA NPs carry at least one drug molecule. In general, embedding such a large molecule to small Au NPs is extremely challenging.

The presence of CB839 on the surface of the AuPVA NPs was further confirmed through UV-VIS spectra, in which an additional absorbance maximum at 240 nm appeared besides the distinctive plasmonic peak at 550 nm (Figure 58). Moreover, IR spectra showed characteristic bands of the CF_3 and amide groups of CB839. Even though the detection of fluorine is difficult, STEM-EDX mapping and EDX spectra of AuPVA-CB839 revealed the presence of F and Au in the same area (Figure 58) and an elevated EDX signal at 677 eV on and around the Au NPs, corresponding to the F-K shell.

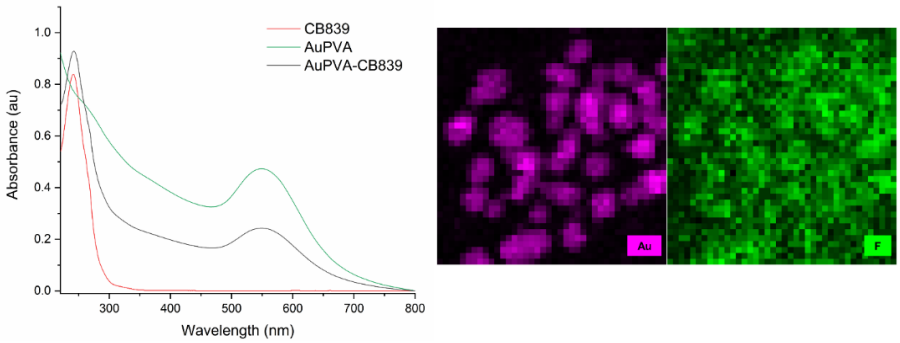

Figure 58. UV-VIS spectra and elemental maps (Au in pink, F in green) of AuPVA-CB839.

The internalization of AuPVA NPs into GSCs was again investigated by functionalization with FITC. The FITC loading efficiency for AuPVA NPs was about 23%. As seen by fluorescence microscopy, the green fluorescence of FITC is present in the studied sphere sections (Figure 59), even after quenching with Trypan Blue. Thus, AuPVA NPs are also suitable for drug delivery into GSCs.

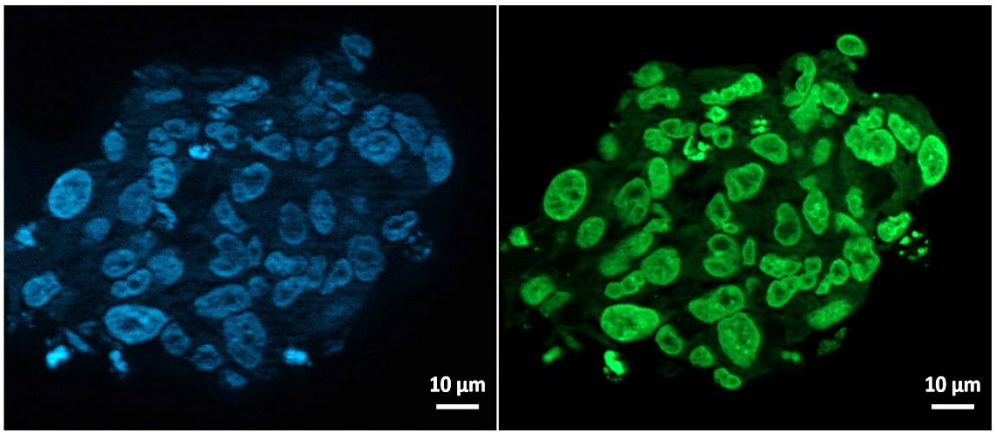

Figure 59. Fluorescence microscopy images of GB cells containing AuPVA-FITC NPs. Left: cells were stained blue with DAPI, right: green fluorescence corresponds to the internalized NPs.

After the characterization of AuPVA-CB839 NPs, the effect of the nano-delivered drug on GSCs was evaluated using the colony formation assay. Compared to the previously employed MTT assay, the colony assay did not require additional efforts to remove remaining Au before measurements, as it does not rely on optical detection. Hence, there were no interferences with the Au NPs. The ability to form monolayer and spheroidic colonies after treatment with CB839 and AuPVA-CB839 NPs was investigated *in vitro* with four different GB cell lines. For each treatment, cells were grown in two conditions: either adherently with poly-D-lysine or in solution with agarose media (Figure 60). Even though both methods presented different susceptibilities to the treatment, the AuPVA-CB839 NPs enhanced the therapeutic effect in all cells tested with both assays, compared to unmodified CB839. The smallest difference in colony formation with CB839 and AuPVA-CB839 NPs was seen for the glutaminase-high expressing U87 and JHH520 cell lines, while the strongest effect was seen in agarose for BTSC407 cells, thought to be resistant to CB839 due to their lower glutaminase activation levels. Thus, the abundancy of the glutaminase enzyme might predict the sensitivity of GB cells towards CB839 and AuPVA-CB839 NPs.

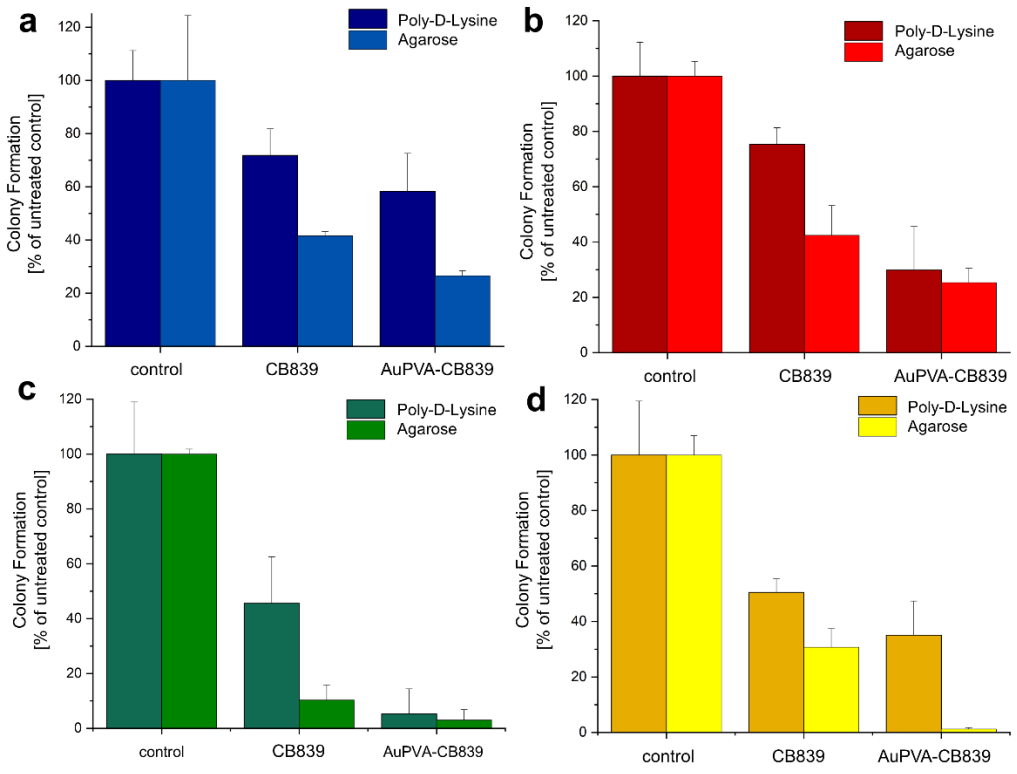

Figure 60. Colony Formation of U87 (a), JHH520 (b), GBM1 (c) and BTSC407 (d) cells after incubation with CB839 and AuPVA-CB839 NPs, using both the 2D poly-D-lysine and the 3D agarose method.

In addition to the effect of CB839-loaded Au NPs on colony formation, a quantification of the amount of CB839 delivered into the cells is pending. Similarly, the effect of Au-CB839 NPs on enzyme activity inhibition still needs to be investigated. Nevertheless, the use of physiological relevant model systems and the functional data on diminished colony formation, unequivocally proves the enhanced therapeutic potential of our nanodelivered CB839 drug, thereby presenting a cornerstone for justifying the further exploitation of this approach in dedicated follow-up studies in animals.

Experiments with AuPEI and AuPVA-CB839 NPs summarize the potential of tackling the molecular heterogeneity of GB with nanotechnology given the subtype specific susceptibilities of GSCs to the NPs. However, further studies concerning a possible association of delivery resistance and molecular subtype are still needed. Furthermore, tests in animal models would enhance the clinical prediction of the efficacy of drug-loaded Au NPs. To create a more targeted therapy, the Au NPs could be additionally equipped with GSC-specific targeting moieties such as antibodies, aptamers or peptides, *e. g.* CD133 and CD44 - directed anchor molecules.

This work raises hope of finding alternatives treatments for GB patients, combining novel pharmaceutics with potent easy-to-adjust theranostic nanoprobes. In the future, the results gained here about drug delivery with Au NPs aim to improve neurooncology care by increasing the bioavailability of drugs with durable anti-cancer effects at relevant tumor sites, while ideally decreasing therapy-induced side effects observed with non-targeted treatments.

6. Experimental Section

In this section, experimental details concerning the results from chapter 4 are listed. For materials and methods used in the publications from chapters 3.1, 3.2 and 3.3 each individual publication should be consulted.

6.1. Chemicals and Solvents

Chemicals and solvents used in experiments from chapter 4 are described in Table 5 in alphabetical order. These were used without further purification unless specifically stated for each reaction.

Table 5. Chemicals and solvents used.

Chemical	Purity (%)	Source
5-Aminolevulinic acid hydrochloride (5-ALA)	98	Sigma Aldrich, Germany
Antibiotic-Antimycotic	-	Gibco, Thermo Fisher Scientific, Germany
L-Ascorbic acid	99	Sigma Aldrich, Germany
B27 supplement	-	Gibco, Thermo Fisher Scientific, Germany
Cetyltrimethylammonium bromide (CTAB)	98	Sigma Aldrich, Germany
Chloroauric acid ($HAuCl_4$)	99.99	Sigma Aldrich, Germany
β-Cyclodextrin (CD)	100	BLD Pharmatech, Germany

Dichloromethane (DCM)	99.8	Fisher Scientific, Germany
Dicyclohexylcarbodiimide (DCC)	99	Sigma Aldrich, Germany
Dimethyl-1,2-diaminocyclohexane (DMDACH)	95	Fluorochem, United Kingdom
Dimethylformamide (DMF)	99.9	Fisher Scientific, Germany
Dimethyl sulfoxide (DMSO)	99.5	Fisher Scientific, Germany
4,4'-Dithiodibutyric acid	95	Sigma Aldrich, Germany
Dulbecco's Modified Eagle Medium (DMEM) without pyruvate	-	Gibco, Thermo Fisher Scientific, Germany
Ethyl acetate	99.5	Sigma Aldrich, Germany
Fetal calf serum (FBS)	-	Gibco, Thermo Fisher Scientific, USA
Ham's F12 Nutrient Mix	-	Gibco, Thermo Fisher Scientific, Germany
Heparin	-	Sigma Aldrich, Germany
Heptakis-(6-deoxy-6-thio)-β-cyclodextrin	95	Carbosynth, United Kingdom
Human basic fibroblast growth factor	-	Peprotech, USA
N-Hydroxysuccinimide	98	Sigma Aldrich, Germany

Iron(II) chloride anhydrous ($FeCl_2$)	99.5	Fisher Scientific, Germany
Methyl-3-nitrobenzoate	99	Sigma Aldrich, Germany
2-Mercaptoethanol	99	Carl Roth, Germany
Phosphate buffer saline (PBS)	-	Gibco, Thermo Fisher Scientific, Germany
pmaxGFP plasmid, 3486 bp. (GFP)	-	Lonza, Germany
Polyethylene glycol M_w~10000 g/mol (PEG10000)	-	Fluka Chemie, Germany
Polyethylene glycol M_w~600 g/mol (PEG600)	-	Fluka Chemie, Germany
Polyethylene glycol-methyletherthiol M_w~800 g/mol (ThioPEG)	-	Sigma Aldrich, Germany
Polyethylenimine 25 kDa branched (PEI)	99	Sigma Aldrich, Germany
Potassium Carbonate (K_2CO_3)	99	Fisher Scientific, Germany
Potassium tetrachloridoaurate (III) ($KAuCl_4$)	98	Sigma Aldrich, Germany

Silver nitrate ($AgNO_3$)	99.0	Sigma Aldrich, Germany
Sodium bisulfite ($NaHSO_3$)	≥58.5 (SO_2)	Acros Organics, Germany
Sodium borohydride ($NaBH_4$)	96	Merck, Germany
Sodium chloride (NaCl)	99.5	Carl Roth, Germany
Sodium citrate dihydrate	99.7	J.T. Baker Chemicals, The Netherlands
Sodium hydroxide (NaOH)	99	AppliChem, Germany
Sodium sulfate (Na_2SO_4) anhydrous	99.5	TCI Europe, Belgium
Tetrahydrofuran (THF)	99.9	Sigma Aldrich, Germany
p-Toluenesulfunic acid sodium salt	96	J&K Scientific, Germany

6.2. Instruments and Methods

6.2.1. Laboratory microwave

Nanoparticle synthesis was conducted in a Discovery laboratory microwave (CEM, Germany) equipped with a reflux condenser. Solutions were irradiated for 2 min at 100 °C and 300 W while stirring.

6.2.2. Dialysis

Purification of the NP solutions with dialysis was done against H_2O using Spectra/Por® membranes (Spectrum Laboratories, Germany) with a molecular weight cutoff of 3.5 kDa or 50 kDa.

6.2.3. Centrifugation

Purification of the NP solutions via centrifugation was done using an Allegra 64R centrifuge from Beckman Coulter, Germany. Samples were centrifuged at 10000 rpm and 4 °C for 20 min in a C0650 conical rotor.

6.2.4. Nuclear magnetic resonance (NMR)

All ^{1}H-NMR spectra were measured at 298 K on an Avance III-600 NMR spectrometer from Bruker, Germany.

6.2.5. Transmission electron microscopy (TEM)

TEM images were recorded on a FEI Tecnai G2 F20 microscope[285] operated at 200 kV accelerating voltage using a Gatan UltraScan 1000P camera. Liquid samples were dropped onto a 200 µm carbon-coated copper grid (Electron Microscopy Sciences #CF200-CU, Germany) and dried in air prior to measurements. Analysis of size and size distribution was done counting over 50 particles with the Gatan Digital Micrograph software.

6.2.6. Dynamic light scattering (DLS) and zeta potential

A Nano S Zetasizer instrument (Malvern, Germany) with a HeNe laser was used to determine the hydrodynamic diameter and zeta potential of Au NPs at a wavelength of 633 nm. Three measurements with four runs were done per sample.

6.2.7. Ultraviolet–visible spectroscopy (UV-VIS)

UV-VIS spectra were measured with a UV-2450 spectrometer (Shimadzu, Japan) between 200 and 800 nm. Spectra were analyzed using the UVProbe software.

6.2.8. Fourier transform infrared spectroscopy (IR)

IR spectra were recorded on a TENSOR 37 spectrometer (Bruker, Germany) in attenuated total reflection mode (Platinum ATR-QL, Diamond) between 550 and 4000 cm^{-1} after removing the solvent of purified Au NP samples.

6.2.9. High-performance liquid chromatography (HPLC)

HPLC measurement were made with a LC 20AT prominence instrument (Shimadzu, Japan) with an SPD-M20A detector and a Luna C18(2) (250 × 4.60 mm, 5 micron) column from Phenomenex®. The sample loop volume was 20 µL, the flow rate was 1 mL/min and absorbance was detected at a wavelength of 254 nm. Before each measurement, the column was flushed with the methanol/H_2O mobile phase (33% methanol/67% H_2O) for 30 min. The run time for each measurement was 13 min. Quantification of the compound of interest was done by peak integration using a calibration curve of the standard substance.

6.3. Ligand and NP Synthesis

6.3.1. ThioPEI

The thiol-functionalized polymer ThioPEI was synthesized according to a procedure described by *Thomas et al*.[258]

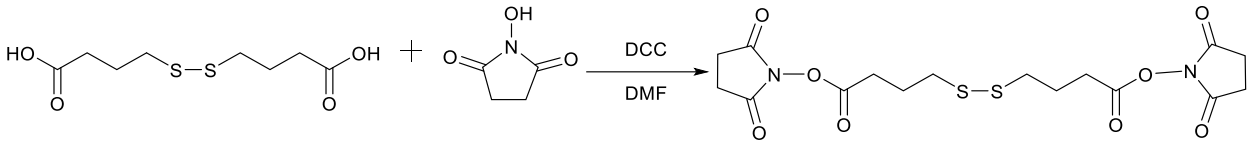

Figure 61. Synthesis of bis-(*N*-hydroxysuccinimido)-4,4'-dithiodibutyrate.

The compounds 4,4'-dithiodibutyric acid (5.96 g, 25 mmol) and *N*-hydroxysuccinimide (7.48 g, 65 mmol) were dissolved in 25 mL dimethylformamide (DMF). While stirring, dicyclohexylcarbodiimide (DCC, 11.35 g, 55 mmol) dissolved in 20 mL DMF was added. The thick yellowish suspension was stirred for 12 h at 5 °C until the dicyclohexylurea by-product precipitated. After addition of 10 mL of ethyl acetate, the precipitated white solid (dicyclohexylurea) was filtered off and the ethyl acetate filtrate was washed twice with a saturated NaCl aqueous solution and dried over anhydrous Na_2SO_4. After ethyl acetate evaporation, the product was dissolved in dichloromethane (DCM), filtered to remove remaining dicyclohexylurea, washed three times with a saturated K_2CO_3 aqueous solution, once with a saturated NaCl solution and dried over Na_2SO_4. 8.0 g (19 mmol) of bis-(*N*-hydroxysuccinimido)-4,4'-dithiodibutyrate were obtained as a light-yellow solid after evaporation of DCM.

Yield: 74%.

^{1}H-NMR (Acetone-d6, 600 MHz, 298 K): δ = 2.8 ppm (s, –C**H**$_2$, 8H), 2.6 ppm (m, –C**H**$_2$, 4H), 2.2 ppm (m, –C**H**$_2$, 4H), 1.7 ppm (m, –C**H**$_2$, 4H).

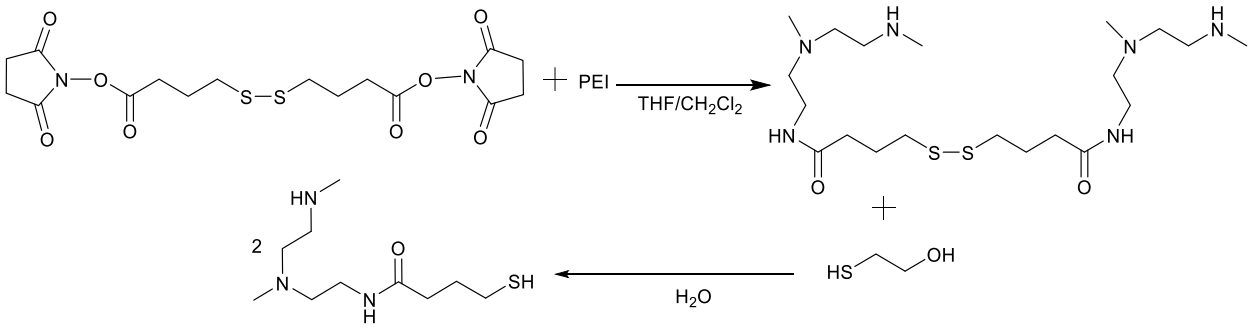

Figure 62. Synthesis of ThioPEI through reduction of the disulfides with 2-mercaptoethanol.

PEI (10 g, 0.4 mmol) was dissolved in 100 mL of a mixture of DCM:THF 5:3. 2 g (4.6 mmol) of the obtained bis-(*N*-hydroxysuccinimido)-4,4'-dithiodibutyrate dissolved in 30 mL THF was then added drop-wise over 3 min to the PEI solution and stirred for 15 h. After solvent evaporation, the remaining viscous product was suspended in 100 mL of water. 4.8 mL of 2-mercaptoethanol was added to this suspension and stirred for 2 h. The solution was filtered, and the filtrate was dialyzed against water using a 50 kDa dialysis tube. After drying, 5 g of ThioPEI were obtained.

Yield: 42%.

^{1}H-NMR (D_2O, 600 MHz, 298 K): δ = 3.8 ppm (t, –C**H**$_2$, 2H), 3.2 ppm (t, –C**H**$_2$, 2H), 3.0 ppm (m, –C**H**$_2$, 4H), 2.9 ppm (s, –C**H**$_2$, 2H), 2.8 ppm (m, –C**H**$_3$, 6H).

6.3.2. Au-ThioPEI NPs

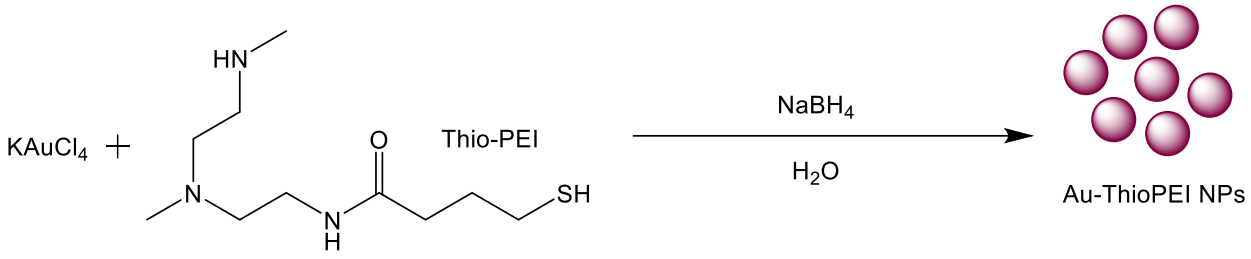

Figure 63. Synthesis of Au-ThioPEI NPs.

0.52 g (0.2 mmol) of ThioPEI were dissolved in 12.5 mL H_2O and stirred with 0.27 g (0.7 mmol) $KAuCl_4$ for 10 min. 1.4 g (37 mmol) of $NaBH_4$ were dissolved in 20 mL H_2O and added slowly to the Au-ThioPEI solution. A direct color change from orange to dark red occurred. After additional stirring for 24 h, the solution was dialyzed against H_2O for 12 h using a 3.5 kDa tube and filtered through a 0.45 µm syringe filter.

6.3.3. Au-PEG NPs

6.3.3.1. "One-pot" method

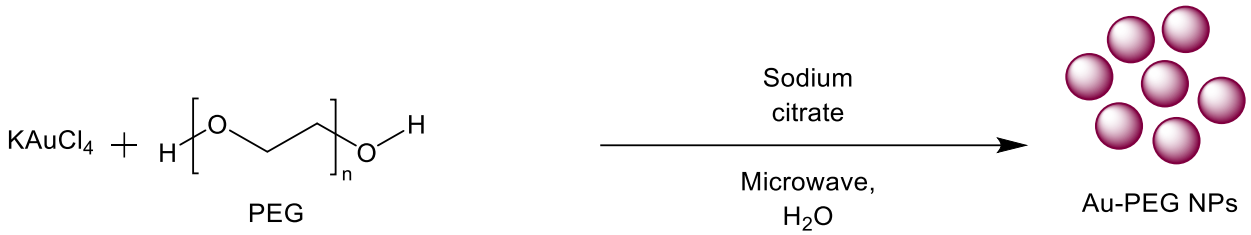

Figure 64. "One-pot" synthesis of Au-PEG NPs.

28 mg (2.8 µmol) of PEG10000 were dissolved in 50 mL water and added to a round bottom flask containing 6.3 mg (17 µmol) of $KAuCl_4$ and 40 mg (136 µmol) of sodium citrate. The solution was placed in a microwave equipped with a reflux condenser and irradiated for 2 min at 100 °C and 300 W while stirring. The red solution was dialyzed against water for 24 h using a 50 kDa tube.

6.3.3.2. Two-step method

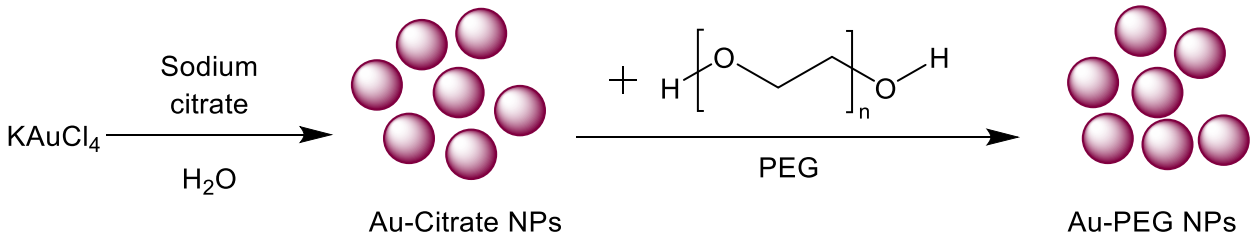

Figure 65. Two step synthesis of Au-PEG NPs.

5 mg (13.2 µmol) $KAuCl_4$ were dissolved in 50 mL H_2O and heated to 100 °C on a heating plate. 23 mg (78.2 µmol) of sodium citrate were added and the solution was stirred until the color changed to dark red. The Au-Citrate NPs were centrifuged (10000 rpm, 20 min, 4 °C) and resuspended in 50 mL H_2O. Subsequently, 2.6 mg (4.3 µmol) of PEG600 were added to the Au-Citrate NP solution, stirred at room temperature for 12 h, centrifuged (10000 rpm, 20 min, 4 °C) and resuspended in 50 mL H_2O.

6.3.4. Au-ThioPEG NPs

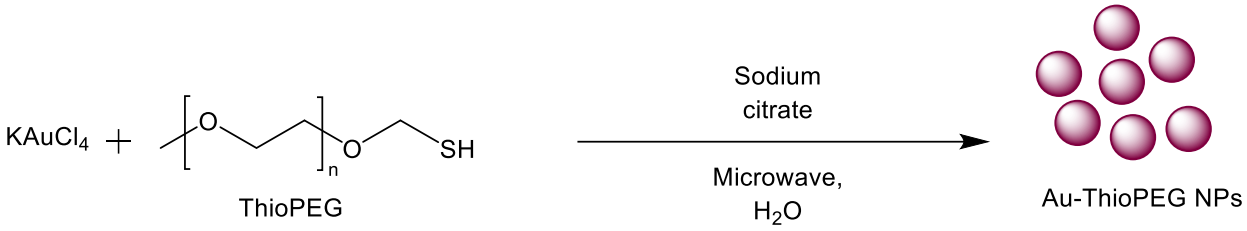

Figure 66. Microwave-assisted synthesis of Au-ThioPEG NPs.

20 mg (33.3 µmol) of ThioPEG were dissolved in 50 mL water and added to a round bottom flask containing 6.3 mg (17 µmol) of $KAuCl_4$ and 40 mg (136 µmol) of sodium citrate. The solution was placed in the microwave and irradiated for 2 min at 100 °C and 300 W while stirring. The red solution was dialyzed against water for 24 h using a 50 kDa tube.

6.3.5. Au-PEI-ThioPEG

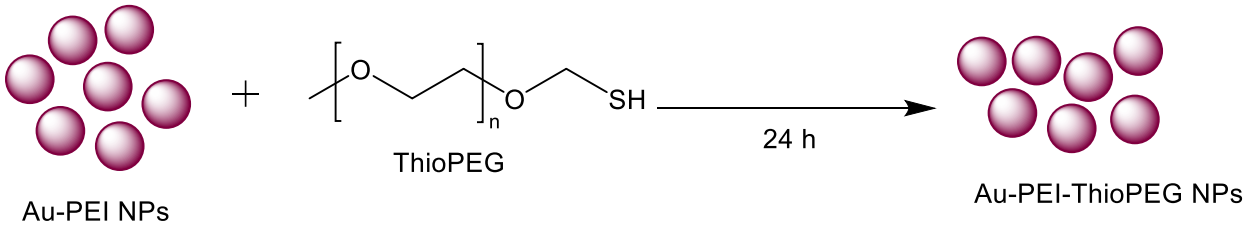

Figure 67. Synthesis of Au-PEI-ThioPEG NPs.

20 mg (33.3 µmol) of ThioPEG were added to 10 mL of an Au-PEI NP solution (for synthesis see AuPEI6 in publication from chapter 3.1), stirred for 24 h at room temperature and dialyzed against water for 24 h using a 50 kDa tube.

6.3.6. Au Nanorods

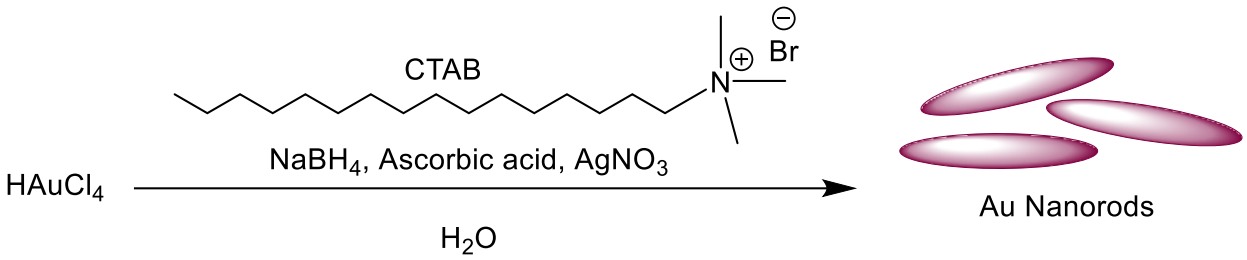

Figure 68. Synthesis of Au nanorods.

The synthesis of Au nanorods with 10 nm in diameter and 45 nm in length was attempted by modification of the seed-mediated growth method published by *Khanal et al*.[264] The method consists of the preparation of a seed solution and a growth solution by previously dissolving several compounds in water. All amounts of the chemicals and H_2O solvents used for the synthesis are indicated in Table 6.

To prepare the seed solution, **A** and **B** (for naming of solutions see Table 6) were mixed and ice-cold **C** was added under vigorous stirring. The solution color changed from green/yellow to brown. Stirring was continued for 5 min. For the growth solution, **D** and **E** were combined without stirring and heated to 25 °C. **F** was added, followed by **G** and the mixture became colorless after 5 s of gently swirling the flask.

Afterwards, 0.8 mL of the seed solution was added to the entire growth solution (~535 mL), stirred for 30 s and heated to 27 °C. Without stirring, the solution color changed to red/brown and the growth of the nanorods was complete after 30 min.

Table 6. Chemicals used for the preparation of the growth and seed solutions. Each compound was dissolved separately in the indicated H_2O volume.

Solution	Compound	Mass (mg)	Amount of substance (µmol)	H_2O volume (mL)
A	CTAB	364.0	998.8	5.0
B	$HAuCl_4 \cdot 3H_2O$	1.0	2.5	5.0
C	$NaBH_4$	3.8	100.4	10.0
D	$AgNO_3$	8.5	50.0	12.5
E	CTAB	18220	49993.1	250.0
F	$HAuCl_4 \cdot 3H_2O$	98.5	250.1	250.0
G	Ascorbic acid	69.4	394.0	5.0

6.3.7. Au-PEI-GFP NPs

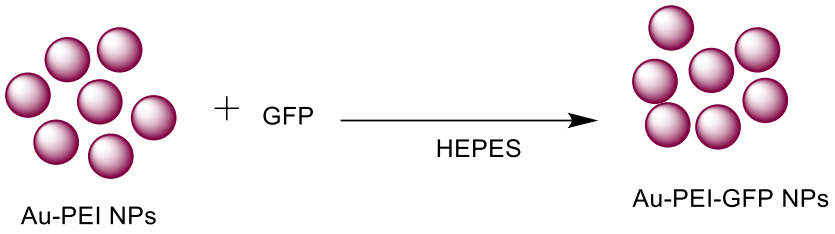

Figure 69. Synthesis of Au-PEI-GFP NPs.

Au-PEI NPs were synthesized according to the method described for AuPEI6 in the publication in chapter 3.1. Different volumes of the aqueous Au-PEI NP solution were combined with 6.3 µL of a suspension containing the GFP plasmid (C = 0.5 g/L) at the ratios w(AuPEI):w(GFP) 4:1, 3:1 and 2:1. After purification by centrifugation, HEPES buffer was added to the pellets to give a final

volume of 1.5 mL. The sample with the ratio w(AuPEI):w(GFP) 2:1 (Au-PEI-GFP2) was chosen for transfection experiments (see section 6.4).

6.3.8. Au-Cyclodextrin NPs

Methods used to synthesize Au-Cyclodextrin NPs were briefly described in Table 3. Modifications to the published routes were done as follows:

Table 3, Entry 1 from ref. 270: 113.5 mg (100.0 µmol) of β-cyclodextrin (β-CD) were suspended in 10 mL of H_2O and mixed with 3.8 mg (10.0 µmol) of $KAuCl_4$ (dissolved in 1 mL H_2O) and 5 mL PBS. The solution was heated to 100 °C, stirred for 30 min and purified by centrifugation.

Table 3, Entry 2 from ref. 271: 2 g (1.8 mmol) of β-CD were suspended in 247 mL H_2O. 3.8 mg (10.0 µmol) of $KAuCl_4$ were dissolved in 1 mL H_2O and added to the β-CD. After 2 min, 100 mg (2.5 mmol) NaOH dissolved in 2.5 mL H_2O were added and the solution was heated to 80 °C until its color changed to pink. The solution was purified by centrifugation.

Table 3, Entry 3 from ref. 272: 3.8 mg (10.0 µmol) of $KAuCl_4$ were dissolved in 100 µL H_2O and added to a solution containing 50 mg (44.1 µmol) β-CD and 10 mL H_2O. 600 µL of an aqueous $NaBH_4$ (C = 0.02 mol/L) solution were added to result in a dark red color. The reaction was stirred for 12 h and purified by centrifugation.

Table 3, Entry 4 from ref. 273: 37.8 mg (100.0 µmol) of $KAuCl_4$ were dissolved in 90 mL H_2O. 1.5 g (1.3 mmol) of β-CD were added and the solution was heated under reflux. A solution of 117.6 mg (400.0 µmol) sodium citrate in 10 mL H_2O was added through a septum and the mixture was refluxed for additional 15 min. After cooling, the solution was purified by centrifugation.

Table 3, Entry 5 also from ref. 273: 4.7 mg (12.5 µmol) of $KAuCl_4$ were dissolved in 50 mL H_2O and mixed with 0.5 g (0.5 mmol) of β-CD and 1 mL of a $NaBH_4$ (0.1 mol/L) solution at 22 °C until the solution turned orange. The reaction was stirred for 18 h at room temperature and purified by centrifugation.

6.3.9. Au-5-ALA NPs

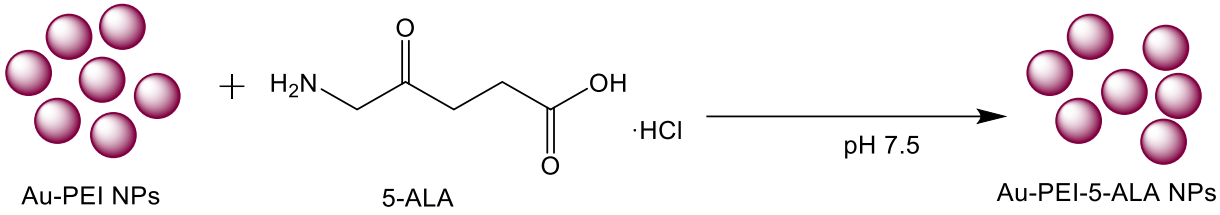

Figure 70. Synthesis of Au-PEI-5-ALA NPs.

16.8 mg (100.0 µmol) of 5-aminolevulinic acid hydrochloride (5-ALA) were dissolved in 100 mL DMEM and filtered with a 0.2 µm syringe filter. 723 µL (~ 2.3 µmol/L Au) of a solution of Au-PEI NPs (AuPEI6 in the publication from chapter 3.1) were added and the pH value of the solution was adjusted to 7.5 using a 1 mol/L NaOH aqueous solution. The final gold concentration of the sample was approximately C_{Au} = 317.5 µmol/L.

6.3.10. MSAB

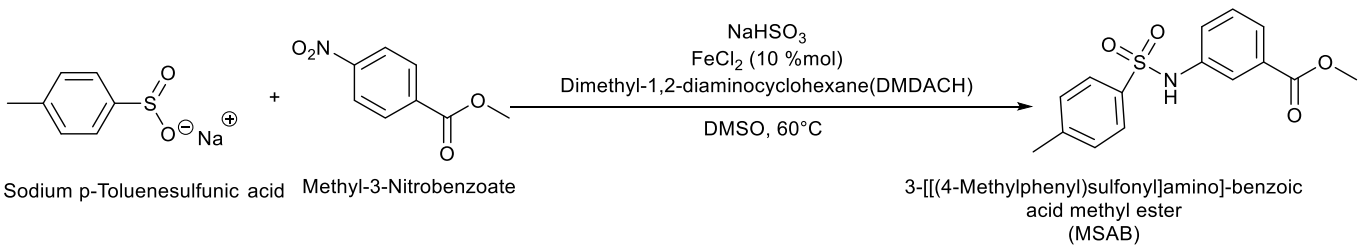

Figure 71. Synthesis of MSAB.

7.8 g (75.0 mmol) of $NaHSO_3$, 6.7 g (37.6 mmol) of p-toluenesulfunic acid sodium salt, 4.5 g (24.8 mmol) methyl-3-nitrobenzoate and 0.3 g (2.4 mmol) $FeCl_2$ were dissolved in 100 mL dimethylsulfoxide (DMSO). 0.7 g (4.9 mmol) of dimethyl-1,2-diaminocyclohexane (DMDACH) were added and the suspension was stirred at 60 °C for 20 h. After addition of 400 mL H_2O, the product was extracted three times with DCM and dried over anhydrous $NaSO_4$. After solvent removal, purification was done by flash chromatography on a silica gel column.

Yield: 94%.

^{1}H-NMR (DMSO-d6, 600 MHz, 298 K): δ = 10.5 ppm (s, –C**H**, H), 7.7 ppm (t, –C**H**, H), 7.6 ppm (m, –C**H**, 2H), 7.4 ppm (m, –C**H**, 4H), 3.8 ppm (s, –C**H**$_3$, 3H), 3.3 ppm (s, –N**H**, H), 2.3 ppm (s, –C**H**$_3$, 3H).

6.3.11. Au-LGK974 NPs

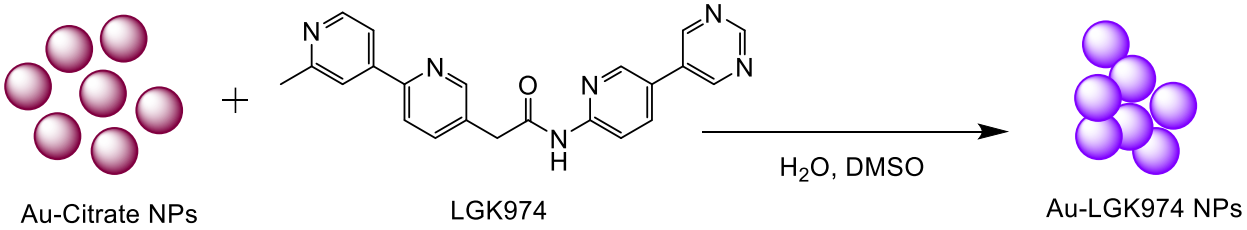

Figure 72. Synthesis of Au-LGK974 NPs.

5 mg (13.2 µmol) $KAuCl_4$ were dissolved in 50 mL H_2O and heated to 100 °C on a heating plate. 23 mg (78.2 µmol) of sodium citrate were added and the solution was stirred until the color changed to dark red. The Au-Citrate NPs were centrifuged and resuspended in 50 mL H_2O. Subsequently, 630 µL of a LGK974 solution in DMSO (10 mmol/L) were added to the Au-Citrate NP solution, stirred at room temperature for 12 h, centrifuged and resuspended in 50 mL H_2O. After initial TEM analysis, the sample was washed with DMSO, centrifuged and resuspended in 50 mL DMSO for further evaluation.

6.4. Cell Experiments

GB cells were generously provided as follows: JHH520 (G. Riggins, Johns Hopkins, Baltimore, USA), Sf188 (E. Raabe, Johns Hopkins, Baltimore, USA), BTSC(407) and 233 (M.S. Carro, Freiburg University, Germany), RAV19 (M. Proescholdt, Regensburg University, Germany). GB cells were cultured in DMEM without pyruvate, 30% Ham's F12 Nutrient Mix, 2% B27 supplement, 20 ng/mL human basic fibroblast growth factor, 20 ng/mL human epidermal growth factor and 5 µg/mL heparin. Human embryonic kidney (HEK) cells were cultured in DMEM without pyruvate supplemented with 10% fetal calf serum. Both media contained 1×Antibiotic-Antimycotic. All cells were cultured at 37 °C and 5% CO_2.

For the transfection experiments of Au-PEI-GFP2 NPs (section 6.3.7), 10000 cells were seeded in 96-well plates and incubated with 50 µL of the suspension containing Au-PEI and GFP at a 2:1 ratio for 6 h. The NP-containing medium was removed, and wells were examined under a bright-field and fluorescence microscope.

7. References

1. H. Goesmann, C. Feldmann, *Angew. Chem.* **2010**, 122, 1402-1437.
2. D. R. Boverhof, C. M. Bramante, J. H. Butala, S. F. Clancy, M. Lafranconi, J. West, S. C. Gordon, *Regul. Toxicol. Pharmacol.* **2015**, 73, 137-150.
3. K. J. Klabunde, S. Wineck, Nanoscale Materials in Chemistry, *Wiley-VCH*, New York, **2001**.
4. I. Khan, K. Saeed, I. Khan, *Arab. J. Chem.* **2019**, 12, 908-931.
5. S. Becht, S. Ernst, R. Bappert, C. Feldmann, *Chem. Unserer Zeit* **2010**, 44, 14-23.
6. G. Schmid, Nanoparticles: From Theory to Applications, *Wiley-VCH*, Weinheim, **2010**.
7. Z. He, Z. Zhang, S. Bi, *Mater. Res. Express* **2020**, 7, 012004.
8. O. Salata, *J. Nanobiotechnol.* **2004**, 2, 3.
9. W. J. Stark, P. R. Stoessel, W. Wohlleben, A. Hafner, *Chem. Soc. Rev.* **2015**, 44, 5793-5805.
10. D. Guo, G. Xie, J. Luo, *J. Phys. D: Appl. Phys.* **2014**, 47, 013001.
11. J. P. Kaiser, L. Diener, P. Wick, *J. Phys.: Conf. Ser.* **2013**, 429, 012036.
12. A. Abramova, A. Gedanken, V. Popov, E. H. Ooi, T. J. Mason, E. M. Joyce, J. Beddow, I. Perelshtein, V. Bayazitov, *Mater. Lett.* **2013**, 96, 121-124.
13. A. Weir, P. Westerhoff, L. Fabricius, K. Hristovski, N. von Goetz, *Environ. Sci. Technol.* **2012**, 46, 2242-2250.
14. P. J. Lu, S. C. Huang, Y. P. Chen, L. C. Chiueh, D. Y. C. Shih, *J. Food Drug Anal.* **2015**, 23, 587-594.
15. W. H. De Jong, P. J. A. Borm, *Int. J. Nanomedicine* **2008**, 3, 133-149.
16. K. Y. Chan, J. Ding, J. Ren, S. Cheng, K. Y. Tsang, *J. Mater. Chem.* **2004**, 14, 505-516.
17. C. Langhammer, I. Zorić, B. Kasemo, B. M. Clemens, *Nano Lett.* **2007**, 7, 3122-3127.
18. X. Luo, A. Morrin, A. J. Killard, M. R. Smyth, *Electroanalysis* **2006**, 18, 319-326.
19. D. Astruc, *Chem. Rev.* **2020**, 120, 461-463.
20. A. Biswas, I. S. Bayer, A. S. Biris, T. Wang, E. Dervishi, F. Faupel, *Adv. Colloid Interface Sci.* **2012**, 170, 2-27.
21. H. Birol, C. R. Rambo, M. Guiotoku, D. Hotza, *RSC Advances* **2013**, 3, 2873-2884.
22. E. L. Ayuk, U. Mariagoretti, S. B. Aronimo, *Chem. Res. J.* **2017**, 2, 97-123.
23. J. Park, J. Joo, S. G. Kwon, Y. Jang, T. Hyeon, *Angew. Chem.* **2007**, 119, 4714-4745.

24. P. G. Jamkhande, N. W. Ghule, A. H. Bamer, M. G. Kalaskar, *J. Drug Deliv. Sci. Technol.* **2019**, 53, 101174.
25. K. Petcharoen, A. Sirivat, *Mat. Sci. Eng. B* **2012**, 177, 421-427.
26. M. Niederberger, *Acc. Chem. Res.* **2007**, 40, 9, 793-800.
27. M. Salavati-Niasari, F. Davar, N. Mir, *Polyhedron* **2008**, 27, 3514-3518.
28. S. Kundu, L. Peng, H. Liang, *Inorg. Chem.* **2008**, 47, 6344-6352.
29. D. Graf, J. Schläfer, S. Garbe, A. Klein, S. Mathur, *Chem. Mater.* **2017**, 29, 5877-5885.
30. A. Garzón-Manjón, T. Löffler, M. Meischein, H. Meyer, J. Lim, V. Strotkötter, W. Schuhmann, A. Ludwig, C. Scheu, *Nanoscale* **2020**, 12, 23570-23577.
31. J. N. Hasnidawani, H. N. Azlina, H. Norita, N. N. Bonnia, S. Ratim, E. S. Ali, *Procedia Chem.* **2016**, 19, 211-216.
32. X. Lu, H. Y. Tuan, B. A. Korgel, Y. Xia, *Chem. Eur. J.* **2008**, 14, 1584-1591.
33. B. K. Park, S. Jeong, D. Kim, J. Moon, S. Lim, J. S. Kim, *J. Colloid Interface Sci.* **2007**, 311, 417-424.
34. J. Song, D. Kim, D. Lee, *Langmuir* **2011**, 27, 13854-13860.
35. V. K. LaMer, R. H. Dinegar, *J. Am. Chem. Soc.* **1950**, 72, 4847-4854.
36. C. B. Whitehead, S. Özkar, R. G. Finke, *Chem. Mater.* **2019**, 31, 7116-7132.
37. W. Ostwald, *Z. Phys. Chem.* **1990**, 34, 495-503.
38. W. Zhao, M. A. Brook, Y. Li, *ChemBioChem* **2008**, 9, 2363-2371.
39. B. V. Derjaguin, T. N. Voropayeva, *J. Colloid Sci.* **1964**, 19, 113-135.
40. S. Mo, X. Shao, Y. Chen, Z. Cheng, *Sci. Rep*. **2016**, 6, 36836.
41. A. R. Studart, E. Amstad, L. J. Gauckler, *Langmuir* **2007**, 23, 1081-1090.
42. S. Laurent, D. Forge, M. Port, A. Roch, C. Robic, L. V. Elst, R. N. Muller, *Chem. Rev*. **2008**, 108, 2064-2110.
43. S. K. Bajpai, Y. M. Mohan, M. Bajpai, R. Tankhiwale, V. Thomas, *J. Nanosci. Nanotechnol.* **2007**, 7, 2994-3010.
44. C. Louis, O. Pluchery, Gold nanoparticles for physics, chemistry and biology, *Imperial College Press*, London, **2012**.
45. J. N. Leonard, América Precolombina, *TIME-LIFE International*, Amsterdam, **1971**.
46. V. W. von Hage, El imperio de los Incas, *Editorial Diana*, Mexico City, **1969**.
47. D. B. Harden, J. M. C. Toynbee, *Archaeologia* **1959**, 97, 179-212.

48. L. Kool, F. Dekker, A. Bunschoten, G. J. Smales, B. R. Pauw, A. H. Velders, V. Saggiomo, *Beilstein J. Nanotechnol.* **2020**, 11, 16-23.
49. M. C. Daniel, D. Astruc, *Chem. Rev.* **2004**, 104, 293-346.
50. D. A. Giljohann, D. S. Seferos, W. L. Daniel, M. D. Massich, P. C. Patel, C. A. Mirkin, *Angew. Chem. Int. Ed. Engl.* **2010**, 49, 3280-3294.
51. M. C. Gimeno, The Chemistry of Gold, *WILEY-VCH*, Weinheim, **2008**.
52. F. Mohr, Gold Chemistry, *WILEY-VCH*, Weinheim, **2009**.
53. C. D. De Souza, B. R. Nogueira, M. E. C. M. Rostelato, *J. Alloys Compd.* **2019**, 798, 714-740.
54. J. Turkevich, P. C. Stevenson, J. Hillier, *Discuss. Faraday Soc.* **1951**, 11, 55-75.
55. M. Brust, M. Walker, D. Bethell, D. J. Schiffrin, R. Whyman, *J. Chem. Soc., Chem. Commun.* **1994**, 801-802.
56. S. D. Perrault, W. C. Chan, *J. Am. Chem. Soc.* **2009**, 131, 17042-17043.
57. J. R. Navarro, F. Lerouge, C. Cepraga, G. Micouin, A. Favier, D. Chateau, M. T. Charreyre, P. H. Lanoë, C. Monnereau, F. Chaput, S. Marotte, Y. Leverrier, J. Marvel, K. Kamada, C. Andraud, P. L. Baldeck, S. Parola, *Biomaterials* **2013**, 34, 8344-8351.
58. S. Singh, A. S. Vidyarthi, V. K. Nigam, A. Dev, *Artif. Cells Nanomed. Biotechnol.* **2014**, 42, 6-12.
59. C.L. Baigent, G. Müller, *Experientia* **1980**, 36, 472-473.
60. K. Okitsu, M. Ashokkumar, F. Grieser, *J. Phys. Chem. B* **2005**, 109, 20673-20675.
61. M. H. Islam, M. T. Y. Paul, O. S. Burheim, B. G. Pollet, *Ultrason. Sonochem.* **2019**, 59, 104711.
62. Y. Zhou, C. Y. Wang, Y. R. Zhu, Z. Y. Chen, *Chem. Mater.* **1999**, 11, 2310-2312.
63. S. K. Seol, D. Kim, S. Jung, Y. Hwu, *Mater. Chem. Phys.* **2011**, 131, 331-335.
64. S. Ram, H. J. Fecht, *J. Phys. Chem. C* **2011**, 115, 7817–7828.
65. A. Q. Zhang, L. J. Cai, L. Sui, D. J. Qian, M. Chen, *Polym. Rev.* **2013**, 53, 240-276
66. N. G. Khlebtsov, L. A. Dykman, *J. Quant. Spectrosc. Radiat. Transf.* **2010**, 111, 1-35.
67. G. A. Wurtz, J. Hranisavljevic, G. P. Wiederrecht, *Nano Letters* **2003**, 3, 11, 1511-1516.
68. T. Zheng, S. Bott, Q. Huo, *ACS Appl. Mater. Interfaces* **2016**, 8, 21585-21594.
69. R. Xu, *Particuology* **2008**, 6, 112-115.
70. W. Haiss, N. T. K. Thanh, J. Aveyard, D. G. Fernig, *Anal. Chem.* **2007**, 79, 4215-4221.

71. A. A. Herzing, M. Watanabe, J. K. Edwards, M. Conte, Z. R. Tang, G. J. Hutchings, C. J. Kiely, *Faraday Discuss.* **2008**, 138, 337-351.
72. V. Petkov, Y. Peng, G. Williams, B. Huang, D. Tomalia, Y. Ren, *Phys. Rev. B* **2005**, 72, 195402.
73. Y. Chen, X. Gu, C. G. Nie, Z. Y. Jiang, Z. X. Xie, C. J. Lin, *Chem. Commun.* **2005**, 4181-4183.
74. S. Shukla, S. Seal, *Nanostr. Mat.* **1999**, 11, 1181-1193.
75. H. Valkenie, V. Malytskyi, P. Blond, M. Retout, A. Mattiuzzi, J. Goole, V. Raussens, I. Jabin, G. Bruylants, *Langmuir* **2017**, 33, 8253-8259.
76. L. B. Casabianca, *Solid State Nucl. Magn. Reson.* **2020**, 107, 101664.
77. H. Häkkinen, *Nature Chem.* **2012**, 4, 443-455.
78. L. Vigderman, E. R. Zubarev, *Adv. Drug Deliv. Rev.* **2013**, 65, 663-676.
79. M. Giersig, P. Mulvaney, *Langmuir* **1993**, 9, 3408-3413.
80. S. Engel, E. C. Fritz, B. J. Ravoo, *Chem. Soc. Rev.*, **2017**, 46, 2057.
81. D. V. Leff, L. Brandt, J. R. Heath, *Langmuir* **1996**, 12, 4723-4730.
82. G. Schmid, R. Pfeil, R. Boese, F. Bandermann, S. Meyer, G. H. M. Calis, J. W. A. van der Velden, *Chem. Ber.* **1981**, 114, 3634-3642.
83. B. Marchetti, Y. Joseph, H. Bertagnolli, *J. Nanopart. Res.* **2011**, 13, 3353-3362.
84. S. Eustis, M. A. El-Sayed, *Chem. Soc. Rev*. **2006**, 35, 209-217.
85. J. Z. Zhang, C. Noguez, *Plasmonics* **2008**, 3, 127-150.
86. A. M. Schwartzberg, T. Y. Olson, C. E. Talley, J. Z. Zhang, *J. Phys. Chem. B* **2006**, 110, 19935-19944.
87. Y. Yang, L. Xiong, J. Shi, M. Nogami, *Nanotechnology* **2006**, 17, 2670-2674.
88. C. J. Orendorff, L. A. Gearheart, N. R. Jana, C. J. Murphy, *Phys. Chem. Chem. Phys.* **2006**, 8, 165–170.
89. M. R. K. Ali, Y. Wu, M. A. El-Sayed, *J. Phys. Chem. C* **2019**, 123, 15375-15393.
90. G. M. F. Calixto, J. Bernegossi, L. M. de Freitas, C. R. Fontana, M. Chorilli, *Molecules* **2016**, 21, 342.
91. P. Mroz, J. T. Hashmi, Y. Y. Huang, N. Lange, M. R. Hamblin, *Expert Rev. Clin. Immunol.* **2011**, 7, 75-91.
92. J. Zheng, C. Zhou, M. Yu, J. Liu, *Nanoscale* **2012**, 4, 4073-4083.

93. J. H. Park, Y. T. Lim, O. O. Park, J. K. Kim, J. W. Yu, Y. C. Kim, *Chem. Mater.* **2004**, 16, 688-692.
94. J. Liu, P. N. Duchesne, M. Yu, X. Jiang, X. Ning, R. D. Vinluan, P. Zhang, J. Zheng, *Angew. Chem.* **2016**, 128, 9040-9044.
95. J. Zheng, C. W. Zhang, R. M. Dickson, *Phys. Rev. Lett.* **2004**, 93, 077402.
96. T. Pons, I. L. Medintz, K. E. Sapsford, S. Higashiya, A. F. Grimes, D. S. English, H. Mattoussi, *Nano Lett.* **2007**, 7, 3157-3164.
97. Y. C. Yeh, B. Creran, V. M. Rotello, *Nanoscale* **2012**, 4, 1871-1880.
98. A. Mooradian, *Phys. Rev. Lett.* **1969**, 22, 185.
99. M. B. Mohamed, V. Volkov, S. Link, M. A. El-Sayed, *Chem. Phys. Lett*. **2000**, 317, 517.
100. J. Zheng, C. Zhou, M. Yu, J. Liu, *Nanoscale* **2012**, 4, 4073.
101. S. C. Wei, P. H. Hsu, Y. F. Lee, Y. W. Lin, C. C. Huang, *ACS Appl. Mater. Interfaces* **2012**, 4, 2652-2658.
102. E. Priyadarshinia, N. Pradhan, *Sens. Actuator. B Chem.* **2017**, 238, 888-902.
103. R. Li, K. Wu, C. Liu, Y. Huang, Y. Wang, H. Fang, H. Zhang, C. Li, *Anal. Chem.* **2014**, 86, 5300-5307.
104. P. A. Rasheed, N. Sandhyarani, *Microchim. Acta* **2017**, 184, 981-1000.
105. M. Azharuddin, G. H. Zhu, D. Das, E. Ozgur, L. Uzun, A. P. F. Turner, H. K. Patra, *Chem. Commun.* **2019**, 55, 6964-6996.
106. Y. Li, H. J. Schluesener, S. Xu, *Gold Bull.* **2010**, 43, 29-41.
107. Y. Xiao, F. Patolsky, E. Katz, J. F. Hainfield, I. Willner, *Science* **2003**, 299, 1877-1881.
108. R. Elghanian, J. J. Storhoff, R. C. Mucic, R. L. Letsinger, C. A. Mirkin, *Science* **1997**, 277, 1078-1081.
109. S. Tang, I. Hewlett, *J. Infect. Dis.* **2010**, 201, 59-64.
110. S. M. Shawky, D. Bald. H. M. Azzazy, *Clin. Biochem.* **2010**, 43, 1163-1168.
111. T. Vo-Dinh, H. N. Wang, J. Scaffidi, *J. Biophotonics* **2010**, 3, 89-102.
112. H. H. Jeong, E. Choi, E. Ellis, T. C. Lee, *J. Mater. Chem. B* **2019**, 7, 3480-3496.
113. A. Pramanik, Y. Gao, S. Patibandla, D. Mitra, M. G. McCandless, L. A. Fassero, K. Gates, R. Tandon, P. C. Ray, *Nanoscale Adv.* **2021**, 3, 1588-1596.
114. Y. Li, Y. Zhang, M. Zhao, Q. Zhou, L. Wang, H. Wang, X. Wang, L. Zhan, *Chem. Commun.* **2016**, 52, 3959–3961.
115. M. A. Fuller, I. Köper, *Nano Convergence* **2019**, 6, 11.

116. H. Lusic, M. W. Grinstaff, *Chem. Rev.* **2013**, 113, 1641-1666.
117. Y. Dou, Y. Guo, X. Li, X. Li, S. Wang, L. Wang, G. Lv, X. Zhang, H. Wang, X. Gong, J. Chang, *ACS Nano* **2016**, 10, 2536-2548.
118. S. Mallidi, S. Kim, A. Karpiouk, P.P. Joshi, K. Sokolov, S. Emelianov, *Photoacoustics* **2015**, 3, 26-34.
119. P. Huang, J. Lin, W. Li, P. Rong, Z. Wang, S. Wang, X. Wang, X. Sun, M. Aronova, G. Niu, R.D. Leapman, Z. Nie, X. Chen, *Angew. Chem. Int. Ed.* **2013**, 52, 13958-13964.
120. C. Loo, A. Lowery, N. Halas, J. West and R. Drezek, *Nano Lett.* **2005**, 5, 709-711.
121. J. Olesiak-Banska, M. Waszkielewicz, P. Obstarczyka, M. Samoc, *Chem. Soc. Rev*. **2019**, 48, 4087-4117.
122. H. L. Perry, R. M. Botnar, J. D. Wilton-Ely, *Chem. Commun.* **2020**, 56, 4037-4046.
123. D. Coluccia, C. A. Figueiredo, M. Y. Wu, A. N. Riemenschneider, R. Diaz, A. Luck, C. Smith, S. Das, C. Ackerley, M. O'Reilly, *Nanomed. Nanotechnol. Biol. Med.* **2018**, 14, 1137-1148.
124. E. Zhang, A. Fu, Y. Yang, *Int. J. Nanomedicine* **2015**, 10, 2115-2124.
125. X. Qian, X. H. Peng, D. O. Ansari, Q. Yin-Goen, G. Z. Chen, D. M. Shin, L. Yang, A. N. Young, M. D. Wang, S. Nie, *Nat. Biotechnol.* **2008**, 26, 83-90.
126. R. Singh, J. W. Lillard Jr, *Exp. Mol. Pathol.* **2009**, 86, 215-23.
127. M. Singh, D. C. Harris-Birtill, S. R. Markar, G. B. Hanna, D. S. Elson, *Nanomedicine* **2015**, 11, 2083-2098.
128. H. Gu, P. L. Ho, E. Tong, L. Wang, B. Xu, *Nano Lett.* **2003**, 3, 1261-1263.
129. M. C. Bowman, T. E. Ballard, C. J. Ackerson, D. L. Feldheim, D. M. Margolis, C. Melander, *J. Am. Chem. Soc.* **2008**, 130, 6896-6897.
130. I. Fratoddi, I. Venditti, C. Cametti, M. V. Russo, *J. Mater. Chem. B* **2014**, 2, 4204-4220.
131. K. C. Hribar, M. H. Lee, D. Lee, J. A. Burdick, *ACS Nano* **2011**, 5, 2948–2956.
132. S. Aryal, J. J. Grailer, S. Pilla, D. A. Steeber, S. Gong, *J. Mater. Chem.* **2009**, 19, 7879-7884.
133. M. Cordeiro, F. F. Carlos, P. Pedrosa, A. Lopez, P. V. Baptista, *Diagnostics* **2016**, 6, 43.
134. L. Dykman, N. Khlebtsov, *Chem. Soc. Rev.* **2012**, 41, 2256-2282.
135. M. Oishi, J. Nakaogami, T. Ishii, Y. Nagasaki, *Chem. Lett.* **2006**, 35, 1046-1047.
136. T. Kawano, M. Yamagata, H. Takahashi, Y. Niidome, S. Yamada, Y. Katayama, T. Niidome, *J. Control. Release* **2006**, 111, 382-389.

137. W. Mao, H. S. Kim, Y. J. Son, S. R. Kim, H. S. Yoo, *J. Control. Release* **2018**, 269, 52-62.
138. S. Ruan, M. Yuan, L. Zhang, G. Hu, J. Chen, X. Cun, Q. Zhang, Y. Yang, Q. He, H. Gao, *Biomaterials* **2015**, 37, 425-435.
139. Y. Fu, Q. Feng, Y. Chen, Y. Shen, Q. Su, Y. Zhang, X. Zhou, Y. Cheng, *Mol. Pharmaceutics* **2016**, 13, 3308-3317.
140. E. C. Dreaden, A. M. Alkilany, X. Huang, C. Murphy, M. A. El-Sayed, *Chem. Soc. Rev.* **2012**, 41, 2740-2779.
141. A. M. Alkilany, R. L. Frey, J. L. Ferry and C. J. Murphy, *Langmuir* **2008**, 24, 10235-10239.
142. Y. Chen, N. Li, Y. Yang, Y. Liu, *RSC Adv.* **2015**, 5, 8938-8941.
143. H. Shelley, R. J. Babu, *J. Pharm. Sci.* **2018**, 107, 1741-1753.
144. H. Zhao, Z. Y. Lin, L. Yildirimer, A. Dhinakar, X. Zhao, J. Wu, *J. Mater. Chem. B* **2016**, 4, 4060-4071.
145. C. K. Kim, P. Ghosh, C. Pagliuca, Z. J. Zhu, S. Menichetti, V. M. Rotello, *J. Am. Chem. Soc.* **2009**, 131, 1360-1361.
146. M. Hrubý, S. K. Filippov, P. Štěpánek, *Eur. Polym. J.* **2015**, 65, 82-97.
147. X. Qin, Y. Li, *ChemBioChem* **2020**, 21, 1236-1253.
148. M. Alle, G. B. Reddy, T. H. Kim, S. H. Park, J. C. Kim, J.C. *Carbohydr. Polym.* **2020**, 229, 115511.
149. M. Saito, H. Saitoh, *Biosci. Biotechnol. Biochem.* **2012**, 76, 1777-1780.
150. J. A. Fortune, T. I. Novobrantseva, A. M. Klibanov, *J. Drug Delivery* **2011**, 2011, 204058.
151. M. S. Yavuz, Y. Cheng, C. M. Cobley, Q. Zhang, M. Rycenga, J. Xie, C. Kim, K. H. Song, A. G. Schwartz, L. V. Wang, Y. Xia, *Nat. Mater.* **2009**, 8, 935-939.
152. D. G. Moon, S. W. Choi, X. Cai, W. Y. Li, E. C. Cho, U. Jeong, L. V. Wang, Y. A. Xia, *J. Am. Chem. Soc*. **2011**, 133, 4762-4765.
153. P. Singh, S. Pandit, V. R. S. S. Mokkapati, A. Garg, V. Ravikumar, I. Mijakovic, *Int. J. Mol. Sci.* **2018**, 19, 1979.
154. M. Ferrari, *Nat. Rev. Cancer* **2005**, 5, 161-171.
155. X. Hu, Y. Zhang, T. Ding, J. Liu, H. Zhao, *Front. Bioeng. Biotechnol*. **2020**, DOI: 10.3389/fbioe. 2020.00990.
156. H. Maeda, H. Nakamura, J. Fang, *Adv. Drug Deliv. Rev*. **2013**, 65, 71-79.
157. C. Minelli, S. B. Lowe, M. M. Stevens, *Small* **2010**, 6, 2336-2357.

158. H. Kim, S. Beack, S. Han, M. Shin, T. Lee, Y. Park, K. S. Kim, A. K. Yetisen, S. H. Yun, W. Kwon, S. K. Hahn, *Adv. Mater.* **2018**, 30, 1701460.
159. X. Cheng, R. Sun, L. Yin, Z. Chai, H. Shi, M. Gao, *Adv. Mater.* **2017**, 29, 1604894.
160. S. Lal, S. E. Clare, N. J. Halas*, Acc. Chem. Res.* **2008**, 41, 1842-1851.
161. S. Pinel, N. Thomas, C. Boura, M. Barberi-Heyob, *Adv. Drug Deliv. Rev.* **2019**, 138, 344-357.
162. D. Kim. Y. Y. Jeong, S. Jon, *ACS Nano* **2010**, 4, 3689-3696.
163. K. Sokolov, M. Follen, J. Aaron, I. Pavlova, A. Malpica, R. Lotan, R. Richards-Kortum, *Cancer Res.* **2003**, 63, 1999-2004.
164. F. Charbgoo, M. Nejabat, K. Abnous, F. Soltani, S.M. Taghdisi, M. Alibolandi, W. Thomas Shier, T. W. J. Steele, M. Ramezani, *J. Control. Release* **2018**, 272, 39-53.
165. L. Shang, K. Nienhaus, G. U. Nienhaus, *J. Nanobiotechnology* **2014**, 12, 5.
166. S. Behzadi, V. Serpooshan, W. Tao, M. A. Hamaly, M. Y. Alkawareek, E. D. Dreaden, D. Brown, A. M. Alkilany, O. C. Farokhzad, M. Mahmoudi, *Chem. Soc. Rev.* **2017**, 46, 4218-4244.
167. B. D. Chithrani, W. C. W. Chan, *Nano Lett.* **2007**, 7, 1542-1550.
168. S. Huo, S. Jin, X. Ma, X. Xue, K. Yang, A. Kumar, P.C. Wang, J. Zhang, Z. Hu, X. J. Liang, *ACS Nano* **2014**, 8, 5852-5862.
169. J. A. Ryan, K. W. Overton, M. E. Speight, C.N. Oldenburg, L. Loo, W. Robarge, S. Franzen, D.L. Feldheim, *Anal. Chem.* **2007**, 79, 9150-9159.
170. M. Kodiha, Y. M. Wang, E. Hutter, D. Maysinger, U. Stochaj, *Theranostics* **2015**, 5, 357-370.
171. S. G. Elci, Y. Jiang, B. Yan, S. T. Kim, K. Saha, D. F. Moyano, G. Y. Tonga, L. C. Jackson, V. M. Rotello, R. W. Vachet, *ACS Nano* **2016**, 10, 5536-5542.
172. Y. S. Chen, Y. C. Hung, I. Liau, G. S. Huang, *Nanoscale Res. Lett.* **2009**, 4, 858-864.
173. O. B. Adewale, H. Davids, L. Cairncross, S. Roux, *Int. J. Toxicol*. **2019**, 38, 357-384.
174. A. M. Alkilany, P. K. Nagaria, C. R. Hexel, T. J. Shaw, C. J. Murphy, M. D. Wyatt, *Small* **2009**, 5, 701-708.
175. J. M. De la Fuente, C. C. Berry, *Bioconjugate Chem*. **2005**, 16, 1176-1180.
176. A. Kroll, M. H. Pillukat, D. Hahn, J. Schnekenburger, *Eur. J. Pharm. Biopharm.* **2009**, 72, 370-377.

177. M. A. Vetten, N. Tlotleng, D. T. Rascher, A. Skepu, F. K. Keter, K. Boodhia, L. A. Koekemoer, C. Andraos, R. Tshikhudo, M. Gulumian, *Part. Fibre Toxicol.* **2013**, 10, 50.
178. N. M. Sanabria, M. Gulumian, *J. Nanobiotechnol.* **2017**, 15, 72.
179. D. Bonvin, H. Hofmann, M. M. Ebersold, *Analyst* **2017**, 142, 2338-2342.
180. Q. Gu, E. Cuevas, S. F. Ali, M. G. Paule, V. Krauthamer, Y. Jones, Y. Zhang, *Int. J. Toxicol.* **2019**, 38, 385-394.
181. D. R. Nogueira, M. Mitjans, C. M. B. Rolim, M. P. Vinardell, *Nanomaterials* **2014**, 4, 454-484.
182. N. M. Monaheng, S. Parania, M. Gulumian, O. S. Oluwafemi, *Toxicol. Res.* **2019**, 8, 868-874.
183. R. Chen, J. Qiao, R. Bai, Y. Zhao, C. Chen, *Anal. Bioanal. Chem.* **2018**, 410, 6051-6066.
184. C. Hoskins, L. Wang, W. P. Cheng, A. Cuschieri, *Nanoscale Res. Lett.* **2012**, 7, 77.
185. J. Ponti, A. Kinsner-Ovaskainen, H. Norlen, S. Altmeyer, A. Cristina, A. Bogni. Luxembourg: Joint Research Centre – Institute for Health and Consumer Protection **2014**. Report No.: 978-92-79-44677-1 (PDF), 1831-9424 (online).
186. M. Yu, J. Zheng, *ACS Nano* **2015**, 9, 6655-6674.
187. M. Longmire, P. L. Choyke, H. Kobayashi, *Nanomedicine* **2008**, 3, 703-717.
188. C. Uhlmann, L. M. Kuhn, J. Tigges, E. Fritsche, U. D. Kahlert, *Curr. Protoc. Stem Cell Biol.* **2020**, 52, e102.
189. T. Koga, I. A. Chaim, J. A. Benitez, S. Markmiller, A. D. Parisian, R. F. Hevner, K. M. Turner, F. M. Hessenauer, M. D'Antonio, N. D. Nguyen, S. Saberi, J. Ma, S. Miki, A.D. Boyer, J. Ravits, K. A. Frazer, V. Bafna, C.C. Chen, P. S. Mischel, G. W. Yeo, F. B. Furnari, *Nat. Commun.* **2020**, 11, 550.
190. Q. T. Ostrom, H. Gittleman, G. Truitt, A. Boscia, C. Kruchko, J. S. Barnholtz-Sloan, *Neuro Oncol.* **2018**, 20, iv1–iv86.
191. K. Anjum, B. I. Shagufta, S. Q. Abbas, S. Patel, I. Khan, S. A. A. Shah, N. Akhter, S. S. U. Hassan, *Biomed. Pharmacother.* **2017**, 92, 681-689.
192. D. N. Louis, A. Perry, G. Reifenberger, A. von Deimling, D. Figarella-Branger, W. K. Cavenee, H. Ohgaki, O. D. Wiestler, P. Kleihues, D. W. Ellison, *Acta Neuropathol.* **2016**, 131, 803-820.
193. V. Rajaratnam, M. M. Islam, M. Yang, R. Slaby, H. Martinez-Ramirez, S. P. Mirza, *Cancers* **2020**, 12, 937.

194. R. G. Verhaak, K. A. Hoadley, E. Purdom, V. Wang, Y. Qi, M. D. Wilkerson, C. R. Miller, L. Ding, T. Golub, J. T. Mesirov, G. Alexe, M. Lawrence, M. O'Kelly, P. Tamayo, B. A. Weir, G. S. Winckler, S. Gupta, L. Jakkula, H. S. Feiler, J. G. Hodgson, C. D. James, J. N. Sarkaria, C. Brennan, A. Kahn, P. T. Spellman, R. K. Wilson, T. P. Speed, J. W. Gray, M. Meyerson, G. Getz, C. M. Perou, D. N. Hayes, *Cancer Cell* **2010**, 17, 98-110.

195. L. B. Wang, A. Karpova, M. A. Gritsenko, J. E. Kyle, S. Cao, Y. Li, D. Rykunov, A. Colaprico, J. H. Rothstein, R. Hong, V. Stathias, M. Cornwell, F. Petralia, Y. Wu, B. Reva, K. Krug, P. Pugliese, E. Kawaler, L. K. Olsen, W. W. Liang, X. Song, Y. Dou, M. C. Wendl, W. Caravan, W. Liu, D. C. Zhou, J. Ji, C. F. Tsai, V. A. Petyuk, J. Moon, W. Ma, R. K. Chu, K. K. Weitz, R. J. Moore, M. E. Monroe, R. Zhao, X. Yang, S. Yoo, A. Krek, A. Demopoulos, H. Zhu, M. A. Wyczalkowski, J. F. McMichael, B. L. Henderson, C. M. Lindgren, H. Boekweg, S. Lu, J. Baral, L. Yao, K. G. Stratton, L. M. Bramer, E. Zink, S. P. Couvillion, K. J. Bloodsworth, S. Satpathy, W. Sieh, S. M. Boca, S. Schürer, F. Chen, M. Wiznerowicz, K. A. Ketchum, E. S. Boja, C. R. Kinsinger, A. I. Robles, T. Hiltke, M. Thiagarajan, A. I. Nesvizhskii, B. Zhang, D. R. Mani, M. Ceccarelli, X. S. Chen, S. L. Cottingham, Q. K. Li, A. H. Kim, D. Fenyö, K. V. Ruggles, H. Rodriguez, M. Mesri, S. H. Payne, A. C. Resnick, P. Wang, R. D. Smith, A. Lavarone, M. G. Chheda, J. S. Barnholtz-Sloan, K. D. Rodland, T. Liu, L. Ding, *Cancer Cell* **2021**, 39, 509-528.

196. E. Perez, D. Capper, *Neuropath. Appl. Neuro*. **2020**, 46, 28-47.

197. S. K. Singh, I. D. Clarke, M. Terasaki, V. E. Bonn, C. Hawkins, J. Squire, P. B. Dirks, *Cancer Res.* **2003**, 63, 5821–5828.

198. A. Dirkse, A. Golebiewska, T. Buder, P. V. Nazarov, A. Muller, S. Poovathingal, N. H. C. Brons, S. Leite, N. Sauvageot, D. Sarkisjan, M. Seyfrid, S. Fritah, D. Stieber, A. Michelucci, F. Hertel, C. Herold-Mende, F. Azuaje, A. Skupin, R. Bjerkvig, A. Deutsch, A. Voss-Böhme, S. P. Niclou, *Nat. Commun.* **2019**, 10, 1787.

199. R. C. Gimple, S. Bhargava, D. Dixit, J. N. Rich, *Genes Dev.* **2019**, 33, 591-609.

200. M. L. Suvà, I. Tirosh, *Cancer Cell* **2020**, 37, 630-636.

201. J. Roche, *Cancers* **2018**, 10, 52.

202. M. K. Jolly, M. Boareto, B. Huang, D. Jia, M. Lu, E. Ben-Jacob, J. N. Onuchic, H. Levine, *Front. Oncol.* **2015**, 5, 155.

203. D. Lathia, S. C. Mack, E. E. Mulkearns-Hubert, C. L. L. Valentim, J. N. Rich, *Genes Dev.* **2015**, 29, 1203-1217.

204. Z. Li, S. Bao, Q. Wu, H. Wang, C. Eyler, S. Sathornsumetee, Q. Shi, Y. Cao, J. Lathia, R. E. McLendon, A. B. Hjelmeland, J. N. Rich, *Cancer Cell* **2009**, 15, 501-513.
205. G. Liu, X. Yuan, Z. Zeng, P. Tunici, H. Ng, I. R. Abdulkadir, L. Lu, D. Irvin, K. L. Black, J. S. Yu, *Mol. Cancer* **2006**, 5, 67.
206. K. L. Mooney, W. Choy, S. Sidhu, P. Pelargos, T. T. Bui, B. Voth, N. Barnette, I. Yang, *J. Clin. Neurosci.* **2016**, 34, 1-5.
207. P. Ellis, B. M. Fagan, S. T. Magness, S. Hutton, O. Taranova, S. Hayashi, A. McMahon, M. Rao, L. Pevny, *Dev. Neurosci.* **2004**, 26, 148-165.
208. L. Y. W. Bourguignon, C. Earle, G. Wong, C. C. Spevak, K. Krueger, *Oncogene* **2012**, 31, 149-160.
209. M. J. Son, K. Woolard, D. H. Nam, J. Lee, H. A. Fine, *Cell Stem Cell* **2009**, 4, 440-452.
210. S. D. Precilla, S. S. Kuduvalli, A. T. Sivasubramanian, *Cell Biol. Int.* **2021**, 45, 18-53.
211. N. Galldiks, I. Law, W. B. Pope, J. Arbizu, K. J. Langen, *Neuroimage Clin.* **2017**, 13, 386-394.
212. Y. Zhou, Z. Peng, E. S. Seven, R. M. Leblanc, *J. Control. Release* **2018**, 270, 290-303.
213. W. M. Pardridge, *Clin. Pharmacol. Ther.* **2015**, 97, 347-361.
214. R. Stupp, W. P. Mason, M. J. van den Bent, M. Weller, B. Fisher, M. J. B. Taphoorn, K. Belanger, A. A. Brandes, C. Marosi, U. Bogdahn, J. Curschmann, R. C. Janzer, S. K. Ludwin, T. Gorlia, A. Allgeier, D. Lacombe, J. G. Cairncross, E. Eisenhauer, R. Mirimanoff, *N. Engl. J. Med.* **2005**, 352, 987-996.
215. M. X. Liu, J. Zhong, N. N. Dou, M. Visocchi, G. Gao, *Acta Neurochir. Suppl.* **2017**, 124, 303-308.
216. M. Li, Y. Cui, X. Li, Y. Guo, B. Wang, J. Zhang, J. Xu, S. Han, X. Shi, *Technol. Cancer Res. Treat.* **2016**, 15, 618-624.
217. P. Sampath, L. D. Rhines, F. DiMeco, B. M. Tyler, M. C. Park, H. Brem, *J. Neurooncol.* **2006**, 80, 9-17.
218. O. Maksimenko, J. Malinovskaya, E. Shipulo, N. Osipova, V. Razzhivina, D. Arantseva, O. Yarovaya, U. Mostovaya, A. Khalansky, V. Fedoseeva, A. Alekseeva, L. Vanchugova, M. Gorshkova, E. Kovalenko, V. Balabanyan, P. Melnikov, V. Baklaushev, V. Chekhonin, J. Kreuter, S. Gelperina, *Int. J. Pharm.* **2019**, 572, 118733.
219. R. Stupp, S. Taillibert, A. Kanner, W. Read, D. M. Steinberg, B. Lhermitte, S. Toms, A. Idbaih, M. S. Ahluwalia, K. Fink, F. Di Meco, F. Lieberman, J. J. Zhu, G. Stragliotto, D. D.

Tran, S. Brem, A. F. Hottinger, E. D. Kirson, G. Lavy-Shahaf, U. Weinberg, C. Y. Kim, S. H. Paek, G. Nicholas, J. Bruna, H. Hirte, M. Weller, Y. Palti, M. E. Hegi, Z. Ram, *JAMA* **2017**, 318, 2306-2316.

220. D. Garnier, O. Renoult, M. C. Alves-Guerra, F. Paris, C. Pecqueur, *Front. Oncol.* **2019**, 9, 118.
221. M. J. Seltzer, B. D. Bennett, A. D. Joshi, P. Gao, A. G. Thomas, D. V. Ferraris, T. Tsukamoto, C. J. Rojas, B. S. Slusher, J. D. Rabinowitz, C. V. Dang, G. J. Riggins, *Cancer Res.* **2010**, 70, 8981-8987.
222. I. Nakano, *Expert Opin. Ther. Targets* **2014**, 18, 1233-1236.
223. W. P. Katt, M. J. Lukey, R. A. Cerione, *Cell Chem. Biol*. **2019**, 26, 1197-1199.
224. E. S. Reckzeh, G. Karageorgis, M. Schwalfenberg, J. Ceballos, J. Nowacki, M. C. M. Stroet, A. Binici, L. Knauer, S. Brand, A. Choidas, C. Strohmann, S. Ziegler, H. Waldmann, *Cell Chem. Biol.* **2019**, 26, 1214-1228.
225. O. Warburg, *Science* **1956**, 124, 269-270.
226. J. De Lartigue, *J. Community Support. Oncol*. **2018**, 16, e47-e52.
227. U. D. Kahlert, M. Cheng, K. Koch, L. Marchionni, X. Fan, E. H. Raabe, J. Maciaczyk, K. Glunde, C. G. Eberhart, *Int. J. Cancer* **2016**, 138, 1246-1255.
228. K. Koch, R. Hartmann, J. Tsiampali, C. Uhlmann, A. C. Nickel, X. He, M. A. Kamp, M. Sabel, R. A. Barker, H. J. Steiger, D. Hänggi, D. Willbond, J. Maciaczyk, U. D. Kahlert, *Cell Death Discov.* **2020**, 6, 20.
229. Clinical Trial ID: NCT03057600. Study of CB-839 in Combination w/ Paclitaxel in Patients of African Ancestry and Non-African Ancestry With Advanced TNBC, available online: https://clinicaltrials.gov/ct2/show/NCT03057600 (accessed on March 3rd, 2021).
230. Clinical Trial ID: NCT04265534. A Study of Telaglenastat (CB-839) With Standard-of-Care Chemoimmunotherapy in 1L KEAP1/NRF2-Mutated, Nonsquamous NSCLC (KEAPSAKE), available online: https://clinicaltrials.gov/ct2/show/NCT04265534 (accessed on March 3rd, 2021).
231. Clinical Trial ID: NCT04607512. Study to Evaluate the ECG Effects of Telaglenastat in Healthy Adult Subjects, available online: https://clinicaltrials.gov/ct2/show/NCT04607512 (accessed on March 3rd, 2021).
232. M. I. Gross, S. D. Demo, J. B. Dennison, L. Chen, T. Chernov-Rogan, B. Goyal, J. R. Janes, G. J. Laidig, E. R. Lewis, J. Li, A. L. MacKinnon, F. Parlati, M. L. M. Rodriguez, P.

J. Shwonek, E. B. Sjogren, T. F. Stanton, T. Wang, J. Yang, F. Zhao, M. K. Bennett, *Mol. Cancer Ther*. **2014**, 13, 890-901.

233. Q. Huang, C. Stalnecker, C. Zhang, L. A. McDermott, P. Iyer, J. O'Neill, S. Reimer, R. A. Cerione, W. P. Katt, *J. Biol. Chem*., 2018, **293**, 3535-3545.
234. S. C. Zimmermann, E. F. Wolf, A. Luu, A. G. Thomas, M. Stathis, B. Poore, C. Nguyen, A. Le, C. Rojas, B. S. Slusher, T. Tsukamoto, *ACS Med. Chem. Lett*., 2016, **7**, 520-524.
235. C. Yu, R. Morshed, B. Auffinger, A. L. Tobias, M. S. Lesniak, *Adv. Drug Delivery Rev.* **2014**, 66, 42-57.
236. M. H. Mohd-Zahid, R. Mohamud, C. A. C. Abdullah, J. Lim, H. Alem, W. N. W. Hanaffi, I. Z. Alias, *RSC Adv.* **2020**, 10, 973-985.
237. M. Mukhtar, M. Bilal, A. Rahdar, M. Barani, R. Arshad, T. Behl, C. Brisc, F. Banica, S. Bungau, *Chemosensors* **2020**, 8, 117.
238. N. Huang, S. Cheng, X. Zhang, Q. Tian, J. Pi, J. Tang, Q. Huang, F. Wang, J. Chen, Z. Xie, *Nanotechnol. Biol. Med*. **2017**, 13, 83-93.
239. Y. Cheng, Q. Dai, R. A. Morshed, X. Fan, M. L. Wegscheid, D. A. Wainwright, Y. Han, L. Zhang, B. Auffinger, A. L. Tobias, E. Rincon, B. Thaci, A. U. Ahmed, P. C. Warnke, C. He, M. S. Lesniak, *Small* **2014**, 10, 5137-5150.
240. Q. Feng, Y. Shen, Y. Fu, M. E. Muroski, P. Zhang, Q. Wang, C. Xu, M. S. Lesniak, G. Li, Y. Cheng, *Theranostics* **2017**, 7, 1875-1889.
241. S. Dixit, K. Miller, Y. Zhu, E. McKinnon, T. Novak, M. E. Kenney, A. M. Broome, *Mol. Pharm.* **2015**, 12, 3250-3260.
242. X. Gao, Y. Qi, Z. Liu, M. Ke, X. Zhou, S. Li, J. Zhang, Z. Ren, C. Liang, M. Ying, *Adv. Mater.* **2017**, 29.
243. K. Saha, S. S. Agasti, C. Kim, X. Li, V. M. Rotello, *Chem. Rev.* **2012**, 112, 2739-2779.
244. H. Karabeber, R. Huang, P. Iacono, J. M. Samii, K. Pitter, E. C. Holland, M. F. Kircher, *ACS Nano* **2014**, 8, 9755-9766.
245. J. F. Hainfeld, H. M. Smilowitz, M. J. O'Connor, F. A. Dilmanian, D. N. Slatkin, *Nanomedicine (London)* **2013**, 8, 1601-1609.
246. J. Choi, J. Yang, J. Park, E. Kim, J. S. Suh, Y. M. Huh, S. Haam, *Adv. Funct. Mater.* **2011**, 21, 1082-1088.
247. H. Li, W. Yang, *Ch. Chem. Lett.* **2013**, 24, 545-552.

248. Y. Ding, Z. Jiang, K. Saha, C. S. Kim, S. T. Kim, R. F. Landis, V. M. Rotello, *Mol. Ther.* **2014**, 22, 1075-1083.
249. O. Gallego, *Curr. Oncol.* **2015**, 22, 273-281.
250. B. Giesen, A. C. Nickel, A. Garzón-Manjón, A. Vargas-Toscano, C. Scheu, U. D. Kahlert, C. Janiak, *J. Inorg. Biochem.* **2020**, 203, 110952.
251. B. Giesen, A. C. Nickel, J. Barthel, U. D. Kahlert, C. Janiak, *Pharmaceutics* **2021**, 13, 295.
252. J. Tsiampali, S. Neumann, B. Giesen, K. Koch, D. Maciaczyk, C. Janiak, D. Hänggi, J. Maciaczyk, *Pharmaceuticals* **2020**, 13, 378.
253. S. Öztürk, Y. X. Xiao, D. Dietrich, B. Giesen, J. Barthel, J. Ying, X. Y. Yang, C. Janiak, *Beilstein J. Nanotechnol.* **2020**, 11, 770–781.
254. A. Schmitz, H. Meyer, M. Meischein, A. Garzón-Manjón, L. Schmolke, B. Giesen, C. Schlüsener, P. Simon, Y. Grin, R. A. Fischer, C. Scheu, A. Ludwig, C. Janiak, *RSC Adv*. **2020**, 10, 12891-12899.
255. C. Schlüsener, D. N. Jordan, M. Xhinovci, T. J. Matemb Ma Ntep, A. Schmitz, B. Giesen, C. Janiak, *Dalton Trans*. **2020**, 49, 7373-7383.
256. K. Klauke, A. Schmitz, A. C. Swertz, B. B. Beele, B. Giesen, C. Schlüsener, C. Janiak, F. Mohr, *New J. Chem.* **2020**, 44, 7719-7726.
257. L. Schmolke, B. Gregori, B. Giesen, A. Schmitz, J. Barthel, L. Staiger, R. A. Fischer, A. J. von Wangelin, C. Janiak, *New J. Chem.* **2019**, 43, 16583-16594.
258. M. Thomas, A. M. Klibanov, *Proc. Natl. Acad. Sci. U.S.A.*, **2003**, 100, 9138-9143.
259. S. D. Perrault, C. Walkey, T. Jennings, H. C. Fischer, W. C. Chan, *Nano Lett.* **2009**, 9, 1909-1915.
260. D. Y. Joh, L. Sun, M. Stangl, A. A. Zaki, S. Murty, P. P. Santoiemma, J. J. Davis, B. C. Baumann, M. Alonso-Basanta, D. Bhang, G. D. Kao, A. Tsourkas, J. F. Dorsey, *PLOS ONE* **2013**, 8, e62425.
261. D. Pissuwan, S. M. Valenzuela, M. B. Cortie, *Biotechnol. Genet. Eng. Rev.* **2008**, 25, 93-112.
262. K. L. Kelly, E. Coronado, L. L. Zhao, G. C. Schatz, *J. Phys. Chem. B* **2003**, 107, 668-677.
263. N. Harris, M. J. Ford, P. Mulvaney, M. B. Cortie, *Gold Bull.* **2008**, 41, 5-14.
264. B.P. Khanal, E.R. Zubarev, *Angew. Chem. Int. Ed.* **2007**, 46, 2195-2198.
265. R. Kumar, L. Binetti, T. H. Nguyen, L. S. M. Alwis, A. Agrawal, T. Sun, K. T. V. Grattan, *Sci Rep*. **2019**, 9, 17469.

266. Y. A. Attia, D. Buceta, F. G. Requejo, L. J. Giovanetti, M. A. López-Quintela, *Nanoscale* **2015**, 7, 11273-11279.
267. M. R. Soboleski, J. Oaks, W. P. Halford, *FASEB J.* **2005**, 19, 440-442.
268. O. Boussif, F. Lezoualc'h, M. A. Zanta, M. D. Mergny, D. Scherman, B. Demeneix, J. P. Behr, *Proc. Natl. Acad. Sci.* **1995**, 92, 7297-7301.
269. S. Honary, F. Zahir, *Trop. J. Pharm. Res.* **2013**, 12, 265-273.
270. N. M. Y. Zhang, M. Qi, Z. Wang, Z. Wang, M. Chen, K. Li, P. Shum, L. Wei, *Sens. Actuators B Chem.* **2019**, 286, 429-436.
271. S. Pande, S. K. Ghosh, S. Praharaj, S. Panigrahi, S. Basu, S. Jana, A. Pal, T. Tsukuda, T. Pal, *J. Phys. Chem. C* **2007**, 111, 10806-10813.
272. P. Brugnerotto, T. R. Silva, D. Brondani, E. Zapp, I. C. Vieira, *Electroanalysis* **2017**, 29, 1031-1037.
273. Y. Liu, K. B. Male, P. Bouvrette, J. H. T. Luong, *Chem. Mater.* **2003**, 15, 4172-4180.
274. G. Palumbo, *Expert Opin. Drug Deliv.* **2007**, 4, 131-148.
275. N. Merclin, P. Beronius, *Eur. J. Pharm. Sci.* **2004**, 21, 347-350.
276. M. K. K. Oo, X. Yang, H. Du, H. Wang, *Nanomedicine (Lond.)* **2008**, 3, 777-786.
277. A. K. Suwala, K. Koch, D. H. Rios, P. Aretz, C. Uhlmann, I. Ogorek, J. Felsberg, G. Reifenberger, K. Köhrer, R. Deenen, H. J. Steiger, U. D. Kahlert, J. Maciaczyk, *Oncotarget* **2018**, 9, 22703-22716.
278. S. Y. Hwang, X. Deng, S. Byun, C. Lee, S. J. Lee, H. Suh, J. Zhang, Q. Kang, T. Zhang, K. D. Westover, A. Mandinova, S. W. Lee, *Cell Rep.* **2016**, 16, 28-36.
279. W. Zhang, J. Xie, B. Rao, M. Luo, *J. Org. Chem.* **2015**, 80, 3504-3511.
280. E. Pretsch, T. Clerc, J. Seibl, W. Simon, Strukturaufklärung organischer Verbindungen mit spektroskopischen Methoden, *Springer-Verlag*, Berlin Heidelberg, **1981**.
281. F. Chemat, E. Esveld, *Chem. Engl. Technol.* **2001**, 24, 735-744.
282. D. R. Baghurst, D. M. P. Mingos, *J. Chem. Soc., Chem. Commun*. **1992**, 6, 674-677.
283. X. Fan, L. Khaki, T. S. Zhu, M. E. Soules, C. E. Talsma, N. Gul, C. Koh, J. Zhang, Y. M. Li, J. Maciaczyk, G. Nikkhah, F. Dimeco, S. Piccirillo, A. L. Vescovi, C. G. Eberhart, *Stem Cells* **2010**, 28, 5-16.
284. U. D. Kahlert, A. K. Suwala, K., Koch, M. Natsumeda, B. A. Orr, M. Hayashi, J. Maciaczyk, C. G. Eberhart, *J. Neuropathol. Exp. Neurol.* **2015**, 74, 889-900.
285. Ernst Ruska-Centre for Microscopy and Spectroscopy with Electrons. FEI Tecnai G2 F20. *J. Large-Scale Res. Facil.* **2016**, 2, 77.